UNIVERSITÀ DEGLI STUDI DI TRIESTE

XXXIII CICLO DEL DOTTORATO DI RICERCA IN FISICA

Progetto di ricerca cofinanziato dal Fondo Sociale Europeo - Programma Operativo della regione Friuli Venezia Giulia 2014/2020 - Asse 3 istruzione e formazione
Borsa FSE - EUSAIR/EUSALP

Exploitation of the potential of Free Electron Lasers through innovative experiments

Settore scientifico-disciplinare: **FISICA DELLA MATERIA**

Dottorando:
Danny **Fainozzi**

Coordinatore:
Prof. Francesco **Longo**

Supervisore di tesi:
Dr. Claudio **Masciovecchio**

ANNO ACCADEMICO 2019/2020

UNIVERSITY OF TRIESTE
PHYSICS DEPARTIMENT

PhD Degree in Condensed Matter Physics
based at Elettra Sincrotrone and
in collaboration with the Paul Scherrer Institute

Elettra Sincrotrone Trieste

PAUL SCHERRER INSTITUT

PSI

Exploitation of the potential of Free Electron Lasers through innovative experiments

Danny **Fainozzi**

PhD Coordinator:	Supervisor:	Referees:
Prof. Francesco **Longo**	Dr. Claudio **Masciovecchio**	Prof. M. **Chergui** Dr. F. **Bencivenga**

XXXIII CYCLE
ACCADEMIC YEAR 2019/2020

Before we begin our banquet, I would like to say a few words. And here they are: Nitwit! Blubber! Oddment! Tweak! Thank you.

- Albus Percival Wulfric Brian Dumbledore

Abstract

The advent of X-Ray Free Electron Lasers (FELs) has opened a new era for exploring the fundamental properties of matter. These machines are the 4^{th} generation light sources and combine the exceptional properties of conventional lasers (ultra-short, brilliant, coherent, and transform limited pulses) and synchrotrons (short and selectable wavelengths, selectable polarizations), allowing to probe the ultra-fast dynamics of atoms and molecules in simple and complex systems at a nano-scale level. The extreme high power together with the excellent transverse coherence of such sources provide about 10 orders of magnitude improvement in peak brightness above that offered by the current synchrotron radiation sources based on electron storage rings, making FELs suitable probes for both the ultrasmall and the ultrafast worlds. In the last decade many unsolved problems in understanding the properties in areas such as atomic, molecular, condensed matter physics, astrophysics and biology have found a solution thanks to the operating FELs. For this reason the number of FEL large scale user facilities is now growing fast all around the world.

In order to provide the required experimental conditions, the emitted FEL light has to be characterized, transported and focused inside the end-stations. This task is extremely important since the FEL radiation is generally of poor use for the experimentalists without any knowledge of its properties and without any manipulation. As a matter of fact, the FEL photon transport and diagnostic is much more challenging compared to the synchrotrons. This is because these 4th generation light sources do not emit constantly in the same configuration, like synchrotrons, but have to be tuned and optimized accordingly to the experimental needs almost before every beamtime. For these reasons the FEL photon optics and diagnostics represent a brand new field of science-technology, requiring clever custom solutions and years of research and development. This thesis work is divided in two main branches: at first, it reviews the basic theory behind FELs and points out possible improvement of these sources. Secondly, it presents some results obtained during new and peculiar experiments performed between 2017 and 2020 in different FELs facilities while showing how further improvements are needed in order to accomplish state of art results unreachable with the current state of synchrotrons and FELs. In Chapter 1, the reader is introduced to the charged particle accelerator theory culminating with its application on one of the main component of a Free Electron Laser: the undulator. In order to provide its special radiation output, a FEL light source makes use of interactions between charged particles and a self-generated electromagnetic radiation inside an undulator. To let the reader easily understand the mechanism behind the radiation generated and its properties, this thesis opens with an approach to the laws of physics that rule the dynamics of the particles. Coupling the Lorentz equation (that rules the electron dynamics) with Maxwell equations (wave equation for electromagnetic radiation) we show the collective dynamics

of electrons throughout the all FEL structure in Chapter 2. In Chapter 3 we present the two main places where this work of thesis has been built: the FERMI FEL in Italy and the SwissFEL machine based at the Paul Scherrer Institute in Switzerland. Here we explore the secrets of their layouts, beamlines and main experiment performed.

Once the reader mastered the fundamental properties of a FEL, we show the main results achieved during this research period at the FERMI FEL and at the SwissFEL. In Chapter 4 we present the very first successfull attempt at X-Ray Transient Grating Spectroscopy, using an incident beam energy of 7.1 keV on a sample of Bismuth Germanate Oxide. In order to confirm some of the results obtained through the X-ray Transient Grating technique, a few satellite measurements and simulations were also performed on the Bismuth Germanate Oxide sample. In Chapter 5 we present what we called a Real-time visualization of ibuprofen dimer vibrations with element- and enantiomeric- selectivity: here we exploit the potential of FELs through an atomic- and enantio-selective ultrafast soft X-Ray absorption experiment that allows the visualization and disentangling of several low-frequency and near lying vibrational modes, involving specific carbon atoms in a racemic mixture of Ibuprofen. In Chapter 6 we explore the world of soft matter: here we introduce the problematics affecting the protein structure research by showing the main results obtained at two synchrotron facilities. Afterward, given the results we obtained, we explore the possibility to overcome such problems by introducing the Coherent and Incoherent Diffraction Imaging techniques at FELs combined to a new approach on protein bidimensional crystallization. Chapter 7 introduces a technique that aims at Catching Conical Intersection through Electronic Coherence and Noise Correlation Spectroscopy: we explore the possibility to use the TRUECARS technique to directly visualize the conical intersection dynamics, which regulates the photo-chemestry of most molecules. Chapter 8 opens with an introduction of an extremely interesting, fast developing technique which goes by the name of Resonant Inelastic X-ray Spettroscopy (RIXS). Here we show the results of the application of the RIXS technique exploiting the Ultrafast charge trapping dynamics in Cu_2O in-gap states: we investigated the charge trapping dynamics in the defect-related in-gap states of Cu_2O, following photoexcitation across the band gap. These mechanisms, still far from being understood, constitute the main energy loss channel in light harvesting and emitting devices. Finally, this Chapter culminates with the Design of a soft X-Rays RIXS spectrometer for SwissFEL: given the construction of new beamlines at SwissFEL, we simulated a new spectrometer to fit the properties required by the RIXS technique in the soft X-Rays.

Contents

Chapter 1

Accelerator Physics

In the following Chapter we present a simple and general approach on the dynamic of charged particles inside a non-specific charged particles accelerator. After that the mathematical and physical tools are given, we introduce one of the main component of a Free Electron Laser: the undulator.

1.1 Particle Accelerator Theory

In a time frame where light sources are amongst the most effective tools to explore the properties of matter, the study of accelerator physics is crucial. Detailed knowledge of the interaction of charged particles with external and intrinsic electromagnetic fields together with the exponentially increasing simulation power on multi-body dynamics, allows the design of accelerators meeting specific characteristics.

1.1.1 Electron beam dynamics

Among the several existing techniques to accelerate charged particles [1], modern linear accelerators (LINACs) use radio frequency (RF) cavities to accelerate them particles to a desired energy [2]. Inside the RF cavities, a strong longitudinal electric field, with frequencies ranging from hundreds of megahertz MHz up to few gigahertz GHz, is maintained. When a particle, in our case an electron, passes through a LINAC cavity, its energy is changed by the interaction with the RF accelerating field. The energy gain/loss is given by:

$$\frac{d(\gamma mc^2)}{dt} = eV\sin(\omega_{\mathrm{RF}} + \phi), \tag{1.1}$$

where V is the peak accelerating voltage of the cavity, ϕ is the phase in between the RF wave and the electron bunch, ω_{RF} is the RF angular frequency, m is the rest mass of the charged particle, e is the electron charge, and c is the speed of light in vacuum. The Lorentz factor γ takes the form

$$\gamma = \sqrt{\frac{1}{1-\beta^2}} \quad \text{with} \quad \beta = \frac{\vec{v}}{c}, \tag{1.2}$$

with $\vec{v}$ being the velocity vector of the electron.
Generally speaking, the dynamics of a charged particle immersed in an electromagnetic

fields is given by the Lorentz force:

$$\frac{d(\gamma m\vec{v})}{dt} = e(\vec{E} + \vec{\beta} \times \vec{B}), \tag{1.3}$$

where $\vec{E}$ and $\vec{B}$ are respectively the electric and the magnetic fields interacting with the charged particle.

In any particle accelerator, the trajectory that each of the particles should follow (the reference trajectory) is defined by design *i.e.,* the interaction between electromagnetic fields and the particles is studied such that them particle are forced to move as close as possible to the design trajectory. In the case where the design orbit is not a straight path [3], the typical fields used for beam guiding are provided by stationary magnetic fields: a typical example is the case of dipole (bending) magnets which are used to curve the trajectory of charged particles along a desired orbit. As the bending angle depends on the particle momentum, the design trajectory is defined for the nominal momentum of the particles p_0. It follows that particles with a momentum $p = p_0 + \Delta p_0$ (for $\Delta p \neq 0$) would follow a different trajectory than the desired one. It is useful to define δp as the relative deviation of the momentum of the particle from the nominal one, *i.e.* $\delta p = \frac{\Delta p_0}{p_0}$. This quantity is of great importance since that deviations of the momentum of the particle tends to spread the beam in the transverse direction (defocusing). Thus, in order to control the beam transverse dimensions, a transverse focusing has to be implemented, which is normally applied using quadrupole magnets [4]. The design orbit typically lies within a plane and all magnets are oriented in such a way that the particle motion can be decoupled in the horizontal and vertical directions [1]. It is convenient to describe the motion of individual particles in terms of coordinates related to a reference particle. At any longitudinal position s along the reference trajectory, the instantaneous position of a particle can be expressed in the curvilinear coordinate system (x, y, s), schematically represented in figure 1.1.

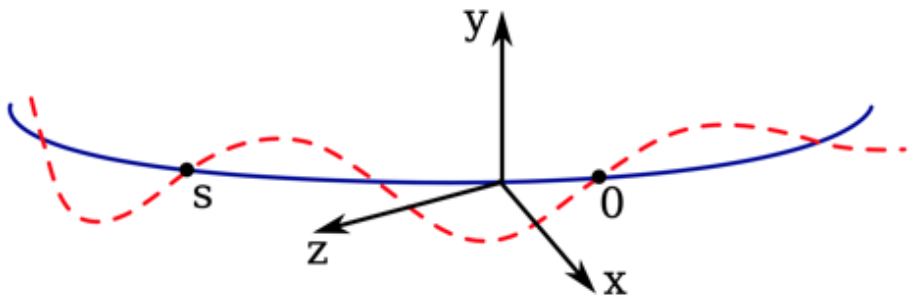

Figure 1.1: *Reference system along the design orbit (blue curve) and oscillations around it (red dashed line). Image courtesy of E. Ferrari and F. Curbis.*

The linear equation of motion for an electron in an accelerator for the independent variable s can be expressed as [3]:

$$\frac{d^2x}{ds^2} = -K_x(s)x + F_x(s) \tag{1.4}$$

where $K_x(s)$ is a function of the magnetic elements present along the beam trajectory and describes the focusing (defocusing), $F_x(s)$ is a measure of the deviation of the field

on the ideal orbit from its ideal value and can be written as

$$F_x(s) = \frac{\Delta B}{B}\frac{1}{\rho(s)} = \frac{\Delta p}{p_0}\frac{1}{\rho(s)} = \frac{\delta p}{\rho(s)} \tag{1.5}$$

where $\rho(s)$ is the local bending radius along the beam trajectory at the position s [3]. A proper arrangement of alternating quadrupolar fields is required to keep particles close to the design trajectory simultaneously in both transverse planes [3, 4]. Equation 1.4 is called an Hill's differential equation [5]. The associated homogeneous equation, in the absence focusing/defocusing approximation (*i.e.*, $K_x(s) = K_0$ is constant), have a general solution that can be expressed as linear combination of $C(s)$ and $S(s)$ for the initial condition at s_0

$$\begin{aligned} x(s) &= C(s)x(s_0) + S(s)x'(s_0) \\ x'(s) &= C'(s)x(s_0) + S'(s)x'(s_0) \end{aligned} \tag{1.6}$$

Here we adopt the matrix formalism with which equation 1.6 can be rewritten in matrix form as:

$$\begin{pmatrix} x(s) \\ x'(s) \end{pmatrix} = \begin{pmatrix} C(s) & S(s) \\ C'(s) & S'(s) \end{pmatrix} \begin{pmatrix} x(s_0) \\ x'(s_0) \end{pmatrix} \tag{1.7}$$

or in short, with obvious notation

$$X(s) = M(s,s_0)\ X(s_0) \tag{1.8}$$

where M is called the transfer matrix, and C and S are cosine and sine-like solutions of Hill's equation satisfying the initial conditions

$$C(s_0) = 1; \quad C'(s_0) = 0; \quad S(s_0) = 0; \quad S'(s_0) = 1. \tag{1.9}$$

The transfer matrices M_i can be written for every specific i^{th} element present along the beam trajectory. The total transfer matrix of a beamline made up of different specific elements $i,..,i$ is obtained via the product of the matrices for the single element $M_i,..,M_i$, calculated by the usual rules of matrix multiplication. In the case of two components, that is;

$$M(s_2,s_0) = M(s_2,s_1)\ M(s_1,s_0). \tag{1.10}$$

The described considerations can be naturally extended to the y plane.
A solution of the inhomogeneous equation 1.4, can be found by using perturbation theory and Green's functions [1, 6], resulting in the particular solution:

$$\eta(s) = S(s)\int_{s_0}^{s}\frac{C(s')}{\rho(s')}ds' - C(s)\int_{s_0}^{s}\frac{S(s')}{\rho(s')}ds' \tag{1.11}$$

where $\eta(s)\cdot\delta p$ describes the deviation of the closed orbit for off-momentum particles (with a fixed Δp) from the reference orbit at position s, provided the electron moves on the design orbit in a small interval around s_0. The new orbit of off-momentum particle is called a chromatic closed orbit, which is shown in figure 1.2.
As for the case of the homogeneous solution, also the general solution of the inhomogeneous equation can be written in matrix notation:

$$\begin{pmatrix} x(s) \\ x'(s) \\ \delta p \end{pmatrix} = \begin{pmatrix} C(s) & S(s) & \eta(s) \\ C'(s) & S'(s) & \eta(s) \\ 0 & 0 & 1 \end{pmatrix} \begin{pmatrix} x(s_0) \\ x'(s_0) \\ \delta p \end{pmatrix} \tag{1.12}$$

Intuitively, we can extend the dynamics description in matrix notation to include both transverse planes and the longitudinal motion of the particles in the beam. To do so, we use a 6-dimensional coordinates vector $\vec{X}(\vec{x}(s))$, where $x(s) = (x, x', y, y', z, \delta p)$ where we introduced the longitudinal position z of the particle, relative to the beam centroid $z_0 = 0$. Thus, summarizing all the considerations above, we can write the matrix equation in the six dimension phase space as

$$\vec{X}(\vec{x}(s)) = R \cdot \vec{X}(\vec{x}(s_0)) \tag{1.13}$$

Any element R_{ij} of matrix R for a particular lattice component indicates the influence of the value assumed by the coordinate j at the start of the element, on the coordinate i at the end of the element. For the sake of carity, it is now useful to introduce a pragmatic example: let's consider two relativistic particles with different momentum p_1 and p_2 that (the reader should now think "of course") move on different paths in an element of the beam line. Considering the simple case of same initial transversal coordinates, their longitudinal separation evolves (at the first order in the energy separation) as

$$\Delta z_f = \Delta z_i + R_{56} \cdot \frac{\Delta p_{12}}{p_0} \tag{1.14}$$

where Δz_i is the initial longitudinal separation (before the element), Δz_f is the longitudinal separation after the element, and $\frac{\Delta p_{12}}{p_0}$ is the relative momentum separation of the two particles. A general approach is presented in the upcoming section 1.1.2.

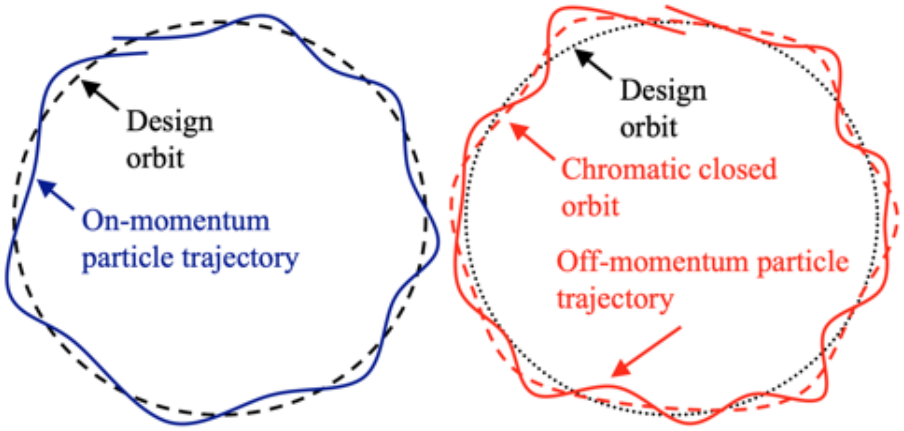

Figure 1.2: *On-momentum particles oscillate around the design orbit while off-momentum particles, due to instabilities, oscillate around a chromatic closed orbit. Adapted from [7])*

Using the Floquet's Theorem [1], we can find a general solution of the homogeneous Hill's equation, which is expressed in the phase-amplitude form [8] as:

$$\begin{aligned} x(s) &= \sqrt{\epsilon_x \beta_x(s)} \cos(\phi_x(s) + \psi_x) \\ y(s) &= \sqrt{\epsilon_y \beta_y(s)} \cos(\phi_y(s) + \psi_y) \end{aligned} \tag{1.15}$$

[1] Floquet's Theorem gives a canonical form for each fundamental matrix solution to periodic linear differential equations of the form $\dot{x} = A(t)x$. It gives a coordinate change that transforms the periodic system to a traditional linear system with constant, real coefficients. When applied to physical systems with periodic potentials, such as crystals in condensed matter physics, the result is known as Bloch's theorem.

where $\beta_x(s)$, $\beta_y(s)$ are the so called Betatron function for the horizontal and vertical axis respectively, while $\phi_x(s)$ and $\phi_y(s)$ are the horizontal and vertical phase advance function. $\epsilon_x(s)$, $\epsilon_y(s)$ and ψ_x, ψ_y are real constants specifying the particular solution. The Betatron functions describes completely the transverse focusing for a given accelerator. From equation 1.15 , we can easily see that the maximum displacement of a particle from the design orbit at position in each direction s is given by the amplitudes for the Betatron functions, that is:

$$\begin{aligned} \Delta_x(s) &= \sqrt{\epsilon_x \beta_x(s)} \\ \Delta_y(s) &= \sqrt{\epsilon_y \beta_y(s)} \end{aligned} \tag{1.16}$$

for the x and y direction, respectively. By plugging the solutions in equation 1.15 inside the homogeneous Hill's equation 1.4, we find [8]

$$\begin{aligned} \gamma_x x^2 + 2\alpha_x x x' + \beta_x x'^2 &= \epsilon_x \\ \gamma_y y^2 + 2\alpha_y y y' + \beta_y y'^2 &= \epsilon_y \end{aligned} \tag{1.17}$$

where we defined the Twiss parameters α and γ performing the following substitutions:

$$\alpha(s) \equiv -\frac{1}{2}\frac{d\beta(s)}{ds}, \quad \gamma(s) \equiv \frac{1+\alpha(s)^2}{\beta(s)}. \tag{1.18}$$

Equations 1.17 define two ellipses in the coordinates space, one in the (x, x') plane and one in the (y, y') plane, both centered at $(0,0)$, with area equal to $\pi\epsilon_x$ and $\pi\epsilon_y$ respectively. The motion of the particles can thus be interpreted as oscillations within an ellipse in a particular space defined by the particle positions and momenta: the phase space. The shape of the ellipses varies along the accelerator according to the transfer matrices M, while the area is a constant of motion, called the Courant-Snyder invariant [9]. The relation of Courant-Snyder parameters to the ellipse is sketched in figure 1.3. The evolution of the electron beam distribution can be described by means of the covariance matrix

$$\sigma_x = \begin{pmatrix} \langle x^2 \rangle & \langle x x' \rangle \\ \langle x' x \rangle & \langle x'^2 \rangle \end{pmatrix} \tag{1.19}$$

evolving from s_0 to s according to the matrix transformation formalism:

$$\sigma_x(s) = M \sigma_x(s_0) M^T \tag{1.20}$$

$\langle x \rangle$ and $\langle x^2 \rangle$ are the first and second moment of the beam distribution. It is possible to demonstrate [6] that the following relation holds:

$$\begin{aligned} \epsilon_x \beta_x(s) &= \langle x(s)^2 \rangle \\ \epsilon_y \beta_y(s) &= \langle y(s)^2 \rangle, \end{aligned} \tag{1.21}$$

where ϵ_x (ϵ_y) is called the horizontal (vertical) geometric emittance [6], and it is defined as follows

$$\epsilon_x = \sqrt{\det(\sigma_x)} = \sqrt{\langle x^2 \rangle \langle x'^2 \rangle - \langle x x' \rangle \langle x' x \rangle} \tag{1.22}$$

The emittance represents the root mean square (rms) area occupied by the beam in the $x - x'$ space (similar definition is also possible for the vertical transverse space). The

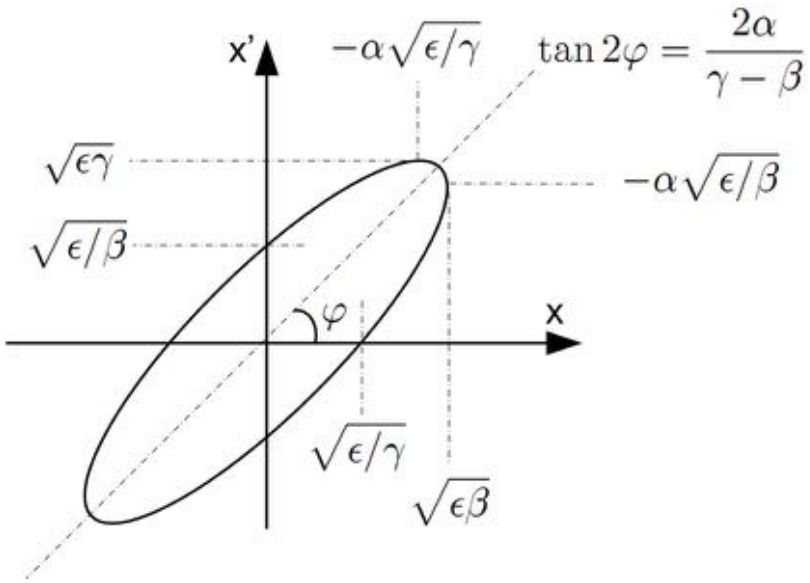

Figure 1.3: *Phase space ellipse. Adapted from [10]*

quantity $\langle x(s)^2 \rangle$, corresponding to the element $(\sigma_x)_{11}$ of the covariance matrix, can be directly measured in a LINAC by looking at the bunch transverse profile. This implies that it is possible to measure the product of emittance and the beta function at the profile monitor location. By implementing the quadrupole scan technique [6] it is further possible to recover the Twiss parameters α, β and γ of the beam at the same location, thus gaining full knowledge of the transverse dynamics of the electron bunch. A correction of the electron beam momentum dispersion is then implemented by placing sextupole magnets or skew quadrupole magnets where the Betatron function β is large.

1.1.2 Magnetic bunch compressor

The astonishing high beam brilliance compared to the beam brilliance of a typical synchrotron, is undoubtedly one of the most important features among the main characteristics that make a FEL such a powerful machine. The discrepancy covers over ten orders of magnitude. In order to reach those values, very short bunches of high-brightness electron beams, thus having a very high peak currents, are required. Usually, these bunches cannot be produced directly in electron guns, due to the space charge forces that would destroy the brilliance within a short distance. Therefore, a bunch length compression is usually implemented [11]. The compression decreases the bunch length by ballistic contraction of its path length through a magnetic chicane, typically composed of four identical bending magnets. All the electrons in the beam are ultra-relativistic, *i.e.,* they approximately travel at the speed of light, nevertheless they do not possess the exact same energy, but rather follow an intrinsic energy distribution around the mean value. The chicane takes advantage of the energy distribution providing a path length depending on the energy of each electron, in particular higher energy electrons will travel on a shorter trajectory. Thus, if the electrons toward the tail of the bunch possess an higher energy than the ones towards the head, the tail will follow a shorter, *i.e.,* faster, path while the ones in the head will follow a longer, slower

path. The net effect is that the bunch edges will approach the central part of the beam reducing the overall bunch length. To introduce the required energy dependence along the beam (time-energy correlation) one can change the accelerating phase of the structures upstream the bunch compressor, from the *crest* (maximum accelerating voltage, $\phi = \frac{\pi}{2}$) to an *off-crest* condition, as schematically described in fig. 1.4 . In this condition the particles towards the tail of the bunch (blue dot) are accelerated more by the RF wave of the accelerating structure than the ones towards the head (red dot), following the relation:

$$V_p = V_c \sin(k_{RF} z + \phi_{RF}) \tag{1.23}$$

where V_c is the accelerating cavity voltage, V_p is the voltage experienced by the particle, K_{RF} is the momentum associated at the radio frequency electric field in the cavity, and ϕ is the phase shift between the particle and the electric field.

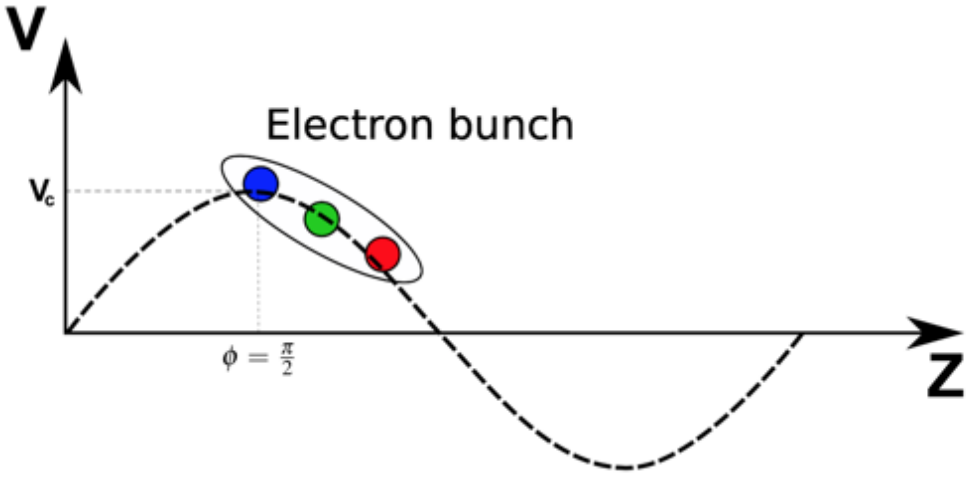

Figure 1.4: *Schematic representation of off-crest acceleration in a LINAC cavity. The cavity is set at a phase that introduces a time-energy correlation inside the electron beam. This is due to the different amplitude of the RF field for different parts of the electron beam. Adapted image, courtesy of S. Di Mitri and E. Ferrari.*

In the following mathematical description, we have chosen a longitudinal coordinate system such that the head of the bunch is located at $z < 0$. We define the relative energy variation that will be used in the following as:

$$\delta E = \frac{\Delta\gamma}{\gamma_0} \tag{1.24}$$

we will also be using the approximation

$$\delta p \approx \delta E \tag{1.25}$$

which holds for ultra-relativistic particles, *i.e.*, $\gamma \gg 1$.
We want to find the value of R_{56} in the simple case of the ordinary chicane presented in fig. 1.5. To do so, we expand the path length dependence on the energy to the first order in δE *i.e.*, we use the relation in eq 1.13 where we now have $x(s) = (x, x', y, y', z, \delta E)$. Considering fig. 1.5, the path length of an electron inside the magnetic chicane will be:

$$s = \frac{2L_1}{\cos\vartheta_0} + L2 \tag{1.26}$$

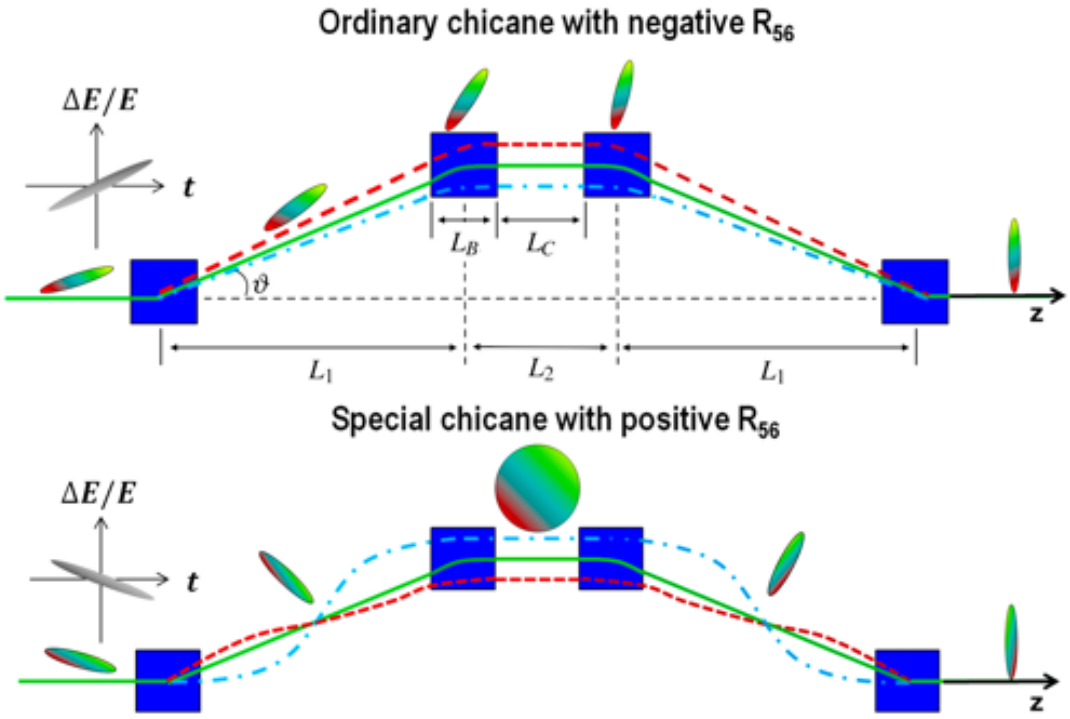

Figure 1.5: *Schematic layout of the ordinary negative R_{56} (top) and the special positive R_{56} chicane (bottom). The blue, green, and red curves represent the trajectories of high energy particle, center energy particle, and low energy particle, respectively. Image adapted from [11].*

while considering an off-momentum electron, it will have a path length equal to

$$s_{\text{off}} = \frac{2L_1}{\cos\vartheta} + L2 \quad \text{where} \quad \vartheta = \frac{\vartheta_0}{1+\delta E} \tag{1.27}$$

The path length difference between the two particle can be then expressed as:

$$\Delta s = s_{\text{on}} - s_{\text{off}} = -2L_1\vartheta_0^2\delta E \tag{1.28}$$

The most general form of transfer-matrix in LINAC section containing horizontal bends (in the absence of x/y coupling and acceleration) takes the form

$$R = \begin{pmatrix} R_{11} & R_{12} & 0 & 0 & 0 & R_{16} \\ R_{21} & R_{22} & 0 & 0 & 0 & R_{26} \\ 0 & 0 & R_{33} & R_{34} & 0 & 0 \\ 0 & 0 & R_{43} & R_{44} & 0 & 0 \\ R_{51} & R_{52} & 0 & 0 & 1 & R_{56} \\ 0 & 0 & 0 & 0 & 0 & 1 \end{pmatrix} \tag{1.29}$$

Thus, considering the same starting point for the on- and off-momentum particles going $s_0 \rightarrow s_1$, we have a final longitudinal slippage for the off-momentum electron equal to:

$$\Delta z = z_1 - z_0 = R_{51}x_0 + R_{52}x_0' + R_{56}\delta E \tag{1.30}$$

In a chicane, by design we have $R_{51} = R_{52} = 0$, which leads to the final form:

$$\Delta z = R_{56}\delta E \tag{1.31}$$

which, using the approximation in 1.25, is the same form as eq. 1.14. Considering also the approximation for ultra-relativistic particles, *i.e.*, $\Delta s \approx \Delta z$, we can finally write:

$$R_{56} = -2L_1\vartheta_0^2. \tag{1.32}$$

A more formal approach is useful in order to define some fundamental quantities in the FELs physics [12]. We can explicitly write down the relative energy change as

$$\delta E = \frac{E(z_0) - E_{\mathrm{BC}}}{E_{\mathrm{BC}}} \tag{1.33}$$

where $E(z_0)$ is the energy gain associated at the accelerating voltage in the cavity (eq. 1.23), and E_{BC} (BC stands for before compression) is the beam energy right before the bunch compression. We can then write:

$$\Delta z_1 = \Delta z_0\Big(1 + R_{56}\frac{1}{E_{\mathrm{BC}}}\frac{dE(z)}{dz_0}\Big) = \Delta z_0(1 + R_{56}\, h) \tag{1.34}$$

where we defined the term h as the linear chirp of the beam. It is important to notice that with this definition, combined with eq. 1.31, we can expand the relative energy variation at the 1$^{\mathrm{st}}$ order in z, *i.e.*,

$$\delta E = hz. \tag{1.35}$$

If we consider an electron beam of energy E_0 entering a LINAC with grant an energy gain equal to $E(z_0) = eV_c\sin(K_{RF}z_0 + \phi_{RF})$ with V_c the peak accelerating voltage and ϕ_{RF} the phase in between the accelerating field and the electrons, the linear energy chirp of the beam and the R_{56} parameter of the chicane can be written as:

$$h = \frac{2\pi}{\lambda_{RF}}\frac{eV_c\cos(k_{RF}z_0 + \phi_{RF})}{E_0}; \qquad R_{56} = -2\vartheta_0^2\Big(\frac{L_T - L_C}{2} - \frac{4}{3}L_B\Big). \tag{1.36}$$

where $L_T = 2L_1 + L_2$ is the total length of the magnetic chicane. From eq. 1.34 it is useful to define the compression factor C as the ratio of the initial and final bunch length, that is:

$$\Delta z_1 \equiv \frac{\Delta z_0}{C} \implies C = \frac{1}{1 + h\cdot R_{56}} \tag{1.37}$$

The initial electron bunch (rms) length is σ_{z_0} . By substituting eq. 1.33 and 1.36 into eq 1.31, it is possible to evaluate the (rms) bunch length after compression, which results to be:

$$\sigma_z = \langle z^2 - \langle z\rangle^2\rangle \simeq \sigma_{z_0}(1 + h\cdot R_{56}) = \frac{\sigma_{z_0}}{C}. \tag{1.38}$$

The peak current of the beam after compression is increased by a factor equal to the compression factor. The beam is compressed for $C > 1$, which implies, from eq. 1.37, that $h\cdot R_{56} < 0$. One can also see, from eq. 1.36, that R_{56} is negative, meaning that a positive chirp is needed to compress the beam.

Up to now we described the linear approximation of the bunch compression, *i.e.*, assuming linear dependence in z and δE. In this approximation any point of the beam undergoes the same compression factor and the shape of the bunch is preserved. This means that by starting with a flat current profile it is possible to get a flat current distribution at the LINAC end, usually preferred for FEL operations. In reality, higher order terms can be present in the beam energy chirp. Considering a second order term, the

transformation of the bunch longitudinal coordinate through the magnetic chicane, and the quantity δE change at the 2nd order as [13]:

$$\Delta z = R_{56}\delta E + T_{566}\delta E^2 \tag{1.39}$$

$$\delta E = hz + h'z^2 \tag{1.40}$$

$$h' = -\frac{1}{2}\left(\frac{2\pi}{\lambda_{RF}}\right)^2 \frac{eV_c \sin(k_{RF}z_0 + \phi_{RF})}{E_0} \tag{1.41}$$

where $T_{566} = -\frac{3}{2}R_{56}$ describes the second order energy dependence of the chicane transport matrix M. It has been shown that the second order terms lead to a non-linear compression for $C > 3$ [14], with a non-linear dependence of the particle position z and a non-linear compression factor along the beam. This leads to the rise of unwanted current spikes at the edges of the bunch. The usage of an harmonic RF accelerating cavity [15, 16] can be adopted in order to also introduce an equal and opposite 2nd order term in the beam energy chirp that cancels out the second order compression factor, thus reinstating a linear compression regime.

1.2 Synchrotron Radiation

1.2.1 The Undulator

An undulator is an insertion device composed of a periodic magnetic structure with period $\lambda_\mu = \frac{2\pi}{k_\mu}$ which generate a magnetic field with amplitude $B = (B_x, B_y, 0)$. Using the reference frame of figure 1.3, the magnetic field can be described as:

$$\begin{aligned} B_x &= B_{0x}\cos(k_\mu z) \\ B_y &= B_{0y}\sin(k_\mu z). \end{aligned} \tag{1.42}$$

The magnetic field is generated by two arrays of permanent magnets with alternating polarity which force the electrons to follow an oscillating trajectory. In the case where $B_{0x} = 0$, the undulator is said to be planar. In this case, the magnetic field is sinusoidal and lies in the $(y - z)$ plane, as shown in figure 1.6 (top - a). In the case where $B_{0x} = B_{0y} = B_0$, the undulator is said to be helical, see figure 1.6 (top - b). In this latter scenario, the magnetic field generated by the structure describes an helix centered on the undulator axis, *i.e.*, its projection on the $(x - y)$ plane is a circle. In the intermediate cases we have $0 \neq B_{0x} \neq B_{0y} \neq 0$ and the undulator is in an elliptical configuration. Its magnetic field can be described as the superposition between a circular and a linear components and its projection on the $(x - y)$ plane is an ellipse.
The interaction between the electrons and the field in the undulator is described by the Lorentz force in eq. 1.3. We can easily see that the electrons oscillate on a trajectory having the same symmetry of the magnetic field by integrating equation 1.3 once. Here we find the expression for the velocity of the electron [17], that is:

$$\begin{aligned} \beta_x &= \frac{K_y}{\gamma}\cos(k_\mu z) \\ \beta_y &= -\frac{K_x}{\gamma}\sin(k_\mu z), \end{aligned} \tag{1.43}$$

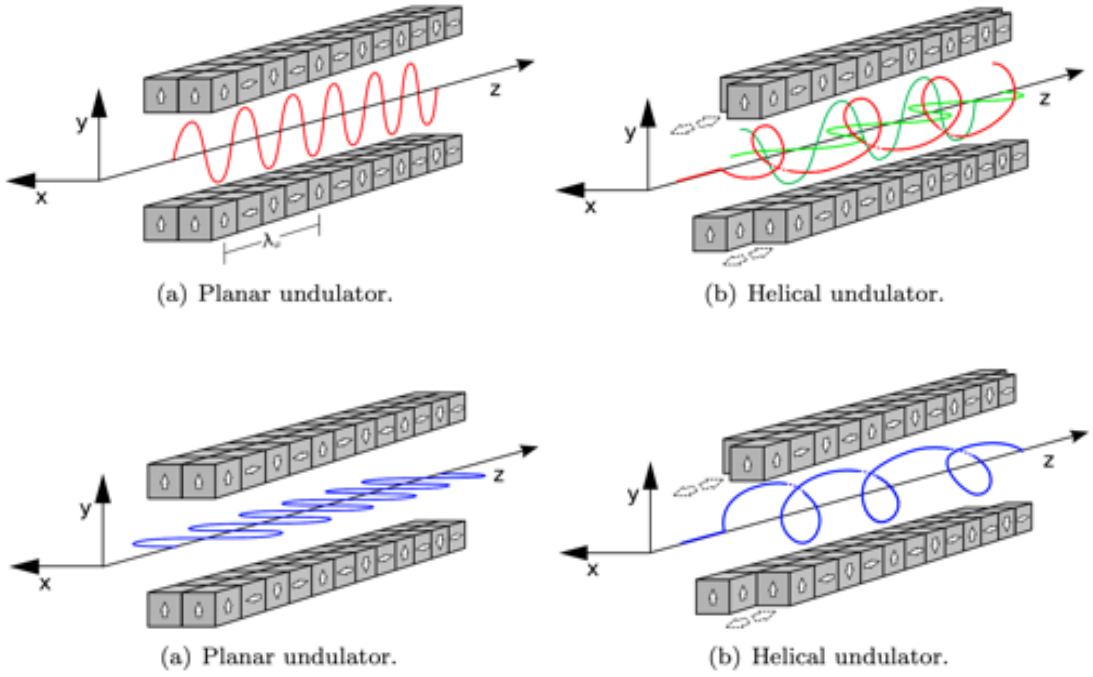

Figure 1.6: *Top: Magnetic field (red continuous line) of an undulator. For the helical case the two field components are also shown (green lines). Bottom: Electron trajectory (blue continuous line) inside an undulator. Images adapted from [11].*

where we defined the undulator strengths $K_{x,y}$ in x and y directions as [17]

$$K_{x,y} = \frac{e\lambda_\mu B_{0x,y}}{2\pi mc}. \tag{1.44}$$

It's now useful to define the total strength parameter as

$$K = \sqrt{K_x^2 + K_y^2}. \tag{1.45}$$

The longitudinal velocity of the electrons (along the z axis) depends on the configuration of the device. Indeed, combining together eqs. 2.4 and the relation $\beta_z = \sqrt{\beta^2 - \beta_x^2 - \beta_y^2}$, we have:

$$\begin{aligned} \beta_z^p &\simeq 1 - \frac{1}{2\gamma^2}\left(1 + \frac{K^2}{2}\right) - \frac{K^2}{4\gamma^2}\cos(2k_\mu z) = \langle\beta_z\rangle - \frac{K^2}{4\gamma^2}\cos(2k_\mu z) \\ \beta_z^h &= \sqrt{1 - \frac{1+K^2}{\gamma^2}} \simeq 1 - \frac{1+K^2}{2\gamma^2}, \end{aligned} \tag{1.46}$$

where we used the letters p and h for the planar and helical cases respectively.
We now have all the elements to calculate R_{56} for an undulator. To do so, we recall eq. 1.31, which can be written as:

$$\Delta z = R_{56}\frac{\Delta\gamma}{\gamma} \tag{1.47}$$

We can also write Δz for an undulator as:

$$\Delta z = c\Delta\beta \cdot \Delta t = c(\beta_1 - \beta_2)\Delta t \approx \frac{c\Delta t}{\gamma^2}\left(1 + \frac{K^2}{2}\right)\frac{\Delta\gamma}{\gamma} \tag{1.48}$$

considering $\Delta t = \frac{N_\mu \lambda_\mu}{c}$ as the time spent to run across the undulator, we have

$$\Delta z = N_\mu \frac{\lambda_\mu}{\gamma^2}\left(1 + \frac{K^2}{2}\right)\frac{\Delta\gamma}{\gamma}. \tag{1.49}$$

where N_μ is the number of periods inside the undulator. By comparing eq. 1.47 to eq. 1.49, we have:

$$R_{56} = N_\mu \frac{\lambda_\mu}{\gamma^2}\left(1 + \frac{K^2}{2}\right) \tag{1.50}$$

which holds for any type of undulator. We can now perform a second integration in order to find the positions along the undulator, so that:

$$\begin{aligned} x &= \frac{K_y}{\gamma k_\mu}\sin(k_\mu z) \\ y &= -\frac{K_x}{\gamma k_\mu}\cos(k_\mu z) \\ z^p &\simeq \langle\beta_z\rangle ct - \frac{K^2}{8\gamma^2 k_\mu}\sin(2k_\mu ct) \\ z^h &= \beta_z^h ct. \end{aligned} \tag{1.51}$$

In the case of a planar undulator the charged particle trajectory on a plane perpendicular to the magnetic field is sinusoidal, while in the propagation direction we have a small sinusoidal oscillation around a linear z position with a periodicity doubled with respect the periodicity of the magnetic field (see figure 1.6 (bottom - a)). For an helical undulator the electrons describe a helix, centered on the axis of the device as shown in figure 1.6 (bottom - b).
Both the planar and helical configurations described above can be achieved with a single device: *i.e.*, an APPLE-II type undulator [18, 19]. An APPLE-II type undulator is a particular kind of insertion device made of two pairs of magnetic chains mounted on rails that can slip one with respect to the other. In this way, one can vary the phase between one chain and the other in a definite and continuous way, switching from planar to helical configuration and passing (continuously) trough all intermediate elliptical configurations.

1.2.2 Spontaneous Radiation

To resume all the above calculations in few words, we just saw that the electrons inside an undulator, subject to a force proportional to the magnetic field inside the undulator itself, are accelerated radially on a sinusoidal trajectory having the same periodicity as the magnetic field. These accelerating charge particle emit synchrotron radiation which in this case is also called spontaneous emission.

The properties of the radiation emitted by an undulator can be described in terms of interference [19] of wave-fronts emitted by the same electron at different points of the magnetic lattice (see figure 1.7). Considering the more simple case of a planar undulator, we saw from eq. 1.51 that electrons are moving along the z direction with a mean drift velocity $\langle\beta_z\rangle$. In the time $\left(\Delta T_{AB} = \frac{\lambda_\mu}{\langle\beta_z\rangle c}\right)$ it takes to the electron to move through one period length from point A to point B, the wave-front of the radiation emitted in A

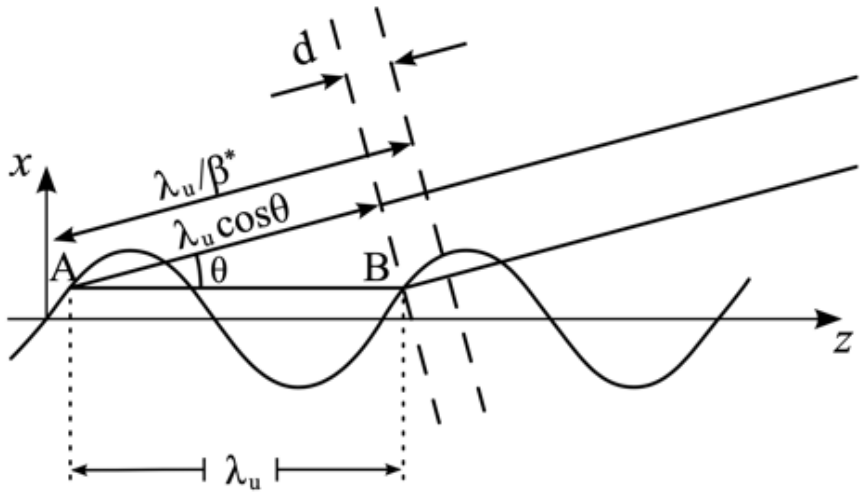

Figure 1.7: *Interference process in an undulator. Image reproduced from [19].*

has advanced by a distance $\frac{\lambda_\mu}{\langle\beta_z\rangle}$, hence the wave-front is ahead of the radiation emitted at point B by a distance d equal to

$$d = \frac{\lambda_\mu}{\langle\beta_z\rangle} - \lambda_\mu \cos\vartheta \tag{1.52}$$

where ϑ is the angle of emission with respect to the electron beam axis. When the distance d is equal to an integer number n of radiation wavelengths (λ_r) there is constructive interference between the radiation emitted by the same electron at equivalent points (*e.g.*, A and B in figure 1.7). Thus we have:

$$n\lambda_r = \frac{\lambda_\mu}{\langle\beta_z\rangle} - \lambda_\mu \cos\vartheta \tag{1.53}$$

We can now insert the expression for the mean drift velocity (eq.1.46) inside eq. 1.53. By expanding the $\cos\vartheta$ term to the second order and neglecting the cross square terms, we get:

$$\lambda_r = \frac{1}{n}\frac{\lambda_\mu}{2\gamma^2}\left(1 + \frac{K^2}{2} + \gamma^2\vartheta^2\right) \tag{1.54}$$

where $n = 1, 2, 3, ...$ is the harmonic number. Defining the fundamental wavelength *i.e.*, $\lambda_r(n=1) \equiv \lambda_0$, we have that the undulator emission occurs at λ_0 and at its harmonics at $n\lambda_0$. This relation holds for any undulator configuration, using the appropriate value of K defined in equations 1.44 and 1.45. Relation 1.54 put in the spotlight one of the most precious features of synchrotron radiation: tunability. In this case, tunability allows to adjust the emission wavelength either by varying the electron energy γ, or the strength parameter K.

It is useful to notice that, inserting eq. 1.54 for the on-axis case (*i.e.*, $\vartheta = 0$) inside eq. 1.50, we can rewrite the R_{56} parameter for an undulator as:

$$R_{56} = 2N_\mu\lambda_0. \tag{1.55}$$

In the transverse direction, the spontaneous emission is only partially coherent due to the well defined spatial period λ_μ of the undulator. In the longitudinal direction, the

spontaneous emission is not coherent since each electron emits radiation independently (there is no definite phase relation with respect to the emission of others electrons). We can summarize the beam coherence using the electron density $\rho(t)$ which is defined as:

$$\rho(t) = \sum_{i=1}^{\infty} \delta(t - t_i) \implies \int_{-\infty}^{+\infty} \rho(t)dt = n \tag{1.56}$$

By performing a simple fuorier transform we get the electron density in the frequency domain

$$\rho(\omega) = \int_{-\infty}^{+\infty} e^{i\omega t}\rho(t)dt = \sum_{i=1}^{\infty} e^{i\omega t_i}. \tag{1.57}$$

The radiation intensity is proportional to the module squared of the electron density, thus we have:

$$I(\omega) \propto |\rho(\omega)|^2 = n + \sum_{i\neq j}^{n} e^{i\omega(t_i - t_j)} \tag{1.58}$$

In the absence of a definite phase relation between electrons, the second term means to zero, and the radiation intensity is therefore proportional to the number of emitting electrons. On the contrary, when a phase relation between different particles builds up, we can express the general emetting time t_i as:

$$t_j = j \cdot dt \tag{1.59}$$

In this latter case, we have:

$$I(\omega) \propto n + \sum_{i\neq j}^{n} e^{i\omega dt(i-j)} \xrightarrow{\omega=\frac{2\pi}{dt}} I(\omega) \propto n + n^2 - n = n^2 \tag{1.60}$$

and the radiation intensity is therefore proportional to the squared number of emitting electrons.

The interference model can supply further information about the spread in wavelength. When the undulator consists of N_μ periods and its total length is therefor $L_\mu = N_\mu \lambda_\mu$, the condition for constructive interference over the entire length becomes:

$$\frac{L_\mu}{\langle \beta_z \rangle} - L_\mu \cos\vartheta = nN_\mu\lambda_r \tag{1.61}$$

Vice versa, the interference becomes destructive when there is one extra wavelength of wave-front separation over the length of the device, *i.e.*,

$$\frac{L_\mu}{\langle \beta_z \rangle} - L_\mu \cos\vartheta = nN_\mu\lambda' + \lambda' \tag{1.62}$$

Subtracting eq. 1.61 and 1.62 yields the range of emitted wavelengths at fixed angle to be

$$\frac{\Delta\lambda}{\lambda} = \frac{1}{nN_\mu} \tag{1.63}$$

which corresponds to the linewidth (Full Width Half Maximum, FWHM) of the emitted radiation at the n^{th} harmonic at and angle ϑ with respect to the beam axis.

There is nearly unanimous agreement across the synchrotron radiation community that a measure of the number of photons emitted per second per bandwidth per unit solid angle and unit area of the source is the proper way to characterize the radiation properties of third-generation sources. What has not gained such uniform acceptance is the nomenclature for this quantity [20] since it can be found in literature under different names. The conclusion reached in [20] states that the term spectral brightness best describes the quantity, thus that is the nomenclature we are going to use.

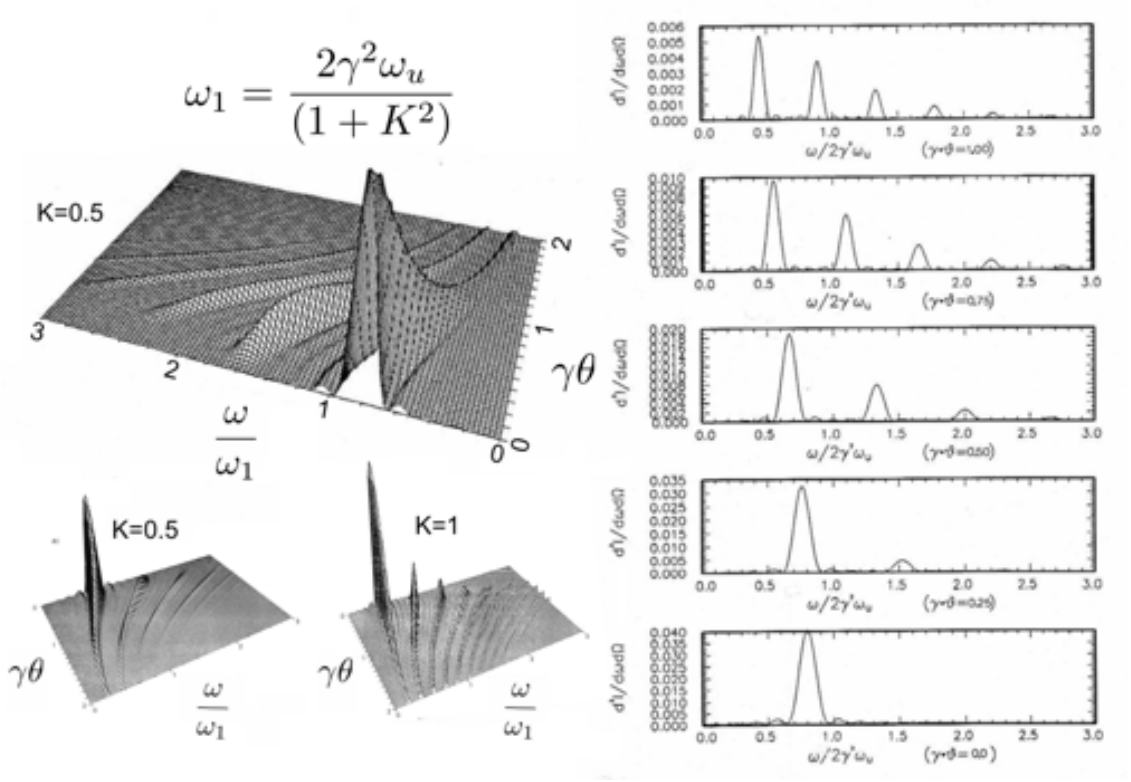

Figure 1.8: *Top left: spectral brightness of an helical undulator with $N_\mu = 5$ and $K = 0.5$ against ω/ω_1 and $\gamma\vartheta$. Bottom left: a comparison of the spectral brigthness for different values of the strength parameter K. Right: spectral brightness cuts for different values of $\gamma\vartheta$. Image adapted from [21] and [22].*

Further information can be achieved by calculating the spectral brightness of the emitted radiation using the well known formalism of the Lienard-Weichert potentials [23]. The spectral brightness can be written as:

$$\frac{d^2I}{d\Omega d\omega} = \frac{e^2\omega^2}{4\pi^2 c}\left|\int_{-\infty}^{+\infty}[\hat{n}\times(\hat{n}-\vec{\beta})]e^{i\omega\left(t-\frac{\hat{n}\cdot\vec{r}(t)}{c}\right)}dt\right|^2 \tag{1.64}$$

where $\hat{n}$ is the (instantaneous) versor that connects the charge and the observer, Ω is the solid angle, ω is the angular frequency of the radiation and $\vec{r}(t)$ is the position of the charge as defined in eq. 1.51. The correction present in the exponential is defined as the retarded time, which is the time elapsed between the radiation emission and its observation at the observer position, due to the speed of light limit. Focusing on the simpler case of the planar undulator, we find that the spectral brightness emitted on axis is:

$$\frac{d^2I}{d\Omega d\omega} = \frac{e^2\omega^2K^2}{16\pi^2\gamma^2 c}\left|\sum_{n(\text{odd})}\left[\left(J_{\frac{n-1}{2}}(\chi)-J_{\frac{n+1}{2}}(\chi)\right)sinc\left[\pi N_\mu\left(n-\frac{\omega}{\omega_r}\right)\right]\right]\right|^2 \tag{1.65}$$

where J_n are the Bessel functions, and χ is defined as:

$$\chi = \frac{K^2}{8\gamma^2}\frac{\omega}{\omega_\mu}. \tag{1.66}$$

In the case of a planar undulator the odd harmonics are emitted both on- and off-axis, while the even harmonics can be found only off-axis. In the case of an helical undulator, as we can see in fig. 1.8, only the fundamental is emitted on-axis, while all the other harmonics are emitted off-axis [17]. The fundamental tone dominates on-axis since the Bessel coefficient for the first harmonic is equal to unity [24]. This previous result is exact only for an electron beam with a divergence equal to zero. If the divergence is different from zero, the resulting spectrum is the convolution between the angular distribution of the radiation and the distribution of the electron bunch. The emitted radiation has a definite polarization with the same symmetry of the motion of the electrons, so it is linear (s or p) if the undulator is in the planar configuration, it is circular (left or right hand) if the device is in the helical configuration, and it is elliptical if the undulator is in the elliptical configuration.

References

[1] PJ Bryant. A brief history and review of accelerators. 1994.

[2] Helmut Wiedemann. *Particle accelerator physics*. Springer Nature, 2015.

[3] Ernest D Courant and Hartland S Snyder. Theory of the alternating-gradient synchrotron. *Annals of physics*, 3(1):1–48, 1958.

[4] JK Lim, P Frigola, G Travish, JB Rosenzweig, SG Anderson, WJ Brown, JS Jacob, CL Robbins, and AM Tremaine. Adjustable, short focal length permanent-magnet quadrupole based electron beam final focus system. *Physical Review Special Topics-Accelerators and Beams*, 8(7):072401, 2005.

[5] LA Pipes. Applied mathematics for engineers and physicists mcgraw hill. *New York p*, 23, 1958.

[6] J Rossbach and P Schmüser. Basic course on accelerator optics. Technical report, P00011673, 1993.

[7] William A. Barletta. Us particle accelerator school, unit 9 - lecture 18 - deviations from the design orbit. https://uspas.fnal.gov/materials/09UNM/Unit_9_Lecture_18_Orbit_deviations.pdf.

[8] Michael Röhrs. Investigation of the phase space distribution of electron bunches at the flash-linac using a transverse deflecting structure. 2008.

[9] V Garczynski. Construction of the courant-snyder invariants for the non-linear equations of motion under presence of the linear coupling. *Nuclear Instruments and Methods in Physics Research Section A: Accelerators, Spectrometers, Detectors and Associated Equipment*, 337(2-3):242–245, 1994.

[10] Benjamin Cheymol. *Development of beam transverse profile and emittance monitors for the CERN LINAC4*. PhD thesis, 2011.

[11] A He, F Willeke, LH Yu, L Yang, T Shaftan, G Wang, Y Li, Y Hidaka, and J Qiang. Design of low energy bunch compressors with space charge effects. *Physical Review Special Topics-Accelerators and Beams*, 18(1):014201, 2015.

[12] Stephen V. Milton. Linac design for fels, lecture mo3, 2015.

[13] Paul Emma. Bunch compressor options for the new tesla parameters. Technical report, SCAN-9903048, 1998.

[14] Simone Di Mitri. *Machine design and electron beam control of a single-pass linac for free electron laser: the FERMI@ Elettra case study*. University Library Groningen][Host], 2011.

[15] Stephen Benson, Michael Borland, DR Douglas, David Dowell, Carlos Hernandez-Garcia, D Kayran, GA Krafft, Robert Legg, Elizabeth Moog, Takashi Obina, et al. X-ray sources by energy recovered linacs and their needed r&d. *Nuclear Instruments and Methods in Physics Research Section A: Accelerators, Spectrometers, Detectors and Associated Equipment*, 637(1):1–11, 2011.

[16] Paul Emma. X-band rf harmonic compensation for linear bunch compression in the lcls. Technical report, Stanford Linear Accelerator Center (SLAC), Menlo Park, CA, 2005.

[17] Hideo Onuki and Pascal Elleaume. *Undulators, wigglers and their applications*. CRC Press, 2002.

[18] Shigemi Sasaki, Koji Miyata, and Takeo Takada. A new undulator for generating variably polarized radiation. *Japanese journal of applied physics*, 31(12B):L1794, 1992.

[19] Shigemi Sasaki. Analyses for a planar variably-polarizing undulator. *Nuclear Instruments and Methods in Physics Research Section A: Accelerators, Spectrometers, Detectors and Associated Equipment*, 347(1-3):83–86, 1994.

[20] DM Mills, JR Helliwell, Å Kvick, T Ohta, IA Robinson, and A Authier. Report of the working group on synchrotron radiation nomenclature–brightness, spectral brightness or brilliance? *Journal of synchrotron radiation*, 12(3):385–385, 2005.

[21] Luca Giannessi. Principles of functioning of the fel, 2018.

[22] R Barbini, F Ciocci, G Dattoli, and L Giannessi. Spectral properties of the undulator magnets radiation: Analytical and numerical treatment. *La Rivista del Nuovo Cimento (1978-1999)*, 13(6):1–65, 1990.

[23] John David Jackson. Classical electrodynamics, 1999.

[24] AM Kalitenko and KV Zhukovskii. Radiation from elliptical undulators with magnetic field harmonics. *Journal of Experimental and Theoretical Physics*, 130:327–337, 2020.

Chapter 2

Free Electron Lasers

2.1 The physics behind FELs

Proposed in 1971 by John M. J. Madey [1] and demonstrated experimentally in 1977 at Stanford [2], Free Electron Lasers have been recognized as promising devices for the generation of EUV/X-Ray radiation with laser-like properties. The working principle of a FEL relies on the interaction between an ultra-relativistic electron beam and a co-propagating electromagnetic wave, in the presence of a static and periodic magnetic field generated by an undulator. Inside the magnetic field, electrons are forced to follow an oscillating trajectory, and the transverse component of their velocity is coupled to the co-propagating wave. This interaction results in a force along the direction of propagation. Depending on their phase with respect to the electromagnetic field, electrons can gain or lose energy. Eventually, the interaction causes a density modulation in the electron bunch: particles distribute in micro-bunches on the scale of the radiation wavelength and its harmonics. Such a bunching is the source of coherent FEL emission. The FEL process starts when there is a net amplification of the electromagnetic wave to the detriment of the energy of the electrons in the bunch. The emitted intensity is amplified along the longitudinal coordinate of the undulator, until the interaction between the electrons and the radiation becomes strongly non-linear: at this points, through mechanisms described in the following, the process reaches saturation and the emitted intensity becomes nearly stationary.

In principle, the electrons can couple with electromagnetic fields with any arbitrary frequency. In general, this does not imply a net energy transfer between the electrons and the wave. In fact, on average, when an electron transfers energy to the field, there is another particle that gains energy at expense of the wave. In order to have a net energy transfer, the coupling must be resonant. Such a condition is schematically represented in fig. 2.1. In fig. 2.1 (a), the electron position (thin arrow) is chosen in a way that it feels a negative component of the electric field of the electromagnetic wave: the particle feels a decelerating force and loses energy. Along its motion inside the undulator, the electron slips back with respect to the wave-front. This behavior is mainly due to two reasons: the electron velocity is lower than the speed of light, and it follows a sinusoidal trajectory while the light follows a straight path. The resonance condition implies that the slippage of the electron with respect to the wave must be equal to one wavelength of the radiation for every undulator period. In fig. 2.1 (b) we can see the result after

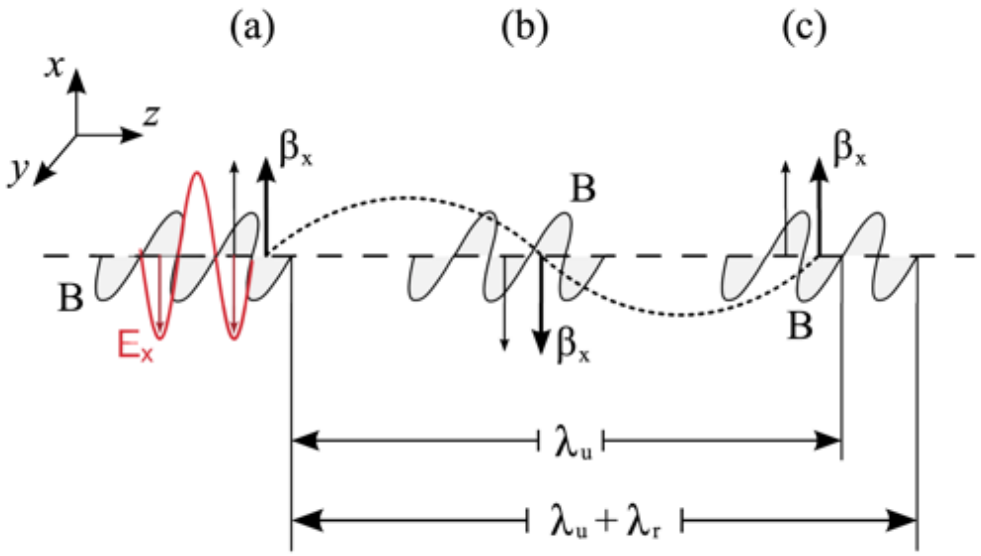

Figure 2.1: *Case of planar undulator. Phases relations between the electromagnetic wave and the electron beam, in resonance condition. Dashed line: electron trajectory. Shadowed parts represent the magnetic component of the co-propagating wave (B). Image adapted from [3].*

a distance equal to half of the undulator period. In this position the electron gains a delay equal to $\frac{\lambda_r}{2}$ with respect to the wave-front. Once again, the electric field and the electron velocity have opposite sign, thus the particle keeps on feeling a decelerating force *i.e.*, it loses energy. In fig. 2.1 (c) the situation equals the one of fig. 2.1 (a): at this point the electron accumulated a delay with respect to the co-propagating wave equal to λ_r. This situation is the only one for which the electron continuously loses energy and transfers it to the radiation field. One can show that, in this case of perfect resonance, half of electrons gain energy while the other half lose energy, thus no net energy transfer is present. This is shown in fig. 2.1 by the presence of another electron (bold arrow) which is in the condition of continuous absorption of energy from the field. The *gedankenexperiment* we just went through teaches us one important lesson: there is a net gain, *i.e.*, wave amplification, if and only if the electron beam is slightly out of resonance. The slippage requirement, that is the amount of time in which the electron runs through λ_μ and the wave-front travels a quantity $\lambda_\mu + \lambda_r$, can be expressed by the condition:

$$\frac{\lambda_\mu}{v_z} = \frac{\lambda_\mu + \lambda_r}{c} \implies \frac{\lambda_\mu(1-\beta_z)}{\beta_z} = \lambda_r \tag{2.1}$$

where β_z is the mean longitudinal velocity of the electron normalized to c of equation 2.4. By substituting the value of β_z, we can see that this relation can be written as [4]:

$$\lambda_r \simeq \frac{\lambda_\mu}{2\gamma^2}\left(1 + \frac{K^2}{2}\right) \tag{2.2}$$

This relation is equivalent to the one for the on-axis spontaneous undulator emission we saw in equation 1.54. Therefore, in order to have amplification of the electromagnetic field which co-propagates with the electrons, the radiation wavelength must be equal to the one that corresponds to the center of spontaneous emission.

2.2 A tedious mathematical description

In the following section, we are going to describe the FEL electron bunch and emitted radiation interaction dynamics, staring from the Lorentz and Maxwell equations. The description can be done in a three dimensional framework but, for simplicity, it can also be reduced to the one dimensional case by means of some approximations. As we are about to see, an approximate analytic description of the high-gain FEL requires the self-consistent solution of the coupled pendulum equations (which follows starting from the Lorentz equation) and the inhomogeneous wave (Maxwell) equation for the electromagnetic field of the light wave.

2.2.1 3 dimensional model

We consider a mono-energetic electron beam moving through an undulator which generates a static magnetic field $B_\mu(z)$, as shown in figures 1.6 a) or 1.6 b). In the same region, we assume the existence of a co-propagating electromagnetic field, produced by the electrons undergoing oscillations imposed by $B_\mu(z)$, that can be describe as

$$\vec{E} = -\frac{1}{c}\frac{\delta \vec{A}}{\delta t} \quad \text{and} \quad \vec{B} = \nabla \times \vec{A} \tag{2.3}$$

where $\vec{A}$ is the vector potential of the radiation field having wavelength λ_r and angular frequency ω_r. The evolution of the momentum and the energy of each electron is determined by the following Newton-Lorentz equations:

$$\begin{aligned} \frac{d(\gamma m\vec{v})}{dt} &= e\Big[\vec{E} + \vec{\beta} \times (\vec{B}_\mu + \vec{B})\Big] \\ \frac{d(\gamma mc)}{dt} &= e\vec{E} \cdot \vec{\beta}. \end{aligned} \tag{2.4}$$

Although the 3D model described above is more general and accounts for the three dimensional effects, it is also possible to describe the FEL process in a 1D framework. Before presenting the equations of the 1D model, we will describe the parametrization we will use, and the so called universal scaling. For the details of the derivation process, we advice [5–7].

2.2.2 Ponderomotive phase, Pierce parameter and universal scaling

Here, for some reason for now obscure to the reader, we introduce the ponderomotive (undulator + wave field) phase ϑ_j of the j^{th} electron, which is defined as:

$$\vartheta \equiv (k_r + k_\mu)z(t) - \omega_r t. \tag{2.5}$$

We further define the so-called fundamental FEL parameter, or Pierce parameter, ρ as:

$$\rho = \frac{1}{\gamma_r}\left(\frac{K}{4}\frac{\omega_p}{ck_\mu}\right)^{\frac{2}{3}} \tag{2.6}$$

where $\omega_p = \sqrt{\frac{4\pi e^2 \eta_e}{m}}$ is the plasma frequency, with η_e the electron number density and γ_r as resonant energy which can be obtained by inverting eq. 2.2 in the on-axis case

(*i.e.*, $\vartheta = 0$), which leads to:

$$\gamma_r = \sqrt{\frac{2\lambda_\mu}{\lambda_r}(1+K^2)}. \tag{2.7}$$

We also define the energy-detuning parameter δ as:

$$\delta = \frac{1}{2\rho}\frac{\langle\gamma\rangle_0^2 - \gamma_r^2}{\gamma_r^2} \tag{2.8}$$

where $\langle\gamma\rangle_0$ is the average electron energy at the undulator entrance. Finally, it is convenient to parametrize the system using the following set of variables, the so called universal scaling:

$$\begin{aligned}
\Gamma_j &\equiv \frac{\gamma_j}{\rho\langle\gamma\rangle_0} \\
\tilde{A} &\equiv \frac{\omega_r}{\omega_p\sqrt{\rho\langle\gamma\rangle_0}}\frac{e\lambda_r E}{2\pi mc^2}e^{i\delta\bar{z}} \\
\bar{z} &\equiv 2\Big(\frac{\gamma_r}{\langle\gamma\rangle_0}\Big)^2 k_\mu\rho z \\
\bar{t} &\equiv 2\Big(\frac{\gamma_r}{\langle\gamma\rangle_0}\Big)^2 k_\mu\rho t \\
\tilde{\vartheta}_j &\equiv \vartheta_j - \delta\bar{z}
\end{aligned} \tag{2.9}$$

2.2.3 1 dimensional model

In the 1D FEL theory, the dependencies on the transverse coordinates x and y are disregarded. Let's introduce the simple case for which we have the electric field $\vec{E} = (E_x, 0, 0)$, where

$$E_x(z,t) = E_0\cos(k_r z - \omega_r t) \tag{2.10}$$

From the definition of the ponderomotive phase ϑ, one can show that the time-variation of the γ factor of the electron and of the phase equal to:

$$\frac{d\gamma}{dt} = -\frac{eE_0K}{2mc\gamma_r^2}\sin\vartheta \quad \text{and} \quad \frac{d\vartheta}{dt} = 2k_\mu c\frac{\gamma-\gamma_r}{\gamma_r}. \tag{2.11}$$

The combination of the two first order equations yields the so called Pendulum Equation of the low-gain (pre-bunching) FEL, which reads:

$$\frac{d^2\vartheta}{dt^2} + \frac{eE_0Kk_\mu}{m\gamma_r^2}\sin\vartheta = 0. \tag{2.12}$$

The equations in 2.11 can be used to plot the trajectories in the (ϑ,γ) phase space. Its name derives from the close analogy with the motion of a mathematical pendulum, *i.e.*, at small amplitude we get a harmonic oscillation while the motion becomes unharmonic with increasing angular momentum. At very large angular momentum one gets a rotation (unbounded motion). The evolution of the electron-beam phase space is shown in figure 2.2.

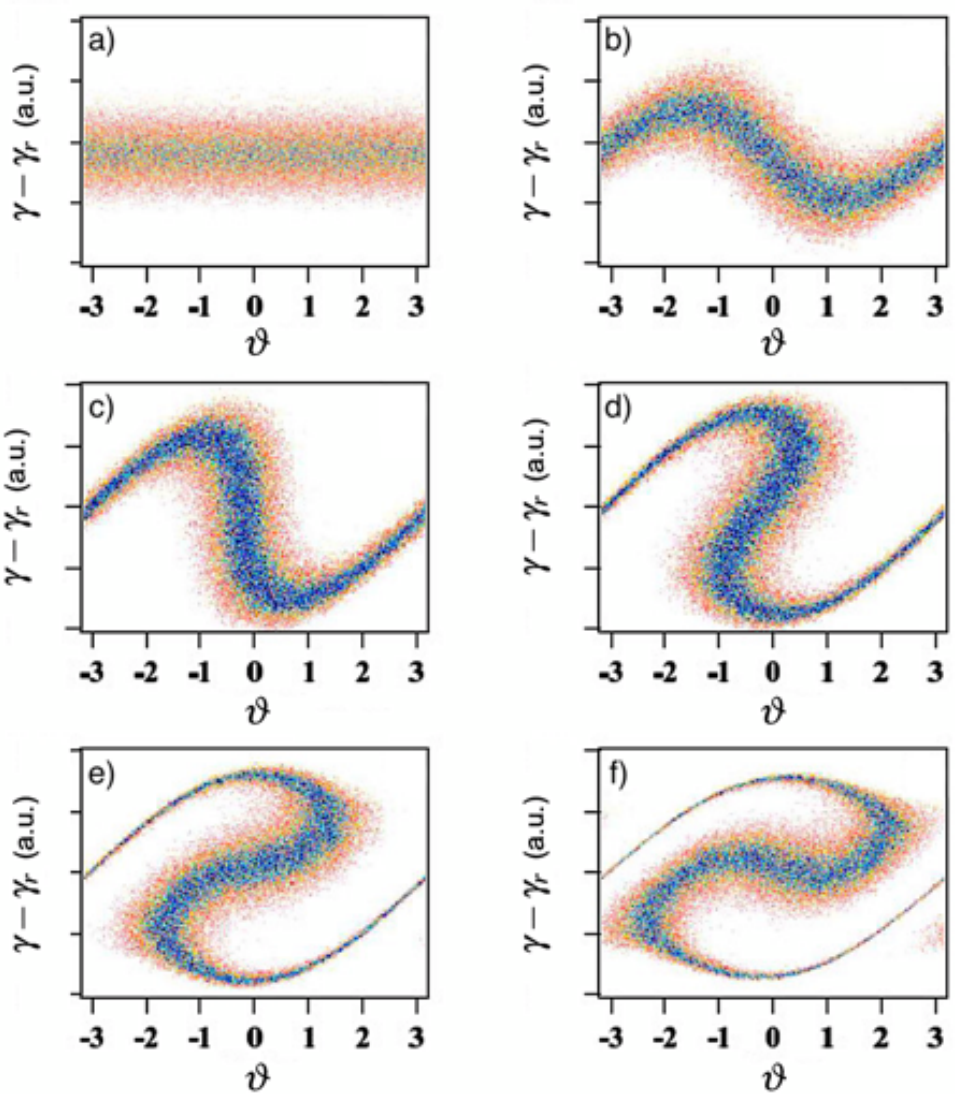

Figure 2.2: *Evolution of the electron-beam phase space. (a) initial distribution, (b) energy modulation, (c) spatial modulation (bunching), (d) slight overbunching, (e) and (f) overbunching. Adapted image, courtesy F. Curbis.*

2.3 Wave amplification

We now determine the conditions leading to wave amplification. These are the conditions under which the system, supposed initially in an equilibrium state, becomes linearly unstable.

2.3.1 Low- and high gain regimes

The wave equation for the radiation field E_x reads:

$$\frac{\partial^2 E_x}{\partial z^2} - \frac{1}{c^2}\frac{\partial^2 E_x}{\partial t^2} = \mu_0 \frac{\partial j_x}{\partial t} \tag{2.13}$$

where the current density j_x is generated by the electron bunch moving on its cosine-like trajectory. In addition, one has to consider the longitudinal space charge field E_z which is generated by the gradually evolving periodic charge density modulation.

In the regime replicating the FEL initial conditions (the so-called Compton regime *i.e.*, $\rho \ll 1$), the energy of the electron beam is high and the charge density is low. It is now useful to define the new variable $\tilde{p}_j$ as:

$$\tilde{p}_j = \Gamma_j - \frac{1}{\rho} = \frac{1}{\rho}\frac{\gamma_j - \langle\gamma\rangle_0}{\langle\gamma\rangle_0}. \tag{2.14}$$

which can be seen as the "momentum" of the j^{th} electron. Assuming the relative energy variation of electrons is

$$\frac{\gamma_j - \langle\gamma\rangle_0}{\langle\gamma\rangle_0} \ll 1 \tag{2.15}$$

and after a lot of tedious mathematical steps spared to the reader (but sadly not to me) and several simplifying assumptions, we obtain:

$$\begin{aligned} \frac{d\tilde{\vartheta}_j}{d\bar{z}} &= \tilde{p}_j \\ \frac{d\tilde{p}_j}{d\bar{z}} &= \tilde{A}_j e^{i\tilde{\vartheta}_j} + \text{c.c.} \\ \frac{d\tilde{A}_j}{d\bar{z}} &= i\delta\tilde{A} + \langle e^{-i\tilde{\vartheta}}\rangle. \end{aligned} \tag{2.16}$$

where we define the electron bunching parameter b as:

$$b \equiv \frac{1}{N_e}\sum_{i=1}^{N_e} e^{-i\tilde{\vartheta}_i} = \langle e^{-i\tilde{\vartheta}}\rangle \tag{2.17}$$

with N_e the number of electrons. It is important to notice that all the time partial derivatives of the above parameters are set to be negligible compared to the space partial derivatives, as we performed the so called Slow Wave Approximation (SVEA: slowly varying envelope approximation) [7]. Starting from an equilibrium state characterized by no initial field ($\tilde{A}_0 = 0$), zero bunching ($b = 0$) and cold beam ($\langle p_j\rangle = 0$), we want to follow the evolution of the system until the wave reaches saturation. By defining $\tilde{A} \equiv |\tilde{A}|e^{i\phi}$, and combining the first and second equation in 2.16, we can once again see that:

$$\frac{d^2\tilde{\vartheta}_j}{d^2\bar{z}} = -2|\tilde{A}|\cos(\tilde{\vartheta}_j + \phi), \tag{2.18}$$

namely, the electron system is described as an ensemble of N coupled pendula having frequency equal to $\sqrt{2|\tilde{A}|}$ (dimensionless synchrotron frequency). With some more complicated steps [6], equations 2.16 can be linearised and twofold differentiated with respect to $\bar{z}$, obtaining the third order differential equation:

$$\frac{d^3}{d\bar{z}^3}\tilde{A} - i\delta\frac{d^2}{d\bar{z}^2}\tilde{A} - i\tilde{A} = 0. \tag{2.19}$$

We can look for a solution having the form $\tilde{A}(\bar{z}) \propto e^{i\lambda\bar{z}}$. By plugging the solution form into equation 2.19, we obtain a cubic equation for λ:

$$\lambda^3 - \delta\lambda^2 + 1 = 0. \tag{2.20}$$

Here we can face two possible outcomes: rather the solution consists of three real roots (in this case the system is stable) or the solution corresponds to one real root ($\lambda = \lambda_1$) and two complex-conjugate roots ($\lambda = \lambda_2 \pm i\lambda_3$). In the latter case the system becomes progressively unstable. The field amplitude grows exponentially along the undulator (until saturation) as:

$$\tilde{A}(\bar{z}) \propto e^{\lambda_3 \bar{z}} \equiv e^{gz} \tag{2.21}$$

where we defined the exponential gain per unit length g as:

$$g = \lambda_3 \frac{4\pi\rho}{\lambda_\mu} \left(\frac{\gamma_r}{\langle\gamma\rangle_0} \right)^2. \tag{2.22}$$

We can now define the gain function G as:

$$G(\bar{z}) \equiv \frac{|\tilde{A}(\bar{z})|^2 - |\tilde{A}|_0^2}{|\tilde{A}|_0^2} \tag{2.23}$$

which for the resonant case *i.e.*, $\delta = 0$, takes the form in fig. 2.3. Here we can distinguish two main regimes: in the low-gain regime the radiation intensity can be treated as approximately constant. Here some transfer of energy between the electrons and the radiation happens, but the main effect is a change in the motion of the electrons so that microbunches start to develop. In the high-gain regime, the microbunching effect becomes strong enough that coherent radiation gives a rapid increase in radiation intensity. This in turn enhances the microbunching: the result is a rapid exponential increase in the radiation intensity with distance along the undulator.

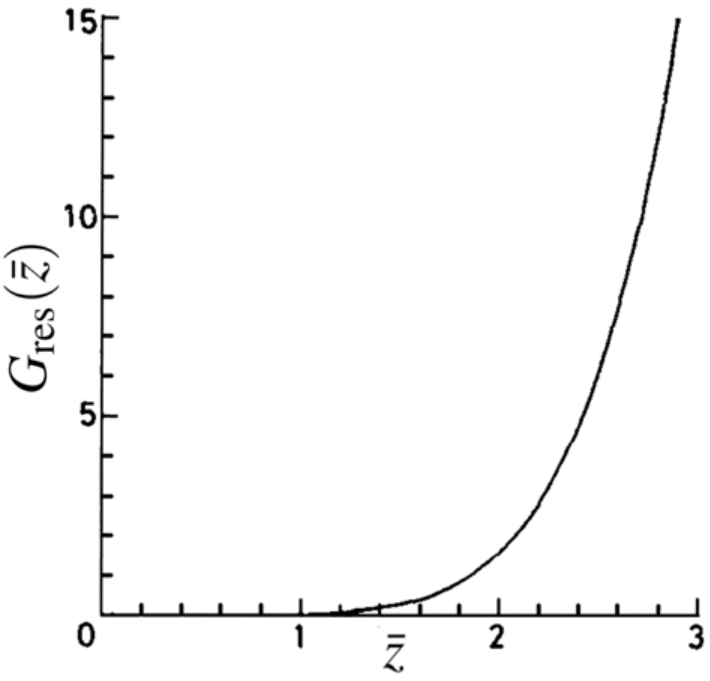

Figure 2.3: *Gain function at $\delta = 0$ of the field as a function of $\bar{z}$. Image adapted from [6].*

Finally, for the simple case $\delta = 0$, one can see that, using the equivalences in eq. 2.9, the electric field grows exponentially as:

$$E(z) \propto e^{\frac{4\pi\sqrt{3}\rho}{2\lambda_\mu} z}, \tag{2.24}$$

while the power grows as:

$$P(z) \propto e^{\frac{4\pi\sqrt{3}\rho}{\lambda_\mu}z}. \tag{2.25}$$

From the latter equation, we can define the power gain length:

$$L_g = \frac{\lambda_\mu}{4\pi\sqrt{3}\rho}. \tag{2.26}$$

2.3.2 Bunching and saturation

The exponential growth cannot continue forever. Here we present the steps that lead the FEL to its the power saturation. We consider the longitudinal mean velocity of electrons $\langle\beta_z\rangle$ and the phase velocity v_p of the ponderomotive field. Initially, when the electron beam interacts with an electromagnetic wave, the particles are randomly phase-distributed with respect to the wave. We can represent the initial situation as in figures 2.2 (a) and 2.4 (a).
After the wave amplification mechanism took place, as the resonance condition ($c\langle\beta_z\rangle = v_p$) is satisfied, half of particles absorb energy from the electromagnetic wave while the other half transfer energy to the wave (low gain): this causes the electrons to cluster where the ponderomotive phase is zero and hence the amplification is zero. The interaction with the ponderomotive wave induces a modulation of the energy of the particles which evolves in spatial modulation, giving the bunching (see fig. 2.4(b) through (d)).
Thus, the overall behaviour of the electrons produces an initial slow increase in radiation power as spontaneous radiation is generated, and microbunching starts to happen (the low-gain regime). This is followed by a rapid (exponential) increase in radiation power, as microbunching develops (driven by the radiation) in the electron beam: this is the high-gain regime. As the beam proceeds further inside the undulator, the spatial modulation arises also where the ponderomotive force is positive and this causes over-bunching, as shown in fig. 2.2 (d) through (f). At this point the process reaches saturation. The saturation is not a stationary state since the system do not reach an equilibrium condition *i.e.,* the electron beam re-absorbs some of the energy from the radiation (see 2.5). This exchange of energy between the electrons and the wave results in an oscillation around the mean value of the saturation power P_{sat}.

An estimation of the saturation power can be performed assuming that the radiation slippage is negligible. In this approximation energy conservation is equivalent to a power conservation since there is no energy transfer from a given longitudinal position to another, *i.e.,*

$$P_{tot} = P_e + P_{FEL} = \text{const} \tag{2.27}$$

where P_e is the power associated to the electron beam and P_{FEL} is the radiation power of the FEL. Saturation is an interferential effect which has the maximum expression when the gain approaches zero. The gain is indeed zero when the bunched beam shifts in phase with respect to the respective phase ϑ_0 by a quantity $\Delta\vartheta \sim \frac{\pi}{2}$, or equivalently, a position dispersion $\Delta z \sim \frac{\lambda_0}{4}$ [7]. A shift of the position of the bunching with respect to radiation is induced by the dispersion in the undulator following eq. 1.47 where R_{56} is defined, for an undulator, by eq. 1.55. In our case the energy detuning $\frac{\Delta\gamma}{\gamma}$ depends on

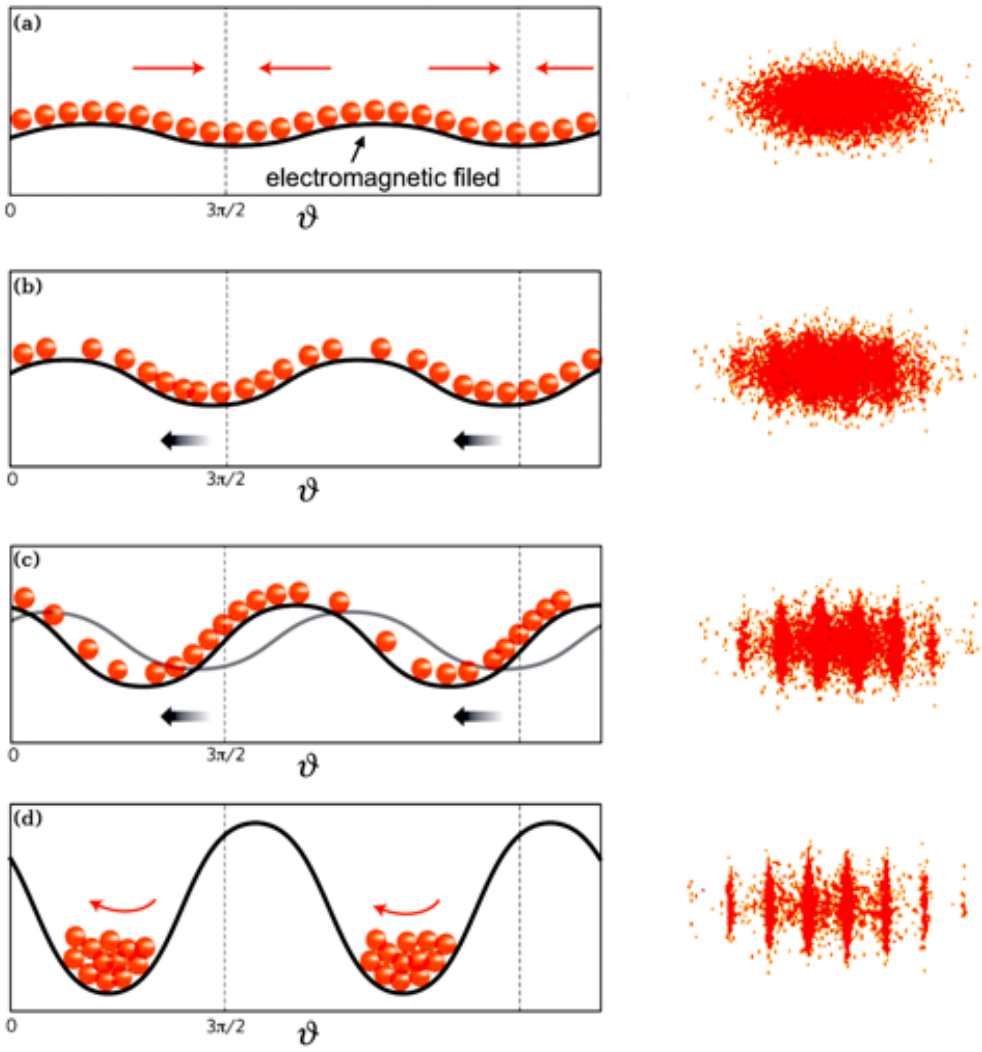

Figure 2.4: *Bunching evolution. (a) electrons are randomly distributed in phase (initial condition corresponds to weak electromagnetic field. (b) and (c) electrons start bunching on the scale of the wavelength and the electromagnetic wave is amplified. (d) electrons drift towards the maximum bunching achievable (at $\vartheta = \vartheta_0 \pm \frac{\pi}{2}$). Image adapted from [8].*

the position along the undulator, thus we can write

$$\Delta(\Delta z, z_0) = 2\frac{\lambda_0}{\lambda_\mu}\int_{z_0}^{z_0+\Delta z}\frac{\Delta\gamma(z')}{\gamma}dz'. \tag{2.28}$$

From eq. 2.25 we know that the power grows exponentially, thus we can write:

$$P_{FEL}(z) = P_0 e^{\frac{z-z_0}{L_g}} \tag{2.29}$$

Where P_0 is the power at some position z_0 along the undulator. According to the energy conservation we have

$$\frac{P_{FEL}}{P_e} = \frac{P_{e_0} - P_{e_f}}{P_{e_0}} = \frac{\Delta P_e}{P_{e_0}} = \frac{\Delta\gamma(z)}{\gamma} \tag{2.30}$$

which can be written as

$$\frac{\Delta\gamma(z)}{\gamma} = \frac{P_0 e^{\frac{z-z_0}{L_g}}}{P_{e_0}}. \tag{2.31}$$

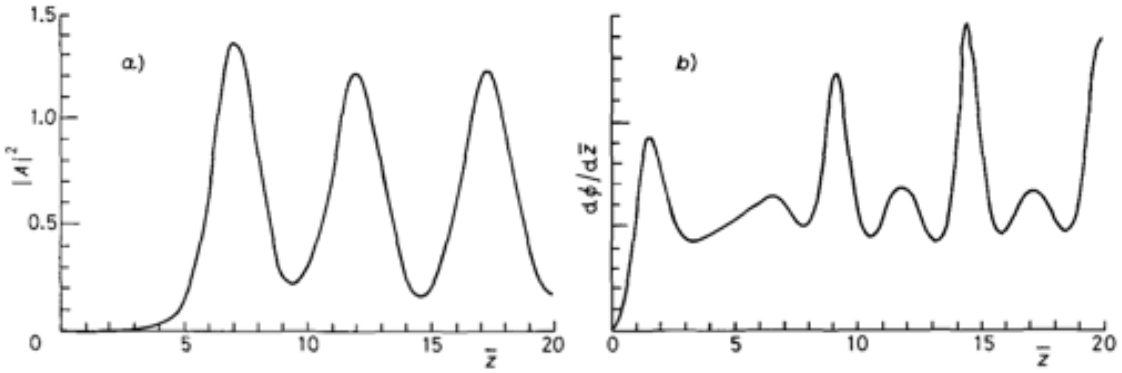

Figure 2.5: *Field intensity $IA|^2$ (a) and phase variation $\frac{d\phi}{s\bar{z}}$ (b) vs $\bar{z}$. Here $N = 100$, $\Re(A_0) = \Im(A_0) = 0.01$, and the electron beam is resonant, unbunched and monoenergetic. Image adapted from [6].*

Substituting eq. 2.31 inside eq. 2.28, we find

$$\Delta(\Delta z, z_0) = 2\frac{\lambda_0}{\lambda_\mu}\frac{P_0}{P_{e_0}}L_g\left(e^{\frac{\Delta z}{L_g}} - 1\right). \tag{2.32}$$

We indicate z_{sat} as the position where the gain goes to zero because of the phase shift. As we stated above, this will happen at

$$z_{sat} = z_0 + \Delta z \quad \text{with} \quad \Delta(\Delta z, z_0) \sim \frac{\lambda_0}{4}. \tag{2.33}$$

It must be noted that the effective energy loss occurs in the last few gain lengths. About 60% of the energy is emitted in the last gain length. We may therefore consider the evolution in the last gain length, where a substantial phase shift due to the energy loss occurs. Using the definition of L_g in eq. 2.26 we find

$$P_{sat} = \frac{\pi\sqrt{e}\rho}{2(e-1)}P_e \sim 1.6\rho P_{e_0}. \tag{2.34}$$

The saturation power is therefore proportional to the Pearson parameter ρ and the initial electron beam power P_{e_0}. From this result one can easily show that saturation is achieved approximately after a distance $L_{sat} \simeq 20L_g$.

2.4 3D model corrections

The simple 1D model we considered up to now does not take into account the effects due to the transverse dynamics of the system. These include the effects coming from the finite dimensions of the electron beam, the angular divergence of the particles and the angular divergence of the radiation. Moreover, one has to take into account the fact that the electron beam is not properly mono-energetic. Such effects can (and in fact do) deteriorate the performance of the system.

2.4.1 Beam energy and emittance spreads

Thus, let's briefly consider the electron beam energy spread $\frac{\Delta\gamma}{\gamma}$ and emittance $\epsilon = r\Delta\phi$ where r is the beam radius and the angular spread. As we showed in Chapter 1, the

emittance represents the (rms) area occupied by the beam. One can show that it is an invariant, *i.e.,* a constant in the electron phase space [9], whose size depends on many effects such as cathode temperature and inhomogeneities and space-charge. Both energy spread and emittance give rise to an in-homogeneously broadened linewidth $\left(\frac{\Delta\omega}{\omega}\right)_i$, which may lead to substantial gain distortion or depression. It is possible to show that the in-homogeneous broadening becomes negligible only if its contribution is less than the homogeneous one; hence, roughly speaking, if $\left(\frac{\Delta\omega}{\omega}\right)_i < \frac{1}{N_\mu}$ in the low gain regime (see 1.63), or $\left(\frac{\Delta\omega}{\omega}\right)_i < \rho$ in the high-gain regime. The restrictions on the electron beam emittance are critical at short wavelengths. This can be shown again by an order-of-magnitude evaluation, by matching the electron beam emittance to the radiation emittance. Actually, by assuming a Gaussian laser beam mode, the diffraction contribution to dispersion is negligible if the Rayleigh range (the distance along the propagation direction of a beam for which the area of the cross section is doubled) is in the order of the undulator length L_μ. This gives [10] a beam waist w_0 (*i.e.,* the radial size of the beam at its narrowest point) and a diffraction limited angular divergence $\Delta\phi$, equal to

$$\begin{aligned} w_0 &\simeq \sqrt{\lambda_0 L_\mu}; \\ \Delta\phi &\simeq \sqrt{\frac{\lambda_0}{L_\mu}}. \end{aligned} \tag{2.35}$$

Combining the results, we have

$$w_0 \Delta\phi \simeq \lambda_0 \tag{2.36}$$

and thus, the electron beam emittance ϵ must satisfy the relation

$$\epsilon \lesssim \lambda_0. \tag{2.37}$$

2.5 FEL configurations

There are several possible FEL configurations. One can distinguish two main methods: the single-pass configuration, where the amplification of the electromagnetic wave occurs in one passage through the undulator (or several undulators), and the oscillator configuration, in which the electromagnetic wave is stored inside an optical cavity and lasing is achieved as the results of a large number of light-electron interaction inside the undulator. Single-pass FEL can be further subdivided into two classes, depending on the origin of the electromagnetic wave which co-propagate with the electron beam inside the undulator: we can distinguish between SASE (Self Amplified Spontaneous Emission) and seeded configurations. In the first case, the electromagnetic field is the result of the spontaneous emission from the electrons while in the latter case, the electromagnetic field possess also a contribution coming from an external source: the seed.

2.5.1 Oscillator configurations

The oscillator configuration is characterized by an optical cavity that encloses the undulator. In order to enhance the emission it is customary to take advantage of the interference created by an optical klystron. The presence of interference fringes enhances the gain of the amplification process. In FEL oscillators, the initial co-propagating field is provided by the spontaneous emission of electrons emitted when the latter pass

through the undulators [2]. The emitted radiation is stored into the optical cavity, made by two mirrors with very high reflectivity, and amplified during many successive interactions with the electron beam, until saturation is achieved. The electron beam can be provided either by a storage ring or a linear accelerator. The oscillator configuration allows to generate FEL radiation in the visible-VUV range or in the Infra Red (IR). In figure 2.6 is shown an example of an FEL in oscillator configuration.

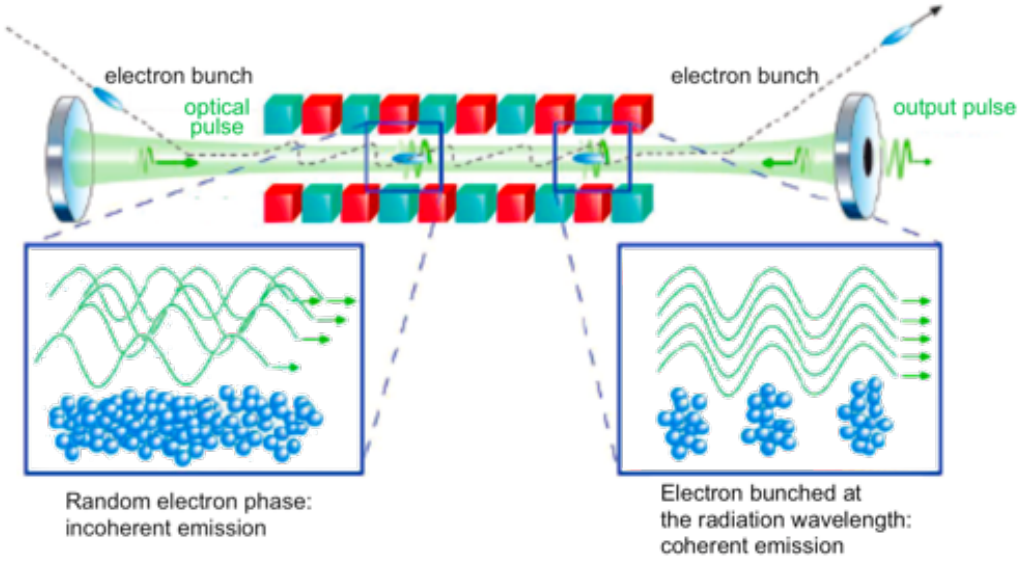

Figure 2.6: *Schematic layout of an oscillator FEL. Image adapted from [11]*

The spectral width of the emitted radiation is mainly determined by the mirrors of the optical cavity, which are normally characterized by a narrow bandwidth (few percent around the central line) and by a high (95% or more) reflectivity. The main limitation of this setup has been due to the lack of robust materials with high reflectivity in the VUV and X-Rays range. This limited the possibility of reaching very short wavelength using this kind of devices. However recent design and technological development flowed into numerous proposals for hard-x-ray cavities [12].

2.5.2 Single-pass configuration

Given the lack of materials with the required high reflectivity necessary to operate oscillator FELs in the X-Ray spectral region, there has been a great interest in developing single-pass FELs which do not require optics. In this configuration, the electron beam interacts with the electromagnetic field and amplifies it in a single pass through the undulator. In figures 2.8 we show a scheme of a single-pass FEL based on a linear accelerator source. When considering single-pass FELs, two different configurations can be distinguished, depending on the origin of the electromagnetic wave which co-propagates with electrons in the undulator: the SASE [13–20] and the seeded configurations [21–27].

2.5.3 SASE FELs

The SASE takes advantage of the spontaneous emission of electrons propagating through the undulator. The FEL amplifier is seeded by the incoherent spontaneous radiation emitted by the beam in the first part of the undulator [28]. The laser power grows exponentially along the undulator [18, 28, 29] with a characteristic gain length

$$L_g = \frac{\lambda_\mu}{4\pi\sqrt{3}\rho}, \tag{2.38}$$

where ρ is the FEL parameter. It is possible to show that saturation is reached after approximately $20L_g$. The electromagnetic wavelength which is amplified by the electrons is given by the resonance condition in eq. 2.2. Quite long undulators (tens of meters) are normally needed for this process to take place. Since it originates from spontaneous emission, the SASE radiation preserves the noisy characteristics of the latter: the emitted radiation is the envelope of a series of random spikes with variable duration, intensity and position inside the envelope. The light characteristic strongly depends on the electron beam properties: for example, if different bunches possess significant different currents, or significant (mean) energy fluctuations, also the radiation will display significant shot-to-shot fluctuations in the intensity and/or in the wavelength [30, 31]. The SASE output has very good spatial mode and is easily tunable, just by changing the energy of the electrons and/or the undulator parameter (like standard synchrotron radiation). However, radiation shows an incoherent temporal structure, resulting from the envelope of a series of micro-pulses with random intensity and phase.

2.5.4 Seeded FELs

The lack of temporal coherence can be overcome using an external source of radiation to seed the amplification process that inherits the coherence properties of the external source itself. There are many different possibilities for the external source *i.e.*, it can be an external laser, the non-linear harmonics produced in gas (HHG) or another FEL [32, 33]. It is very important to note that while HHG seeds are available at wavelengths down to the extreme ultraviolet, seeding is not feasible at X-ray wavelengths due to the lack of conventional x-ray lasers. Nonetheless, the self-seeding scheme [32] has been recently successfully implemented to seed a SASE-based source. In this scheme the SASE radiation produced in the first part of the undulator is monochromatized via a dedicated soft [34] or hard [35] monochromator. Such radiation is then used to seed the electron beam in the second part of the undulator in a direct seeded amplifier scheme. The main differences in output intensity and monochromaticity can be seen in figure 2.7, where a comparison between the self-seeding scheme and SASE scheme of the SACLA XFEL is shown.

2.5.5 High Gain Harmonic Generation

A different approach to take advantage of the seed coherence properties, as well as to reach short wavelengths, uses the electron beam as an active medium to generate radiation at harmonics of the seed laser [21, 23–26]. One of the most efficient schemes to generate harmonic radiation relies on at least two independent undulators (see figure 2.8), the second one being tuned to one of the harmonics of the first. The first undulator, called modulator, is tuned in order to be resonant at the same wavelength of the

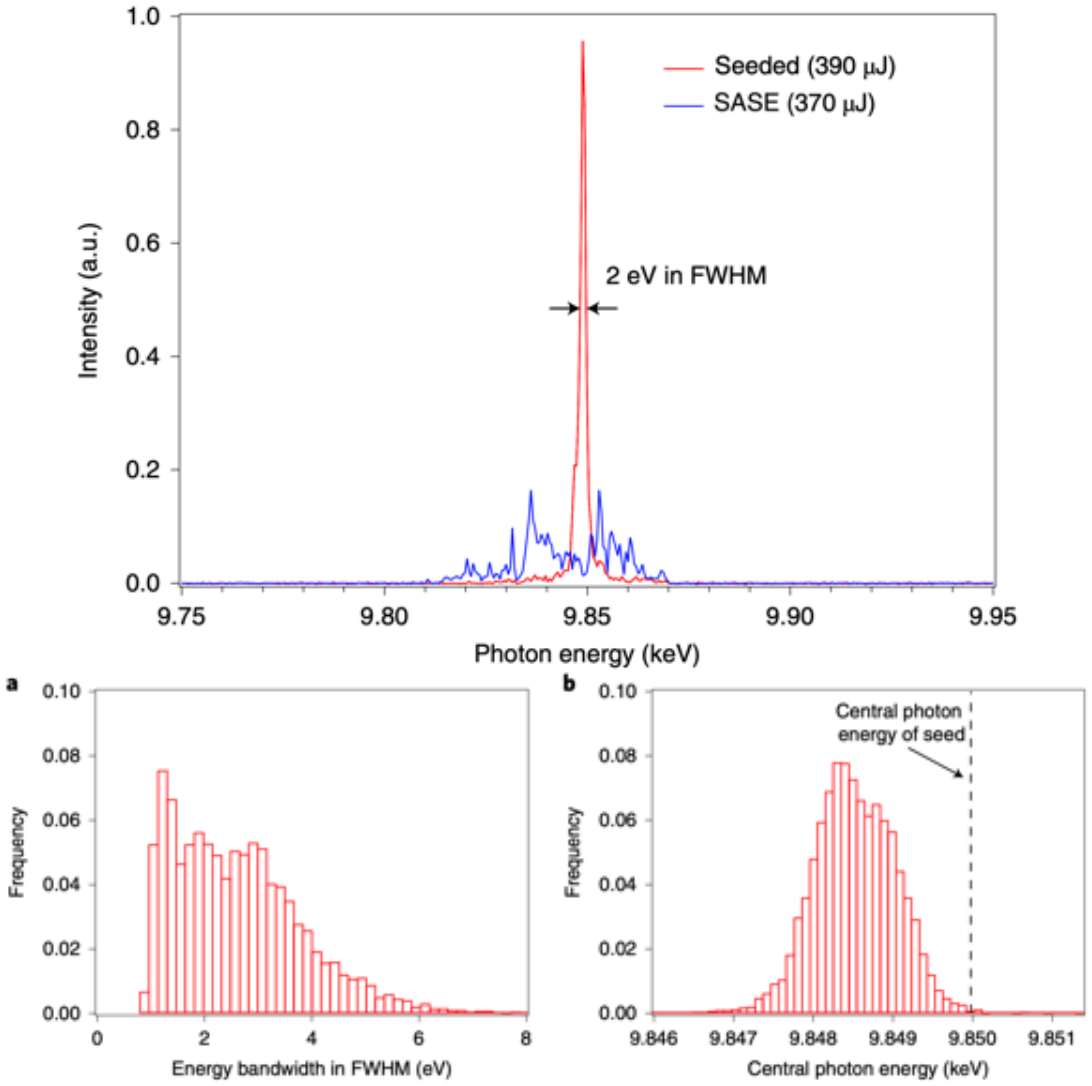

Figure 2.7: *Top: Comparison of typical single-shot spectra for the second section of undulators of the SACLA XFEL with (pulse energy of 390 μJ) and without (pulse energy of 370 μJ) the seed. Bottom: Histograms of the energy bandwidth in FWHM (a) and the central photon energy of the seeded-XFELs (b). Image adapted from [36].*

external seed. The seed is focused inside the modulator and transversally superimposed to the electron beam, as well as synchronized in time in order to have an effective interaction between the electrons and the seed itself. The laser-electron interaction produces energy modulation in the particle distribution, which can be converted into spatial modulation (bunching) via the usage of a short magnetic chicane, also called dispersive section, placed between the undulators. The dispersive section modifies the electrons path depending on their energy. Fourier analysis of the electron beam density emerging from the dispersive section evidences the presence of bunching at the seed laser wavelength and its harmonics. According to [21] the bunching fraction at the exit of the dispersive section can be expressed as:

$$b_m = J_m(m\Delta\gamma_s D)e^{-\frac{m^2\sigma_\gamma^2 D^2}{2}} \tag{2.39}$$

where m is the harmonic number, the coefficient $D = \frac{R_{56}}{\gamma_0 \lambda_m}$ contains the emitted radiation wavelength $\lambda_m = \frac{\lambda_0}{m}$, γ_0 is the electron beam Lorentz factor, $\Delta\gamma_s$ is the seed-induced energy modulation amplitude, and J_m is the m^{th} order Bessel function. The result expressed in eq. 2.39 only holds in the hypothesis that the seed laser intensity is constant along the modulator, its radius σ_r is much greater than that of the electron beam σ_x, and more importantly, that the (incoherent) energy spread of the electron beam follows a Gaussian distribution which sigma is σ_γ (rms). A different distribution of the electron beam energy can influence the bunching coefficient of the HGHG process [8]. The electron beam is then injected into the second undulator, called radiator, and tuned at one of the harmonics of the seed, where it emits coherent radiation that can be amplified via the FEL process up to saturation. According to eq. 2.39, the bunching at harmonic m is significant only if $\Delta\gamma_s \leq m\sigma_\gamma$. However, in order to have an effective FEL gain in the radiator, $\frac{\Delta\gamma_s}{\gamma_0}$ must not overcome the FEL parameter $\rho \sim 10^{-3}$ [6]. These two conditions competes in a trade-off, which can be summarised in a requirement on the normalised energy spread:

$$\frac{\sigma_\gamma}{\gamma_0} \leq \frac{\rho}{m}. \tag{2.40}$$

The result in eq. 2.40 effectively limits the possible maximum harmonic number, *i.e.*, the minimum wavelength reachable, at which significant FEL radiation can be emitted using the scheme (see section 3.1.2 for the FERMI's parameters). To overcome this limit describe above, a successive HGHG stage with modulator, dispersive section and radiator can follow the first one, using the radiation coming from the first radiator as seed. This is the case of the second FEL line of FERMI (named FEL-2) that will be presented in Chapter 3 and actually used in Chapters 6 and 8.

2.5.6 Echo-enabled harmonic generation

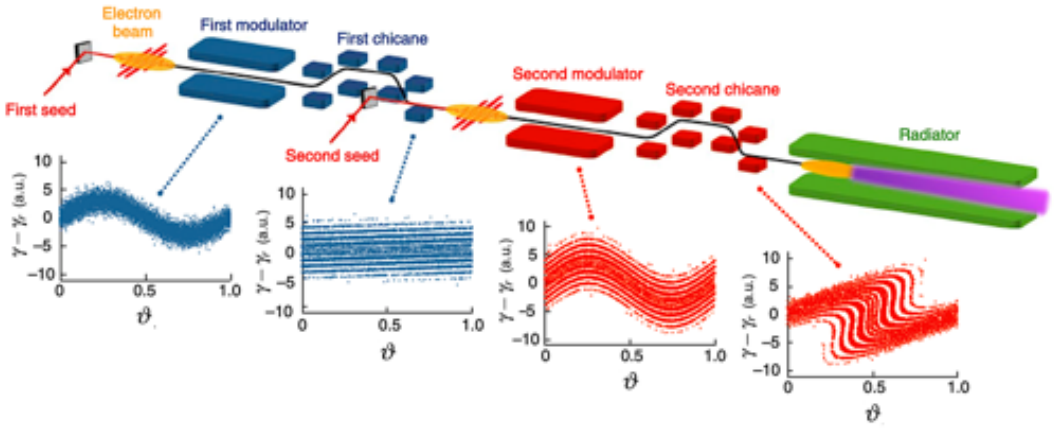

Figure 2.8: *Scheme of the echo-enabled harmonic generation approach technique. A single-pass FEL with multiple stages of modulation and dispersion which ultimately introduce a fine structure in the phase space. Image adapted from [39].*

The above mentioned limitations could be overcome with different techniques (*e.g.*, [27, 37, 38]). One of the most promising scheme is the echo-enabled harmonic generation [37] approach which is based on multiple stages of modulation and dispersion to modify the electron beam's longitudinal phase space (LPS) introducing fine struc-

tures in it. Those structures permit efficient emission of FEL radiation at higher harmonic numbers compared to standard HGHG even if a relatively large energy spread is present at the undulator entrance. A schematic example of this approach can be seen in fig. 2.8.

2.6 The State of Art of FELs

We conclude this Chapter presenting the current status of the FEL-based sources, focusing on single-pass devices. For a detailed list of existing FEL projects, see *e.g.*, [40].

Name	Location	Accelerator	Wavelength [nm]	Beam energy [GeV]	Q [pC]	I [kA]
EuXFEL	Hamburg, Germany	SC	0.05 - 4.7	14.0	250	5.0
SACLA	Riken, Japan	NC	0.063 - 0.3	8.45	300	4.0
PAL XFEL	Pohang, South Korea	NC	0.1	10.0	200	3.0
SwissFEL	Villigen, Switzerland	NC	0.1 - 7	5.8	200	3.0
LCLS	Stanford, USA	NC	0.12 - 1.5	14.0	2500	3.0
LCLS-II	Stanford, USA	SC	0.6	4.5	150	3.5
FERMI	Basovizza, Italy	NC	4 - 100	1.5	700	0.7
FLASH	Hamburg, Germany	NC	4.1 - 45	1.2	500	2.5
FLASH-II	Hamburg, Germany	NC	4.0	1.2	1000	1.2
SXFEL	Shanghai, China	SC	8.8 - 200	0.84	500	0.6

Table 2.1: *Main parameters of the principal single-pass VUV and X-Ray FEL facilities. They all are in operation and open to User experiments. The accelerator can be normal conducting (NC), superconducting (SC). If not specified, it is a LINAC. Data from [40, 62].*

The FEL idea was first proposed in 1971 by J.M.J. Madey [1], while the first FEL operation has been obtained at Stanford [2], in 1977, with emission of coherent radiation in the IR range. The visible range was reached on the ACO storage ring [41] in 1983. The principle of SASE was proposed in 1980 [17] and 1984 [18]. The first demonstration of saturation has been achieved at LEUTL (Low Energy Undulator Test Line, Advanced Photon Source, Argonne, USA) [42] in 2000. The High Gain Harmonic Generation (HGHG) scheme has proposed in 1991 [21] and tested at Deep Ultra Violet FEL (National Synchrotron Light Source, BNL, USA) with the generation of the first coherent UV FEL radiation at 266 nm [23, 24, 43] in 2000. In recent years a number of machines started user operations in the VUV, soft and hard X-Rays wavelength range. Based on the SASE scheme is FLASH [44, 45] (Free-electron Laser in Hamburg) at DESY (Germany) first lasing was achieved in 2000 and it reached the shortest wavelength at 4.1 nm. Linac Coherent Light Source [46] (SLAC, Stanford, USA) obtained first lasing in 2009 and is currently operating in the soft and hard X-Rays up to 12.82 KeV (0.967 Å) on the second version of the FEL, LCLS-II [47]. SACLA (SPring-8 Compact SASE Source) [48] at Spring-8 (Japan) lased in 2011 and its shortest wavelength is 0.634 Å. Both FLASH and LCLS had an upgrade phase (phase-II) to extend the capabilities of the sources and to overcome the limitations arisen during the first years of operations. Based on the HGHG seeded scheme are FERMI (Elettra, Italy), with operation range of $4 - 100$ nm [33, 49, 50], FLASH [51] at DESY, and SDUV-FEL at Shanghai [52, 53]. In the last few years, a new FELs based on SASE, targeting shortest wavelength (≤ 0.1 nm have been completed: the European XFEL [54] (DESY, Germany), SwissFEL (PSI) [55, 56], and PAL XFEL (Pohang, South Korea) [57]. Single-pass experiments can also

be based on storage rings. In particular, based on the HG scheme, are present at Elettra [58, 59] in Italy and UVSOR [60] in Japan. The DELTA project [61] at the Dortmund University, also based on a storage ring, can produce radiation at wavelengths ~ 20 nm. A summary of the FEL projects is reported in table 2.1.

References

[1] John MJ Madey. Stimulated emission of bremsstrahlung in a periodic magnetic field. *Journal of Applied Physics*, 42(5):1906–1913, 1971.

[2] David AG Deacon, LR Elias, John MJ Madey, GJ Ramian, HA Schwettman, and Ti I Smith. First operation of a free-electron laser. *Physical Review Letters*, 38(16):892, 1977.

[3] R. Bakker. *PhD Thesis*. PhD thesis, University of Twente, 1993.

[4] Giuseppe Dattoli, Alberto Renieri, and Amalia Torre. *Lectures on the free electron laser theory and related topics*. World Scientific, 1993.

[5] W Colson. The nonlinear wave equation for higher harmonics in free-electron lasers. *IEEE Journal of Quantum Electronics*, 17(8):1417–1427, 1981.

[6] R Bonifacio, F Casagrande, G Cerchioni, L de Salvo Souza, P Pierini, and N Piovella. Physics of the high-gain fel and superradiance. *La Rivista del Nuovo Cimento (1978-1999)*, 13(9):1–69, 1990.

[7] Luca Giannessi. Principles of functioning of the fel, 2018.

[8] Eugenio Ferrari. Advances in seeded free electron lasers: Generation and control of stable and fully coherent x-ray pulses in conventional and exotic configurations. 2016.

[9] John David Lawson. The physics of charged-particle beams. 1977.

[10] Miles V Klein and Thomas E Furtak. Optics 2nd edition. *op2*, 1986.

[11] NS Mirian. Oscillator fel. 2014.

[12] Kai Li and Haixiao Deng. Gain-guided x-ray free-electron laser oscillator. *Applied Physics Letters*, 113(6):061106, 2018.

[13] Claudio Pellegrini. The history of x-ray free-electron lasers. *The European Physical Journal H*, 37(5):659–708, 2012.

[14] SV Milton, E Gluskin, SG Biedron, RJ Dejus, PK Den Hartog, JN Galayda, K-J Kim, JW Lewellen, ER Moog, V Sajaev, et al. Observation of self-amplified spontaneous emission and exponential growth at 530 nm. *Physical review letters*, 85(5):988, 2000.

[15] M Babzien, I Ben-Zvi, P Catravas, J-M Fang, TC Marshall, XJ Wang, JS Wurtele, V Yakimenko, and LH Yu. Observation of self-amplified spontaneous emission in the near-infrared and visible wavelengths. *Physical Review E*, 57(5):6093, 1998.

[16] J Andruszkow, B Aune, V Ayvazyan, N Baboi, R Bakker, V Balakin, D Barni, A Bazhan, M Bernard, A Bosotti, et al. First observation of self-amplified spontaneous emission in a free-electron laser at 109 nm wavelength. *Physical Review Letters*, 85(18):3825, 2000.

[17] AM Kondratenko and EL Saldin. Generation of coherent radiation by a relativistic-electron beam in an undulator. *SPhD*, 24:986, 1979.

[18] R Bonifacio, C Pellegrini, and LM Narducci. Collective instabilities and high-gain regime free electron laser. In *AIP Conference Proceedings*, volume 118, pages 236–259. American Institute of Physics, 1984.

[19] JB Murphy and C Pellegrini. Generation of high-intensity coherent radiation in the soft-x-ray and vacuum-ultraviolet region. *JOSA B*, 2(1):259–264, 1985.

[20] R Brinkmann et al. The european xfel project. In *FEL*, volume 6, page 24, 2006.

[21] Li Hua Yu. Generation of intense uv radiation by subharmonically seeded single-pass free-electron lasers. *Physical Review A*, 44(8):5178, 1991.

[22] A Doyuran, M Babzien, T Shaftan, LH Yu, LF DiMauro, I Ben-Zvi, SG Biedron, William Graves, E Johnson, S Krinsky, et al. Characterization of a high-gain harmonic-generation free-electron laser at saturation. *Physical Review Letters*, 86(26):5902, 2001.

[23] Li-Hua Yu, L DiMauro, A Doyuran, WS Graves, ED Johnson, R Heese, S Krinsky, H Loos, JB Murphy, G Rakowsky, et al. First ultraviolet high-gain harmonic-generation free-electron laser. *Physical review letters*, 91(7):074801, 2003.

[24] Adnan Doyuran, Louis DiMauro, William Graves, Richard Heese, Erik D Johnson, Sam Krinsky, Henrik Loos, James B Murphy, George Rakowsky, James Rose, et al. Experimental study of a high-gain harmonic-generation free-electron laser in the ultraviolet. *Physical Review Special Topics-Accelerators and Beams*, 7(5):050701, 2004.

[25] E Allaria, F Curbis, M Coreno, M Danailov, B Diviacco, C Spezzani, M Trovó, and G De Ninno. Experimental characterization of nonlinear harmonic generation in planar and helical undulators. *Physical review letters*, 100(17):174801, 2008.

[26] G De Ninno, E Allaria, M Coreno, S Chowdhury, F Curbis, MB Danailov, B Diviacco, M Ferianis, E Karantzoulis, EC Longhi, et al. Self-induced harmonic generation in a storage-ring free-electron laser. *Physical review letters*, 100(10):104801, 2008.

[27] E Allaria and Giovanni De Ninno. Soft-x-ray coherent radiation using a single-cascade free-electron laser. *Physical review letters*, 99(1):014801, 2007.

[28] H Haus. Noise in free-electron laser amplifier. *IEEE Journal of Quantum Electronics*, 17(8):1427–1435, 1981.

[29] GIUSEPPE Dattoli, ANGEL Marino, ALBERT Renieri, and FRANCESCO Romanelli. Progress in the hamiltonian picture of the free-electron laser. *IEEE Journal of Quantum Electronics*, 17(8):1371–1387, 1981.

[30] P Pierini and WM Fawley. Shot noise startup of the 6 nm sase fel at the tesla test

facility. *Nuclear Instruments and Methods in Physics Research Section A: Accelerators, Spectrometers, Detectors and Associated Equipment*, 375(1-3):332–335, 1996.

[31] Kwang-Je Kim. Three-dimensional analysis of coherent amplification and self-amplified spontaneous emission in free-electron lasers. *Physical review letters*, 57(15):1871, 1986.

[32] Gianluca Geloni, Vitali Kocharyan, and Evgeni Saldin. A novel self-seeding scheme for hard x-ray fels. *Journal of Modern Optics*, 58(16):1391–1403, 2011.

[33] E Allaria, D Castronovo, P Cinquegrana, P Craievich, Massimo Dal Forno, MB Danailov, G D'Auria, A Demidovich, G De Ninno, S Di Mitri, et al. Two-stage seeded soft-x-ray free-electron laser. *Nature Photonics*, 7(11):913–918, 2013.

[34] Daniel Ratner, R Abela, J Amann, C Behrens, D Bohler, G Bouchard, C Bostedt, M Boyes, K Chow, D Cocco, et al. Experimental demonstration of a soft x-ray self-seeded free-electron laser. *Physical review letters*, 114(5):054801, 2015.

[35] J Amann, W Berg, V Blank, F-J Decker, Y Ding, P Emma, Y Feng, J Frisch, D Fritz, J Hastings, et al. Demonstration of self-seeding in a hard-x-ray free-electron laser. *Nature photonics*, 6(10):693–698, 2012.

[36] Ichiro Inoue, Taito Osaka, Toru Hara, Takashi Tanaka, Takahiro Inagaki, Toru Fukui, Shunji Goto, Yuichi Inubushi, Hiroaki Kimura, Ryota Kinjo, et al. Generation of narrow-band x-ray free-electron laser via reflection self-seeding. *Nature Photonics*, 13(5):319–322, 2019.

[37] Gennady Stupakov. Using the beam-echo effect for generation of short-wavelength radiation. *Physical review letters*, 102(7):074801, 2009.

[38] Haixiao Deng and Chao Feng. Using off-resonance laser modulation for beam-energy-spread cooling in generation of short-wavelength radiation. *Physical review letters*, 111(8):084801, 2013.

[39] Primož Rebernik Ribič, Alessandro Abrami, Laura Badano, Maurizio Bossi, Hans-Heinrich Braun, Niky Bruchon, Flavio Capotondi, Davide Castronovo, Marco Cautero, Paolo Cinquegrana, et al. Coherent soft x-ray pulses from an echo-enabled harmonic generation free-electron laser. *Nature Photonics*, 13(8):555–561, 2019.

[40] http://sbfel3.ucsb.edu/www/vl_fel.html.

[41] M Billardon, P Elleaume, JM Ortega, C Bazin, M Bergher, M Velghe, Y Petroff, DAG Deacon, KE Robinson, and JMJ Madey. First operation of a storage-ring free-electron laser. *Physical review letters*, 51(18):1652, 1983.

[42] SV Milton, E Gluskin, ND Arnold, C Benson, W Berg, SG Biedron, M Borland, Y-C Chae, RJ Dejus, PK Den Hartog, et al. Exponential gain and saturation of a self-amplified spontaneous emission free-electron laser. *Science*, 292(5524):2037–2041, 2001.

[43] L-H Yu, M Babzien, I Ben-Zvi, LF DiMauro, A Doyuran, William Graves, E Johnson, S Krinsky, R Malone, I Pogorelsky, et al. High-gain harmonic-generation free-electron laser. *Science*, 289(5481):932–934, 2000.

[44] W al Ackermann, G Asova, V Ayvazyan, A Azima, N Baboi, J Bähr, V Balandin, B Beutner, A Brandt, A Bolzmann, et al. Operation of a free-electron laser from the extreme ultraviolet to the water window. *Nature photonics*, 1(6):336–342, 2007.

[45] http://flash.desy.de/accelerator/.

[46] Paul Emma, R Akre, J Arthur, R Bionta, C Bostedt, J Bozek, A Brachmann, P Bucksbaum, Ryan Coffee, F-J Decker, et al. First lasing and operation of an ångstrom-wavelength free-electron laser. *nature photonics*, 4(9):641–647, 2010.

[47] http://lcls.slac.stanford.edu.

[48] Tetsuya Ishikawa, Hideki Aoyagi, Takao Asaka, Yoshihiro Asano, Noriyoshi Azumi, Teruhiko Bizen, Hiroyasu Ego, Kenji Fukami, Toru Fukui, Yukito Furukawa, et al. A compact x-ray free-electron laser emitting in the sub-ångström region. *nature photonics*, 6(8):540–544, 2012.

[49] E Allaria, Roberto Appio, L Badano, WA Barletta, S Bassanese, SG Biedron, A Borga, E Busetto, D Castronovo, P Cinquegrana, et al. Highly coherent and stable pulses from the fermi seeded free-electron laser in the extreme ultraviolet. *Nature Photonics*, 6(10):699–704, 2012.

[50] www.elettra.trieste.it/FERMI.

[51] Joern Bödewadt, Sven Ackermann, R Aßmann, N Ekanayake, B Faatz, G Feng, I Hartl, R Ivanov, Ph Amstutz, A Azima, et al. Recent results from fel seeding at flash. *TUBC3, These Proceedings, IPAC*, 15, 2015.

[52] Chen Jian-Hui, Deng Hai-Xiao, Gu Qiang, Li Dong-Guo, Wang Dong, Zhang Meng, and Zhao Zhen-Tang. Operating the sduv-fel with the echo-enabled harmonic generation scheme. *Chinese Physics C*, 33(8):706, 2009.

[53] ZT Zhao and D Wang. Progress in the sduv-fel and development of x-ray fels in shanghai. In *Proceedings of the 2010 Free-Electron Laser Conference*, pages 23–28, 2010.

[54] http://xfel.desy.de/technical_information/photon_beam_parameter/.

[55] R Ganter et al. Swissfel status report. 2015.

[56] https://www.psi.ch/swissfel/swissfel.

[57] In Soo Ko, Heung-Sik Kang, Hoon Heo, Changbum Kim, Gyujin Kim, Chang-Ki Min, Haeryong Yang, Soung Youl Baek, Hyo-Jin Choi, Geonyeong Mun, et al. Construction and commissioning of pal-xfel facility. *Applied Sciences*, 7(5):479, 2017.

[58] C Spezzani, E Allaria, Giuseppe Cautero, M Coreno, F Curbis, MB Danailov, A Demidovich, B Diviacco, E Karantzoulis, RK Ivanov, et al. Sub-picosecond coherent vuv source on the elettra storage ring. *Nuclear Instruments and Methods in Physics Research Section A: Accelerators, Spectrometers, Detectors and Associated Equipment*, 596(3):451–458, 2008.

[59] G De Ninno, E Allaria, M Coreno, F Curbis, MB Danailov, E Karantzoulis, A Locatelli, TO Menteş, MA Nino, C Spezzani, et al. Generation of ultrashort coherent vacuum ultraviolet pulses using electron storage rings: a new bright light source for experiments. *Physical review letters*, 101(5):053902, 2008.

[60] Masahiro Katoh, M Hosaka, A Mochihashi, J Yamazaki, K Hayashi, Y Hori, T Honda, K Haga, Y Takashima, T Koseki, et al. Construction and commissioning of uvsor-ii. In *AIP Conference Proceedings*, volume 705, pages 49–52. American Institute of Physics, 2004.

[61] D Nölle, F Brinker, M Negrazus, D Schirmer, and K Wille. Delta, a new storage-ring-fel facility at the university of dortmund. *Nuclear Instruments and Methods in Physics Research Section A: Accelerators, Spectrometers, Detectors and Associated Equipment*, 296(1-3):263–269, 1990.

[62] S Di Mitri and M Cornacchia. Electron beam brightness in linac drivers for free-electron-lasers. *Physics Reports*, 539(1):1–48, 2014.

Chapter 3

FERMI & SwissFel

During this PhD time frame, I performed experiments at two main Free Electron Laser facilities: the FERMI FEL in Trieste, Italy, and the SwissFEL in Villigen, Switzerland. These two FELs had been built to lase with different methods and at different wavelength. In the following section we will focus our attention on the characteristics, the design and on the working procedures of these machines.

3.1 FERMI

The FERMI single-pass seeded FEL is a user facility that produce high-quality photon pulses in the EUV and soft-X-Ray spectral range [1, 2]. FERMI is composed of three main parts: the linear accelerator (LINAC), the two FEL lines and the user beamlines. The infrastructure for the LINAC and the FEL lines has being built 5 m underground for radiation protection purposes. The FERMI LINAC provides the electron beam necessary for the operations of the FEL. The electron bunches are generated in a high-gradient photocathode gun and accelerated by a normal conducting linear accelerator up to the required beam energy, typically ranging between 1.0 GeV and 1.5 GeV. The first undulator line, FEL-1 [3], produces coherent radiation in the spectral range between 100 nm and 20 nm. The second undulator line, FEL-2 [4], covers the spectral range between 20 nm and 4 nm. Both FEL lines are based on the HGHG scheme, single stage for FEL-1 and double-stage for FEL-2.

3.1.1 FERMI LINAC

The main LINAC is divided into 4 logical groups, namely LINAC1 to LINAC4 (L1-L4 in fig. 3.1). It is composed of different types of accelerating structures, *i.e.*, seven 4.5 meter long SLAC-type, constant gradient structures (L1 and L2), with maximum energy gain per cavity of 47 MeV and seven, 6.1 meter long Backward-Traveling Wave (BTW) structures (L3 and L4), with maximum energy gain per cavity of 140 MeV. The first LINAC sections (L1) accelerate the beam and produce the energy chirp needed for bunch compression in the first bunch compressor (BC1). In L1, it is also located an harmonic x-band cavity (11.4 GHz) which is used to linearize the compression. A second bunch compressor (BC2) is placed downstream L2 and L3. It is usually kept straight and the overall bunch compression is performed in one stage only, with nominal compression factor $C = 10$. Here, the reader can notice that there is still some empty space (bright lightblue boxes) for possible future installation of LINAC cavities for further increase the final beam energy. Along the LINAC there are 4 electron-beam spectrometer

stations, where a bending magnet spectrometer is used to diagnose the beam energy (red dots in fig. 3.1). The final bunch duration (after compression) is $\sim 300\ fs$ (rms), with peak current ranging between 500-700 A depending on the bunch charge.

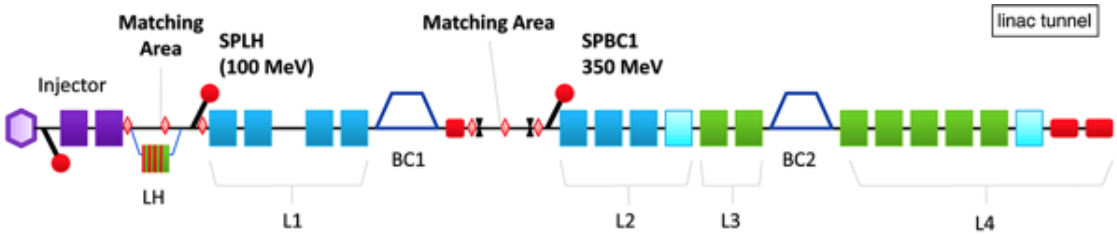

Figure 3.1: *Linac layout of the FERMI FEL. The linac includes the injector, the laser heater (LH) area, different types of accelerating structures accommodated in LINAC 1 (L1), LINAC 2 (L2), LINAC 3 (L3), and LINAC 4 (L4), two magnetic chicanes for bunch length compression (BC1 and BC2), three optics matching area, the laser heater spectrometer line (SPLH), the first compressor spectrometer line (SPBC1), and the diagnostic beam dump (DBD). A transfer line brings the electron beam to the undulators line of FEL-1 or FEL-2. Image adapted from [5].*

3.1.2 FERMI lines

FEL-1

After being accelerated to the desired energy, the electron beam is injected into the undulator line where the FEL action takes place. FEL-1 undulator system is composed of a modulator and a radiator as we can see in figure 3.2 a - top). The modulator has a total length of 3 m and a magnetic period $\lambda_\mu = 100\ mm$, for a total of 30 magnetic periods. The modulator resonance can be tuned by varying the gap in between the magnetic arrays, in order to maintain the resonance condition for different electron beam energies and seed laser wavelengths. The radiator is composed of six APPLE-II type undulator sections specifically designed for meeting the stringent FEL requirements [6]. As we saw in Chapter 2, the APPLE-II scheme allows for the first time the implementation of a high-gain FEL with polarization control. Each radiator section has a length of 2.4 m, a magnetic period $\lambda_\mu = 55\ mm$ and their resonance can be arbitrarily tuned, again by varying the gap. This requires the presence of phase shifter devices which are installed in each section break. They are required to maintain the correct phase relation between the electron beam and the FEL radiation in between one radiator section and the next. In the break sections are also installed a quadrupole magnet, to manipulate the beam size, and a Beam Position Monitor (BPM) for beam trajectory control. An external UV laser provides the seed signal, that needs to be accurately synchronized with the electron beam. The stringent synchronization requirements are achieved at FERMI with an all-optical timing system [7] that provides a stable reference to all machine systems, including the radio-frequency plants, the photo-injector and the seed laser. In order for the seeding process to be effective, both transverse and longitudinal superposition between the electron beam and the seed laser have to be ensured. The transverse alignment is done superimposing the electron bunch with the seed laser onto two YAG screens placed at the two ends of the modulator. For the longitudinal alignment a fast photodiode can be used for a cursory superposition (within 200 ps), while the final longitudinal alignment is done adjusting a remotely controlled optical delay line along the seed laser path, while looking at the FEL signal.

FEL-2

To overcome the limitations due to the rather small range of wavelength of FEL-1, the FEL-2 beamline had been installed parallel to the former. FEL-2 is specifically designed [1] to operate as a two-stage HGHG cascade in the range of wavelength between 20 nm and 4 nm. The fresh-bunch configuration enhances the FEL emission at high harmonic orders by avoiding a gain depression due to the energy spread induced by the interactions in the first-stage FEL [4]. The layout of the FERMI FEL-2 beam line is shown in figure 3.2 (a - bottom). The first stage is a small replica of FEL-1, with a linearly polarized modulator (M1), dispersive section and a radiator (R1) constituted of two, 55 mm-period APPLE-II type undulators. The coherent radiation emitted is the seed of the second stage. The first stage usually operates in the low-gain regime due to the limited length of the radiator. After the first stage, a magnetic delay line chicane (DL) is present, which is used for the required time delay for the fresh-bunch mode. The delay line introduces a controllable time delay on the electron bunch with respect to the first stage radiation up to 1 ps. Typical values of the delay are set to be around 200 fs. Other than creating the required delay for the fresh bunch, the associated chromatic dispersion ($R_{56} \leq 120\ mm$) removes nearly all the coherent bunching in the electron beam created in the first stage. This prevents emission from the bunched part of the beam in the second stage, creating an unwanted spurious emission. The second stage is also based on the HGHG scheme *i.e.,* it is constituted by a second-stage modulator (M2), physically identical to the first-stage radiators, and a second-stage radiator (R2) composed of six, 35 mm-period, APPLE II type undulators having a length of 2.4 m. The second stage usually works in high-gain regime, where both the FEL radiation intensity and coherent bunching exponentially increase along the second part of the radiator.

Amplification occurs at one selected harmonic n of the seed. However, in HGHG, the seed energy required to prepare the electron beam for FEL emission becomes larger and larger for higher harmonics (*i.e.,* shorter FEL wavelengths). For high harmonics, the resulting strong electron-beam energy modulation reduces the FEL gain, limiting the scheme in fig. 3.2 a - bottom) to $n < 15$ ($\lambda \sim 20\ nm$) for the FEL-1 single HGHG scheme, or to $n \sim 60 - 70$ (*i.e.,* $\lambda \sim 4 - 5\ nm$) in case of the FEL-2 two-stage HGHG. Moreover, at such high n, the sensitivity to the shape of the electron-beam phase space becomes critical and may severely affect the FEL radiation in terms of longitudinal coherence, pulse energy, and shot-to-shot stability. In addition, the HGHG scheme cannot cover the whole harmonic range, as the final harmonic number is a product between the harmonic numbers of the individual stages. Last, but not least, the two-stage setup uses a relatively large portion of the e-beam to accommodate the double seeding process, which makes the implementation of double-pulse operation difficult. The drawbacks of the two-stage HGHG can be overcome by using a recently proposed technique [9] called Echo-Enabled Harmonic Generation (EEHG), where the electron-beam is shaped using two seed lasers to enable FEL emission at high harmonics. The EEHG scheme used at FERMI is shown in figure 2.8. The method requires a much weaker energy modulation compared to HGHG and is also intrinsically less sensitive to the initial electron-beam imperfections, making it a strong candidate for producing highly stable, nearly fully coherent, and intense FEL pulses, down to soft X-Ray wavelengths. The FEL-2 configuration for EEHG is shown in figure 3.2 (b). In the experiment performed, it had been demonstrated the first high-gain lasing of an EEHG FEL in the soft-X-Ray region at $\lambda = 7.3\ nm$ and $\lambda = 5.9\ nm$ *i.e.,* the 36^{th} and the 45^{th} harmonics of the seed wave-

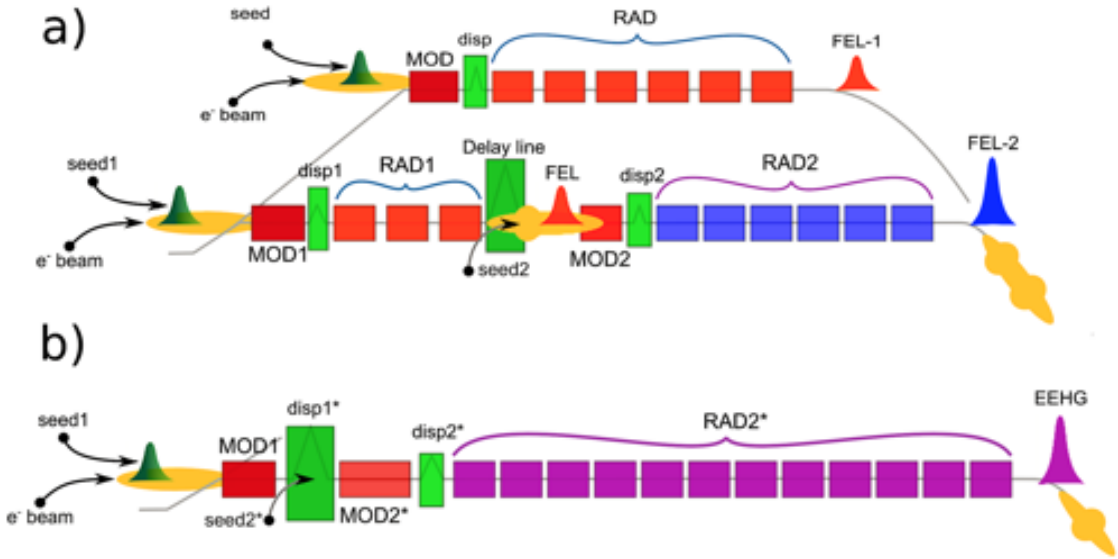

Figure 3.2: *(a) The beamlines layout of FERMI. The top part shows the FEL-1 beamline based on the standard HGHG setup. The seed laser, i.e., the 260 nm third harmonic of a Ti : SA laser or an Optical Parametric Amplifier (OPA), interacts with the electron bunch in the modulator (MOD). The dispersive section (disp) generates a micro-bunched e-beam that emits coherent light at one of the seed harmonics in the radiator (RAD). The beamline can produce stable FEL pulses at wavelengths down to 20 nm using six radiator sections with an individual length of 2.4 m. The bottom part shows the FEL-2 beamline, which is based on a two-stage HGHG cascade. In the first radiator (RAD1), coherent light is produced at a wavelength of around 20 nm ($n \sim 13^{th}$ harmonic of the seed). A strong chicane (delay line) is then used to delay the e-beam with respect to this light and seed a fresh portion of the electron bunch in the second modulator (MOD2). The second radiator (RAD2) then emits pulses at an harmonic of the first stage ($n \sim 4$), reaching saturation at wavelengths around 5 nm or shorter. Currently, six radiator sections are installed, while there is space for an additional two. This beamline (with minor component modifications) will be used for the first EEHG experiment at FERMI. (b) Advanced EEHG layout under consideration at FERMI. The beamline will have a more compact design and up to 12 radiator sections, to ensure saturation of the output power at wavelengths around 3 nm or shorter. Image adapted from [8].*

length respectively. At $n > 45$, the limitation of the present FERMI setup did not allow reaching saturation by the radiator?s end. Nevertheless, they could observe coherent harmonic emission with relatively clean spectra up to $n = 101$.

3.1.3 PADReS and endstations

The FEL beamlines are completed by the photon diagnostics system, which is placed just before the experimental end-stations (see figure 3.3), and is used to characterize the FERMI FEL pulses. PADReS (Photon Analysis Delivery and Reduction System) is the section of FERMI devoted to characterize, manipulate and deliver the FEL photons to the experimental end-stations in the experimental hall downstream [10]. It is positioned after the undulators of both FEL lines, right before the final end-stations in the FERMI experimental hall. Here, the diagnostics provide information about several parameters of the photon beam, like intensity, spectral distribution, position, shape and coherence. Many of the diagnostics (such as intensity, spectral distribution, and position) are available through a non-invasive methods and therefore are available on a shot-to-shot basis, while others (coherence, beam profile, etc.) can be measured only in

a destructive way. As show in figure 3.3, the experimental hall contains a total of five experimental endstations. A brief description of each one of them can be found in the following section.

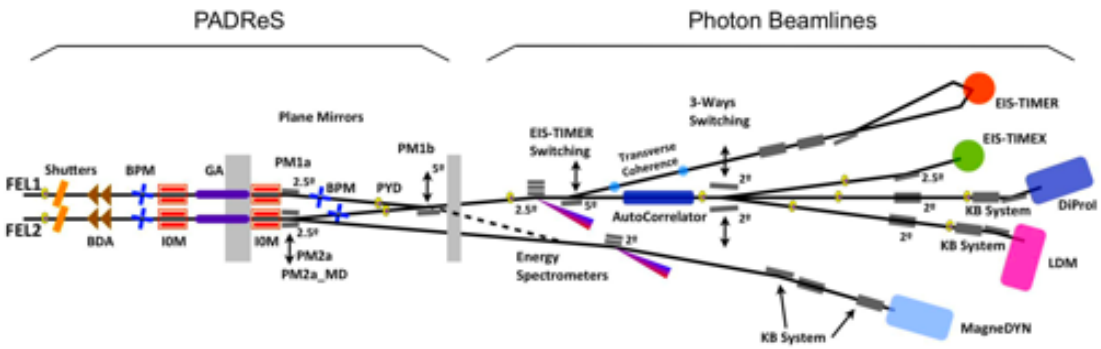

Figure 3.3: *Current FERMI diagnostic and endstation layout. Image adapted from [11].*

EIS

The Elastic and Inelastic Scattering (EIS) beamline consists of two separate end-stations (EIS-TIMEX and EIS-TIMER), dedicated to two different research projects, with common goal of performing time-resolved pump-probe experiments. Each end-station takes advantage of different key properties of the FERMI source. One of the main experiments performed during this thesis time frame, being the real-time visualization of the Ibuprofen dimer vibrations with element- and enantiomeric- selectivity, was performed here at the EIS-TIMEX endstation.

EIS-TIMEX

This endstation is designed for ultrafast time-resolved studies of condensed matter under non-equilibrium conditions occurring on the sub-picosecond time scale in FEL- or laser-heated materials. Experiments are also aimed at exploring the warm dense matter (WDM) regime resulting from thermalization of the electron and ion subsystems on the picosecond time scale. The experimental chamber and the sample environment are quite flexible in order to accommodate various possible configurations for single-shot experiments, including simple EUV and soft X-Ray absorption/reflection and pump-probe experiments where the probe can be either an external laser or the FEL itself.

EIS-TIMER

This endstation is a FEL-based Four-Wave-Mixing instrument [12] that exploit the time structure, harmonic content and coherence properties of the source. Two non-collinear FEL pulses (pump) are overlapped, in time and space, at the sample. Their interference originates a transient standing electromagnetic wave, called the transient grating (TG), with a spatial periodicity in the $1 - 100\ nm$ range. The TG imposes a nanoscale modulation of sample parameters, whose time evolution can be monitored by measuring the diffraction of a third, time-delayed, coherent pulse (probe) which impinges the sample at the Bragg angle. The time-dependent diffracted signal encodes relevant information on several kinds of dynamics, ranging from slow ($> ns$ scale) diffusion processes to fast

(sub-fs scale) electron dynamics. The implementation of this experimental scheme in the VUV range, before used only with optical lasers, is extremely useful for shedding light into the physics of disordered systems, since it will make accessible the mesoscopic kinematic region that are not in the reach of available instruments. Nanoscale TG experiments also allow sensitive probing of thin films/interfaces, transport properties and correlations in nanostructured materials. However, as we will in Chapter 4, this is not the only way to achieve a TG experiment base on the Four-Wave-Mixing technique.

DiProI

For the DiProI end-station, the main scientific case is ultra-fast Coherent Imaging and nano-spectroscopies [13]. It implements the Coherent Diffraction Imaging (CDI) technique in order to obtain the structural information on a non-periodic sample before the radiation damage occurres. Although the object is destroyed by the intense FEL pulse, the information contained in the diffraction pattern is preserved due to the different time scale between the scattered photons and the atoms motion. The collected information on a bi-dimensional CCD detector is used to reconstruct the object image by recovering the missing phase through computational algorithm [14]. The shot-to-shot temporal and energy stability of the seeded FEL pulses at FERMI has opened extraordinary opportunities for CDI and in particular for Resonant Coherent Diffraction Imaging (R-CDI), overcoming some of the limitations imposed by the partial longitudinal coherence of the SASE-FELs. The end-station exploits the FERMI tunability to perform CDI experiments with strong resonant enhancement of the magnetic scattering signal, *e.g.,* on *Co* and *Fe* edges. Another unique characteristic of the source exploited by the end-station is the polarization control, which allows for single-shot resonant magnetic scattering in holography approach for accessing the dynamics of magnetic processes [15]. An introduction to CDI is presented in Chapter 7.

LDM

The Low Density Matter (LDM) end-station [16] has been built for studying atomic, molecular and cluster physics. It is a modular end-station that can accommodate a broad range of detectors and systems for target preparation and investigation. The combined capabilities of the photon source (*e.g.,* high brilliance, short pulse length, variable polarization, coherence, photon transport) and of the end-station, allow for the investigation of very dilute systems, matter under extreme irradiation conditions causing, *e.g.,* multiple electronic excitation, multiple ionization, Coulomb explosion, non-linear optics, and dichroism.

MagneDyn

The beamline Magneto Dynamics (MagneDyn) [11] study the electronic states and the local magnetic properties of excited and transient states of complex systems by means of the time-resolved X-Ray Absorption Spectroscopy (tr-XAS) technique and time-resolved Resonant Inelastic X-Ray Spectroscopy (tr-RIXS) . This enables experimental access to the transient magnetic states of matter, opening unprecedented opportunities in the fields of femtomagnetism, spintronics, strongly electron and magnetic correlated systems, carbon based materials. One of the main experiments performed during this

thesis time frame, being the Ultrafast charge trapping dynamics in Cu_2O in-gap states presented in Chapter 8, was performed at the MagneDyn endstation.

3.2 SwissFEL

The SwissFEL single-pass SASE FEL is a user facility that produce high-quality photon pulses in the soft- and hard-X-Ray spectral range. SwissFEL, like FERMI, is composed of three main parts: the linear accelerator (LINAC), the two FEL lines and the user beamlines. The SwissFEL LINAC provides the electron beam necessary for the operations of the FEL. The electron bunches are generated in a high-gradient photocathode gun and accelerated by a normal conducting linear accelerator up to the required beam energy, typically in the range between 2.1 GeV and 5.8 GeV. The first undulator line, ARAMIS, covers the wavelength range $1 - 7$ Å, and ATHOS, the second undulator line, covers the wavelength range $6.5 - 50$ Å [17]. Both FEL lines are based on the SASE scheme. A self-seeded mode is planned for 2022.

3.2.1 SwissFEL LINAC

The linear accelerator of SwissFEL consists of an S-band photoinjector LINAC and 3 C-band booster LINACs that increase the electron energy to 2.1 GeV, 3.0 GeV and 5.8 GeV, respectively. A two-stage magnetic bunch compression after the injector (BC1) and the first LINAC (BC2) is used to reach a nominal peak current of 3 KA. The LINAC can simultaneously drive two XFELs operated in SASE mode at 100 Hz, the hard X-Ray ARAMIS undulator ($0.1 - 0.7$ nm) at 5.8 GeV and the soft X-Ray ATHOS undulator ($0.65 - 5$ nm) at 3.0 GeV (just finished). SwissFEL can be tuned from high charge mode (200 pC) to low charge mode (10 pC), providing between 50 fs and 5 fs (FWHM) short pulses, respectively.

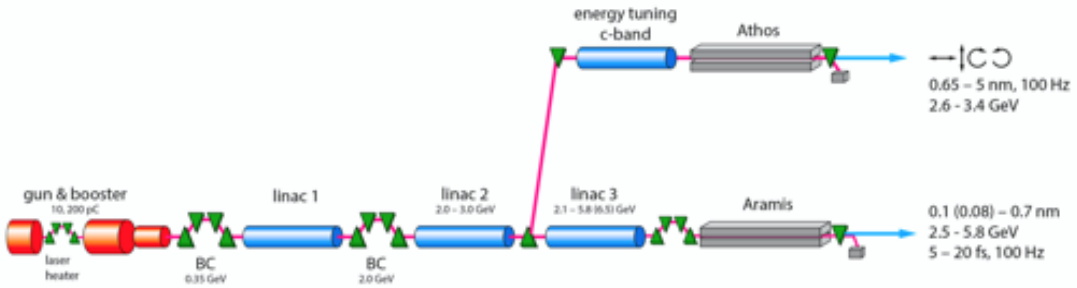

Figure 3.4: *The linear accelerator of SwissFEL which consists of an S-band photoinjector LINAC, 3 C-band booster LINACs, and a two-stage magnetic bunch compression. Image adapted from [18].*

3.2.2 SwissFEL lines

ARAMIS

ARAMIS [19] uses a segmented planar, variable-gap short-period undulator (15 mm, $K = 0.1 - 1.8$) with a novel type of permanent magnet (dysprosium-enriched NdFeB) to generate horizontally linear polarized light, at 0.1% bandwidth in normal, *i.e.*, monochromatized, SASE mode (the average bandwidth achieved for the non-monochromatized

mode, also called *pink beam* is 0.4%). The magnet array is mounted inside of the vacuum tank. To reach the required parameters, the inter-magnet gap which is available for the beam is as small as 4.5 mm. The use of dysprosium-enriched NdFeB magnets allows these undulators to be operated at room temperature, thus avoiding a costly liquid nitrogen cooling system, as is normally required for undulators with comparable parameters. A total of 12 undulators of this type, each 4 m long, have to be aligned in a row within tight tolerances to ensure that the ARAMIS FEL can reach the SASE saturation regime. A four-magnet electron energy collimator before the undulators facilitates two special modes, namely the large-bandwidth mode (relative bandwidth $\sim$4%) and an attosecond mode which exploits full compression of a 10 pC pulse which produces sub-femtosecond short pulses. Self-seeding at angstrom wavelengths with increased spectral brightness with respect to SASE is foreseen for the future. Electron bunch arrival-time monitors (BAMs) with electro-optical detection scheme are installed after each bunch compressor and at the end of the undulator. They provide non-destructive, shot-to-shot arrival-time information relative to a highly stable pulsed optical reference with resolution better than 5 fs and less than 10 fs drift per day [20]. In addition, two C-band transverse deflecting structures are installed at the end of the third linac measuring the longitudinal charge profile and the arrival time of the compressed bunches in two-bunch mode with a resolution of a few femtoseconds. The ARAMIS optical beamline design enables fast ($<$ 1 min) switching of the FEL beam between the three experimental stations Alvra, Bernina and Cristallina [21].

ATHOS

For the ATHOS FEL, the undulator period length is more relaxed (38 mm, $K = 1 - 3.5$), and the permanent magnet arrays can therefore be situated outside of the vacuum chamber. These undulators are built in the APPLE configuration (APPLE X undulators, where X comes from the possibility to move each magnet arrays radially at 45 degrees angle), which allows for a full control of the FEL polarization and wavelength by adjusting the mechanical position of the magnet arrays with high precision. Movements of the magnet arrays with submicron accuracy have to be performed in the presence of very strong magnetic forces, making the mechanical design of the mover systems particularly challenging. The feature of polarization control will be particularly advantageous for magnetization dynamics experiments. Furthermore, the ATHOS undulator modules are only 2 m long with short magnetic chicanes between each segment [22]. This allows for new modes of operation with higher peak brightness in comparison to standard SASE lasing. The chicane in-between the undulators can be used to delay the electron bunch to ensure that the lasing slice always gets supplied with fresh electrons. Such schemes allow for the spectral width of the FEL radiation to be narrowed and for an increased longitudinal coherence. The ATHOS undulator line is designed to also allow for a conventional SASE operation. The ATHOS soft X-ray experimental area is contained within one large hutch with a floor space of 692 m^2. Space within this hutch is allocated for the optical laser and the three experimental stations. Two experimental stations, one for condensed matter (Furka) and one for atomic, molecular and optical sciences (AMO), will be ready for the first experiments in 2021, while the third station (ATHOS 1 branch) is not yet defined and not yet financed either.

3.2.3 Endstations

Alvra

Alvra specializes in measuring the ultrafast dynamics of photochemical and photobiological systems using a variety of X-Ray scattering and spectroscopic techniques. Alvra consists of two instruments: Alvra Prime and Alvra Flex. Prime is a chamber designed to use a range of techniques, including serial femtosecond crystallography (SFX), X-Ray scattering (XS), and X-Ray absorption and emission spectroscopy (XAS and XES) over the full SwissFEL hard X-Ray photon energy range of $1.8 - 12.4\ KeV$. Flex is a flexible instrument designed to accommodate user experiments with an X-Ray spectrometer that can be used for many different types of measurements, including inelastic X-Ray scattering (IXS) and high energy resolution off-resonant spectroscopy (HEROS). During the year abroad at SwissFEL, I was part of the Alvra group under the supervision of Dr. Chris Milne.

Bernina

The Bernina instrument is designed for studying ultrafast phenomena in condensed matter and material science. Ultrashort pulses from an optical laser system covering a large wavelength range can be used to generate specific non-equilibrium states, whose subsequent temporal evolution can be probed by selective X-Ray scattering techniques in the range $1.8 - 12.4\ KeV$. For that purpose, the X-Ray beamline is equipped with optical elements which tailor the X-Ray beam size and energy, as well as with pulse-to-pulse diagnostics that monitor the X-Ray pulse intensity, position, as well as its spectral and temporal properties. The experiments can be performed using multiple interchangeable endstations differing in specialization, diffractometer and X-Ray analyser configuration and load capacity for specialized sample environment. After testing the instrument in a series of pilot experiments in 2018, regular user operation begun in 2019 [19]. One of the main experiments performed during this thesis time frame, being the X-ray Transient Grating Spectroscopy on Bismuth Germanate Oxides presented in Chapter 4, was performed at the Bernina endstation.

Cristallina

The Cristallina endstation will be the third instrument of the SwissFEL ARAMIS hard X-Ray beamline and serves both quantum science (Cristallina-Q) and serial femtosecond crystallography (Cristallina-MX). Diffract-before-destroy schemes will be employed to image biological macromolecules at work and quantum many-body states under extreme conditions. Offline and beamline experimental capabilities will be uniquely combined at Cristallina and complemented by a beamline which is optimized for highly focused, sub-femtosecond X-ray pulses. The beamline layout and hutch occupation are designed for flexible movement of heavy infrastructure, such as the fixed-target instrument SwissMX and bespoke low-temperature, high-magnetic field sample environments. First light is scheduled for 2021 and user operation from 2022 onwards. This endstation will possibly be the state of art of protein based CDI and IDI techniques, presented in Chapter 8.

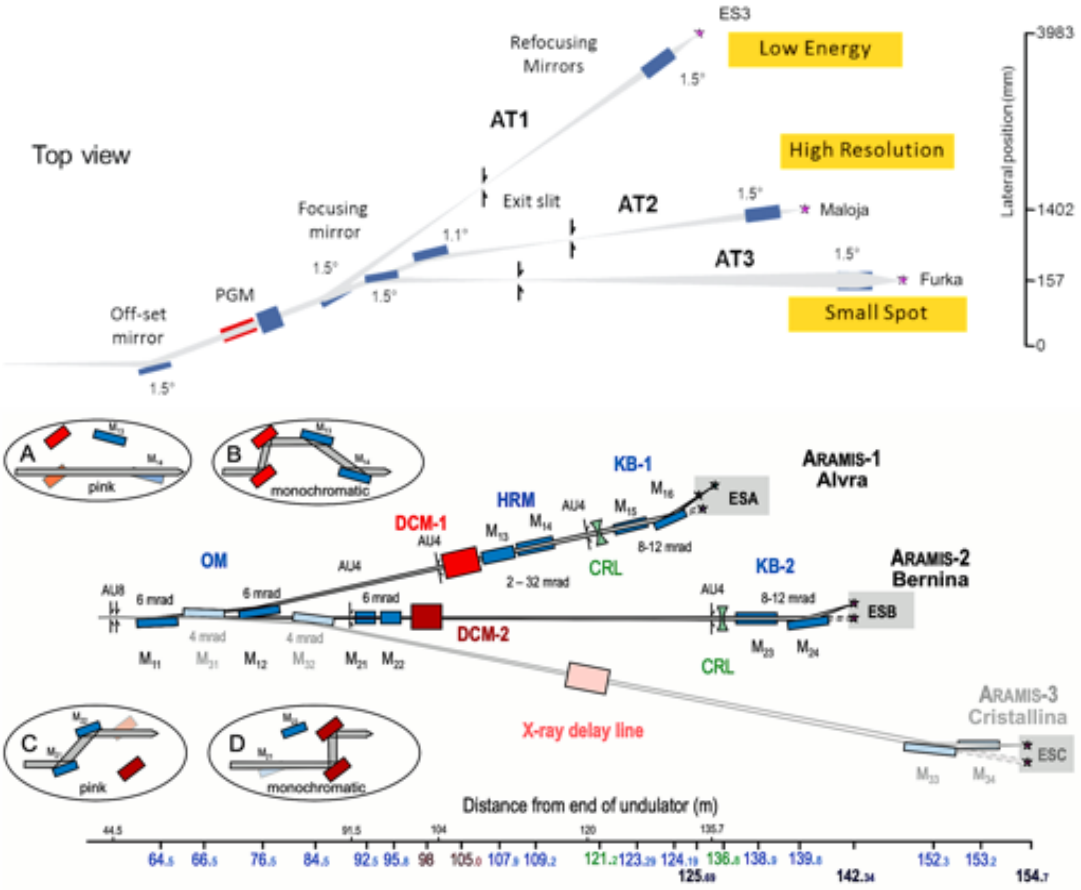

Figure 3.5: *Schematic layout of the X-ray optics at the ARAMIS (top) and ATHOS beamlines (bottom). The FEL-beam is distributed by horizontally deflecting offset mirrors to the ARAMIS-1 and ARAMIS-3 beamlines. The ARAMIS-2 beamline utilizes vertically deflecting offset mirrors or alternatively the DCM-2. Insets A and B show the configurations for the pink and monochromatic mode of ARAMIS-1, insets C and D the corresponding settings for ARAMIS-2. Image adapted from [23].*

Maloja

The Maloja experimental station at the ATHOS 2 branch will be designed as a highly versatile tool for atomic, molecular and optical physics, chemical sciences, soft X-Ray imaging, and novel approaches in non-linear X-Ray spectroscopy. The X-Ray pulses from the ATHOS undulator will be delivered with the minimum required three bounces from a single offset mirror and two KB mirrors. This optical layout will minimize transport losses and preserve the pulse wavefront. A short focal length of 1.5 *m* from the downstream KB mirror is chosen to achieve a micrometre-sized focus and therefore sufficient fluence for multi-photon excitations of the targets while maintaining enough space for laser incoupling elements and differential pumping between the last optical element and the experimental station. A specific characteristic of the Maloja station will be the combination of an X-Ray FEL with an infrared laser-driven attosecond high-harmonic generation (HHG) source. The combination of the two sources with their specific strengths will provide new tools for unravelling and controlling ultrafast chemical dynamics in gases, clusters and liquids from an entirely new point of view. In particular, electronic and nuclear dynamics could be measured in real time in isolated gas-phase molecules and clusters, solvated molecules, transition-metal complexes and

nanoparticles in their natural environment. The femtosecond to sub-femtosecond intense X-ray pulses from the ATHOS undulator and the HHG source will be optimally exploited in combination with the element specificity of soft X-ray spectroscopy and the nanoscale resolution of X-ray imaging [24].

Furka

The Furka experimental station for condensed matter and quantum materials at the ATHOS beamline will be dedicated to time-resolved Resonant Inelastic and Elastic X-ray Scattering (tr-RIXS and tr-REXS) as well as soft X-ray diffraction (tr-SXD) to study ultrafast dynamics in correlated materials and, more generally, in quantum matter. Many of the properties of quantum materials originate from couplings between charge, orbital, spin and lattice degrees of freedom. These couplings lead to cross-correlations among different physical observables, which develop towards the application of emergent functions [25]. Mott transition, high-temperature superconductivity, topological superconductivity, colossal magnetoresistance, giant magneto-electric effect and topological insulators are just a few examples of remarkable functions and properties that arise from the collective behaviour of the different degrees of freedom. Ultrafast techniques, especially femtosecond spectroscopy or time-resolved X-ray diffraction, supported by the advent of ATHOS, now open new opportunities for direct measurements of the coupling strength between the different degrees of freedom at temperatures < 10 K, with unprecedented precision. In femtosecond pump-probe experiments, selective excitation is used to probe: (i) low-energy electronic, magnetic and structural dynamics; (ii) coupling and ordering dynamics of charge, orbital, spin and lattice in correlated systems; (iii) phase transitions and quasiparticle excitations away from equilibrium; (iv) correlations and fluctuations in non-equilibrium systems; (v) coupling, control and switching in quantum matter. In the future, a second chamber is foreseen with the aim of investigating non-linear optical effects on solid materials as well as imaging techniques. Possible extensions to time-resolved X-ray magnetic circular dichroism (tr-XMCD) could be explored as well by taking advantage of the circular polarized radiation provided by ATHOS in combination with an externally applied magnetic field. Part of this thesis had been used to study a new high-resolution spectrometer that will be used within the Furka beamline, presented in Chapter 8.

References

[1] CJ Bocchetta et al. Fermi@ elettra fel conceptual design report. *Elettra-Sincrotrone, Trieste, Italy*, 2007.

[2] Enrico Allaria, Carlo Callegari, Daniele Cocco, William M Fawley, Maya Kiskinova, Claudio Masciovecchio, and Fulvio Parmigiani. The fermi@ elettra free-electron-laser source for coherent x-ray physics: photon properties, beam transport system and applications. *New Journal of Physics*, 12(7):075002, 2010.

[3] E Allaria, Roberto Appio, L Badano, WA Barletta, S Bassanese, SG Biedron, A Borga, E Busetto, D Castronovo, P Cinquegrana, et al. Highly coherent and stable pulses from the fermi seeded free-electron laser in the extreme ultraviolet. *Nature Photonics*, 6(10):699–704, 2012.

[4] E Allaria, D Castronovo, P Cinquegrana, P Craievich, Massimo Dal Forno, MB Danailov, G D'Auria, A Demidovich, G De Ninno, S Di Mitri, et al. Two-stage seeded soft-x-ray free-electron laser. *Nature Photonics*, 7(11):913–918, 2013.

[5] S Di Mitri, M Cornacchia, C Scafuri, and Magnus Sjöström. Electron beam optics and trajectory control in the fermi free electron laser delivery system. *Physical Review Special Topics-Accelerators and Beams*, 15(1):012802, 2012.

[6] Mirko Kokole, Tadej Milharčič, Giorgio Soregaroli, and Marco Tedeschi. Magnetic characterization of the fel-1 undulators for the fermi@ elettra free-electron laser. In *Proc. FEL*, pages 664–666, 2010.

[7] M Ferianis, A Bucconi, G Gaio, G Mian, M Predonzani, F Rossi, and Sincrotrone Trieste SCpA ELETTRA. The copper free fermi timing system: implementation and results. In *Proc. Beam Instrumentation Workshop*, volume 398402, 2010.

[8] Primož Rebernik Ribič, Eléonore Roussel, Gregory Penn, Giovanni De Ninno, Luca Giannessi, Giuseppe Penco, and Enrico Allaria. Echo-enabled harmonic generation studies for the fermi free-electron laser. In *Photonics*, volume 4, page 19. Multidisciplinary Digital Publishing Institute, 2017.

[9] Primož Rebernik Ribič, Alessandro Abrami, Laura Badano, Maurizio Bossi, Hans-Heinrich Braun, Niky Bruchon, Flavio Capotondi, Davide Castronovo, Marco Cautero, Paolo Cinquegrana, et al. Coherent soft x-ray pulses from an echo-enabled harmonic generation free-electron laser. *Nature Photonics*, 13(8):555–561, 2019.

[10] Marco Zangrando, Daniele Cocco, Claudio Fava, Simone Gerusina, Riccardo Gobessi, Nicola Mahne, Eric Mazzucco, Lorenzo Raimondi, Luca Rumiz, and Cristian Svetina. Recent results of padres, the photon analysis delivery and reduction system, from the fermi fel commissioning and user operations. *Journal of Synchrotron Radiation*, 22(3):565–570, 2015.

[11] Cristian Svetina, Martina Dell'Angela, Nicola Mahne, Marco Malvestuto, Fulvio Parmigiani, Lorenzo Raimondi, and Marco Zangrando. Magnedyn: the future beamline for ultrafast magnetodynamical studies at fermi. In *Advances in X-Ray/EUV Optics and Components IX*, volume 9207, page 92070E. International Society for Optics and Photonics, 2014.

[12] F Bencivenga, R Cucini, Flavio Capotondi, A Battistoni, R Mincigrucci, E Giangrisostomi, A Gessini, M Manfredda, IP Nikolov, E Pedersoli, et al. Four-wave mixing experiments with extreme ultraviolet transient gratings. *Nature*, 520(7546):205–208, 2015.

[13] F Capotondi, E Pedersoli, N Mahne, RH Menk, G Passos, L Raimondi, C Svetina, G Sandrin, M Zangrando, M Kiskinova, et al. Invited article: Coherent imaging using seeded free-electron laser pulses with variable polarization: First results and research opportunities. *Review of Scientific Instruments*, 84(5):051301, 2013.

[14] Henry N Chapman, Anton Barty, Michael J Bogan, Sébastien Boutet, Matthias Frank, Stefan P Hau-Riege, Stefano Marchesini, Bruce W Woods, Saša Bajt, W Henry Benner, et al. Femtosecond diffractive imaging with a soft-x-ray free-electron laser. *Nature Physics*, 2(12):839–843, 2006.

[15] C von Korff Schmising, B Pfau, M Schneider, CM Günther, M Giovannella, J Perron, B Vodungbo, L Müller, F Capotondi, E Pedersoli, et al. Imaging ultrafast demagnetization dynamics after a spatially localized optical excitation. *Physical review letters*, 112(21):217203, 2014.

[16] Cristian Svetina, Cesare Grazioli, Nicola Mahne, Lorenzo Raimondi, Claudio Fava, Marco Zangrando, Simone Gerusina, Michele Alagia, Lorenzo Avaldi, Giuseppe Cautero, et al. The low density matter (ldm) beamline at fermi: optical layout and first commissioning. *Journal of Synchrotron Radiation*, 22(3):538–543, 2015.

[17] Hans-Heinrich Braun and Rafael Abela. *Athos conceptual design report*. Paul Scherrer Institut, 2017.

[18] https://www.psi.ch/en/swissfel/accelerator.

[19] Gerhard Ingold, Rafael Abela, Christopher Arrell, Paul Beaud, Pirmin Böhler, Marco Cammarata, Yunpei Deng, Christian Erny, Vincent Esposito, Uwe Flechsig, et al. Experimental station bernina at swissfel: condensed matter physics on femtosecond time scales investigated by x-ray diffraction and spectroscopic methods. *Journal of synchrotron radiation*, 26(3):874–886, 2019.

[20] V Arsov, M Aiba, M Dehler, F Frei, S Hunziker, M Kaiser, A Romann, and V Schlott. Commissioning and results from the bunch arrival-time monitor downstream the bunch compressor at the swissfel injector test facility. *Proc. FEL?14*, pages 433–936, 2014.

[21] R Follath, U Flechsig, C Milne, J Szlachetko, G Ingold, B Patterson, L Patthey, and R Abela. Optical design of the aramis-beamlines at swissfel. In *AIP Conference Proceedings*, volume 1741, page 020009. AIP Publishing LLC, 2016.

[22] Romain Ganter, Simona Bettoni, Hans-Heinrich Braun, Marco Calvi, Paolo Craievich, Rolf Follath, Christopher Gough, Florian Löhl, Martin Paraliev, Luc Patthey, et al. Overview of the soft x-ray line athos at swissfel. In *38th Int. Free Electron Laser Conf.(FEL2017), Santa Fe, USA*, 2017.

[23] Christopher J Milne, Thomas Schietinger, Masamitsu Aiba, Arturo Alarcon, Jürgen Alex, Alexander Anghel, Vladimir Arsov, Carl Beard, Paul Beaud, Simona Bettoni, et al. Swissfel: the swiss x-ray free electron laser. *Applied Sciences*, 7(7):720, 2017.

[24] Rafael Abela, Arturo Alarcon, Jürgen Alex, Christopher Arrell, Vladimir Arsov, Simona Bettoni, Markus Bopp, Christoph Bostedt, H-H Braun, Marco Calvi, et al. The swissfel soft x-ray free-electron laser beamline: Athos. *Journal of synchrotron radiation*, 26(4), 2019.

[25] Yoshinori Tokura, Masashi Kawasaki, and Naoto Nagaosa. Emergent functions of quantum materials. *Nature Physics*, 13(11):1056–1068, 2017.

Chapter 4

X-Ray Transient Grating Spectroscopy[1]

In this chapter, we are going to cover every important step we went through in order to obtain the first ever successful result in an X-Ray Transient Grating experiment. As the reader should know by now, the newly developed temporally and spatially coherent X-ray Free Electron Lasers sources make possible the realization of ultrafast and nonlinear X-ray spectroscopies. Lessons from the optical regime show that exquisite information on matter can be obtained from such techniques, both in the time and frequency domains. Among them, Transient Grating is a versatile background-free Four Wave Mixing (FWM) technique used to probe *e.g.*, vibrational, magnetic, and electronic degrees of freedom and their relaxation in the time domain. Here, we demonstrate for the first time an X-ray Transient Grating experiment in the hard X-ray regime (7.1 keV) on Bismuth Germanate Oxide. X-rays offers multiple advantages for creating transient gratings: their deep penetration depth is able to probe the bulk properties of the materials, their element sensitivity can address core-excited states relaxations and their short wavelength can create excitation gratings with unprecedented high transfer momentum. The first advantage is demonstrated by non-resonant X-ray transient gratings on Bismuth Germanate Oxide, with time traces showing a clear sensitivity to optical phonons. A trace of acoustic phonons might be present, although superimposed to an unexpected signal we associated to the piezoelectric properties of the crystal. In order to confirm the presence of the acoustic phonons we performed a parallel optical Transient Grating experiment. Finally, the X-Ray Transient Grating approach demonstrates hard X-ray transient grating and paves the way for ultrafast coherent FWM techniques implying multiple non-collinear X-ray interactions.

4.1 The Transient Grating technique

Among the many FWM techniques, the degenerate case of Transient Grating (TG) spectroscopy provides an excellent time-resolved, background-free, window into coherent relaxations and excited carrier transport. It allows the study of a large variety of properties on different materials, *e.g.* relaxation dynamics of carriers [1], spin-waves creation and propagation [2], electron-phonon coupling [3], molecular dynamics [4], heat prop-

[1] Cristian Svetina, Jeremy Rouxel, Danny Fainozzi, *et al*. Hard x-ray transient grating spectroscopy on bismuth germanate. *Nature Photonics (review)*, 2021.

agation in diffusive and ballistic regime [5], to name a few. Its implementation in the optical and Extreme Ultra Violet (EUV) regimes relies on the interference between two crossed pump beams, the angle in between being 2ϑ, that generates an excitation grating on the sample, thus creating a transient periodic modulation in the refractive index of the material. The periodicity Λ of such transient grating can be expressed as

$$\Lambda = \frac{\lambda}{2\sin\vartheta} \tag{4.1}$$

with λ being the pumps (degenerate) wavelength. A delayed probe is then diffracted from the generated grating and the scattered beam is heterodyne- or homodyne-detected, depending on the presence (former) or the absence (latter) of a reference local field (often being another diffracted order of probe beam). The scattered beam wavevector $\vec{k}_s$ is given by the phase matching condition, that is:

$$\vec{k}_s = \vec{k}_1 - \vec{k}_2 + \vec{k}_3 \tag{4.2}$$

where $\vec{k}_1$ and $\vec{k}_2$ are the wavevectors of the two pump beams, and $\vec{k}_3$ is the probe one. It is also useful to defined the mismatch parameter $\Delta\vec{k}$ as

$$\Delta\vec{k} = \vec{k}_1 - \vec{k}_2 + \vec{k}_3 - \vec{k}_s. \tag{4.3}$$

Unlike pump-probe spectroscopy, TG is said to be a background-free technique since the signal is emitted in a direction, given by the phase matching condition, where no unwanted transmitted pump beams are present. This guarantees an excellent signal-to-noise ratio. TG also provides spatial and temporal information simultaneously: the periodicity of the excitation grating transfers a momentum $|\vec{q}|$ equal to

$$|\vec{q}| = \frac{2\pi}{\Lambda} \tag{4.4}$$

After a fast decay due to the electronic response, the remaining relaxation is linked to excited carrier transport and depends on the chosen length scale. For instance, at very short periodicities, the transport process consists in a single interaction for each carrier, known as the ballistic regime, while at larger periodicity, multiple scattering events dominates and lead to the diffusive regime. This can clearly be seen by measuring the relaxation timescales as a function of the excitation grating periodicity [5]. Until the present work, EUV has been the highest photon frequency domain at which TG has been successfully implemented [6] with the aim to achieve higher momentum transfer and to use element sensitivity, but limited to light elements and to tens of nanometer penetration depth, given the short attenuation length. The extension of TG in the X-ray range (XTG) would allow to add the extra features of atomic selectivity and bulk probing and to increase even more the momentum transfer at the sample. Consequently, XTG provides a unique possibility to study the ultrafast electronic response, the optical and acoustic properties, and the heat diffusion in the bulk at the nanometer scale. The method of crossing the excitation beams typically used for generating the TG (see figure 4.1 - left) becomes very hard moving towards the soft and hard X-rays regimes due to the grazing incidence geometry of the optics involved. In a recent paper we proposed a simple method to generate excitation gratings on a sample by implementing the Talbot effect (see figure 4.1 - right) for convergent Free Electron Laser Gaussian beams [7]. The beauty of this approach is that it requires just a simple alignment of phase gratings

that generate the spatially and temporally overlapped phase-locked interfering beams without requiring complicated and tedious alignment procedure. The only alignment needed is for the probe in a similar fashion as for any pump-probe experiment but, of course, in phase matching condition.

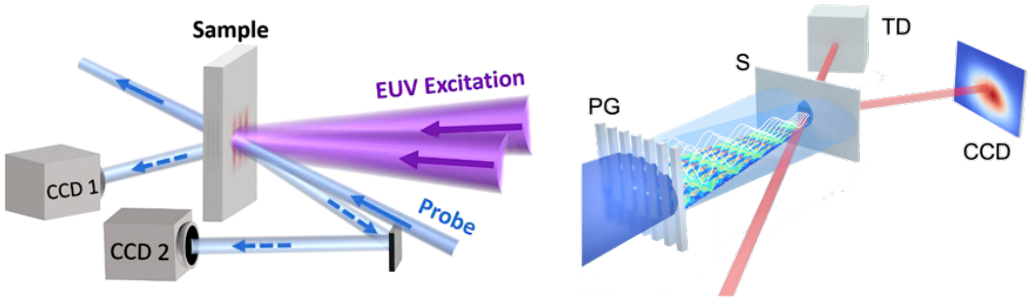

Figure 4.1: *Left: Schematic of the EUV experiment at FERMI adapted from [8]. Two EUV pulses launch coherent phonons producing a transient diffraction grating in the sample, which is monitored via diffraction of a time-delayed 400 nm probe pulse. Diffracted probe beams (dashed arrows) are detected by CCD cameras. Right: Schematic of the XTG setup. In dark blue, the incoming ultrashort X-ray pulse is diffracted by a transmission phase grating (PG). Interferences between the two first orders diffracted beams generate a Talbot carpet,* i.e., *a region of self images of the originating phase grating. The sample (S) experiences a transient grating excitation with smaller periodicity due to the convergence of the incoming beam. In red, a delayed optical pulse probing the relaxation of the transient grating by being diffracted on the 2D detector (CCD) and transmitted on to a diode (TD).*

4.2 The Talbot effect

In this study we present the first measurements of transient gratings in the hard X-ray regime performed at the Bernina endstation [9] at SwissFEL [10] relying on the Talbot self-imaging effect for convergent Gaussian beams with high time resolution. Here, we briefly review how to evaluate the Talbot effect for a general 1D transmission grating. More details on the effect can be found in the literature [11]. The calculation is conducted within Fresnel theory of diffraction. First, we introduce a generic grating which, since it has a periodic structure, can be described in its Fourier representation $T(x)$ as:

$$T(x) = \sum_n c_n e^{-ink_G x} \tag{4.5}$$

where x is the transverse spatial coordinate of the grating, k_G is defined as $\frac{2\pi}{d}$ (d being the pitch of the grating) and the coefficients c_n are defined as:

$$c_n = \frac{1}{d}\int_{-\frac{d}{2}}^{+\frac{d}{2}} T(x)e^{ink_G x}dx \tag{4.6}$$

The gratings used during this experiment were binary phase grating made out of synthetic diamond, produced at the Laboratory for Micro- and Nanotechnology (PSI) through chemical vapor deposition (CVD). For a binary phase grating, one can show that the Fourier transform $T(x)$ of the grating take the form

$$T(x) = \begin{cases} A_1 e^{i\phi_1} & \text{if } 0 < |x| \leq \frac{ad}{2} \\ A_2 e^{i\phi_2} & \text{if } \frac{ad}{2} < |x| \leq \frac{d}{2} \end{cases} \tag{4.7}$$

where a is the groove ratio, A_1 and A_2 are the amplitudes of the grating and ϕ_1 and ϕ_2 are the phases of the grating. Using eq. 4.7 inside eq. 4.6, the general solution for the coefficients is

$$c_n = \frac{i}{nk_G}\left(A_2 e^{i\phi_2} - A_1 e^{i\phi_1}\right) + \frac{e^{-in2\pi a}}{nk_g}\left(A_1 e^{i\phi_1} - A_2 e^{i\phi_2}\right). \tag{4.8}$$

In the case of perfect $\frac{\pi}{2}$ grating we have $A_1 = A_2 = 1$, $\phi_1 = 0$, and $\phi_2 = \frac{\pi}{2}$. Thus, eq. 4.8 becomes:

$$c_n = \frac{1+i}{nk_G}\left(e^{-in2\pi a} - 1\right). \tag{4.9}$$

Assuming the coordinate z at the grating location to be z_G, the electric field at the phase grating is given by $E_0(x,y,z_G)T(x)$, with $E_0(x,y,z_G)$ being the incident electric field. After the interaction with the grating, the electric field can be calculated at any position by performing a Fresnel propagation, which is defined as:

$$E(x,y,z) = \frac{ik}{2\pi z} e^{-ikz} \int\int_{-\infty}^{+\infty} E_0(x',y',z_G) T(x') e^{-\frac{ik(x'-x)^2}{2z}} e^{-\frac{ik(y'-y)^2}{2z}} dx'dy' \tag{4.10}$$

where $k = \frac{2\pi}{\lambda}$ is the radiation wavevector. Solving the integral for an incident plane wave $E_0(x',y',z_G) = E_0 e^{-ikz_G}$ and setting the origin at the grating location (*i.e.*, $z_G = 0$), we get

$$E(x,y,z) = E_0 e^{-ikz} \sum_n c_n e^{-ink_G x} e^{\frac{in^2 k_G^2}{2k} z}. \tag{4.11}$$

For a glimmer of clarity, in order to avoid the feeling of witnessing wizardry tricks, the calculation is actually performed step by step in the Appendix. It is now useful to define the Talbot distance Z_T as

$$Z_T = \frac{2\pi k}{k_G^2} \tag{4.12}$$

from which can be easily seen that if we have $z = nZ_T$, where $n \in \mathbb{N}$, the electric field displays an interference pattern with the same periodicity as the transmission grating. For a Gaussian beam the same procedure applies. In this case the Fresnel calculation is more challenging and the Talbot effect leads to interference gratings with smaller/larger pitches with respect to the initial diffraction gratings ones, due to the convergence/divergence of the photon beam. By defining the incoming Gaussian beam as

$$G(x,y,z) = A_0 \frac{\omega_0}{\omega(z)} e^{-\frac{x^2+y^2}{\omega(z)^2}} e^{-\frac{ik(x^2+y^2)}{2R(z)}} e^{-i(kz-\phi(z_G))} \tag{4.13}$$

where ω_0 is the waist of the beam and

$$\omega(z) = \sqrt{1 + \left(\frac{2z}{k\omega_0^2}\right)^2}, \quad R(z) = z\left[1 + \left(\frac{2z}{k\omega_0^2}\right)^2\right], \quad \tan\phi(z) = \frac{2z}{k\omega_0^2}. \tag{4.14}$$

By performing the Fresnel propagation following the procedure of eq. 4.10, the final result is [12]:

$$E(x,y,z) = A_0 \frac{\omega_0}{\omega(z)} e^{-ik(z+z_G)} e^{-\frac{x^2+y^2}{\omega(z)^2}} e^{-\frac{ik(x^2+y^2)}{2R(z)}} e^{-i(\phi(z_G)+\phi(z))} \sum_n c_n e^{-\frac{in^2 k_G^2}{4a(z)} z} e^{\frac{inkk_G}{2za(z)} x}. \tag{4.15}$$

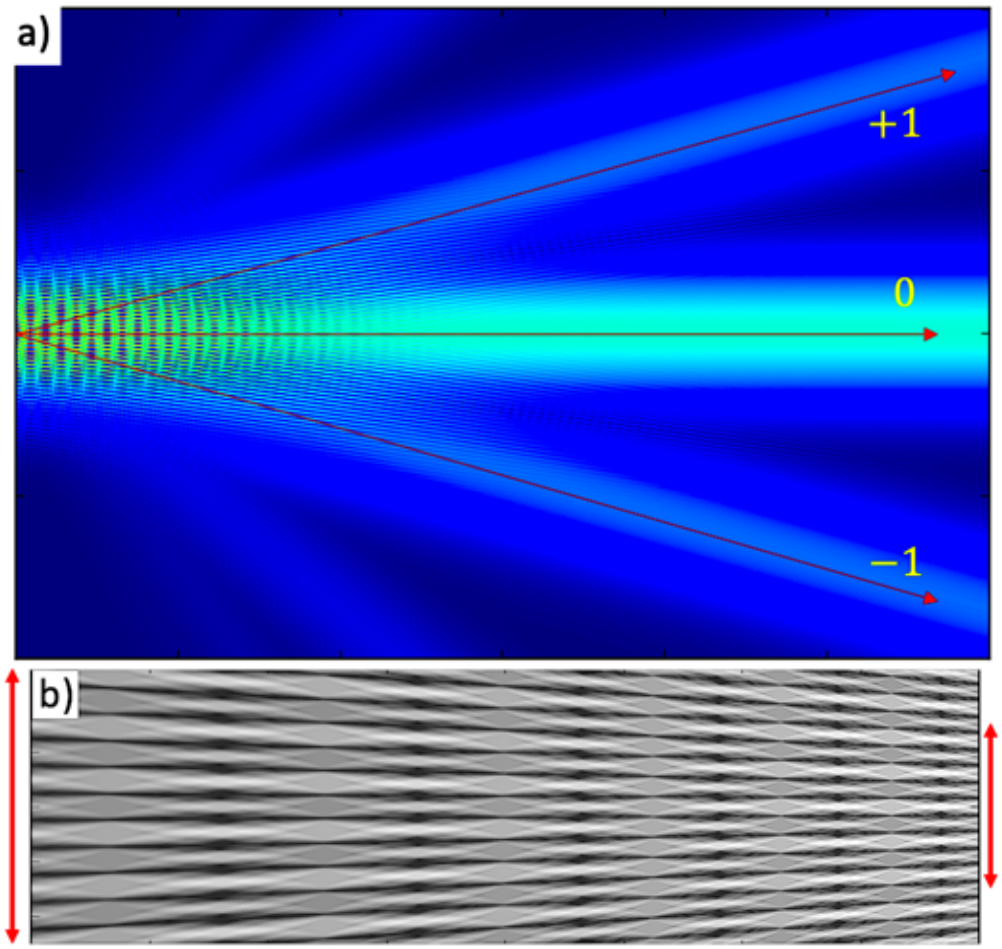

Figure 4.2: *Top, Fresnel simulation of a converging Gaussian beam, coming from the left, diffracted by a transmission grating. Diffraction orders emerge from the grating and interfere generating a Talbot carpet. Bottom, detail of the Talbot carpet for a convergent Gaussian beam. The red arrows indicate the original diffraction grating pitch (left) and the XTG pitch after several Talbot planes (right).*

where

$$\alpha(z) = \frac{1}{\omega(z_G)^2} + \frac{ik}{2}\left(\frac{1}{R(z_G)} + \frac{1}{z}\right). \tag{4.16}$$

When this term is explicit, the solution presents two new terms if compared to the plane wave case: the localization and magnification terms. The former accounts for the displacement of the Talbot planes which is not constant while the second accounts for the pitch of the interference pattern and has the following form:

$$M(z) = \left[\left(\frac{R(z_G)+z}{R(z_G)}\right)^2 + \left(\frac{2z}{k\omega_0^2}\right)^2\right]\frac{z}{R(z_G)+z} \tag{4.17}$$

which is less than the unity for convergent Gaussian beams. As a consequence, the XTG interference pattern has a smaller pitch compared to the diffraction grating. A schematic of the full Talbot geometry is displayed in fig. 4.2 a) and a Fresnel simulation displaying the shrinking of the pitch due to the convergent Gaussian beam is shown in fig. 4.1 (right) and in fig. 4.2 b). Another important quantity to be considered is the separation distance, which is the distance from the grating for which the first orders of

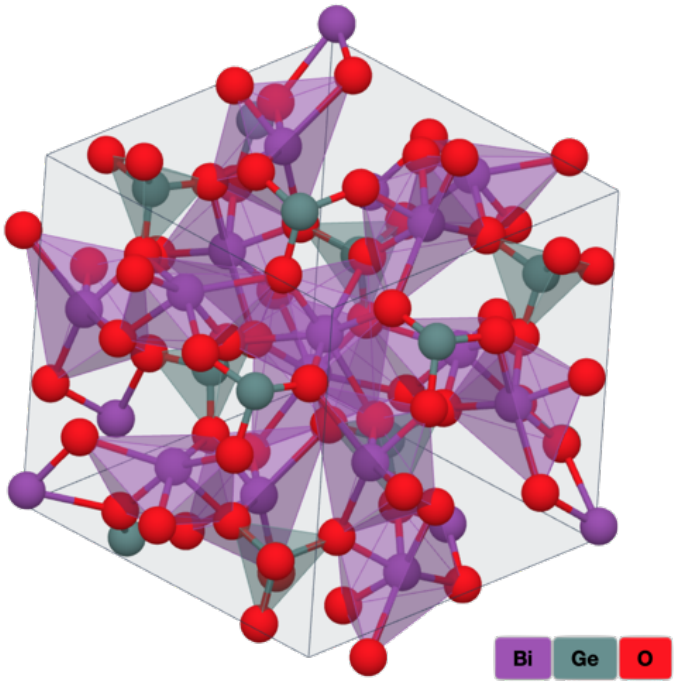

Figure 4.3: *The unit cell of $Bi_4Ge_3O_{12}$. Image adapted from [37].*

diffraction stop overlapping. For a Gaussian beam it can be shown to take the form:

$$z_{sep} = \frac{\omega(z_G)}{2\tan\beta} \tag{4.18}$$

with $\beta = \arcsin\left(\frac{\lambda}{d}\right)$ being the angle of diffraction of the first orders.

4.3 The sample

Bismuth Germanate (BGO) is an optically isotropic material which has become very popular due to its electro-optic, electro-mechanical and scintillator properties [13, 14]. BGO crystals have found a wide range of applications as particle scintillation detectors for high-energy physics [15], holographic data storage material [16], in high-resolution positron emission tomography, as solid state laser host when activated with trivalent rare-earth ions [17] and as an electro-optic material for optical voltage, current, and electric power sensors [18]. BGO, in its $Bi_4Ge_3O_{12}$ conformation, is a cubic crystalline material build up of isolated GeO_4 tetrahedra and strongly deformed BiO_6 octahedra with the eulytine structure [19] (see figure 4.3), point group $I\bar{4}3d$ (220), 76 atoms per unit cell and a Face Centered Cubic (FCC) Bravais lattice with lattice parameter $a = 10.497$ Å [20].

4.4 Experimental setup

The XTG experiment presented relies on the use of diffraction phase gratings to generate the transient excitation gratings (XTG) on the sample position. Figure 4.4 represents the experimental geometry. The incident FEL beam (in yellow) is diffracted by the

phase grating and then impinges on the sample. The Talbot effect generates a transient excitation grating on the sample. A delayed probe laser (in blue) is incident on the sample at the phase matching angle and is diffracted by the excitation grating on the sample. Finally, the diffracted probe is homodyne-detected by a CCD camera. In the following section, we present the experimental geometry, details on the X-ray pump and optical probe, information on the diffraction gratings and on the detectors.

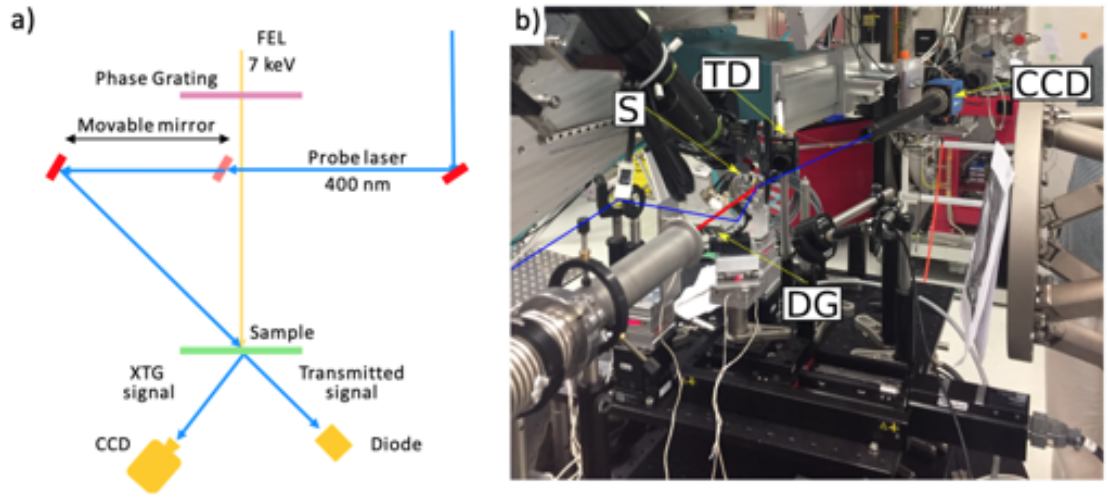

Figure 4.4: *a) Experimental geometry used at Bernina, SwissFEL, to implement the transient grating. b) Annotated picture of the experiment.*

4.4.1 Experimental geometry

The incident X-ray beam is focused with bendable Kirkpatrick-Baye (KB) mirrors (details in section 4.4.3) and impinges on a phase grating. The Talbot effect creates a periodic pattern (Talbot carpet shown in fig. 4.2) having periodicity planes at distances equal to the Talbot distance Z_T (see eq. 4.12) by the interference of the diffracted orders. Such interference spatially lasts as long as the orders of diffraction overlap, thus setting a maximal possible distance between the phase grating and the sample position, usually referred as separation distance z_{sep} (see eq. 4.18). Moreover, the convergence of the X-ray beam ensures that the excitation grating possess a smaller pitch than the phase grating's (de-magnification factor), this pitch being controlled by the X-ray focusing, the distance between the focus and the phase grating, and the relative distance between the grating and the sample. For a $\frac{\pi}{2}$ phase grating, the transmitted 0^{th} order is present; it must be noted that the 0^{th} induces some interaction in the sample, but it does not contribute to the diffracted XTG signal due to the phase-matching condition. This effect is not present in a perfect π phase grating. In our experiment, the gratings and the sample were mounted on the General Purpose Station (GPS) at the Bernina endtstation, with an overall separation of 150 *mm* between them.

4.4.2 Binary Phase Gratings

The gratings used during this experiment were binary phase grating made out of synthetic diamond, supplied by Diamond Materials GmbH, and produced at the Laboratory for Micro- and Nanotechnology (PSI) through chemical vapor deposition (CVD).

The gratings were fabricated using similar approach as reported by Makita at al. [21]. Briefly, a 10 μm thick diamond membranes supported by a Silicon frame were first cleaned in $H_2SO_4 : H_2O_2$ 2 : 1 solution at 120 $^\circ C$ to remove organic contamination. Then, the membranes were sputter-coated with 10 nm thick Cr layer and subsequently spin-coated with ~ 1 nm thick negative tone resist FOX16 followed by baking at 100 $^\circ C$ for 3 min on a hotplate. The resist was patterned in electron beam lithography system Raith EBPG 5000 PlusES using 100 keV accelerating voltage. After the exposure, the samples were developed for 8 min in *Microposit* 351 : H_2O 1 : 3 solution at room temperature, then rinsed in DI water and isopropanol. The patterned resist gratings were hard baked at 300 $^\circ C$ for 1 hour on a hotplate to increase etch selectivity between the resist and diamond. Unmasked Cr layer was removed in Cl_2/O_2 plasma revealing the underlying diamond for subsequent etching. Finally, the HSQ grating pattern was transferred into diamond by oxygen plasma etching in Oxford PlasmaLab 100 with the following etching parameters: chamber pressure of 10 $mTorr$, 30 $sccm$ O_2 flow rate, powers of ICP and RF were 750 W and 100 W, respectively. During the beamtime for the XTG experiment, at least 5 different grating were tested. Here we report the main result based on the usage of two of them. The first one is a π phase grating of 1650 nm pitch. This configuration, combined with a convergent gaussian beam provided by the KB mirrors, generated an excitation grating of ~ 660 nm at the sample position. In this case we estimated z_{sep} to be ~ 335 mm while the relative separation of the Talbot planes Z_T in the sample area was ~ 5 mm. The second grating used was a $\frac{\pi}{2}$ phase grating with a pitch of 960 nm, which induced an excitation grating with a periodicity of ~ 770 nm. The z_{sep} and Z_T parameters were estimated to be 240 mm and 1.7 mm, respectively. Formulas use to estimate these parameters for arbitrary diffraction gratings and geometry are given in section 4.2. In figure 4.5 we show the Scanning Electron Microscopy (SEM) images of the gratings used during the experiment, while in fig. 4.6 we show a printed grating on a gold surface placed at the nominal sample position obtained from the π diamond phase grating with a pitch of 1650 nm showing a periodicity of ~ 770 nm.

4.4.3 The X-ray pump

High intensity horizontally polarized X-ray pulses were delivered by SwissFEL with a time duration of ~ 50 fs (FWHM) and a repetition rate of 50 Hz. The FEL was tuned to 7.134 keV by adjusting the electron bunch energy $\langle\gamma\rangle_0$ and changing the insertion devices K parameter. The emitted radiation had a bandwidth $\frac{\Delta\omega}{\omega} \sim 0.3\%$ and was used in pink beam mode (*i.e.,* without the monochromator) for all the BGO measurements. The FEL beam was focused on a scintillator coupled with a CCD camera through a microscope (X-ray eye) 750 mm downstream the grating by tuning the curvature of the focusing KB mirrors. Then, the vertical focus was adjusted to finally obtain an horizontal strip of excitation with size 250×150 μm^2 (for σ_x and σ_y respectively) on the sample, matching approximately the size of the non-collinear projection of the optical probe on the sample surface at all phase matching angles. The beam intensity provided by the SwissFEL ranged between 300 μJ and 800 μJ, while the intensity at the sample was kept to be ~ 1.5 μJ.

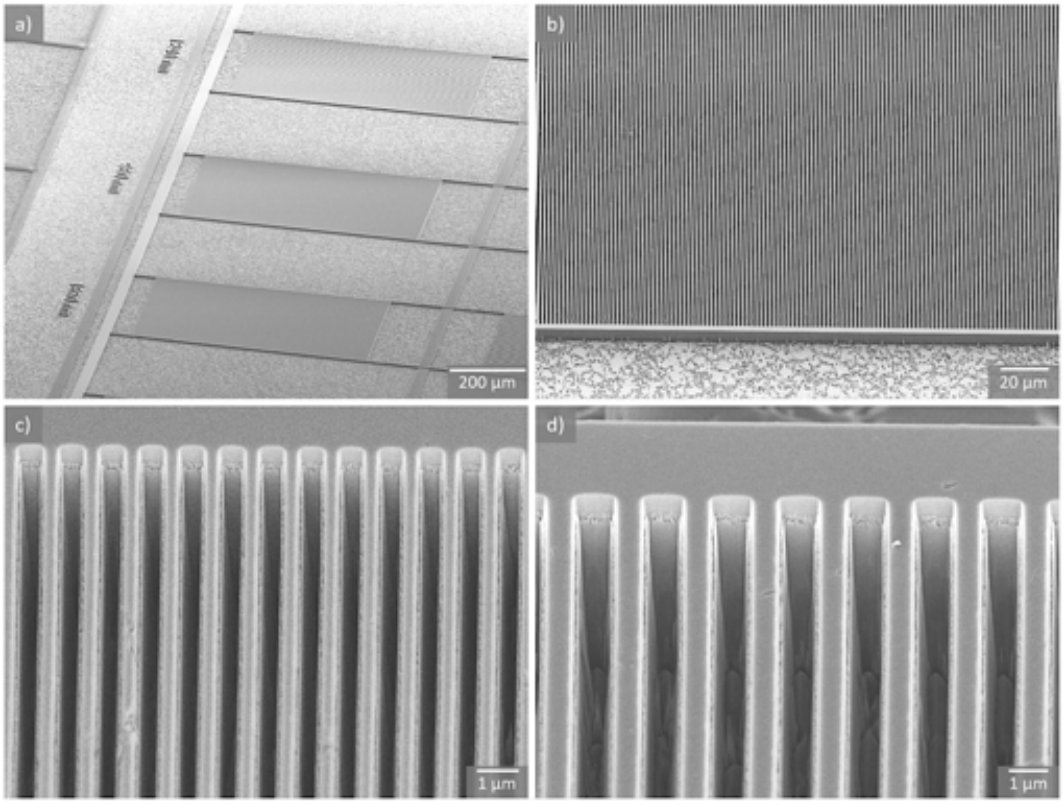

Figure 4.5: *45-degree-tilt-view SEM images of diamond gratings used in the experiment: a) an overview of diamond membrane with a few gratings; b) closer look at the 1650 nm pitch grating; c) and d) zoomed in images of 960 nm and 1650 nm pitch gratings, respectively.*

4.4.4 The laser probe

The optical probe was generated from a Ti:Sapphire laser delivering 35 fs pulses at nominally 800 nm (10 mJ). A Barium borate (BBO) crystal was used to generate the second harmonic (400 nm) with an intensity $\sim 1.2\ \mu J$. A bandpass filter (40 nm bandwidth) was used to remove the unwanted fundamental harmonic while a waveplate was used to control the intensity. Further filtering was passively done by several bandpass reflecting mirrors. The spot size at the sample was tuned to $70 \times 45\ \mu m^2$ (FWHM) using a lens. The arrival time of the probe laser was tuned by a delay stage upstream the sample and the final reflection to the sample was accomplished by a D-shape mirror to accommodate for small phase matching angles. This D-shape mirror was mounted on a linear stage (see fig. 4.4) in order to change the phase matching angle when different gratings were being used. The time overlap between the X-ray pump and the optical probe was readjusted for every phase-matching angle.

4.4.5 Detectors

The optical beams (the one used in Timing Tool and the one diffracted through XTG) were measured by a Charged Coupled Device (CCD) 4.2 PCO-edge camera. A 2f-2f lens (200 mm half distance) was installed in front of the CCD, imaging the sample at the chip, thus allowing to reduce the background at the detector on the CCD camera. In order to control the angle of detection for different phase matching conditions, the

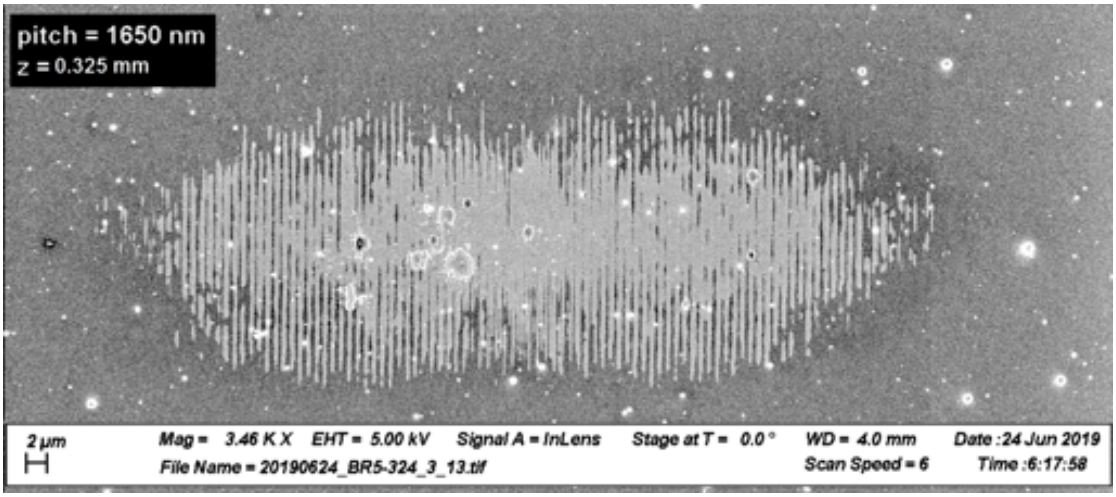

Figure 4.6: *Printed grating on a gold surface placed at the nominal sample position from the π diamond phase grating with a pitch of 1650 nm showing a periodicity of $\sim$ 770 nm. Transient excitation gratings are obtained by decreasing the X-ray fluence below damage threshold.*

CCD camera was mounted on an heavy load $\delta - \gamma$ diffractometer at $\sim$ 800 *mm* from the sample position and moved in the diffraction plane of the experiment. Then the ϑ angle was scanned in order to locate the diffracted XTG signal nearby the calculated value. A typical diffracted XTG spot recorded with the detector is displayed in figure 4.7. The signal amplitude was obtained by integrating over the signal area while the weak background was subtracted using and area where the XTG signal is absent. This weak background was originated from the isotropic scattering of optical beam from the sample. Dark shots (unpumped signal) were recorded too and used for normalizing the data as well as to check that the sample was not being printed on during the measurements.
Finally, an ultra-fast diode was positioned in transmission along the optical probe path with the purpose to measure the laser transmitted through the sample (see fig. 4.4).

Results

According to F. Bencivenga *et al.* [6], the XTG expected signal can be evaluate through the following expression:

$$I_{XTG} = |\chi^{(3)}|^2 I_{FEL}^2 I_{Las} e^{-\alpha_{Las} L_z} sinc^2\left(\frac{|\Delta\vec{k}| L_{int}}{2}\right), \tag{4.19}$$

where χ^3 is the third order susceptivity, I_{FEL} is the intensity of each ± 1 diffractive beams (considered equal due to the geometry of the gratings), I_{Las} is the intensity of the 400 *nm* probe laser, and the *sinc* term is the usual representation of the phase matching factor in a finite size sample [22–24]. We set L_{int} equal to the absorption coefficient at 7.134 *keV* estimated to be $\sim$ 6.076 μm. Finally, just for completeness, we added the exponential factor to account for the absorption of the radiation inside the sample, where L_z and α are the sample length crossed by the beams and the absorption coefficient at the involved frequencies, respectively [25]). While in the optical case this is often negligible (as it is for the present case), at EUV/soft X-ray wavelengths this term compares with the typical size of the interaction volume (*i.e.*, $\alpha L_z \simeq 1$), and it must be taken into

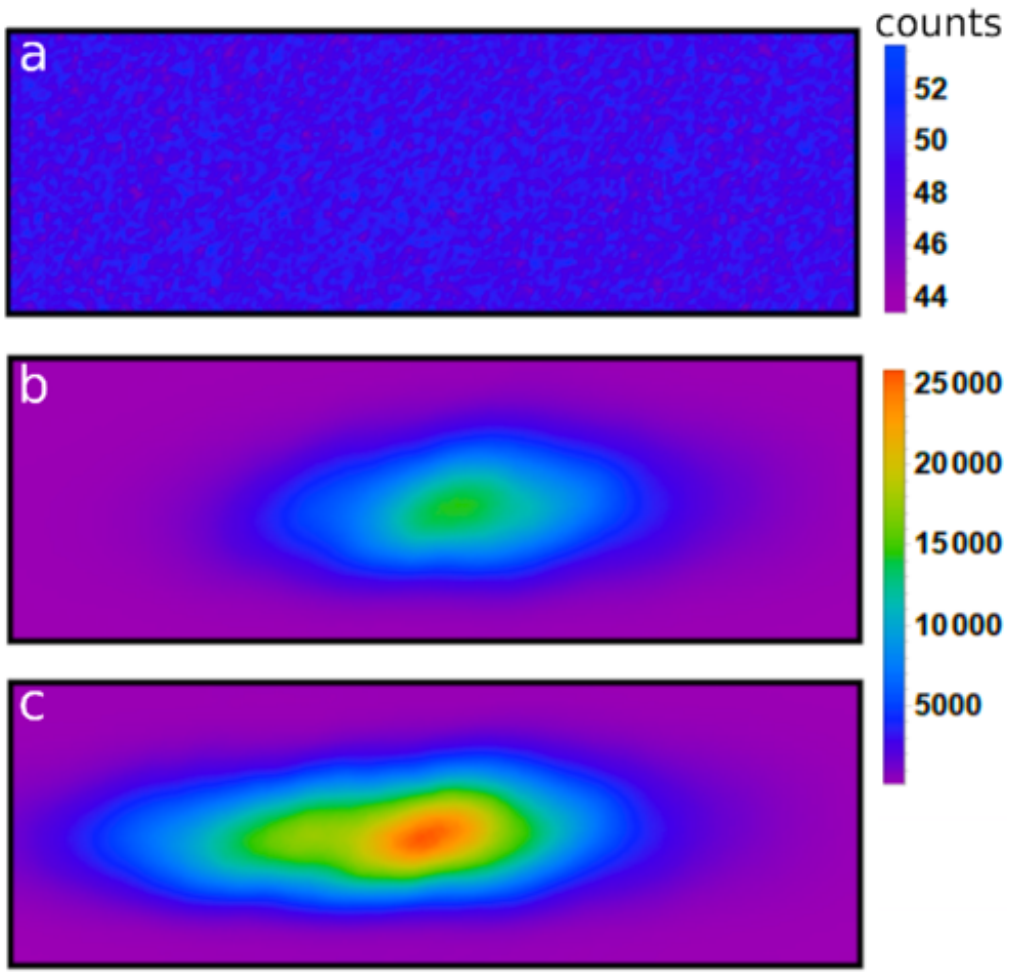

Figure 4.7: *Signal spots on the CCD detector at different time delays Δt between the X-ray pump and the optical probe. a) Before time-zero,* i.e., *$\Delta t < 0$, no XTG signal is observable. b) For $t = t_0$* (i.e., *at $\Delta t \sim 0$), which defined as the saddle point in between the background and the maximum of the signal, the XTG signal rises and quickly reaches a maximum. In panel c), the signal at $\Delta t = 150\ fs$ (maximum of the signal).*

account. To be sure of the entity of the signal, we checked on the expected quadratic behavior of the XTG signal with respect to the FEL intensity (see equation 4.19). This was accomplished through an X-rays pump intensity scan at a fixed $\Delta t = 2\ ps$ time delay on the time trace induced by a 770 nm excitation grating. In fig. 4.8 the data is compared to a quadratic fit with very good agreement demonstrating the nonlinearity of the signal. The outlying point at 0.6 of transmission (%) is due to a miscalibration of the solid-state attenuator used during the scan, but was nonetheless kept for consistency. We have estimated the efficiency of the XTG process η_{XTG} by calculating the ratio of the XTG signal and the intensity of the probe pulse. The obtained value is 1.32×10^{-4} which confirms that the efficiency seems to be larger in the hard X-rays compared to the EUV [6]. This can be explained due to the larger penetration depth of the X-rays with respect to the EUV. In fact, when we normalize the efficiency by the penetration length expected in the two cases, we obtain a similar value to the one reported in [8]. The module of the third order susceptibility $|\chi^{(3)}|$ has been estimated for the same config-

uration giving $|\chi^{(3)}| = 4.23 \cdot 10^{-20}\ m^2V^{-2}$, in good agreement with the expected value, given the phase matching condition. These results prove the capability to exploit XTG to measure bulk properties of matter.

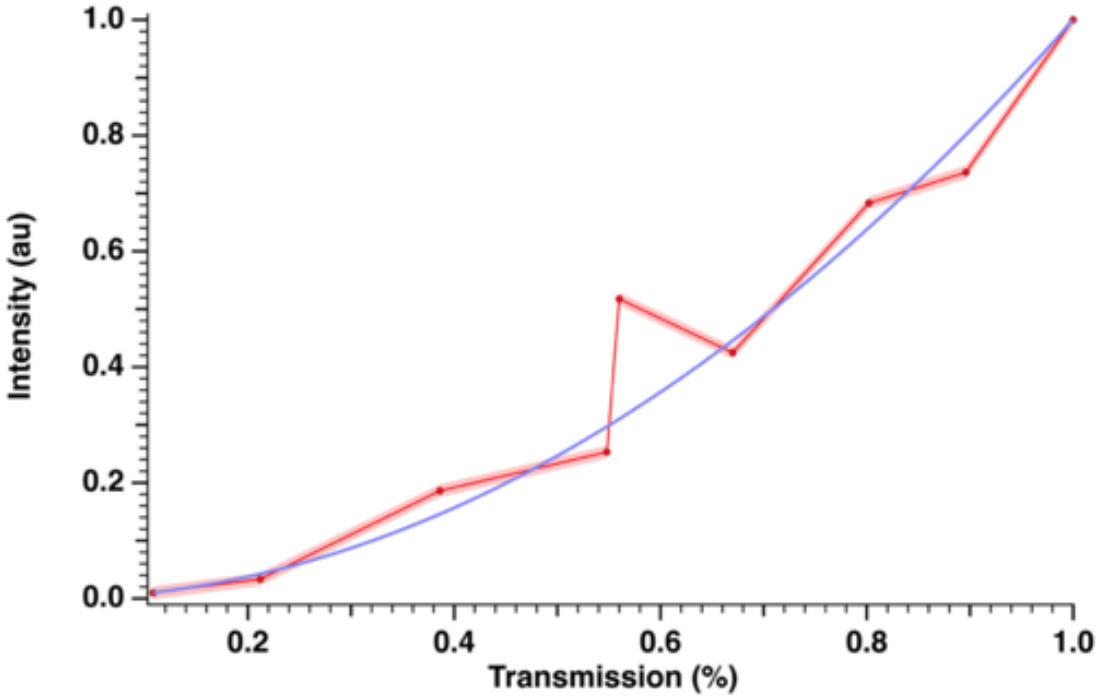

Figure 4.8: *Scaling of the XTG signal with the incoming X-ray fluence at 7.134 keV and 2 ps delay. The experimental measures (in red) are compared with a quadratic scaling expected for this nonlinear process.*

4.5 BGO time trace with 960 nm $\frac{\pi}{2}$ phase grating

In fig. 4.9 a) and b) we show the XTG time trace of the BGO obtained using the 960 nm phase grating, corresponding to a nominal excitation XTG pitch of about 770 nm. The signal displays multiple regimes of relaxation: the electronic ultrafast response (hundreds of femtoseconds), the appearance of an optical phonon mode lasting several picoseconds followed by a slow increase in the signal intercalated with coherent acoustic phonons. The short time scans (up to 5 ps) have been fitted with a double exponential function:

$$S_{\mathrm{XTG}} = \left| \frac{1}{2}\left[1 + \mathrm{erf}\left(\frac{t - t_0}{\sigma}\right)\right]\left(A_1 e^{-\frac{(t-t_0)}{t_1}} + A_2 e^{-\frac{(t-t_0)}{t_2}} + A_3\right)\right|^2 \tag{4.20}$$

where t_0 is the time zero between X-rays and probe, calculated as the saddle point in between the background and the maximum of the signal. A_1 and A_2 are amplitudes of the fast and slow decay channels with lifetimes τ_1 and τ_2. The quantity σ is the rise time at t_0 and indicates, with a good approximation, the time resolution of the experiment. The decay lifetimes values from the fitting procedure are $t_1 = 42 \pm 4\ fs$ and $t_2 = 1049 \pm 49\ fs$, while $\sigma = 80 \pm 6\ fs$. The latter values agree with the convolution between the X-ray pulse (40-50 fs) and the laser pulse (80-90 fs). The residual of the short time scans (fig. 4.9 c)) displays a clear periodic oscillation which corresponds to the A_1 optical phonon mode which has a frequency of $2.605 \pm 0.004\ THz$. The obtained

value is in very good agreement with the ones reported in literature [8, 26] and with 2.61 THz expected from the phonon dispersion curve on the corresponding momentum transfer. The long time trace have been fitted with an exponential function and the residuals have been Fourier transformed (fig. 4.10 d)). The obtained spectrum displays several frequencies components: at 6.9 ± 1.1 GHz (later we will see that this peak are a superposition of two frequencies), 23.5 ± 0.1 GHz, 47.4 ± 0.4 GHz and 70.9 ± 1.7 GHz. Those frequencies will be deeply discussed in the next section. Details on the fitting results are given in section 4.8.1.

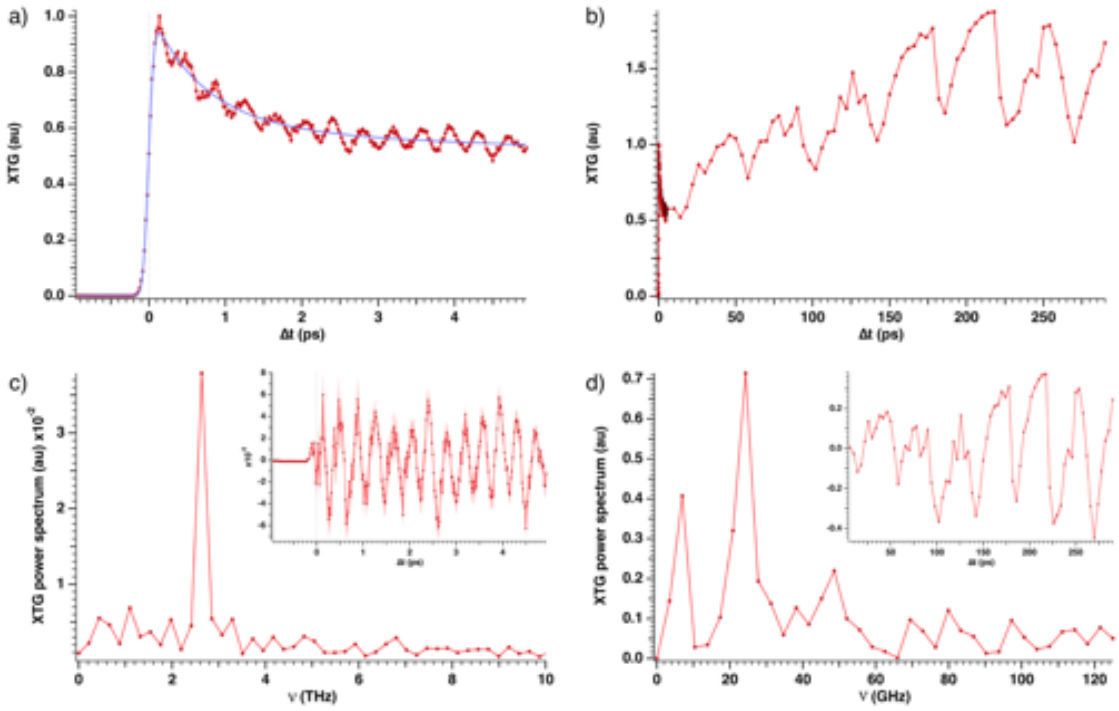

Figure 4.9: *X-ray Transient Gratings results on BGO at 7.134 keV with an excitation grating pitch of 770 nm. a) Time trace at short times (< 5 ps). The fast oscillations are attributed to optical phonons coherence. b) Full time trace. After the fast electronic and phononic relaxation, the slower oscillations are associated to acoustic phonons and heat diffusion. c) Fourier transform of the fast oscillatory component showed in the insert (residuals from the fit in a)). d) Fourier transform of the slow oscillatory component showed in the insert (residuals from the fit (not showed) in b)).*

4.6 BGO time trace with 1650 nm π phase grating

In this section, we present XTG measurements on BGO with a 1650 nm pitch π phase grating corresponding to a nominal excitation XTG pitch of about 660 nm. For this measurements, a fast diode was used in transmission to detect the pump-probe signal. The short and long XTG time traces are displayed in fig. 4.10 a) and b), respectively. The lower signal-to-noise (SN) ration compared to the trace shown in the main text is attributed to a a slightly off-set geometry with respect to the phase matching condition. Also, a contribution to the lower SN ration can be imputed to some instabilities of the FEL source arisen during the measurement. As for the case reported for the 960 nm grating, the short time trace displays an exponential ultra-fast decay. By Fourier transforming the residual, the optical phonon modulation is identified to be equal to

2.6 ± 0.1 THz and is displayed in fig. 4.10 c). The long time trace have been fitted with an exponential function and the residuals have been Fourier transformed (fig. 4.10 d)). The obtained spectrum displays several frequencies components: at 6.9 ± 1.0 GHz (also in this case, we will see that this peak are a superposition of two frequencies), 24.1 ± 0.1 GHz, 47.8 ± 0.3 GHz and 69.9 ± 2.6 GHz, similarly to the trace shown previously. In this particular case, also the probe laser intensity I_{trans} was recorded in transmission by means of an ultrafast diode. Fig. 4.11 a) shows the fast response measured by the diode: the raising time, defined as the σ_{diode} in the erf function used to fit the transient traces, is $\sigma_{diode} = 159 \pm 13$ fs. As expected, the signal from the diode in transmission does not display any signature of the optical phonon (in the short time trace), while in the long time scale, fig. 4.11 b), the long lived oscillatory components at 3.2 ± 0.5 GHz, 24.0 ± 0.1 GHz, 47.9 ± 0.3 GHz and 70.7 ± 1.1 GHz are present. Since no heterodyne detection was done with this detector, we can safely assume that the coherent $\chi^{(3)}$ is very small and that these oscillations can be attributed to an incoherent modulation of the optical index due to the high photon energy of the XFEL pulses (the four point correlation function of $\chi^{(3)}$ can be factorized). Thus, these frequencies, both present in the XTG traces and in transmission, are attributed to the direct effect of pumping BGO with a periodic modulation. To our knowledge such evidences have never been reported. In section 4.8.2 we present a possible explanation to this phenomenon, supported by calculations. Anyway, additional experiments will be carried to understand the nature and underlying mechanism involved in the generation of these frequencies.
To access the longitudinal acoustic phonon (LA) that may be present in the XTG signal, we have fitted the trace with the frequencies and phases obtained from the diode trace, and subsequently performed a Fourier transform of the residual. The result is displayed in fig. 4.12, where a clear peak at $7.1(\pm 1.2)$ GHz is present together with its second harmonic. This value is in very good agreement with the measurements carried out in the optical regime: *i.e.*, 6.22 ± 0.02 GHz (the optical TG experiment is presented in Chapter 5). This subtraction also permitted to disentangle two peaks overlapping in the same region, one being the acoustic phonon and the other being also present in the diode trace. The latter was estimated to be at 3.2 ± 1.0 GHz. Furthermore, we made the strong supposition that the transmission spectrum would undergo a negligible change for the 770 nm with respect to the 660 nm. Within this supposition we used the same features of the diode, and the estimate LA frequency for the 770 nm grating (see Chapter 5), to calculated the value 3.1 ± 0.7 GHz for this peak in the 770 nm grating case. The presence of the LA peak proves that even if almost hidden behind an unattended signal, we were also able to see weaker features such as the longitudinal acoustic phonon.

4.7 Data Processing

In this section, we present the data reduction procedure applied to the shot-to-shot raw data. This includes the jitter correction (section 4.7.1), the intensity normalization (section 4.7.2) and the stitching of scans acquired over multiple acquisitions. Furthermore, we also describe how the uncertainties have been calculated (4.7.4) as well as the XTG efficiency and $\chi^{(3)}$ estimations (4.7.5).

4.7.1 Timing tool correction

As the reader knows, a Self Amplified Spontaneous Emission (SASE) FELs do not take advantage of external seed lasers. As a consequence, the pump (or probe) laser is an in-

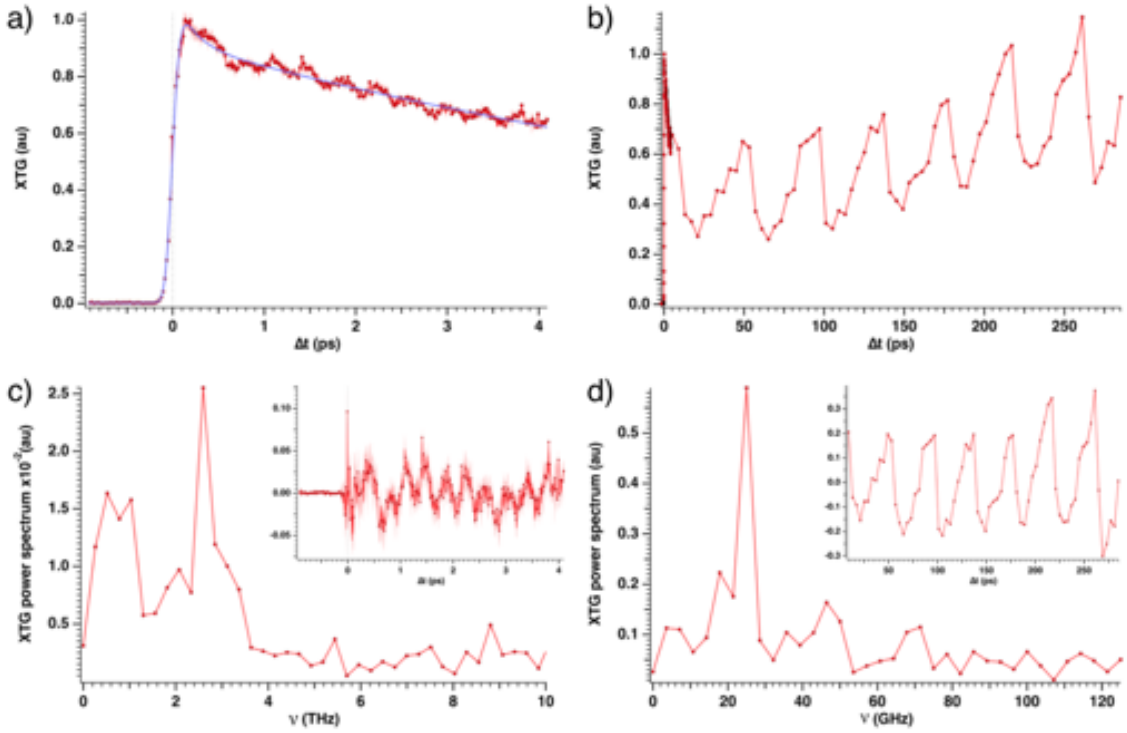

Figure 4.10: *X-ray Transient Gratings results on BGO at 7.134 keV with an excitation grating pitch of 660 nm. a) Time trace at short times (< 5 ps) and residuals from the fit in blue. The fast oscillations are attributed to optical phonons coherence. b) Full time trace and its residuals from the fit. After the fast electronic and phononic relaxation, the slower oscillations are associated to acoustic phonons and heat diffusion. c) Fourier transform of the fast oscillatory component showed in the insert (residuals from the fit in a)). d) Fourier transform of the slow oscillatory component showed in the insert (residuals from the fit (not showed) in b)).*

dependent system synchronized with the FEL timing system. Nevertheless, the relative arrival time between the pump (or probe) laser compared to the FEL beam is affected by short term fluctuations (known as jitter) which can be as high as hundred of femtoseconds, thus affecting the overall time resolution. The jitter is usually measured by means of dedicated diagnostics systems, named timing tools, such as Spatial Encoding, Spectral encoding and Terahertz streaking methods, which provide the relative arrival time on a shot-to-shot basis. During our experiment we have taken advantage of a spatial encoding timing tool which relies on the ultrafast induced transparency of a screen by the interaction with the X-rays. Here we briefly explain how the timing tool was implemented: a portion of the laser was directed on a Ce:YAG screen positioned right after the KB mirrors, with an incidence angle $\sim 45°$, and the transmitted laser beam was then measured with a PCO Edge 5.5 CCD camera. In this way different horizontal pixels of the CCD camera correspond to different relative arrival times between the X-ray and the optical pulses. By measuring the variation in position of the ultrafast change of the transmitted signal it is then possible to retrieve the jitter for each shot and to rearrange the data with a resolution as low as few femtoseconds. The expected resolution was estimated to be $\sim 2.65\ fs/\text{pixel}$.
For each shot, the CCD camera array was vertically binned and resulted in traces similar to the one presented in figure 4.13 a). To find the center of the rising slope, each trace was fitted using a polynomial function (blue curve in fig. 4.13 a)). Then, the re-

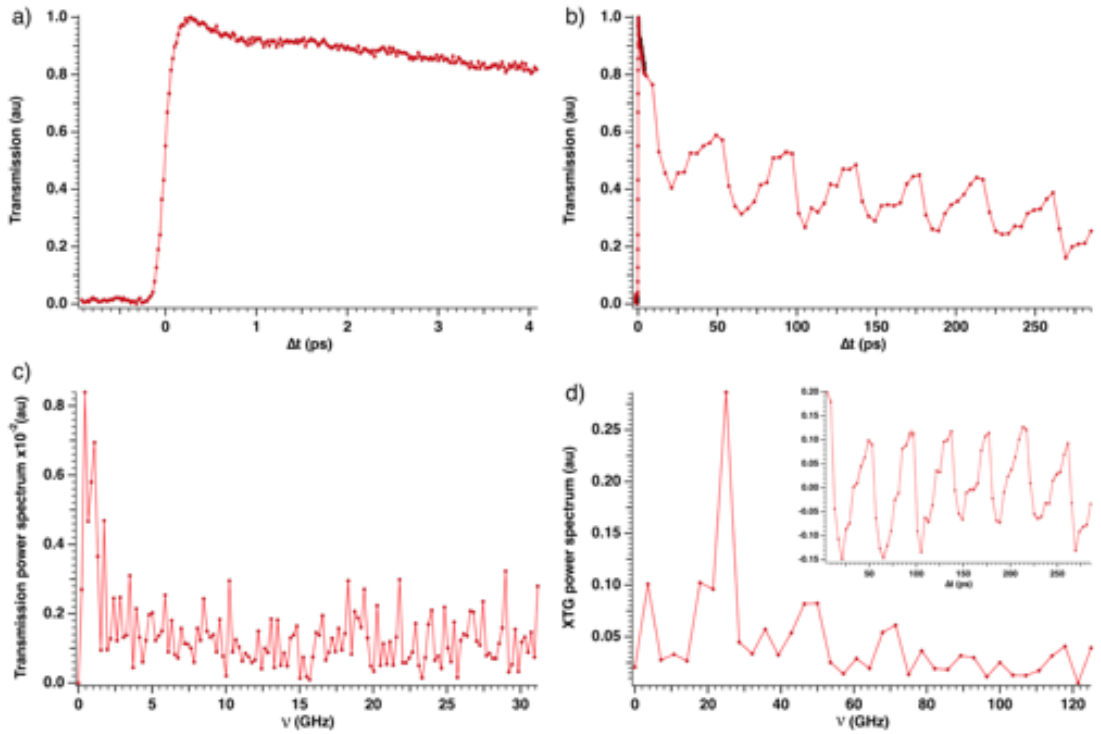

Figure 4.11: *Transient absorption on BGO with a 660 nm excitation grating produced by the diffraction grating having a pitch of 1650 nm). a) Short time component showing a fast transient, but lacking of subsequent oscillations. b) Long time trace showing the same, unattended oscillation of the XTG signal. c) Fourier transform of the residual obtained from the fit. d) Fourier transform of the residual (insert in d)).*

sulting polynomial was derived and its maximum was used as the rising slope center value (see fig. 4.13 b)). For each scan, the Gaussian-like distribution of these pixel values Δp_i was shifted by its mean following the relation $\Delta p_i \longrightarrow \Delta p_i - \frac{1}{n}\sum_n \Delta p_n$. A calibration of the timing tool provided a conversion rate between pixels on the CCD and their time delays Δt_i^{tt} in fs/pixel. These obtained jitter values were then added to the pump-probe delay Δt_{pp} set by the delay stages for each shot, in order to obtain their timing tool corrected delays $\Delta t_i = \Delta t_{pp} + \Delta t_i^{tt}$. Finally, the timing tool corrected data was re-binned, leading to a largely increased time resolution now limited by the pulses lengths rather than the time jitter. In fig. 4.14, we display the XTG signal for a 770 nm excitation grating before and after the timing tool correction.

4.7.2 I_0 correction

The XTG and diode signals were also normalised with respect to the incoming FEL intensity on a shot-to-shot basis. Each FEL shot intensity was measured using the photon beam position monitor (PBPS) of SwissFEL [10] made of a thin 200 nm Si_3N_4 membrane that back-scatters a small portion of the incoming beam onto four diodes. The mean signal on the four diodes was used to deduce the I_0 pulse intensity. The XTG signal scales as equation 4.19. The I_{Las} jitter was negligible during the acquisition. Moreover, the $I_{FEL}^{+1} = I_{FEL}^{-1}$ intensities are proportional to the total FEL intensity $I_{FEL}^{\pm 1} = \vartheta_{gr} I_{FEL}$, ϑ_{gr} being the efficiency of the diffractive zone plate. The I_0 correction on the experimental

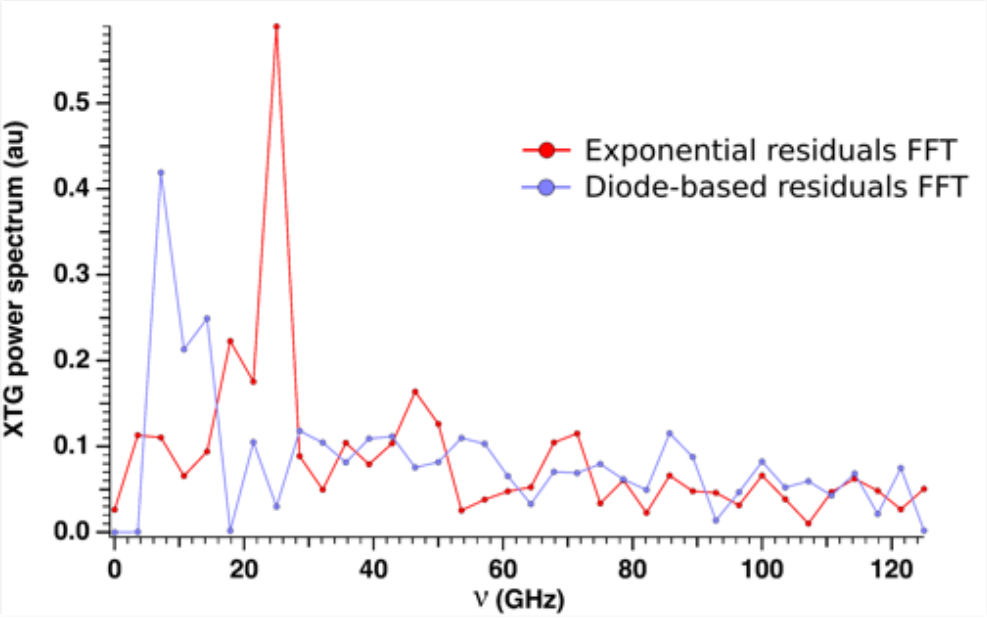

Figure 4.12: Fourier transform of the residuals of the XTG long time trace. In red, the residuals have been obtained by simply subtracting an exponential function (reproduction from fig. 4.10 d)). In blue, the main frequency after the subtraction of the features obtained from the transmission diode signal.

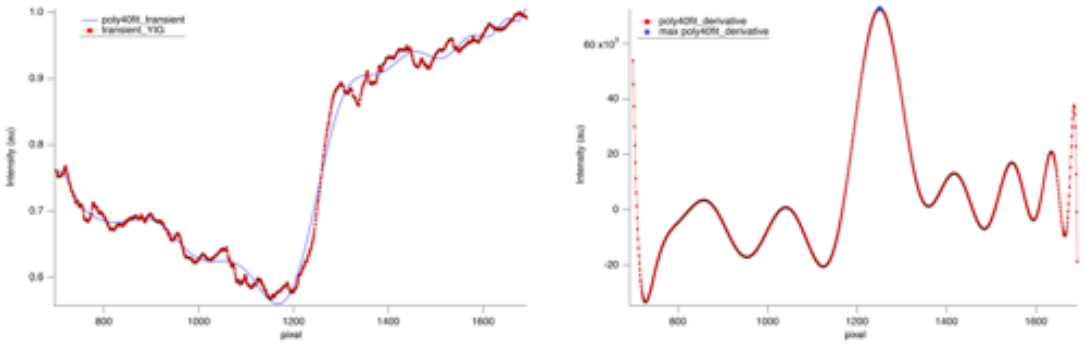

Figure 4.13: *Left: Vertical binning of a single transmitted optical beam on the PCO and its polynomial fit. The slope indicates a change of transmission induced by the coincident X-ray pulse. Right: derivative of the polynomial fit. Its maximum point provides an accurate measurement of the center of the slope while its variation is a good estimate of the time jitter. The pixel / fs conversion is done by an independent calibration of the timing tool.*

XTG signal was thus calculated as:

$$I_{XTG} = \frac{I_{XTG}^{exp}}{I_0^2} \tag{4.21}$$

4.7.3 Stitching

Some traces were acquired over multiple scans due to various FEL instabilities. These traces had to be stitched together to provide a full time trace, taking in account some changes in the FEL parameters, in particular shifts in the mean value of I_{FEL}. We took

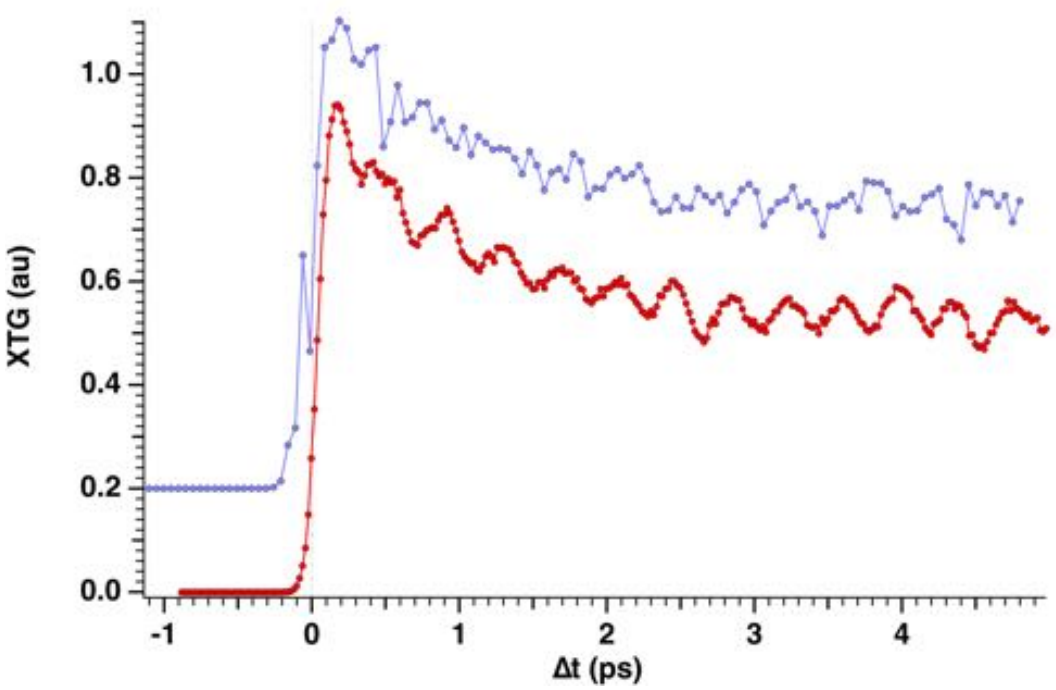

Figure 4.14: *Blue: XTG signal before timing tool correction. Red: After the timing tool correction. The blue curve has been vertically shifted for the display.*

into account this shift by stitching our traces considering the time overlap and adjusting the intensity using the proportionality condition expected by equation 4.19 and (4.21). Considering the mean value of I_0 moving to $I_0 + \Delta I_0$ in two subsequent scans, we expect the shift ΔI_{XTG} of the signal to be

$$\frac{I_{\mathrm{XTG}}}{I_0^2} = \frac{I_{\mathrm{XTG}} + \Delta I_{\mathrm{XTG}}}{(I_0 + \Delta I_0)^2} \quad \Longrightarrow \quad \Delta I_{\mathrm{XTG}} = I_{\mathrm{XTG}} \left[\frac{(I_0 + \Delta I_0)^2}{I_0^2} - 1 \right] \tag{4.22}$$

4.7.4 Uncertainty estimation

The uncertainty estimation was evaluated as a type A uncertainty within each bin after the time tool correction. In each time bin, the standard deviation was evaluated and used as an uncertainty in subsequent analyses. Data curve fittings were weighted by the uncertainty to give more weights to the points with the lowest uncertainties. This procedure provided fitting parameters with a much lower estimated standard deviation on them (see section 4.8.1.)

4.7.5 Efficiency and $\chi^{(3)}$ estimation

Following the procedure given by [6] we estimated the efficiency η_{eff} of the XTG process and the susceptibility value at the electronic peak. The efficiency was calculated as the ratio between the incoming probe intensity I_{laser} and the outgoing XTG signal intensity $\eta_{\mathrm{eff}} = \frac{I_{\mathrm{laser}}}{I_{\mathrm{XTG}}} = 1.32 \times 10^{-4}$. The $\chi^{(3)}$ value was estimated using its classical definition, which can be expressed for our configuration, recalling equation 4.19, as:

$$|E_{XTG}|^2 = |\chi^{(3)}|^2 |E_{FEL}^{+1}|^2 |E_{FEL}^{-1}|^2 |E_{Las}|^2 sinc^2\Big(\frac{|\Delta\vec{k}| L_{int}}{2}\Big), \tag{4.23}$$

where $E_{FEL}^{\pm 1}$ is the electric field of the two FEL diffracted ± 1 orders and E_{Las} is the electric field of the probe laser. To get to the electric field value expressed in V/m starting from an intensity measurement in μJ we first converted the intensity $I[\mu J]$ into a more suitable form following the relation

$$I[\mathrm{W\ m^{-2}}] = \frac{I[\mu J]}{\Delta t \sigma_x \sigma_y} \tag{4.24}$$

Where Δt is the time duration of the event which we set equal to the rise time σ_{XTG} and $\sigma_{x/y}$ is the x/y dimension of the overlap between pump and probe on the sample which were 250 μm and 150 μm FWHM respectively. Finally, the electric field value is obtained using the relation $E = \sqrt{\frac{2I}{Z_0}}$, Z_0 being the vacuum permittivity. This relation between the electric field and the intensity leads to equation 4.19. We estimated the electric field values to be $E_{FEL}^{\pm 1} = 5.86 \cdot 10^8\ V/m$ and $E_{Las} = 5.14 \cdot 10^{11}\ V/m$, thus leading to the susceptibility value

$$|\chi^{(3)}| = \frac{E_{\mathrm{XTG}}}{E_{FEL}^{-1} E_{FEL}^{+1} E_{Las}} = \frac{\sqrt{\eta_{\mathrm{eff}}}}{(E_{FEL}^{\pm 1})^2} = 2.68 \cdot 10^{-20}\ \mathrm{m^2/V^2}. \tag{4.25}$$

The *sinc* term in equation 4.23, reflecting the satisfaction of the phase matching condition, was calculated considering the transversal and longitudinal directions separately. In the transversal direction, the incoming FEL beam produces a grating through a momentum exchange equal to $|\vec{q}| = \frac{2\pi}{d}$, d being the pitch of the grating. The transversal component of the wave vector of the scattered probe is generated by the same transferred momentum $|\vec{q}|$, thus implying the automatic satisfaction of the phase matching condition $\Delta\vec{k}_T = 0$, where we used the subscript T for transverse (and L for longitudinal). The longitudinal component, instead, is not restricted to satisfy any particular relation. Of course, $\Delta\vec{k}_L$ must be calculated inside the sample, which possess a refraction index equal to $\eta_{\mathrm{BGO}}^{400} = 2.2$ at 400 nm, implying the simultaneous presence of refraction. To account the changing of the experimental incidence angle ϑ_{exp} due to refraction, we applied the Snell law, that is:

$$\vartheta_{in} = \mathrm{asin}\left(\frac{\eta_{\mathrm{air}}}{\eta_{\mathrm{BGO}}} \sin\vartheta_{\mathrm{exp}}\right) \tag{4.26}$$

with ϑ_{in} being the new internal angle inside the sample. We can now apply the phase matching condition to calculate the outgoing angle $\cos\vartheta_{\mathrm{in}}$, that is:

$$\vartheta_{\mathrm{out}} = \mathrm{asin}\left(-\frac{1}{|\vec{k}_{\mathrm{BGO}}^{400}|}(|\vec{q}| - \vec{k}_{\mathrm{BGO}}^{400} \sin\vartheta_{\mathrm{in}})\right) \tag{4.27}$$

where $\vec{k}_{\mathrm{BGO}}^{400} = \eta_{\mathrm{BGO}}^{400} \frac{2\pi}{\lambda}$ is the wave vector of the 400 nm probe laser inside the sample. Finally, we can calculate the longitudinal component $\Delta\vec{k}_L$ as:

$$\Delta\vec{k}_L = \vec{k}_{\mathrm{BGO}}^{400}(\cos\vartheta_{\mathrm{in}} - \cos\vartheta_{\mathrm{out}}). \tag{4.28}$$

Thus, considering also the phase matching condition term in eq. 4.23, where we set the interaction length as the absorption length $L_{int} = 6.076\ \mu m$ at 7134 keV for BGO [27] and $|\Delta\vec{k}| = 0.52\ \mu m^{-1}$ from the experimental geometry, we obtain:

$$|\chi^{(3)}| = \frac{2.68 \cdot 10^{-20}}{\mathrm{sinc}\left(\frac{|\Delta\vec{k}| L_{int}}{2}\right)} = 4.23 \cdot 10^{-20}\ \mathrm{m^2/V^2}. \tag{4.29}$$

4.8 Data Analysis

4.8.1 Data fitting

Considerations from the previous section allow us to define the following model to represent the XTG measured data.

$$S_{\mathrm{XTG}} = \left| \frac{1}{2}\left[1+\mathrm{erf}\left(\frac{t-t_0}{\sigma}\right)\right]\left(A_1 e^{-\frac{(t-t_0)}{t_1}} + A_2 e^{-\frac{(t-t_0)}{t_2}} + C_3\cos(2\pi\nu_3(t-t_0))e^{-\frac{(t-t_0)}{t_3}} + \right.\right.$$
$$\left.\left. + C_4\cos(2\pi\nu_4(t-t_0))\right|^2 + f_{\mathrm{piezo}}(\Delta t) \right. \tag{4.30}$$

We account for overdamped oscillation by adding two exponential decays t_1 and t_2. The known optical phonon at 2.6 THz is assigned to the damped oscillation terms with frequency ν_3. The frequency ν_4 account for the long term signal modulation associated with the acoustic phonon. In our model, we also introduce the term $f_{\mathrm{piezo}}(\Delta t)$ accounting for the contribution from the charge motions caused by piezoelectricity. t_0 and σ are experimental parameters accounting for the time zero shift from arbitrary units to the absolute time zero of the time trace and for the instrument response function respectively. The frequency components in $f_{\mathrm{piezo}}(\Delta t)$ can be predicted using a simple electrokinetic model, see section 4.8.2, and are subtracted from the data to extract only the phonon modulations (see section 4.6). The Frequency ν_4 is used as a fixed parameter in the fit and is constrained by the values obtained from optical TG measurement: 5.33 GHz for a 770 nm excitation pitch and 6.22 GHz for 660 nm one. The short time traces are fitted with eq. 4.20 and the resulting fitting parameter are given in tables 4.1 and 4.2. When fitting only the short trace, the contributions $C_4\cos(2\pi\nu_4(t-t_0))$ and $f_{\mathrm{piezo}}(\Delta t)$ becomes a constant and account for the parameter A_3 of eq. 4.20. For convenience, we recall eq. 4.20:

$$S_{\mathrm{XTG}} = \left| \frac{1}{2}\left[1+\mathrm{erf}\left(\frac{t-t_0}{\sigma}\right)\right]\left(A_1 e^{-\frac{(t-t_0)}{t_1}} + A_2 e^{-\frac{(t-t_0)}{t_2}} + A_3\right)\right|^2 \tag{4.31}$$

	A_1	A_2	A_3	t_1 (ps)	t_2 (ps)	t_0 (ps)	σ (ps)
estimate	0.72	0.247	0.742	0.042	1.05	0.05	0.080
standard error	0.09	0.007	0.002	0.004	0.05	0.01	0.006

Table 4.1: *Fit parameters on the short XTG time trace of BGO, using eq. 4.20, with an excitation grating pitch of 770 nm.*

Finally, table 4.3 provides a summary of all frequencies appearing in the signal and their corresponding uncertainty for an excitation grating with a 660 nm pitch.
In fig. 4.15, we display a fit of the whole dataset using eq. 4.30 and by fixing the fast time scales using the results in table 4.1 (for the fast response) and the frequency components obtained from the Fourier transform of the residuals including the longitudinal acoustic phonon as well as the additional frequencies seen also in transmission. In the fit only the components labelled as C_i were kept as free parameters.

	A_1	A_2	A_3	t_1 (ps)	t_2 (ps)	t_0 (ps)	σ (ps)
estimate	0.91	0.37	0.60	0.049	6.05	0.10	0.103
standard error	0.03	0.05	0.05	0.003	1.25	0.01	0.005

Table 4.2: *Fit parameters on the short XTG time trace of BGO, using eq. 4.20, with an excitation grating pitch of 660 nm.*

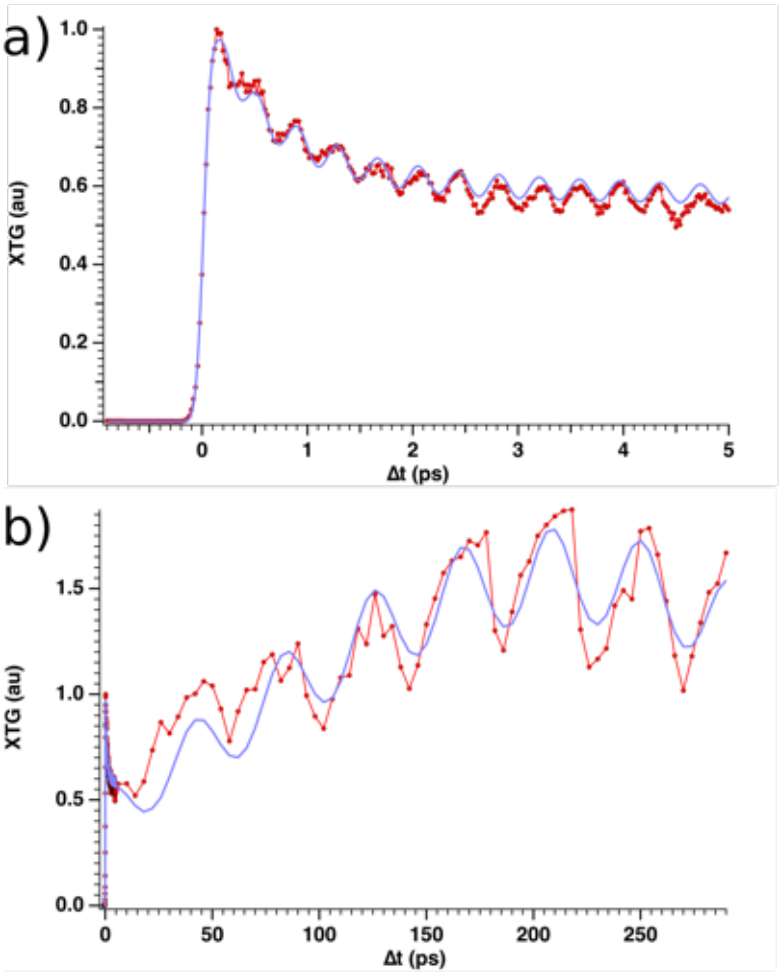

Figure 4.15: *Global fit of the data with eq. 4.30. The short lifetimes have been fixed by a fit on the short time trace, the fast and long modulation are fixed at the maximum of the Fourier transform of the residuals and the low frequency modulation is fixed to the value obtained from optical measurements.*

4.8.2 Transient nanocapacitors generated inside BGO

In this section, we present a simple model that predicts the low and high frequencies present in the XTG traces and in diode trace. When high energy photons impinge on the sample with a spatial periodic modulation, electrons diffuse into the destructive interference regions. Thus, a spatial charge modulation in the bulk of the material is created. In case of a piezoelectric material, for which a linear electromechanical interaction between the mechanical and electrical states of the material occurs, the dimensions of the piezo change and electrical charges distribute inside the material (this is

	ν_3 (THz)	ν_4 (GHz)	ν_5 (GHz)	ν_6 (GHz)	ν_7 (GHz)
estimate	2.605	6.2	23.5	47.4	70.5
standard error	0.004	1.1	0.1	0.4	1.4

Table 4.3: *Frequencies extracted from the XTG data obtained on BGO with a 660 nm pitch excitation grating. ν_3 stands for the optical phonon of BGO, ν_4 represent the longitudinal phonon, ν_5, ν_6 and ν_7 are the frequencies obtained from the piezoelectric model. Uncertainties of frequencies ν_3, ν_5 and ν_6 have been obtained from fitting the data with a sine function while uncertainties on ν_4 and ν_7 have been computed from the standard deviation of the Fourier peak since their residuals are too weak for the fit to be accurate.*

referred as the direct piezoelectric effect). In turn, this generates an induced electric field within the material which forces the lattice to react creating a mechanical strain (called the reverse piezoelectric effect). These effects lead to a series of resonances inside the material which can be described as a circuit with a capacitance in parallel with another capacitance and inductance, as showed in figure 4.16. The former generates the low impedance frequency (named resonant frequency, f_R) while the latter generates the maximum impedance frequency (named anti-resonant frequency, f_A).

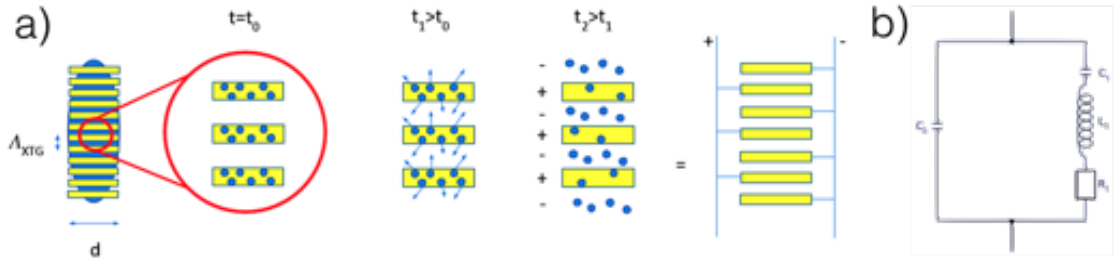

Figure 4.16: *a) the charge displacement evolution inside the piezoelectric material due to the direct and inverse piezo effects. b) the equivalent circuit having a capacitance in parallel with another capacitance and inductance.*

When a spatially periodic transient electromagnetic field is applied on BGO, the illuminated regions have less electrons (positively charged) and the dark regions have more electrons (negatively charged). As a consequence, a multi plate capacitor is transiently generated within the bulk material. This causes a series of coherent transverse oscillations to appear. The resonant frequency can be generally calculated by:

$$f_R = \frac{\nu}{2L} \tag{4.32}$$

knowing the sound velocity ν and the separation between the plates $L = \Lambda_{XTG}/2$. From the optical measurements, the speed of sound in the transverse direction perpendicular to the XTG excitation is 2507 m/s (see 4.20). This gives a resonant frequency of 3.25 GHz and 3.79 GHz for 770 nm and 660 nm XTG pitch respectively, in good agreement with the values found in the data analysis. The estimated speed of sound can be corroborated by calculating the compliance tensor element c_{44} by means of the formula $c_{44} = \rho\nu^2 = 0.447 \times 10^{11}\mathrm{N/m^2}$ [28] with $\rho = 7.12\mathrm{g/cm^3}$ being the BGO density. This result is in agreement with the value $c_{44} = 0.436 \times 10^{11}\mathrm{N/m^2}$ reported in literature [14]. From the equivalent circuit perspective, the equivalent capacitance can be calculated as

Frequencies	measured (GHz)	model (GHz)
1	3.1 ± 0.7	3.25
2	23.5 ± 0.1	23.9
3	47.4 ± 0.4	47.7
4	70.9 ± 1.7	71.6

Table 4.4: *Comparison between the frequency measured with the XTG and the piezoelectric model describe by equation 4.36*, for a gratin of 770 nm.

the sum of the capacitance of a single plate:

$$C_{eq} = \sum_i C_i = (N-1)C \tag{4.33}$$

with N the total number of capacitors (the number of fringes) and C the single capacitance from a half ellipse plate:

$$C = \epsilon_0 \epsilon_r 2\pi \frac{\sigma_V d}{2L} \tag{4.34}$$

with σ_V the vertical FEL beam size, d the X-ray penetration depth, ϵ_0 and ϵ_r the vacuum and relative permittivity. Using the experimental values ($\epsilon_r = 15.2$, $\sigma_V = 64$ μm, $d = 6$ μm, and $L = \Lambda_{XTG}/2$), the equivalent capacitances are equal to 19.8 pF and 16.9 pF for the 660 nm and 770 nm XTG pitch, respectively. The equivalent inductance can be calculated through the relation

$$L_{eq} = \frac{1}{C(2\pi f_R)^2} \tag{4.35}$$

which gives 120 pH and 140 pH for the 660 nm and 770 nm XTG pitch, respectively. The antiresonance frequency can be calculated by solving the following relation [28]:

$$\left(\frac{2\pi f_A L}{2v}\right)\cot\left(\frac{2\pi f_A L}{2v}\right) = -\frac{k_{31}^2}{1-k_{31}^2}, \tag{4.36}$$

with

$$k_{31} = d_{31}\sqrt{\frac{c_{44}}{\epsilon_r}} \tag{4.37}$$

where d_{31} the piezoelectric constant [29]. The resulting frequencies are 20.5 GHz and 41.0 GHz (second harmonic) for 660 nm XTG pitch, and 23.9 GHz, 47.7 GHz (second harmonic) and 71.6 GHz for 770 nm XTG pitch. These results are remarkably in good agreement with the measured values.

This result indicates that by exciting with a spatial periodic modulation (transient grating) a piezoelectric material with high photon energy photons (X-rays), a set of coherent oscillations can be generated from few GHz up to tens of GHz. The resonant and anti-resonant frequencies can be tuned on demand by acting on the XTG pitch. For instance, by decreasing the XTG pitch down to 15 nm, the expected resonant and anti-resonant frequencies are expected to be 170 GHz and 1 THz respectively.

4.9 Conclusions

We have reported the first experimental realization of Transient Grating Spectroscopy driven by an X-FEL. By exploiting the Talbot effect for convergent FEL Gaussian beams we have investigated BGO and TTO samples with 7.1 keV FEL pulses and probed the bulk dynamics observing relaxation features at short and long-time scales. We believe that this relatively simple approach can be easily implemented in every X-FEL facility enabling to perform this kind of experiments both on solids and liquids and thus opens a new field in nonlinear optics. In the current implementation, the optical probe is the main limitation to the temporal and spatial resolution. Nevertheless, even in this setting, the nanometric and femtosecond scales probed are relevant for a broad range of materials such as magnetic systems, heterostructures and light harvesting complexes, to name a few. Furthermore, in the case our model will be proven right, the possibility to generate transient nanocapacitors within the sample opens new unprecedented possibilities in the study of nanodevices, especially for very small XTG pitches. The use of XTG offers various advantages compared to other ultrafast spectroscopic techniques by combining the strengths of X-rays with TG spettroscopy. First, the very small wavelength of X-rays brings the possibility to generate extremely small excitation gratings in the future (high momentum transfers), with sizes as small as few nanometers or even below. To that end, a Full X-ray XTG, *i.e.*, with a delayed X-ray probe, will bring the capability to probe excitation gratings down to that scale (see the next section). This will permit to access regime of transport so far inaccessible, with the promise to shining light to the open problem of how to handle the heat transfer in nano-systems and nano-devices. Second, X-rays can be made element- and site-sensitive by tuning them at some chosen core resonance. Using this effect, it will be possible to generate excited carrier from chosen element and study their subsequent transport. Moreover, combined with the shortness of new X-ray sources (few-fs or below), measurements of the coherent relaxation of core-hole states will become accessible and will add valuable information core excited state dynamics. Finally, the Talbot geometry used for the XTG facilitates the measurement of various grating pitches. Extensive measurements of the momentum transfer dependence are reachable at unprecedented scales. This would enable to quickly change the transfer momentum (switching gratings) enabling scans of the momentum transfer in a fast and reliable fashion.

4.10 A look into the future of XTG

In the following section, I am briefly going to present the near-future extension of the XTG technique. Given the very promising results showed above, we intend to conduct the first Full X-ray Transient Grating (FXTG) experiment in which both the pump and the probe are in the X-ray regime. The goal of the experiment is two-fold: (i) To demonstrate the feasibility of full X-ray four-wave mixing. We are planning to use an innovative way of generating TGs with the converging Talbot effect. The proposed approach allows us to easily control the momentum transfer by varying the XTG pitch down to nanometer scale. (ii) To investigate ultrafast dynamics and transport of charge and heat carriers in crystalline Silicon. The experiment will access a transport length scale that has been inaccessible so far. In our scheme, adapted to the Japanese XFEL at SACLA, we plan to use two XFEL pulses with two different photon energies (two-color scheme), one to pump the sample and one to probe. The two pulses need to be delayed

so we plan to use the XFEL chicane delay line for time separations up to 300 fs which will be needed for the first part of the experiment. Then we will increase the time delay between the FEL pulses to several ps, for which we will use the Split-and-Delay Optics (SDO) already present at SACLA.

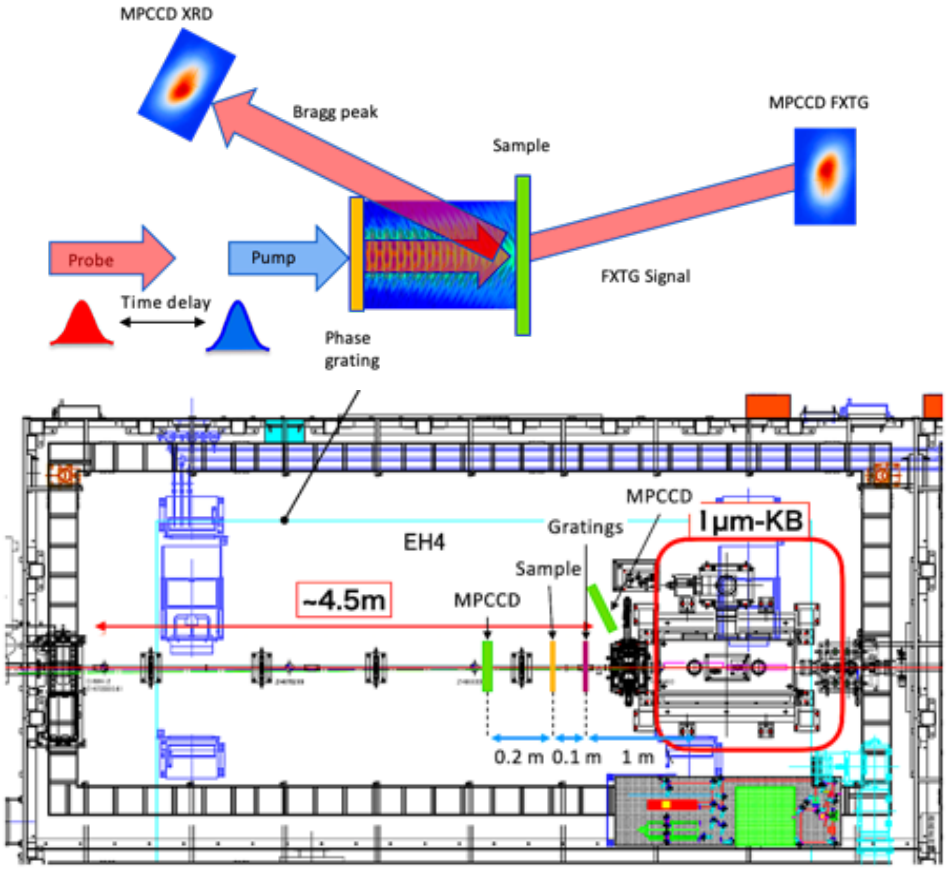

Figure 4.17: *A sketch of the experimental setup and a top view of the EH4c is presented in figure 4.17 a) and b), respectively.*

The FEL pulses will be 5 keV (pump) and 9.8 keV (probe) with an average intensity of about 100 μJ each. The beams will be defocused at the sample by means of the KB mirrors already present at EH4c. The expected beam size at the sample will be about 150×150 μm^2 (H×V, FWHM). The size might be adjusted to increase the fluence at the sample if needed, by moving the setup closer to the focus. About 1000 mm downstream the KB system, a set of transmission gratings (specifically designed by PSI for this experiment) will be installed. They will be mounted on a dedicated holder allowing the XFEL beams to be transmitted to the sample. The gratings will have three translations and one rotation (tilt) to allow for proper alignment. In between the KB and transmission gratings, it would be convenient to use a tube filled with Helium for reducing the attenuation due to absorption from air. About 150 mm downstream the gratings the sample will be mounted on a dedicated holder allowing for measurements in transmission. It will be able to translate in all directions and to rotate for better alignment in tip and tilt. The sample will be moved in the longitudinal direction to accommodate for different transfer momentum (different excitation gratings). The XTG signal scat-

tered off the sample will be detected by a MPCCD detector in transmission. It will be mounted on a translation stage allowing to move the detector along the beam direction to optimize the signal. Between the sample and MPCCD a tube filled with Helium for reducing the attenuation due to absorption from air would be useful. Permanent grating imprints will be initially used at the sample position to generate a static signal in the same direction as the XTG for alignment purpose of the detector and the probe. After the alignment of the gratings and sample the XTG signal will be detected at the 2D detector as a function of different short-time delays (provided by the machine) followed long-time scans (provided by SDO). This process will be repeated for different XTG transfer moment (pitches), from several microns to tens of nanometers. This will be done at room temperature on Silicon. A second MPCCD will be mounted in back scattering geometry detecting the structural $(3\bar{3}5)$ Bragg peak and the sidebands generated by the XTG excitation A sketch of the experimental setup and a top view of the EH4c is presented in figure 4.17 a) and b). At the current state of the art in nanofabrication, gratings with a pitch as small as 50 nm can be fabricated.

A version of this experiment, including a new heterodyne detection method, has also been prepared and submitted to LCLS II.

4.11 Ancillary measurements

Here we report results from a heterodyne-detected transient grating experiment on BGO at room temperature. Aiming at the acoustic phonon frequency, this measurement wanted to be a satellite experiment of the XTG. Acoustic relaxations have been identified in a time-frequency window not covered by previous spectroscopic studies and their characteristic dynamic parameters have been measured as a function of transferred momenta magnitude and direction. A Laue diffraction measurement have been performed in order to identity the crystallography plane in which the transferred momentum lies. A detailed comparison with theoretical simulations based on the Laue diffraction results, performed by the supercell approach, has been worked out.

4.11.1 BGO relaxation dynamics through Heterodyne Transient Grating[2]

The reported experiment relies on the optical TG studied through the heterodyne detection approach. Although presenting important differences with respect to the novel XTG method, this variation of the technique is extremely well known thus we are not going to cover a complete description of it. The extremely curious reader will find the complete description of this variation of TG experiments here [30–32]. Nevertheless, it is worth spending a couple of words on the heterodyne detection scheme. The excitation, as one can see in figure 4.18, is produced by two high-power laser pulses, described by $\vec{E}^{\,\mathrm{ex}}_{1,2} = E(t)\hat{e}^{1,2}\cos(\vec{k}\cdot\vec{r} - \omega_l t)$ [33], obtained by splitting a single pulsed laser beam, make them interfere with each other, thereby producing an impulsive, spatially periodic variation of the dielectric constant, $\delta\epsilon_{ij}(t)$, inside the sample. This spatial variation is characterised by a wave vector $\vec{q}$, where $\vec{q} = \vec{k}_1 - \vec{k}_2 = \hat{q}\frac{2\omega_l}{c}\sin\vartheta$. A second CW laser beam, described by $\vec{E}^{pr} = E(t)\hat{e}^{pr}\cos(\vec{k}_p\cdot\vec{r} - \omega_{pr}t)$, typically of different

[2] Danny Fainozzi, *et al*. BGO relaxation dynamics through Heterodyne Transient Grating. *To be submitted*, 2021.

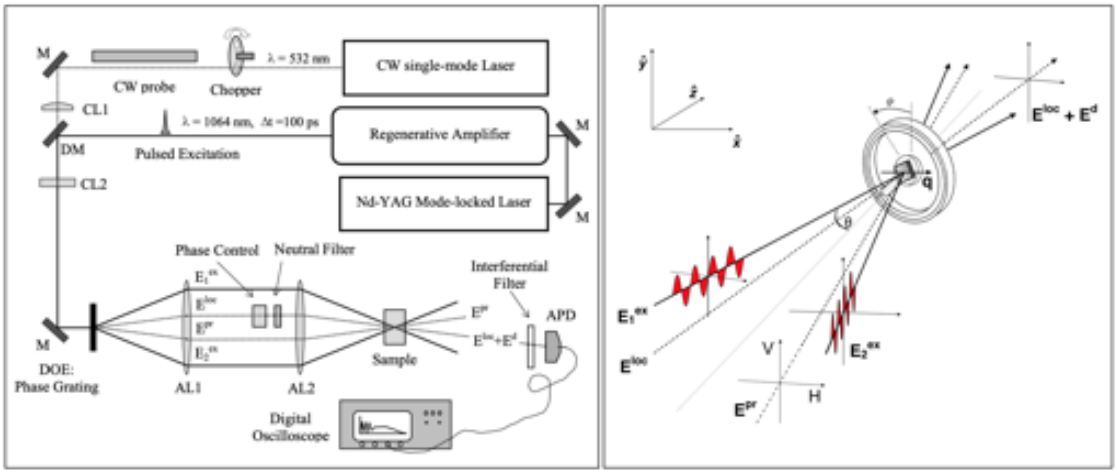

Figure 4.18: *Left - here we show the experimental setup, including the laser system. The label M stands for the mirrors, CL1,2 label the cylindrical lenses, and DM labels a dichroic mirror. DOE is the diffractive optic element, AL1,2 are the achromatic lenses, and APD is an avalanche photodiode. Right - here we report the sketch of the polarization configuration and beam directions.* E_1^{ex} *and* E_2^{ex} *are the excitation laser pulses and* E^{pr} *and* E^d *are the probing and diffracted beams, respectively. The optical heterodyne detection is obtained with the local field,* E^{loc}*. For each beam the possible polarization directions are reported. In particular in the present work we used equal direction of polarizations for the two excitation fields (VV) and for the probe and diffracted beam (again VV). The measured polarization of the diffracted beam is selected by the polarization of the local field. The sample was mounted on an hollow goniometer, able to rotate on the whole circle angle,* i.e., 2π*, with a* $0.5°$ *precision.*

wavelength, is acting as a probe. It impinges on the induced grating at the Bragg angle producing a diffracted beam, spatially separated from the pump and the probe beams. This diffracted beam is the signal measured in a TG experiment, yielding the dynamic information from the relaxing grating. Thus, considering the entities in fig. 4.18, we can write down the signal as

$$\begin{aligned} S(q,t) \propto \langle |E^d(q,t) + E^{loc}|^2 \rangle = \\ = \langle |E^d(q,t)|^2 \rangle + \langle |E^{loc}|^2 \rangle + \\ + 2\langle |E^d(q,t)| \rangle \langle |E^{loc}| \rangle \cos(\Delta\phi) \end{aligned} \tag{4.38}$$

where $\Delta\phi$ is the phase difference between the diffracted E^d and the local E^{loc} fileds, and $\langle \cdot \rangle$ represent the time averaging over the optical period. The three terms in the right-hand side of eq. 4.38, are the homodyne, the local field, and the heterodyne contributions from left to right respectively. We experimentally isolated this last term subtracting two signals characterized by different phases. Recording a first signal, S_+, with $\Delta\phi_+ = 2n\pi$ ($n \in \mathbb{N}$) and then a second one, S_+, with $\Delta\phi_+ = (2n+1)\pi$, we have:

$$S^{\mathrm{HD}}(q,t) = [S_+ + S_-] \propto \langle |E^d(q,t)| \rangle \langle |E^{loc}| \rangle \tag{4.39}$$

There are two major advantages in using the heterodyne instead of the homodyne detection. First, it improves substantially the signal-to-noise ratio in the all-time window, both because of the signal increment and because of the discharge of all the spurious signals that are not phase sensitive. Second, it enhances enormously the sensitivity since the recorded signal is directly proportional to $\langle |E^d(q,t)| \rangle$ instead of being proportional to its square.

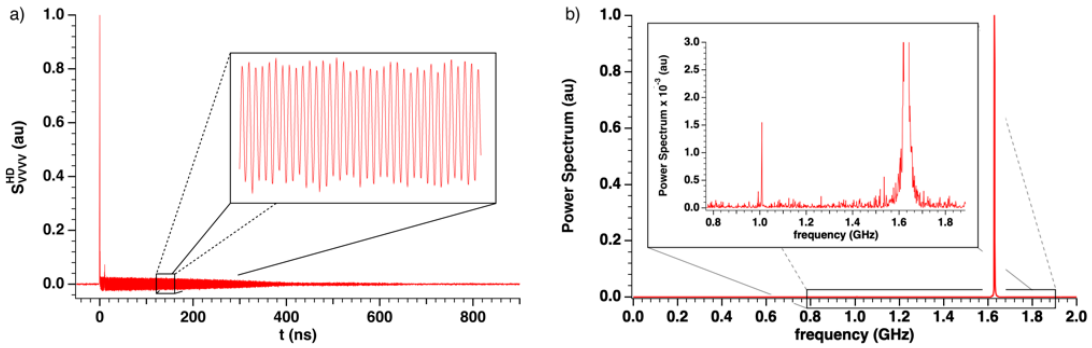

Figure 4.19: *a) - The long trace S^{HD}_{VVVV} acquired up to 900 ns. In the insert, a zoom in underling the oscillation given by acoustic phonons. b) - The FFT of the S^{HD}_{VVVV} signal, showing two main frequencies labelled as the Longitudinal acoustic phonon (LA) and one of the Transversal acoustic phonon (TA).*

The experimental setup

Accordingly to Laue Diffraction measurements, the BGO sample was cut along the (310) crystallographic plane, and shows an azimuth (in plane) angle of $\sim 45°$ with respect to the $[100]$ crystallographic direction when the angle on the goniometer read $\vartheta = 0$. The sample dimensions were 10 mm x 10 mm x 1 mm ($L \times W \times T$). The optical setup, shown in figure 4.18, uses a phase grating as a diffractive optical element (DOE). By controlling the depth of the grooves and their spacing, it is possible to obtain very high-diffraction efficiency *i.e.*, $\geq 80\%$ for the first two diffraction orders. Since the experimental setup must diffract the pump and the probe lasers (1064 nm and 532 nm, respectively) with only one grating, a compromise must be used. The chosen DOE gives a 12% diffraction efficiency on first order for the 532 nm laser and a 38% diffraction efficiency for the first order of the 1064 nm laser. Gratings possessing different spacing may be used to change the $\vec{q}$ vector. With the aid of a dichroic mirror (DM), the excitation and the probe beams are sent collinearly on the DOE that subsequently produces the two excitation pulses ($E^{ex}_{1,2}$), the probe (E^{pr}), and the reference beam (E^{loc}). These beams are collected by a first achromatic lens (AL1), cleaned by a spatial mask used to block other diffracted orders, and then recombined and focused on the sample through a second lens (AL2). The local laser field is also attenuated by a neutral density filter and its phase is adjusted by passing through a couple of quartz slabs properly etched. The excitation grating produced on the sample is the mirror image of the enlightened DOE phase pattern. If AL1 and AL2 have the same focal length, the excitation grating has half the spacing of DOE [34]. This type of setup automatically gives the Bragg condition on all the beams and it produces a very stable phase locking between the probe and the reference beam, a crucial parameter to realize the heterodyne detection. To properly test the acoustic damping, the excitation beam is focalized by a cylindrical lens (CL2) on the DOE and the so produced grating on the sample is extended in the $\vec{q}$ direction for ~ 5 mm; vice versa, the probe beam is focalized in a circular spot of 0.5 mm on the sample, through the two lens CL1 and CL2. For this measurement, we reduced the laser energy on the sample to the possible lowest level to avoid undesirable thermal effects, and the CW beams have been gated in a window of ~ 1 ms every 10 ms by using a mechanical chopper synchronized with the excitation pulses. The mean exciting energy was 7 mW (35 J per pulse at 100 Hz), while the probing energy was set to 6 mW. The reference beam intensity is very low and it is experimentally adjusted, using a variable neutral filter, to be about 100 times the intensity of the diffracted signal. With these intensities,

the experiment is deeply inside the linear-response regime and no dependence of HD-TG signal shape on the intensities of the beams can be detected. The HD-TG signal, after optical filtering, is measured and recorded by the New Focus DC-Coupled Photoreceiver (12 GHz bandwidth) interfaced to a Tektronix oscilloscope with a limiting bandwidth of 7 GHz and a sampling rate of 20 Gs/s. The BGO crystal is mounted on an hollow goniometer with a 0.5° precision, which allows to rotate the sample freely in the $\hat{x} - \hat{y}$ plane. The signal measured from the BGO sample was recorded in the 0-1 μs range with a 50 ps time step. Each data is an average of 5000 recording, enough to produce an excellent signal-to-noise ratio. In order to get rid of the homodyne contribution to the signal together with other spurious contributions, and at the same time increase substantially the quality of the data [35], we performed every measurement at two different phases ϕ of the local field, having a $\Delta\phi = \pi$ in between, following eq. 4.39. We measured the relaxation process of BGO as a function of the rotation angle ϑ for six different $|\vec{q}|$ values: $|\vec{q}| = 0.6283, 1.0134, 1.3674, 1.7915, 2.0854,$ and $2.4961\ \mu m^{-1}$. The wave vectors are evaluated by the geometry of the experiment and are affected by an error being ∼0.8% for the first two values, ∼0.6% for the two terms in the middle, and ∼0.4% for the last two values. For each wave vector, we take data as a function of the angle ϑ every 45° in a full circle range. For $|\vec{q}| = 2.4961 \mu m^{-1}$ we also performed the measurement with a 15° step for the first half circe. In figure 4.19 (a), we show in linear-scale some representative HD-TG data on BGO. This figure shows how the density dynamics of BGO is characterized by, at least, two main dynamical processes: a fast response to the sudden heating the sample and the following local temperature relaxation due to the thermal diffusivity, and an acoustic phonon due to the sudden density variation. In figure 4.19 (b), we show the corresponding normalized FFT of the representative HD-TG BGO data in figure 4.19 (a). This figure shows a peak around 1.63 GHz representing the longitudinal acoustic (LA) phonon. In the insert of the figure, we show a zoom in where, around 1 GHz, we spot a fainter trace of one transversal acoustic (TA) phonon. The presence of the TA is due to the sample being cut in the (310) crystallographic plane for which the transferred momentum $\vec{q}$ does not lie perfectly in the $\hat{x} - \hat{y}$ plane but, instead, presents a small component in $\hat{z}$. The frequency values of LA and TA phonons are extrapolated by fitting the FFT with Gaussian functions to precisely find the peak position. The error associated to each frequency is chosen to be the standard deviation of the Gaussian curve.

In figure 4.20 a) we present the linear dispersion of the LA phonon measured at 45°. The angle scale was set during the experiment to be 0 when the sample was arranged with a specific side parallel to the ground. This condition should have matched one of the crystallographic direction of the BGO crystal, which was expect to produce a maximum or a minimum on the frequency rotational dispersion. In figure 4.20 b) we show the rotational dispersion of the LA phonon measured at $|\vec{q}| = 2.4961$ and the corresponding sound speed propagation in the material. In figure 4.20 c) and d) we present the corresponding linear and rotational dispersions for the TA phonon. The rotational dispersion of the LA phonon shows a periodicity of π which lead us to fit it with a double sine function. On the contrary, the rotational dispersion of the TA shows a periodicity of $\pi/2$ which lead us to fit it with a single sine function. The linear fit produced for each rotational angle and the sinusoidal fits produced for each transferred momenta are used to produce the 3D dispersion in figure 4.20 e) and f), where the sinusoidal amplitudes of the fits, which are visible as black lines in the figures, are magnified around the mean value for a give momentum by a factor 25 and 15 for the LA and TA phonon respectively. Given the parameters of the fit, we can model the 3D dispersions as fol-

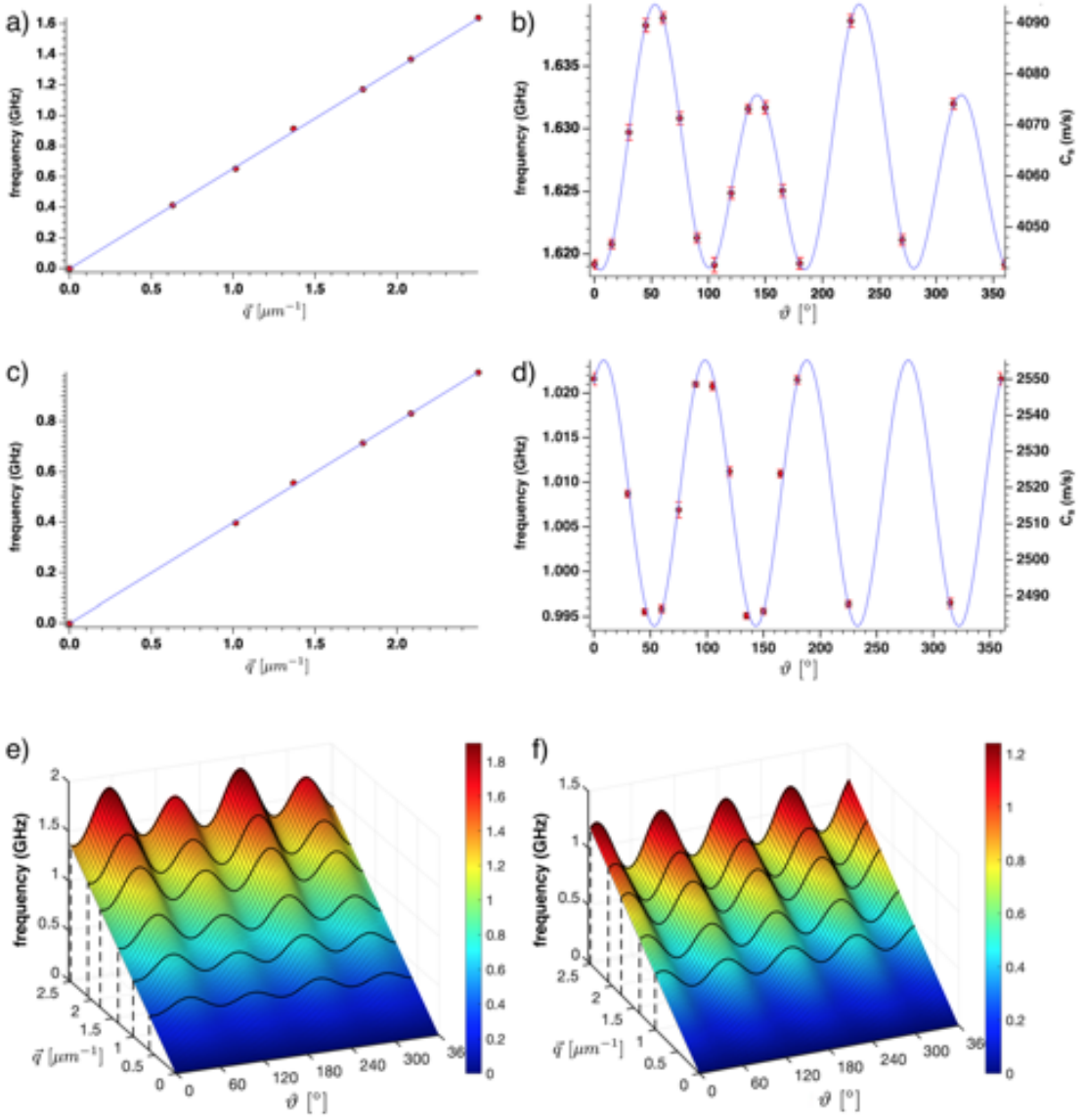

Figure 4.20: *a) and b) - from left to right we present the linear and angular dispersion of the Longitudinal Acoustic phonon for a transferred momentum $|\vec{q}|$ equal to $|\vec{q}| = 2.4961\ \mu m^{-1}$. c) and d) - from left to right we present the linear and angular dispersion of one of the Transversal Acoustic phonon for a transferred momentum $|\vec{q}|$ equal to $|\vec{q}| = 2.4961\ \mu m^{-1}$. e) and f) - the 3D reconstruction of the linear and angular dispersion of the LA and TA, from left to right respectively. For clarity, the oscillations have been enhanced by a factor of 25 (LA) and 15 (TA) around the mean value for a give momentum. In black, we show every fit performed on the angular dispersion at different momenta.*

lows

$$LA(|\vec{q}|,\vartheta) = A|\vec{q}| + B|\vec{q}|\sin(f_1\vartheta + \varphi_1) + C|\vec{q}|\sin(f_2\vartheta + \varphi_2) \tag{4.40}$$

for the LA phonon, and as

$$TA(|\vec{q}|,\vartheta) = A|\vec{q}| + B|\vec{q}|\sin(f_1\vartheta + \varphi_1) \tag{4.41}$$

for the TA phonon. The values of the parameters are shown in table 4.11.1.

	$LA(\lvert\vec{q}\rvert,\vartheta)$	$TA(\lvert\vec{q}\rvert,\vartheta)$
A	0.6521 ± 0.0002	0.4041 ± 0.0001
B	-0.0035 ± 0.0004	0.0060 ± 0.0002
C	0.0015 ± 0.0004	/
f_1	0.0701 ± 0.0006	0.0700 ± 0.0002
f_2	0.0351 ± 0.0008	/
φ_1	0.99 ± 0.08	0.96 ± 0.02
φ_2	-0.31 ± 0.14	/

Tab. 2 *The values of the parameters obtained from the functions 4.40 and 4.41, used to fir the 3D dispersion of the LA phonon and TA phonon, respectively.*

4.11.2 LAUE diffraction

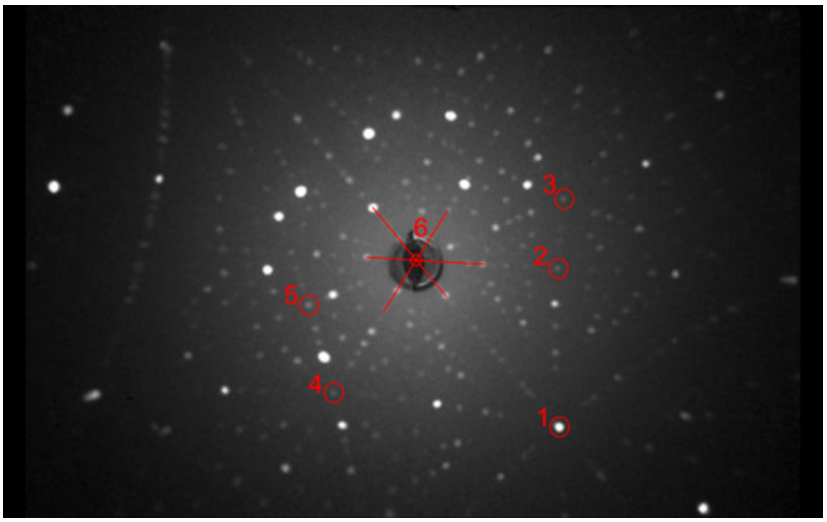

Figure 4.21: *Laue diffraction from the BGO crystal. In the red circle, the peaks used in the simulation for the retrieval of the crystallographic direction.*

	h	m	l
1	$\bar{1}$	0	0
2	$\bar{6}$	$\bar{1}$	1
3	$\bar{4}$	$\bar{1}$	1
4	$\bar{4}$	$\bar{1}$	$\bar{1}$
5	$\bar{5}$	$\bar{2}$	$\bar{1}$
6	$\bar{3}$	$\bar{1}$	0

Table 4.5: *Miller indices of the peaks used during the data simulation. Accordingly to the peak labelled as 6, in the middle of the detector, the BGO crystal was cut along the* (310) *crystallographic plane.*

As stated before, given the cubic structure of BGO, and the geometry of our sample, we expected it to be cut along one of its three main crystallographic direction. This condition was in turn expect to produce a maximum or a minimum on the frequency rotational dispersion at the dispaersion angle $\phi = 0$ on our reference frame. Since this condition was not matched, we performed a LAUE diffraction experiment aiming at obtaining the cutting direction of the crystal. Laue X-ray microdiffraction experiments were conducted at the microXAS beamline of the Swiss Light Source at the Paul Scherrer Institute in Villigen, Switzerland. A pink light beam with energies in the range of

10-23 keV focused to a spot size of 0.7×0.9 mm^2 was used, and diffraction data were collected with a MarCCD detector. The reconstruction of the cutting plane was obtained using the OrientExpress software.

The BGO crystal, having dimensions of 10 mm $\times$ 10 mm $\times$ 1 mm ($L \times W \times T$), was positioned vertically along one of the 10 mm sides. After reconstruction, from the position of the (100) peak, we can see that the crystal seems to be cut with an azimuth (in plane) angle of $\sim 45^\circ$ with respect to the $[100]$ crystallographic direction. Accordingly to the $(\bar{3}\bar{1}0)$ peak position, the BGO crystal had been cut along the (310) crystallographic plane. This is the reason behind the presence of both LA phonon and TA phonon in the S^{HD}_{VVVV} spectrum.

4.11.3 Phonon calculation model

The response function contains in general a large amount of information about the system dynamics, and an *ab initio* calculation have been carried out. Phonon calculations were performed by the supercell approach. The initial BGO crystal structure used to perform phonon calculation is obtained from the Materials Project [36, 37] while displacements and force constrains were calculated using VASP [38]. Phonon frequencies were calculated from the force constants using the PHONOPY code [39]. For the quasi harmonic approximation (QHA) calculations, supercells containing $1 \times 1 \times 1$ unit cells were used, since it fulfilled the requirement of having at lead a 1 nm lattice parameter for the VASP calculations.
Starting from the cutting direction in the reciprocal space $(\bar{3}\bar{1}0)$, we applied a vector base change from the Body Centered Cubic (BCC) base (in which the Miller indexes are presented) to the FCC base (corresponding to the Bravais lattice of the BGO crystal), thus obtaining a cutting direction in the real space equal to $(\bar{4}\bar{3}\bar{1})$. The calculations were performed for transferred momentum vectors $\vec{q}$ lying in a plane perpendicular to the $(\bar{4}\bar{3}\bar{1})$ direction having a plane equation equal to $-4\alpha - 3\beta - \gamma = 0$ with α, β and γ free parameters. The $\vec{q}$ vectors spanned the plane by being rotated by an angle $\Delta\vartheta = \frac{\pi}{4}$ for each step. The resulting set of vectors were subsequently written on the reciprocal space base *i.e.,* the BCC vector base, and normalized to a given value *i.e.,* one of the $\vec{q}$ used in the optical TG experiment. Finally, starting from the Γ point, they were used to set the direction of the band structure calculation in the PHONOPY code. In figure 4.22 we show the results of the simulation. From 4.22 left) we can clearly see that for small transferred momenta, the expected linear behaviour shows a quadratic component that becomes more and more negligible going towards higher momenta *i.e.,* reporting frequency values (5.65 GHz) close to the expected experimental ones (6.83 GHz) for a transferred momenta $|\vec{q}| = 10.47$ μm^{-1} given by a 660 nm grating. In 4.22 right) we show the angular dispersion compared to the experimental one. Here we can clearly see similar features. The frequencies and phases used to obtain the fit of the simulation were the same used to obtain the fit of the experimental data. Furthermore, the amplitude of the oscillation are of the same order of magnitude as the experimental ones. Finally, we report this results with a word of caution for everyone giving for granted quantities coming from even accurate simulations as this one. For complex systems with many atoms, even the smaller approximation can lead to a divergent result from the real one. With this lesson in mind, I invite whoever is going to read this dissertation to exploit the potential and beauty of experiments instead of relying only on simulations.

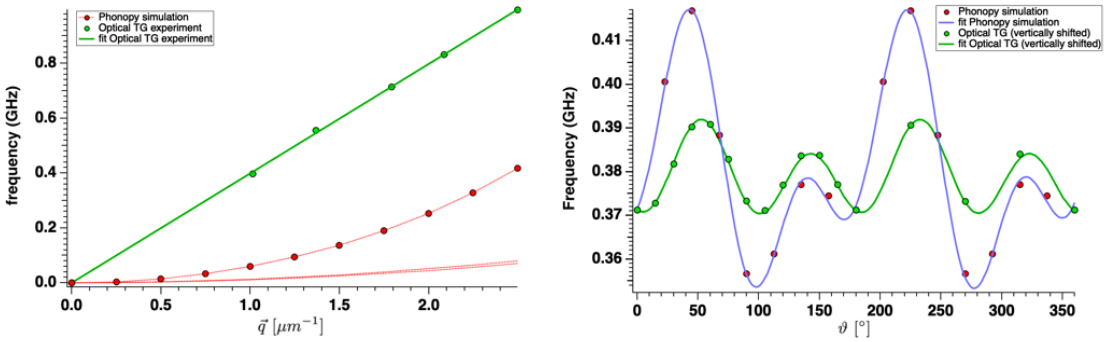

Figure 4.22: *Left - in red the acoustic phonon dispersion from the simulation plotted against the changing transferred momentum. The dispersions result to be slightly quadratic instead to be a straight line as it can be seen from the confrontation with the experimental result (in green). Furthermore, the frequency values result to be lower than the experimental ones. Right - in red the acoustic phonon angular dispersion from the simulation plotted against the angle at a transferred momentum* $|\vec{q}| = 2.4961\ \mu m^{-1}$. *In blue the fit obtained using the same frequencies and phases as the experimental one. In green, the experimental trace shifted in order to match the simulation at* $\vartheta = 0$.

4.12 Conclusions

We reported the propagation of the high frequency acoustic waves in Bismuth Germanate in its $\mathbf{Bi_4Ge_3O_{12}}$ configuration. The heterodyne-detected transient grating experiment revealed to be particulary appropriate to these investigation producing data of excellent quality, also compatible with the acoustic frequencies values obtained in the X-Ray TG experiment [40]. We further showed a Laue diffraction measurement exploiting the BGO crystal to be cut in its (310) crystallographic plane, which explained the acquisition of a signal from both LA and TA phonons in the TG experiment. Finally we compared these optical TG results with a a simulation of the phonon dispersion obtained by the supercell approach using the VASP and PHONOPY codes, which resulted to be in good agreement concerning the angular dispersion, but in poor agreement regarding the momentum dispersion for our low transferred momenta.

References

[1] Emily J Brown, Qingguo Zhang, and Marcos Dantus. Femtosecond transient-grating techniques: Population and coherence dynamics involving ground and excited states. *The Journal of chemical physics*, 110(12):5772–5788, 1999.

[2] J Janušonis, T Jansma, CL Chang, Q Liu, A Gatilova, AM Lomonosov, V Shalagatskyi, T Pezeril, VV Temnov, and RI Tobey. Transient grating spectroscopy in magnetic thin films: Simultaneous detection of elastic and magnetic dynamics. *Scientific reports*, 6:29143, 2016.

[3] Timothy F Crimmins, AA Maznev, and Keith A Nelson. Transient grating measurements of picosecond acoustic pulses in metal films. *Applied Physics Letters*, 74(9):1344–1346, 1999.

[4] Y Nishiyama, M Fukuda, M Terazima, and Y Kimura. Study of the translational diffusion of the benzophenone ketyl radical in comparison with stable molecules

in room temperature ionic liquids by transient grating spectroscopy. *The Journal of chemical physics*, 128(16):164514, 2008.

[5] Chengyun Hua and Austin J Minnich. Transport regimes in quasiballistic heat conduction. *Physical Review B*, 89(9):094302, 2014.

[6] F Bencivenga, R Cucini, Flavio Capotondi, A Battistoni, R Mincigrucci, E Giangrisostomi, A Gessini, M Manfredda, IP Nikolov, E Pedersoli, et al. Four-wave mixing experiments with extreme ultraviolet transient gratings. *Nature*, 520(7546):205–208, 2015.

[7] Cristian Svetina, Roman Mankowsky, Gregor Knopp, Frieder Koch, G Seniutinas, Benedikt Rösner, A Kubec, Maxime Lebugle, Iacopo Mochi, Martin Beck, et al. Towards x-ray transient grating spectroscopy. *Optics Letters*, 44(3):574–577, 2019.

[8] AA Maznev, F Bencivenga, Andrea Cannizzo, F Capotondi, R Cucini, RA Duncan, Thomas Feurer, TD Frazer, L Foglia, H-M Frey, et al. Generation of coherent phonons by coherent extreme ultraviolet radiation in a transient grating experiment. *Applied physics letters*, 113(22):221905, 2018.

[9] Gerhard Ingold, Rafael Abela, Christopher Arrell, Paul Beaud, Pirmin Böhler, Marco Cammarata, Yunpei Deng, Christian Erny, Vincent Esposito, Uwe Flechsig, et al. Experimental station bernina at swissfel: condensed matter physics on femtosecond time scales investigated by x-ray diffraction and spectroscopic methods. *Journal of synchrotron radiation*, 26(3):874–886, 2019.

[10] Christopher J Milne, Thomas Schietinger, Masamitsu Aiba, Arturo Alarcon, Jürgen Alex, Alexander Anghel, Vladimir Arsov, Carl Beard, Paul Beaud, Simona Bettoni, et al. Swissfel: the swiss x-ray free electron laser. *Applied Sciences*, 7(7):720, 2017.

[11] Paul Latimer and Randy F Crouse. Talbot effect reinterpreted. *Applied optics*, 31(1):80–89, 1992.

[12] S Szapiel and K Patorski. Fresnel diffraction images of periodic objects under gaussian beam illumination. *Optica Acta: International Journal of Optics*, 26(4):439–446, 1979.

[13] SG Raymond and PD Townsend. The influence of rare-earth ions on the low-temperature thermoluminescence of bi4ge3o12. *Journal of Physics: Condensed Matter*, 12(9):2103, 2000.

[14] Paul A Williams, AH Rose, KS Lee, DC Conrad, Gordon W Day, and Paul D Hale. Optical, thermo-optic, electro-optic, and photoelastic properties of bismuth germanate (bi 4 ge 3 o 12). *Applied Optics*, 35(19):3562–3569, 1996.

[15] SE Brunner and DR Schaart. Bgo as a hybrid scintillator/cherenkov radiator for cost-effective time-of-flight pet. *Physics in Medicine & Biology*, 62(11):4421, 2017.

[16] G Montemezzani, P Günter, et al. Electro-optic and photorefractive properties of bi 4 ge 3 o 12 crystals in the ultraviolet spectral range. *JOSA B*, 9(7):1110–1117, 1992.

[17] Osamu Kamada and Kazuhiko Kakishita. Electro-optical effect of bi4ge3o12 crystals for optical voltage sensors. *Japanese journal of applied physics*, 32(9S):4288, 1993.

[18] Changsheng Li, Xiang Cui, and Toshihiko Yoshino. Optical electric-power sensor by use of one bismuth germanate crystal. *Journal of Lightwave technology*, 21(5):1328, 2003.

[19] S.F. Radaev, L.A. Muradyan, Yu.F. Kargin, V.A. Sarin, V.N. Kanepit, and V.I. Simonov. Neutron diffraction study of single crystals of bi4 ge3 o12 with eulytine structure. *Kristallografiya*, 35:361–364, 1990.

[20] TI Milenov, PM Rafailov, R Petrova, Yu F Kargin, and MM Gospodinov. X-ray diffraction study of a bi4ge3o12 crystal. *Materials Science and Engineering: B*, 138(1):35–40, 2007.

[21] Mikako Makita, Petri Karvinen, Vitaliy A Guzenko, Naresh Kujala, Patrik Vagovic, and Christian David. Fabrication of diamond diffraction gratings for experiments with intense hard x-rays. *Microelectronic Engineering*, 176:75–78, 2017.

[22] Yuen-Ron Shen. The principles of nonlinear optics. *wi*, 1984.

[23] Shaul Mukamel. *Principles of nonlinear optical spectroscopy*, volume 6. Oxford university press New York, 1995.

[24] RF Begley, AB Harvey, and Robert L Byer. Coherent anti-stokes raman spectroscopy. *Applied Physics Letters*, 25(7):387–390, 1974.

[25] AA Lutman, R Coffee, Y Ding, Z Huang, J Krzywinski, T Maxwell, Marc Messerschmidt, and H-D Nuhn. Experimental demonstration of femtosecond two-color x-ray free-electron lasers. *Physical review letters*, 110(13):134801, 2013.

[26] Z Chen, Y Gao, BC Minch, and MF DeCamp. Coherent optical phonon generation in bi3ge4o12. *Journal of Physics: Condensed Matter*, 23(38):385402, 2011.

[27] https://henke.lbl.gov/optical_constants/.

[28] Shigeyuki Somiya. *Handbook of advanced ceramics: materials, applications, processing, and properties*. Academic press, 2013.

[29] J Zelenka. Electromechanical properties of bismuth germanium oxide (bi12geo20). *Czechoslovak Journal of Physics B*, 28(2):165–169, 1978.

[30] Hans Joachim Eichler, Peter Günter, and Dieter W Pohl. *Laser-induced dynamic gratings*, volume 50. Springer, 2013.

[31] Renato Torre. *Time-resolved spectroscopy in complex liquids*. Springer, 2007.

[32] Robin Jon Hawes Clark and Ronald E Hester. Time resolved spectroscopy. *trs*, 1989.

[33] Wayne D Kimura. *Electromagnetic Waves and Lasers*. Morgan & Claypool Publishers, 2017.

[34] AA Maznev, KA Nelson, and JA Rogers. Optical heterodyne detection of laser-induced gratings. *Optics letters*, 23(16):1319–1321, 1998.

[35] R Torre, A Taschin, and M Sampoli. Acoustic and relaxation processes in supercooled orthoterphenyl by optical-heterodyne transient grating experiment. *Physical Review E*, 64(6):061504, 2001.

[36] Anubhav Jain, Shyue Ping Ong, Geoffroy Hautier, Wei Chen, William Davidson Richards, Stephen Dacek, Shreyas Cholia, Dan Gunter, David Skinner, Gerbrand Ceder, et al. Commentary: The materials project: A materials genome approach to accelerating materials innovation. *Apl Materials*, 1(1):011002, 2013.

[37] https://materialsproject.org/materials/mp-23560/.

[38] http://phonondb.mtl.kyoto-u.ac.jp/ph20180417/d023/mp-23560.html.

[39] Atsushi Togo and Isao Tanaka. First principles phonon calculations in materials science. *Scripta Materialia*, 108:1–5, 2015.

[40] Cristian Svetina, Jeremy Rouxel, Danny Fainozzi, et al. Hard x-ray transient grating spectroscopy on bismuth germanate. *Nature Photonics (review)*, 2021.

Chapter 5

Element- and enactomeric-selective visualisation of vibrations[1]

In the following Chapter, we demonstrate an element-specific ultrafast soft X-ray absorption experiment that allows to visualize and disentangle low-frequency nearly degenerate vibrational modes involving specific Carbon atoms in a racemic mixture of Ibuprofen (IBP, 4-isobutyl-2-phenylpropionic acid). Furthermore, we demonstrate how the control over the polarization of the EUV pulses adds enantiomeric selectivity, tying it together with the element-selectivity and mode-specificity.

5.1 The scientific case

In chemistry, biology and materials science, the ability to access interatomic interactions and their ultrafast dynamics has become possible with the advent of femtosecond lasers [1]. In particular, the observation of vibrational wave packets via optical (UV-visible-IR) spectroscopies has been a major achievement due to its capability in tracking the molecule's motion [2–4]. However, optical spectroscopies only detect the effect of the molecular vibrations on the global electronic surfaces. As the reader know, new tuneable, pulsed and polarized X-Ray FELs, can overcome this barrier, permitting to be chemical and, of primary importance for biochemistry, enantiomeric selective. This selectivity may be complemented by taking into account the natural chemical shifs of atoms belonging to different molecular moieties. In this work we report a pump-probe (PP) experiment where, by combining the polarization control with fine energy tuneability, we are able to monitor three low frequency vibrational modes, belonging to atoms of the same chemical species but located in different enantiomers and moieties. In biochemical reactivity, such as protein-target (enzymes, RNA, micro RNA) interactions the low-frequency regime ($< 300\ cm^{-1}$) of the vibrational spectrum is mainly responsible for, and the most affected by the biological function, as it reflects the global and continuous changes in the molecular geometry [5]. Furthermore, mapping the motion of light atoms, such as C, N, O, F, involved in molecular vibrations with periods as slow as a few 10's of ps (*i.e.*, vibrational frequencies down to below few cm^{-1}) is a crucial step since it allows to address various binding processes with the element- and site-specificity. Steady-state and ultrafast vibrational terahertz (THz) to infrared (IR)

[1] Riccardo Mincigrucci, *et al*. Element- and enantiomer-selective visualization of ibuprofen dimer vibrations. *Nature (review)*, 2021.

spectroscopies are the most used to access ground state vibrational modes, however they are limited to dipole-allowed vibrational transitions, while disentangling near-degenerate vibrational modes is challenging. Steady-state Raman spectroscopy is characterised by weaker signals and also obeys selection rule, in addition to the requirement of an efficient suppression of the elastic peak at low frequencies [6, 7]. One approach for accessing low frequency modes in the time-domain is Impulsive Stimulated Raman Scattering (ISRS) [8]. It exploits the fact that the very short pump pulse is spectrally broad, encompassing several vibrational levels of the ground electronic state at once, therefore stimulating Raman transitions to the ground state, thereby creating a coherent superposition of vibrational states, *i.e.*, a ground state wave packet. Monitoring the wave packet dynamics in the time domain can circumvent the limitations due to the finite spectral resolution of steady-state spectroscopies. Low frequency modes then become easier to detect given their long oscillation periods. While this is of great value for getting insights into biological samples such as the structure of protein/nucleic acid complexes, optical radiation lacks of element-specificity. Atomic level specificity can be exploited to identify which atom of which elements are involved in the conformational rearrangements during the formation of complexes and to unravel dynamical aspects of the interactions between residues and bases involved in bio-recognition. This is possible using short-wavelength (hard X-rays to extreme ultraviolet, EUV) radiation that can be tuned to specific core-transitions of the various atomic elements. In recent years, short-wavelength spectroscopies have successfully been extended into the ultrafast regime [9], allowing the observation of vibrational wave packets around specific atoms in molecular systems [10].Femtosecond X-ray Absorption or Emission Spectroscopy can map the time evolution of interatomic vibrations with element-selectivity. On the contrary, this approach is limited to systems containing heavy atoms that have relatively low frequency modes, and efficiently absorb or scatter hard X-rays [10, 11]. Another important aspect for biological systems is enantiomeric selectivity. Most biological molecules are naturally present in nature as chiral, *i.e.*, they exist in two different forms, called enantiomers, having the same chemical composition while being the non-superposable mirror images of each other. However, biological activity is generally homo-chiral, therefore distinguishing between enantiomers is a central issue in many relevant fields such as medicine, pharmacology and toxicology, to cite a few. The method most commonly used to detect enantiomers is circular dichroism (CD) spectroscopy, which exploits the fact that circular polarized light is absorbed differently by left-handed and right-handed enantiomers given the different selection rules imposed by geometry. In the spirit of monitoring the evolution of biological systems, subpicosecond time-resolved CD optical spectroscopies have been implemented [12–14] to study the absorption bands of amino-acid residues, nucleobases and peptide chains [14, 15]. Extending these capabilities to core-level spectroscopies allows to discriminate biological activities (binding, reactivity) with atomic-specificity within a selected enantiomer. Simulations have shown that X-ray CD signals of molecular systems vary with the electronic coupling to substitution groups, the distance between the X-ray absorbing element and the chiral center, as well as geometry and chemical structure [16]. Combining CD spectroscopy with element-selectivity of light atoms such as C, N, O is particularly attractive for the study of biological systems [17]. Since the core transitions of these elements lie in the energy range between 280 eV (C) and 530 eV (O), the usage of ultrashort sources of circularly polarized solf X-ray pulses is needed. To date, High Harmonic Generation (HHG) sources cannot provide polarization control in the desired photon energy range [18, 19], however, circularly polarized soft X-ray pulses

have been generated at the FERMI FEL, in the Carbon K-edge region [20]. Combining all the above features, here we demonstrate an element-specific ultrafast soft X-ray absorption experiment that allows to visualize and disentangle low-frequency nearly degenerate vibrational modes involving specific Carbon atoms in a racemic mixture of Ibuprofen, exploiting the FERMI polarization control of the EUV pulses which adds enantiomeric selectivity at the element-selectivity and mode-specificity.

5.2 The sample

IBP is an over-the-counter anti-inflammatory non-steroidal drug that is commonly and widely used [21]. In the solid racemic mixture, the two enantiomers, labelled (S+)- and (R-), form a cyclic dimer through intermolecular hydrogen bonds between the carboxyl groups of two adjacent molecules [22], as shown in figure 5.1. The conformational stability of this dimeric arrangement has been revealed by X-ray diffraction and Raman scattering [23]. IBP was first used as a racemic mixture but later, focus of the pharmaceutical industries shiled to the (S+)-ibuprofen when it was found that this form enhances the effect of analgesia in animals (including humans), more rapidly than the (R-)-enantiomer does. The bio-activity of the two enantiomers, and in particular the cross-monomer allosteric inhibition, in which S-IBP can competitively block the action of one monomer of the cyclo-oxygenase (COX) enzyme, composed by two equal halves, is however not fully understood [24].

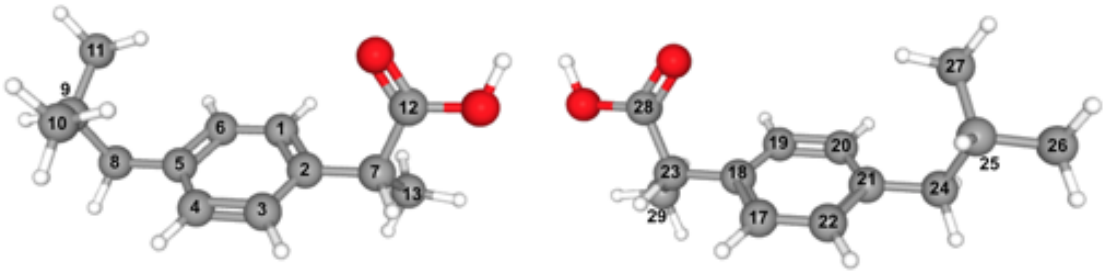

Figure 5.1: *From left to right, the (R-)- and (S+)-Ibuprofen dimers. Numbers identify each single atom in the two chiral molecules.*

5.3 Ancillary measurements

In order to obtain the best parameter configuration to use in the experiments, some satellite measurements and simulations, including Raman spectroscopy, Optical and UV absorption spectroscopy and Carbon K-edge spectroscopy, were performed.

5.3.1 Raman spectroscopy

For the sake of obtaining the values of the interested vibrational frequency to exploit in the experiment, we recorded the low-frequency Raman spectrum of the IBP dimer (figure 5.2), even if already reported in the literature, *e.g.*, [25]. A micro-Raman apparatus was used to acquire the spectra at room temperature in backscattering geometry, under cross-polarization, by using a triple-monochromator spectrometer (Horiba Jobin Yvon,

model T64000) set in double-subtractive/ single configuration and equipped with 1800 grooves/mm gratings. The Raman modes were excited by a 647.1 nm Ar/Kr ion laser and detected using a CCD camera (256 $\times$ 1024 pixels) cryogenically cooled by liquid Nitrogen. The incident radiation was focused onto the sample surface with a spot size of about 1 μm^2 through an 80X objective having a $NA = 0.75$. The calibration of the frequency shift was obtained using the emission lines of an Argon lamp substituted to the sample. In this configuration, the set-up resolution was $\sim 0.36\ cm^{-1}$/pixel over the scanned spectral range. To interpret fig. 5.2, the Raman spectrum was simulated using Gaussian 03, a program suite [26] with unrestricted density functional theory (DFT). The nonlocal B3LYP functional hybrid method was employed and the standard 6-31G(d) basis set was used for the geometry optimization and vibrational energy analysis. DFT calculations reveal that the lowest frequency Raman band consists of three near-degenerate intermolecular vibrational modes, which characterise different conformations of the global dimeric structure as depicted in figure 5.2. The lowest frequency mode ($\omega_1 = 21.5\ cm^{-1}$), is more localized on the S-dimer and involves a rotation of the benzene ring around the 2-5 axis, *i.e.*, a torsional deformation of both the phenyl ring and the isobutyl group (figure 5.2 top right). The $\omega_2 = 22.6\ cm^{-1}$ mode involves an out-of- plane twisting (the plane defined by the carboxyl groups) accompanied by a $C = CH_3$ stretch (figure 5.2 middle right). Similar to the lowest frequency mode, in the R-dimer (figure 5.2 bottom right), the mode at $\omega_3 = 28.8\ cm^{-1}$ involves large displacements of the same molecular groups, in the form of a rotation of the benzene ring around the 18-21 axis and the close isobutyl group. Low-frequency vibrational wave packets, made out by the three low-lying ω_1 to ω_3 modes, can be all generated at once by ISRS on crystallized ibuprofen and probed by Carbon K-edge absorption spectroscopy.

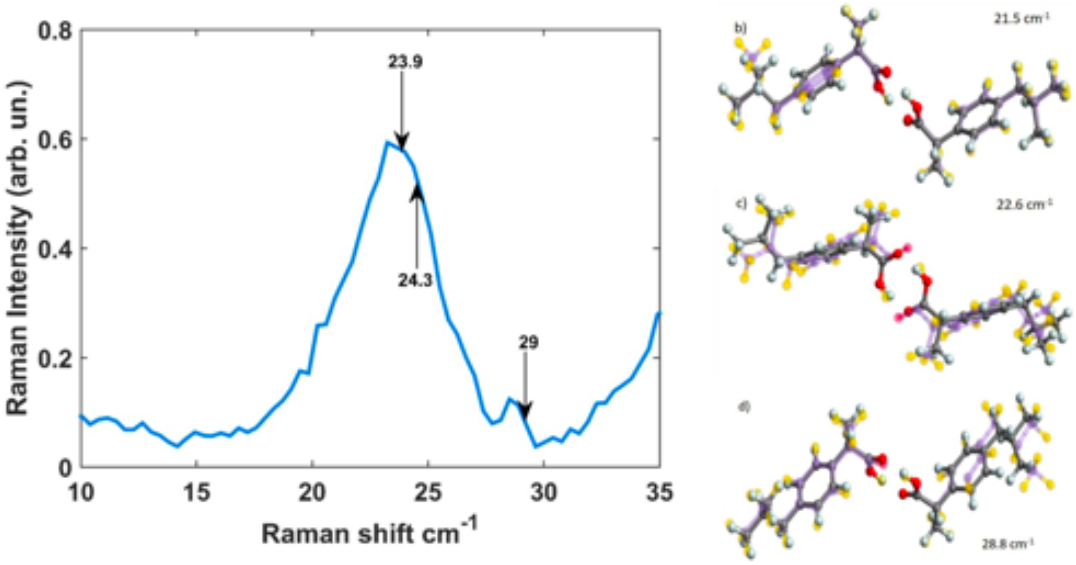

Figure 5.2: *Left - Measured Raman spectrum (solid blue line). The black arrows indicate the frequency modes obtained in our experiment. From top right to bottom right - the three intermolecular modes of the dimer. The structures appearing in contrasted and semi-transparent colours, correspond to the minimum and maximum deformations for the calculated intermolecular modes of the dimer.*

5.3.2 Optical UV absorption spectrum

In order to obtain the best pump wavelength to use in the experiment *i.e.,* to maximise the absorption, an ultraviolet (UV) absorption spectrum of IBP can be found in literature [27] (see fig. 5.3). It exhibits a structured band with a maximum at 262 nm (~ 4.7 eV). To understand the transitions involved in the absorption process, we calculated the optical UV spectrum using a multi configurational self-consistent field (MCSCF) calculations at the cc-pVDZ/RASSCF(6/6) level of theory using the MOLPRO package [28]. The simulation, giving three absorption bands at 273 nm, 266 nn, and 262 nm, is compared to the experimental spectrum in figure 5.3.

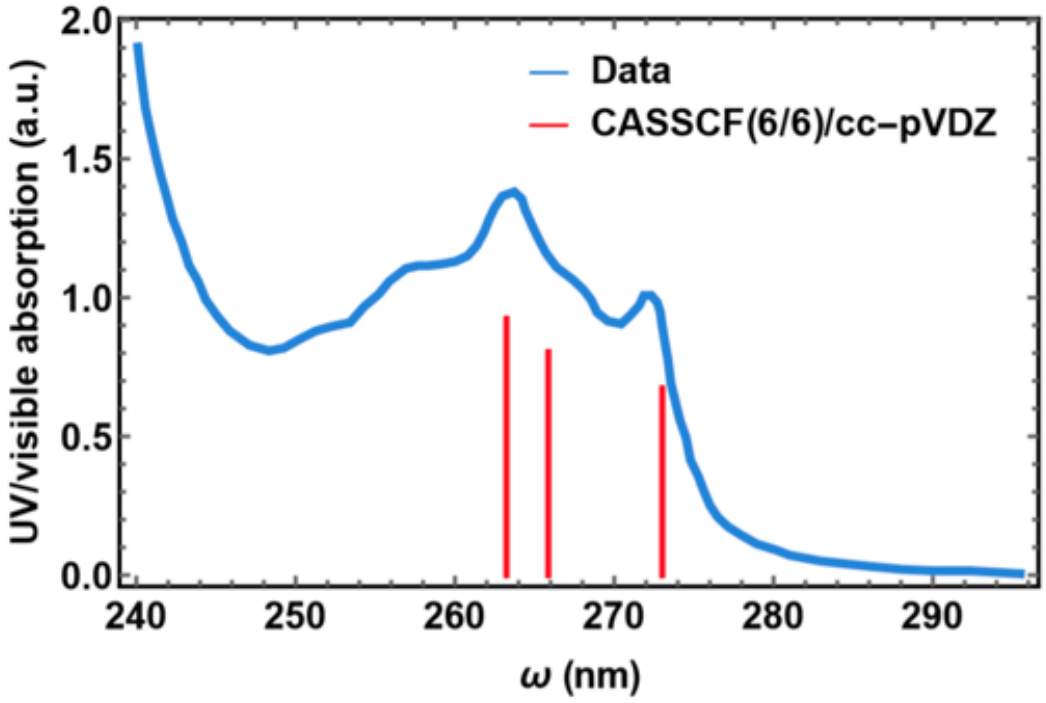

Figure 5.3: *Ultraviolet absorption spectrum of the ibuprofen dimer at room temperature5,6. The red trace is the calculated spectrum shifted by 3.5 eV to match the experimental one.*

To match the experimental spectrum, a shift of 3.5 eV was applied to the transition energies found by the MCSCF calculations and the resulting agreement is satisfactory. The shift originates from basis set incompleteness, active space size limitation and relativistic effects [29]. It can be diminished by using second-order perturbation theory CASPT2 and RASPT221. In the MCSCF approach, each eigenstate is represented by a sum of determinant, each of them corresponding to a configuration of different occupied and unoccupied orbitals. For the cc-pVDZ/RASSCF(6/6) level of theory chosen, the considered six orbitals range from $HOMO-2$ to $LUMO+2$. The 273 nm transition is dominated by $HOMO \rightarrow LUMO+1$ and $HOMO-1 \rightarrow LUMO$ excited determinants, the 266 nm one by $HOMO \rightarrow LUMO$, $HOMO-1 \rightarrow LUMO+1$, $HOMO-2 \rightarrow LUMO$ and $HOMO \rightarrow LUMO+2$ singly excited determinant, and a $HOMO \rightarrow LUMO$ doubly excited determinant. Finally, the 263 nm transition is composed of $HOMO-2 \rightarrow LUMO+1$ and $HOMO-1 \rightarrow LUMO+2$ singly excited determinant, and $HOMO/HOMO-1 \rightarrow LUMO+1$, $HOMO-1 \rightarrow LUMO/LUMO+1$ doubly excited determinants.

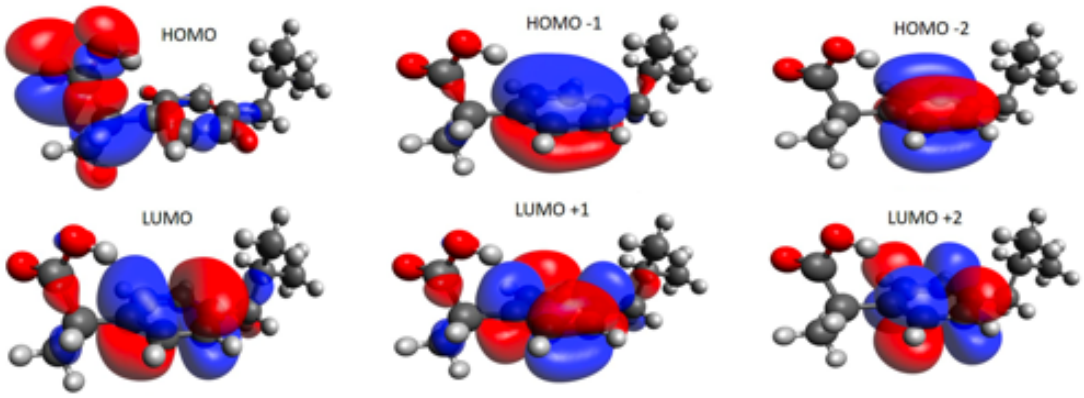

Figure 5.4: *Orbitals of the IBP involved in the transitions shown in figure 5.3.*

5.3.3 Carbon K-edge absorption

In order to obtain the best energy for the probe beam, we performed an X-Ray Absorption Spectroscopy (XAS) experiment at the K-edge of Carbon using left- (LC) and right-circular (RC) polarization of light. The absorption spectra were obtained acquiring and averaging 3500 shots for each FEL photon energy and polarization. FEL photon energies between 293.5 eV and 285 eV were generated by high gain harmonic generation (HGHG) of the 60^{th} harmonic of the seed laser was tuned between 4.9 eV and 4.7 eV in steps of about 0.02 eV. Energies range between 283.7 eV and 279.2 eV were instead obtained by amplifying the 55^{th} harmonic of the seed laser tuned between 5.16 eV and 5.1 eV in steps of about 0.02 eV. In both configurations, the polarization was varied by changing the phase of the magnetic field inside the APPLE II undulators. The spectra are shown in figure 5.5 a) and they exhibit distinct differences. In particular, the spectrum obtained using LC light shows an enhanced intensity at the edge (285-286 eV) compared to the RC counterpart, while above 287 eV, the RC light has a higher transmission. The difference between these two spectra, normalized by their sum, is shown in fig. 5.5 b), which gives the Carbon K-edge circular dichroism.
To calculate the C K-edge absorption spectrum, we used restricted active space core-excited states calculations (RASSCF) [30] for each Carbon 1s core orbitals. This multireference method has been used successfully to compute molecular core-excited states [31]. The Douglas-Kroll- Hess Hamiltonian at the second order was used to account for relativistic corrections important for core excited state computation. For each carbon atom, the computation was achieved by first rotating the 1s Carbon orbital into the active space (AS), freezing it to double occupancy without re-optimization and carrying a RASSCF calculation. This step ensures that the transition matrix elements, and the subsequently calculated core excited states, are computed within the same active space labelling. Then, the core orbital is restricted to single occupancy and the two lowest lying core excited states are computed. Finally, transition electric dipole matrix elements are computed between ground, valence and core excited states. In order to ensure the suitability of the chosen active space, the RASSCF calculations were repeated for different active space sizes until convergence was reached. The stick spectrum shown in 5.5 was calculated at the cc-pVDZ/ RASSCF(9/8) level including in the AS the $HOMO-3, HOMO-2, HOMO-1, HOMO, LUMO, LUMO+1, LUMO+2$ relevant Carbon 1s orbital. Our interpretation is based on this AS computation since it is consistent with the AS obtained within the UV absorption spectrum, while being

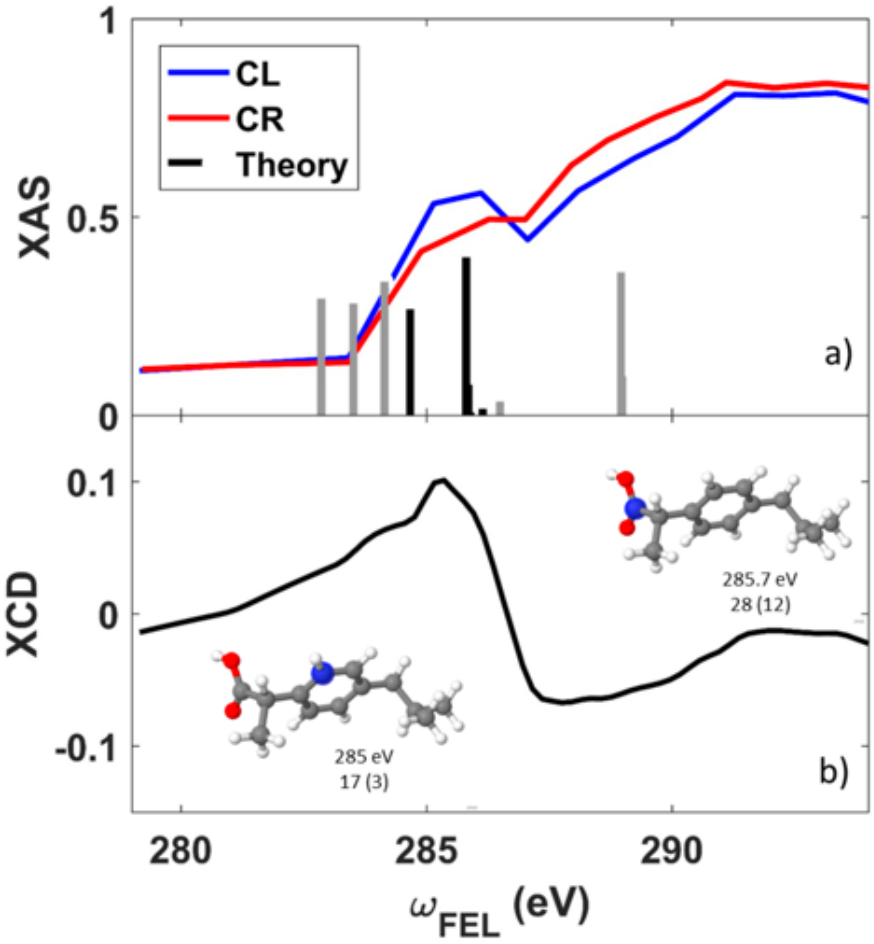

Figure 5.5: *a) Steady-state Carbon K-edge absorption spectrum of S-IBP recorded with circularly left (blue trace) and right (red trace) polarized light. The sticks represent the calculated transition position and relative strengths. Black sticks are the transitions investigated in the present work. Grey sticks are other Carbons core transitions. b) Steady-state Carbon K-edge X-ray circular dichroism (XCD) signal calculated as the difference of the L and R spectra shown in panel a), normalized by their sum. Insets in panel b) show, in blue, the selected atoms by the corresponding probe wavelength.*

a larger active space. Strength of the transitions (sticks' hight in figure 5.5) are calculated using the relation $d = \langle \phi_i | r | \phi_f \rangle$, where ϕ_i is the initial core orbital of the Carbons and ϕ_f is the final configuration, that for the first transition have mainly a $LUMO$ or $LUMO + 1$ character. Low frequency oscillations are expected to significantly change the geometry of the molecule and consequently the value of the transitions by altering the projections. On the contrary, high frequency oscillations are generally connected to smaller amplitudes and thus smaller change in the projections which may remain hidden in the experimental noise. We focus our study in two classes of atoms: the ones possessing a transition energy of $\sim 285.7\ eV$ (blue atom in fig. 5.5 left) and those with an energy of $\sim 285\ eV$ (blue atom in fig 5.5 right). This labelling refers to the identical atoms in the two enantiomers. The energy difference can mostly be ascribed to the chemical shift of the K-edge energy due to different local environments around the atoms.

5.4 The experimental setup

The pump-probe experiment was conducted at the EIS-TIMEX end-station of the FERMI Free Electron Laser facility in Trieste, Italy). The sample was photoexcited with laser pulses at a photon energy of 4.7 eV, resonant with the IBP absorption an energy/pulse below 1 μJ and pulse duration of 80 fs. The pump beam is focused onto a spot size of 90×90 μm^2 full-width-at- half-maximum (FWHM). It impinges the sample at an angle of 10 degrees, relatively to the surface normal, while the FEL probe pulse is at normal incidence. This pump pulse generates low-frequency modes of the IBP dimer by impulsive stimulated Raman scattering (ISRS). The soft X-ray Free Electron Laser photon energy where chosen to match the transitions identified by the theoretical calculations (black sticks in fig. 5.5 a)). To prevent long-term IBP photo degradation and to optimize the spatial overlap, the FEL spot size was set to 80 μm FWHM and the energy/pulse was reduced to about 160 nJ. The estimated FEL pulse duration is about 30 fs FWHM. Sample degradation was excluded by visual inspection performed through a Questar QM100 tele-microscope. In order to minimize radiation damage effects (detectable as a monotonic increase in the measured transmission of the spot), after each time scan the sample was moved to a pristine region The soft X-ray intensity transmitted through the sample was detected by a Multi-Channel Plate (MCP) placed on the FEL beam axis and calibrated using an identically hydrophilized Silicon Nitride membrane. The calibration was performed by recording the signal level (I_1) on the MCP as a function of the incoming FEL intensity (I_0) and modelling the trend as a second order polynomial. This way, it is possible to estimate the expected I_1 for any given I_0 value and to calculate the IBP layer transmission shot-by-shot, as the ratio between the measured I_1 and the one calculated with the second order polynomial defined above. The procedure was repeated for every probe energy/polarization (experimental configuration). Time traces were collected by continuously scanning the pump-probe delay (at a velocity of 0.5 ps/s) and recording the transmission of the soft X-ray beam. The measurements were repeated three times for each experimental setting. The data were subsequently merged and binned in 50 fs steps. The data points displayed in the time traces are the mean values of the bin content while error bars are the standard deviations of the bin entries.

5.5 Results

Figure 5.7 shows the time evolution of the signal upon impulsive excitation of the system at different EUV photon energies and polarizations of the probe beam. All traces reveal periodic intensity modulations (5-10 % amplitude of the transmission signal) around the mean value.
The data in panel a) were obtained at a probe energy of 285.7 eV and with RC polarized light. Panels b) and c) show time scans acquired using a probe photon energy of 285.0 eV with CL and CR polarization, respectively. Panels a) and b) exhibit a clear modulation with a sine dependence, as expected for Raman processes [32], with a ~ 1.5 ps period. Despite the lower signal-to-noise (S/N) ratio, sinusoidal oscillations can be distinguished in panel (c) as well. This lower S/N is due to the fact that the CR signal at 285 eV is weak and rides on a background of increasing continuum absorption, which extends towards higher photon energies (see figure 5.5 a)). This should be contrasted with the CL signal at the same energy. The three traces were fitted to the following

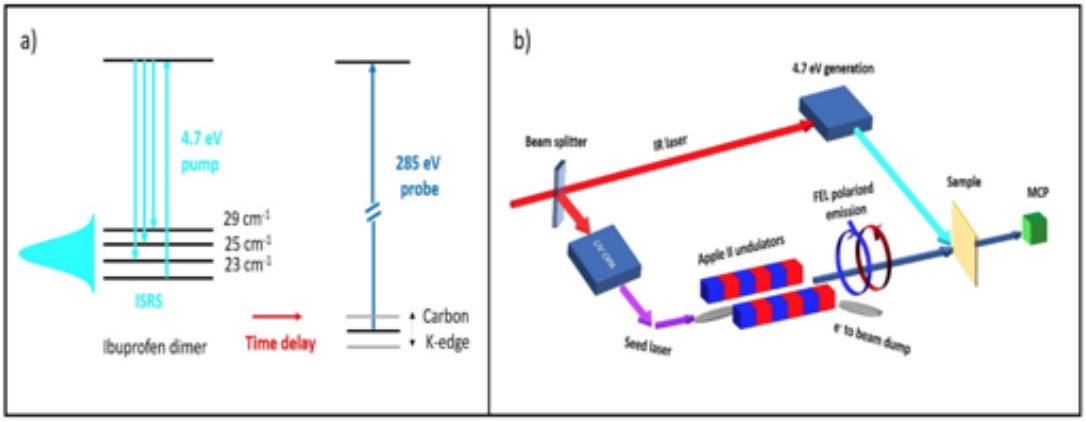

Figure 5.6: *a) Pulse scheme of the experiment with the relevant energy levels: the 4.7 eV pump pulse (cyan arrows) generates a coherent superposition of vibrational levels in the HOMO by ISRS. These modes are then probed with element- selectivity by the soft X-ray pulse (blue arrows) tuned to the carbon K-edge. b) the experimental lay-out. A 786 nm femtosecond laser pulse is split and delivered to an optical parametric amplifier (OPA) where it is up converted to generate the* $\sim$ *4.76 eV pulse that initiate the Free Electron Laser process, as well as a frequency-tripling to generate the 4.7 eV pump pulse. The seeded electron bunch is propagated through a chain of Apple II undulators, allowing control of the polarization and energy of the soft X-ray photons.*

damped sinusoidal functions

$$y(t) = y_0 + \vartheta(t) A e^{-\frac{t}{\tau}} \sin(2\pi\nu t) \tag{5.1}$$

where y_0 is the unperturbed value for the transmittivity of the IBP layer, $\vartheta(t)$ is the Heaviside theta function, A is the amplitude of the oscillation induced by the pump pulse, τ is the decay time of the oscillatory mode, and ν is the frequency of the oscillation. The function does not contain any contribution due to the instrumental resolution since the dynamic studied is much slower compared to the instrumental resolution itself. The fitting procedure using eq. 5.1 yield the frequencies and damping constants given in table 5.1.

Probe (eV)	y_0	$A(\%)$	τ (ps)	ν (cm^{-1})	calculated (cm^{-1})
285.7 CR	50.5 ± 0.03	2.0 ± 0.9	2.5 ± 2	24.3 ± 0.9	22.6
285.0 CL	68.9 ± 0.01	4.0 ± 2	1.7 ± 1	23.9 ± 1.1	21.5
285.0 CR	55.5 ± 0.03	6	2.8	29 ± 0.7	28.8

Table 5.1: *Parameters of the fit of the temporal traces using the damped sine function in eq. 5.1. In contrast, low frequency steady state Raman spectrum exhibits only one band centered around 25* cm^{-1} *whose width increase starting from* $\sim$ *5* cm^{-1} *at 100 K to* $\sim$ *10* cm^{-1} *at 300 K, as reported in [25].*

All fit parameters were left free except for the data set at 285 eV CR where, due to the lower signal-to-noise ratio, we only fit the oscillation frequency. In this case, the y_0 value is set to the mean value of the negative delay data points, the amplitude of the oscillation was set to 6% (maximum of the trace minus the y_0 value), and the damping time was set to 2.8 ps (close to the one obtained for the 285.7 eV CR configuration). This artificially reduces the uncertainty on the only free parameter. These frequencies are in agreement with both the calculated and measured lowest Raman peaks. The damping times of these three modes correspond to 10 to 20 cm^{-1} spectral widths, which explains

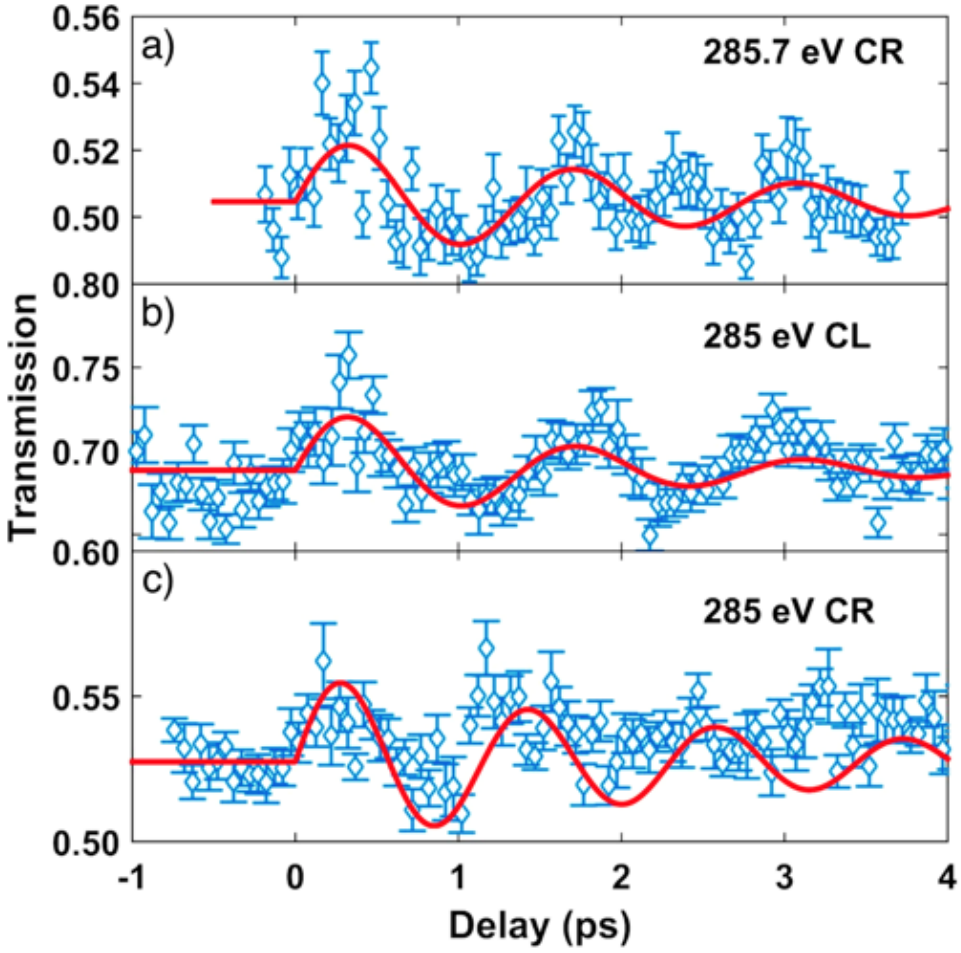

Figure 5.7: *Time-resolved X-ray transmission signal of the racemic IBP sample measured using probe pulses of a) 285.7 eV with circular right polarization: b) 285 eV with circular left polarization and; c) 285 eV with circular right polarization. Red lines are fits to the data with damped sinusoidal functions whose parameters are given in table 5.1.*

why they could not be resolved by Raman spectroscopy. Finally, the small bumps lying outside the fit traces present in waveforms a) and c) in fig. 5.7, can be explained as local oscillations of the FEL intensity.

5.6 Conclusions

The ability to access the dynamics of a selected atom in molecules, as largely discussed in the introduction, has been a longstanding goal for theorists and experimentalists. The present results pave the way for the direct investigation of the drug/target intermolecular vibrational dynamics, with the potential to understand the marked differences in biological activities of enantiomers, or easily follow the dynamic of metal complexes [33]. More generally, such detailed level of understanding may lead to new design strategies of bioactive molecules such as vibrational/deformational engineering by the usege of isotopes to modify the vibrational behaviour of an identified atom or molecular moiety while keeping unaltered the electronic properties. Finally, an actinic pulse could be added to the present super-selective PP approach, triggering photoac-

tive reactions and tracking the behaviour of selected atoms during the chemical process.

References

[1] Ahmed H Zewail. Femtochemistry: Atomic-scale dynamics of the chemical bond using ultrafast lasers (nobel lecture). *Angewandte Chemie International Edition*, 39(15):2586–2631, 2000.

[2] Shota Tsuru, Marta L Vidal, Mátyás Pápai, Anna I Krylov, Klaus B Møller, and Sonia Coriani. Time-resolved near-edge x-ray absorption fine structure of pyrazine from electronic structure and nuclear wave packet dynamics simulations. *The Journal of Chemical Physics*, 151(12):124114, 2019.

[3] Simon P Neville, Majed Chergui, Albert Stolow, and Michael S Schuurman. Ultrafast x-ray spectroscopy of conical intersections. *Physical review letters*, 120(24):243001, 2018.

[4] VA Apkarian and N Schwentner. Molecular photodynamics in rare gas solids. *Chemical Reviews*, 99(6):1481–1514, 1999.

[5] Gerard Giraud, Jan Karolin, and Klaas Wynne. Low-frequency modes of peptides and globular proteins in solution observed by ultrafast ohd-rikes spectroscopy. *Biophysical journal*, 85(3):1903–1913, 2003.

[6] Yuqing Zhang, Yuqing Gu, Jing He, Benjamin D Thackray, and Jian Ye. Ultrabright gap-enhanced raman tags for high-speed bioimaging. *Nature communications*, 10(1):1–12, 2019.

[7] Yao Guo, Weixuan Zhang, Hanchun Wu, Junfeng Han, Yongliang Zhang, Shenghuang Lin, Chunru Liu, Kang Xu, Jingsi Qiao, Wei Ji, et al. Discovering the forbidden raman modes at the edges of layered materials. *Science advances*, 4(12):eaau6252, 2018.

[8] Lisa Dhar, John A Rogers, and Keith A Nelson. Time-resolved vibrational spectroscopy in the impulsive limit. *Chemical Reviews*, 94(1):157–193, 1994.

[9] CJ Milne, TJ Penfold, and M Chergui. Recent experimental and theoretical developments in time-resolved x-ray spectroscopies. *Coordination Chemistry Reviews*, 277:44–68, 2014.

[10] Tetsuo Katayama, Thomas Northey, Wojciech Gawelda, Christopher J Milne, György Vankó, Frederico A Lima, Zoltán Németh, Shunsuke Nozawa, Tokushi Sato, Dmitry Khakhulin, et al. Tracking multiple components of a nuclear wavepacket in photoexcited cu (i)-phenanthroline complex using ultrafast x-ray spectroscopy. *Nature communications*, 10(1):1–8, 2019.

[11] Kristjan Kunnus, Morgane Vacher, Tobias CB Harlang, Kasper S Kjær, Kristoffer Haldrup, Elisa Biasin, Tim B van Driel, Mátyás Pápai, Pavel Chabera, Yizhu Liu, et al. Vibrational wavepacket dynamics in fe carbene photosensitizer determined with femtosecond x-ray emission and scattering. *Nature communications*, 11(1):1–11, 2020.

[12] Mirko Scholz, Marius Morgenroth, Min Ju Cho, Dong Hoon Choi, Kawon Oum, and Thomas Lenzer. Ultrafast broadband transient absorption and circular dichroism reveal relaxation of a chiral copolymer. *The Journal of Physical Chemistry Letters*, 10(17):5160–5166, 2019.

[13] Mathias Bonmarin and Jan Helbing. Polarization control of ultrashort mid-ir laser pulses for transient vibrational circular dichroism measurements. *Chirality: the pharmacological, biological, and chemical consequences of molecular asymmetry*, 21(1E):E298–E306, 2009.

[14] Malte Oppermann, Benjamin Bauer, Thomas Rossi, Francesco Zinna, Jan Helbing, Jérôme Lacour, and Majed Chergui. Ultrafast broadband circular dichroism in the deep ultraviolet. *Optica*, 6(1):56–60, 2019.

[15] François Auvray, David Dennetiere, Alexandre Giuliani, Frédéric Jamme, Frank Wien, Bastien Nay, Séverine Zirah, François Polack, Claude Menneglier, Bruno Lagarde, et al. Time resolved transient circular dichroism spectroscopy using synchrotron natural polarization. *Structural Dynamics*, 6(5):054307, 2019.

[16] Yu Zhang, Jérémy R Rouxel, Jochen Autschbach, Niranjan Govind, and Shaul Mukamel. X-ray circular dichroism signals: a unique probe of local molecular chirality. *Chemical science*, 8(9):5969–5978, 2017.

[17] Jason D Biggs, Yu Zhang, Daniel Healion, and Shaul Mukamel. Multidimensional x-ray spectroscopy of valence and core excitations in cysteine. *The Journal of Chemical Physics*, 138(14):144303, 2013.

[18] Ofer Kfir, Patrik Grychtol, Emrah Turgut, Ronny Knut, Dmitriy Zusin, Dimitar Popmintchev, Tenio Popmintchev, Hans Nembach, Justin M Shaw, Avner Fleischer, et al. Generation of bright phase-matched circularly-polarized extreme ultraviolet high harmonics. *Nature Photonics*, 9(2):99–105, 2015.

[19] Pei-Chi Huang, Carlos Hernández-García, Jen-Ting Huang, Po-Yao Huang, Chih-Hsuan Lu, Laura Rego, Daniel D Hickstein, Jennifer L Ellis, Agnieszka Jaron-Becker, Andreas Becker, et al. Polarization control of isolated high-harmonic pulses. *Nature Photonics*, 12(6):349–354, 2018.

[20] E Allaria, D Castronovo, P Cinquegrana, P Craievich, Massimo Dal Forno, MB Danailov, G D'Auria, A Demidovich, G De Ninno, S Di Mitri, et al. Two-stage seeded soft-x-ray free-electron laser. *Nature Photonics*, 7(11):913–918, 2013.

[21] Kim D Rainsford. *Ibuprofen: A critical bibliographic review*. CRC Press, 2003.

[22] German L Perlovich, Sergey V Kurkov, Lars Kr Hansen, and Annette Bauer-Brandl. Thermodynamics of sublimation, crystal lattice energies, and crystal structures of racemates and enantiomers:(+)-and (±)-ibuprofen. *Journal of pharmaceutical sciences*, 93(3):654–666, 2004.

[23] ML Vueba, ME Pina, and LAE Batista De Carvalho. Conformational stability of ibuprofen: assessed by dft calculations and optical vibrational spectroscopy. *Journal of pharmaceutical sciences*, 97(2):845–859, 2008.

[24] Benjamin J Orlando, Michael J Lucido, and Michael G Malkowski. The structure

of ibuprofen bound to cyclooxygenase-2. *Journal of structural biology*, 189(1):62–66, 2015.

[25] JJ Lazarević, Snežana Uskoković-Marković, Milena Jelikić-Stankov, M Radonjić, D Tanasković, N Lazarević, and ZV Popović. Intermolecular and low-frequency intramolecular raman scattering study of racemic ibuprofen. *Spectrochimica Acta Part A: Molecular and Biomolecular Spectroscopy*, 126:301–305, 2014.

[26] Michael J Frisch and Alice B Nielsen. *Gaussian 03 Programmer's Reference*. Gaussian, 2003.

[27] Ming-Yan Ma, Ying-Jie Zhu, Liang Li, and Shao-Wen Cao. Nanostructured porous hollow ellipsoidal capsules of hydroxyapatite and calcium silicate: preparation and application in drug delivery. *Journal of Materials Chemistry*, 18(23):2722–2727, 2008.

[28] Hans-Joachim Werner, Peter J Knowles, Gerald Knizia, Frederick R Manby, and Martin Schütz. Molpro: a general-purpose quantum chemistry program package. *Wiley Interdisciplinary Reviews: Computational Molecular Science*, 2(2):242–253, 2012.

[29] Patrick Norman and Andreas Dreuw. Simulating x-ray spectroscopies and calculating core-excited states of molecules. *Chemical reviews*, 118(15):7208–7248, 2018.

[30] Per Åke Malmqvist, Alistair Rendell, and Bjoern O Roos. The restricted active space self-consistent-field method, implemented with a split graph unitary group approach. *Journal of Physical Chemistry*, 94(14):5477–5482, 1990.

[31] Meiyuan Guo, Erik Kallman, Lasse Kragh Sorensen, Mickael G Delcey, Rahul V Pinjari, and Marcus Lundberg. Molecular orbital simulations of metal 1s2p resonant inelastic x-ray scattering. *The Journal of Physical Chemistry A*, 120(29):5848–5855, 2016.

[32] Gregory A Garrett, TF Albrecht, JF Whitaker, and Roberto Merlin. Coherent thz phonons driven by light pulses and the sb problem: What is the mechanism? *Physical review letters*, 77(17):3661, 1996.

[33] Katherine H Thompson and Chris Orvig. Metal complexes in medicinal chemistry: new vistas and challenges in drug design. *Dalton transactions*, (6):761–764, 2006.

Chapter 6

Future of Protein Structure & X-ray Diffraction Experiments

In this Chapter we focus our attention on the main problem affecting the structure determination of molecules and proteins. We briefly introduce the two leading techniques used to probe the structure of proteins, being X-ray Diffraction (XRD) and Cryo Electron Microscopy (Cryo EM), and exploit their limitation. On the limitation of XRD, we present a simple work on a 2D crystal of Bacteriorhodopsin focused on obtaining a single crystal diffraction patter. We show that it is possible to obtain the same resolution using Synchrotron and FEL based techniques on 2D crystals. Given the results, we concluded that the path towards the structure retrieval of proteins showing a natural inability to crystallize requires different methodologies with respect to the ones used nowadays. Thus, we present a new methodology that should overcome the protein crystalization limit. Using a multidisciplinary approach, we propose to create a two-dimensional protein array with defined orientation attached on a self-assembled-monolayer. We take advantage of a developing literature-based, flexible toolbox capable of assembling different proteins on a functionalised surface while keeping them under physiological conditions during the experiment. Finally we study the opportunity to probe them through ultrashort and ultra-bright pulses of X-ray Free Electron Lasers which have made attainable the dream to determine protein structure before radiation damage starts to destroy the samples.

6.1 Introduction

Revealing the structure of complex biological macromolecules such as proteins, is an essential step for understanding the chemical mechanisms that determine the diversity of their functions. The determination of the structure of proteins as well as other macromolecules has historically been prerogative of X-ray crystallography. One of the requirements of the technique is the usage of high-quality crystals, which need to be sufficiently large to efficiently diffract X-rays while withstanding radiation damage. This method suffers from two noteworthy constraints, making structure determination extremely difficult or sometimes impossible. The first problem is that the majority of bio-molecules hardly form sufficiently large, high quality crystals or do not crystalize at all [1]. This restriction is most severe for large protein complexes, such as membrane proteins such as receptors, transporters, and enzymes, which participate in a plethora of fundamental biological processes, therefore being responsible of many cellular dys-

functions and potential targets for new therapeutic agents. The second limitation is the unavoidable X-ray radiation damage. Crystal size and radiation damage are inherently linked, since reducing the dose delivered to a single molecule requires large crystals amplifying the signal through Bragg diffraction. Therefore, synchrotron-based experiments are usually performed with cryo-cooled crystals in order to reduce the mass-transport rate due to radiation damage.

However, some proteins such as membrane proteins, have been observed to form two-dimensional (2D) crystals, a sample geometry that to date has not been suitable for high-resolution forward-scattering X-ray analysis due to limitations of radiation damage. Grazing incidence X-ray diffraction (GIXRD) has permitted the collection of X-ray powder diffraction patterns from 2D protein crystals at the air-water interface [2], but it must be noted that this technique uses reflected, instead of transmitted X-rays, and thus the typical beam footprint (between 5 and 100 mm^2) is much larger than the average 2D crystal grain size (1 μm^2 for Purple Membrane) resulting in the simultaneous probing of multiple, random oriented, individua 2D crystals. The footprint problem can be overcome taking advantage of Transmission XRD (TXRD), exploiting beam size as narrow as 1 μm^2 [3], while impinging on the sample at normal incidence. An alternative explored in the last few years is Transmission Electron Microscopy (TEM), which has yielded protein structures from 2D crystals from both soluble proteins [4] and membrane proteins [5]. The trend on released protein structure for TEM based technique is currently growing exponentially with the passing years [6]. However, for each of these above mentioned methods, achieving high-resolution structures from 2D crystals can be significantly hindered by radiation damage. Furthermore, the Cryo EM technique requires samples being kept at very low temperature, *i.e.,* far from the functionality temperature and conditions of the protein natural environment. The low temperature condition have high probability to change the arrangement of the protein itself leading to a structure determination (and the correspondent functionality) different from the one possessed by the protein in its natural environment. Furthermore, Cryo EM requires samples being 200 kDa or larger, meaning that small molecules cannot be resolved by this technique. The impossibility of obtaining high resolution data from 2D protein crystals in their natural environment, given the combination of the too low beam intensity of synchrotron facilities, and the unavoidable X-ray radiation damage, is exposed in the following GIXRD and TXRD experiment results. Nevertheless, both GIXRD and TXRD techniques are suitable to reach quite good resolution also from 2D crystals of protein.

The recent commissioning of X-ray Free Electron Lasers (XFELs) exploiting extremely short femtosecond-duration pulses, and having a peak brightness many (~ 10) orders of magnitude greater than synchrotron sources, permits the collection of X-ray diffraction from even smaller samples including 2D crystals [7], and single particles [8] at doses significantly exceeding the normal tolerable room-temperature radiation dose [9], thus theoretically permitting a single-shot Coherent Diffractive Imaging performed before the destruction of the object, with diffraction-limited resolution. This ambitious goal calls for the development of new experimental methodologies [10, 11]. The first attempts to solve the structure of large biomolecules saw the development of serial femtosecond crystallography (SFC) at room temperature, as well as the use of liquid jets for continuous delivery of micro/nano crystals under the FEL beam. The structure is subsequently determined from the collection of many thousands diffraction pat-

terns [12–14]. Time-resolved SFC experiments highlighted photo-induced changes in the electronic structure due to charge transfer, encoded in the diffraction pattern of the microcrystals under examination [15, 16]. Interestingly, serial nano-crystallography has also become feasible, in a cooled environment, with focused beams at synchrotrons [17]. Many experimental tool such as microfluidic devices for protein crystallization and custom chips for on-chip diffraction studies have been developed and demonstrated [18]. One of the main limitations for a broad applicability of SFC is that a very large number of crystals (*i.e.*, thousands) are required to obtain complete data sets. Considering that only a relatively small fraction of successful hits generates useful diffraction patterns, SFC still lacks an easy, reliable and inexpensive way of producing a high number of nanocrystals in order to become a routine analytical tool. The limited access to perfect crystals has been an unsolved problem in protein crystallography for decades, further adding to the difficulty in solving the structure of complex bio-molecules. It is interesting to note that some recent diffraction studies performed on XFEL on imperfect crystals have demonstrated that this is not an insurmountable constraint. The weak continuous scattering arising when the crystals become disordered contains key information to overcome the resolution limits and to solve the tricky phase puzzle [19]. Given the interference nature of diffraction, for time scales comparable with the coherence scales of the sample, the continuously modulated background fully encodes the waves diffracted from individual single molecules. Thus, by using Coherent Diffraction Imaging methods, it is possible to achieve real-space images of macromolecules with higher lateral resolution than what is obtainable by ordinary Bragg diffraction. Coherent Diffraction Imaging methods will be explored deeply in section 6.4. A common feature of all the achievements summarized above is that all the proteins structures solved at synchrotrons or FELs sources are based on the use of 3D crystals. It is interesting to note how, even in the case of *in vivo* room temperature SFC experiments, the protein crystal does not represent the protein in its more natural 2D arrangement. Until now 2D-crystallography has almost exclusively been the area of transmission electron microscopy (TEM). Significant progress in protein structure determination and lipid interaction has been made thanks to the use of cryo-TEM and the development [6, 20, 21] of algorithms for recovering amplitude and phase information from recorded TEM images. Given the reduced amount and fixed-target sample delivery in near-native environment, single-shot 2D protein crystallography with FELs was suggested as an attractive alternative [7] and has been recently demonstrated by proof-of-principle experiments at LCLS. One can also argue that the 2D approach adds the ability to explore protein function and dynamics and it is also an intermediate step towards the extremely ambitious atomic imaging of individual bio-molecules. As in the 3D case, sample preparation is also a crucial step for the 2D counterpart, where fixed-target solutions have to be developed. For 2D cryo-TEM studies, most often the proteins crystals are grown embedded within a lipid bilayer, whereas the first XFEL experiments used dices of silicon nitride windows for harvesting 2D crystals, which are then covered with a thin carbon film. These first experiments indicated that in order to overcome the present resolution limits of 7 Å [22], and truly exploiting the unique XFEL properties, an improvement of both sample preparation, experimental technique, and data analysis is crucial.

Thus, after the GIXRD and TXRD results, we present two techniques that could overcome all the problems listed above, taking advantages of the ultra-fast, ultra-bright and fourier-limited radiation emitted from state of art X-ray FELs. Coherent Diffraction

Imaging (CDI), and lately Incoherent Diffraction Imaging (IDI) [23] from monolayer 2D protein crystals using an XFEL could provide a new approach for structure determination of proteins that fail to readily form macroscopic 3D crystals. In particular, this approach may benefit structure determination of membrane proteins that can be grown into 2D crystals embedded within a lipid bilayer which mimics their native environment and avoids additives used in 3D crystallization, and temperature control, that may perturb the native protein conformation or functionality.

6.2 GIXRD at Elettra

X-ray crystallography has been, and it is nowadays, the leading technique in structural determination of the atomic and molecular structure of a crystal, in which the crystalline structure causes a beam of incident X-rays to diffract into many specific directions. By measuring the angles and intensities of these diffracted beams, a crystallographer can produce a three-dimensional picture of the density of electrons within the crystal. From this electron density, the mean positions of the atoms in the crystal can be determined, as well as their chemical bonds, their crystallographic disorder, and various other information. Since many materials can form crystals *e.g.*, salts, metals, minerals, semiconductors, as well as various inorganic, organic, and biological molecules, X-ray crystallography has been fundamental in the development of many scientific fields. In its first decades of use, this method determined the size of atoms, the lengths and types of chemical bonds, and the atomic-scale differences among various materials, especially minerals and alloys. The method also revealed the structure and function of many biological molecules, including vitamins, drugs, proteins and nucleic acids such as the famous case of the double DNA helix. X-ray crystallography is still the primary method for characterizing the atomic structure of new materials and in discerning materials that appear similar by means of other experiments. X-ray crystal structures can also account for unusual electronic or elastic properties of a material, shed light on chemical interactions and processes, or serve as the basis for designing pharmaceuticals against diseases. Crystals are regular arrays of atoms, and X-rays can be considered waves of electromagnetic radiation. Atoms scatter X-ray waves, primarily through the atoms' electrons. Just as an ocean wave striking a lighthouse produces secondary circular waves emanating from the lighthouse, so an X-ray striking an electron produces secondary spherical waves emanating from the electron. This phenomenon is known as elastic scattering, and the electron (or lighthouse) is known as the scatterer. A regular array of scatterers produces a regular array of spherical waves. Although these waves cancel one another out in most directions through destructive interference, they add constructively in a few specific directions, determined by Bragg's law:

$$2d \sin \vartheta = n\lambda, \tag{6.1}$$

with the magnitude of the momentum transfer $\vec{q}$ being:

$$|\vec{q}| = \frac{4\pi}{\lambda} \sin \vartheta \tag{6.2}$$

Here d is the spacing between diffracting planes, ϑ is the incident angle with respect the diffractive plane, n is any integer, and λ is the wavelength of the beam. These specific directions appear as spots on the diffraction pattern called reflections. Thus, X-ray diffraction results from an electromagnetic wave (the X-ray) impinging on a regular

array of scatterers (the repeating arrangement of atoms within the crystal). Grazing Incidence X-ray Diffraction (GIXRD), typically from a crystalline structure uses small incident angles for the incoming X-ray, so that diffraction can be made surface sensitive. It is used to study surfaces and layers because wave penetration is limited. Distances are in the order of nanometres. Below the critical angle of the surface material studied (typically 80%), an evanescent wave is established for a short distance and is exponentially damped. Therefore, Bragg reflections are only coming from the surface structure. In Powder XRD, the sample is usually in a powdery form, meaning that the crystalline domains are randomly oriented in the sample. Therefore when the 2D diffraction pattern is recorded, it shows concentric rings of scattering peaks corresponding to the various d spacings in the crystal lattice.

Wafers

Two types of substrate dices were used for this work. 0.25 cm^2 squared pure Silicon and a variant consisting of a 10 nm surface gold deposition on the Silicon dice. AFM measurements were carried out on the samples. Silicon showed a roughness (Ra) $\sim$ 1 Å while Golden samples showed a Ra $\sim$ 1.3 nm.

Bacteriorhodopsin

Purple membranes (PM) were purchased from Sigma Aldrich. The two-dimensional crystals were washed with water and suspended in 0.5% (w/v) glucose to a final protein concentration of 0.5 mg/ml just before application onto the sample carrier for X-ray diffraction data collection and let them dry in a visible light-deprived environment.

Methods

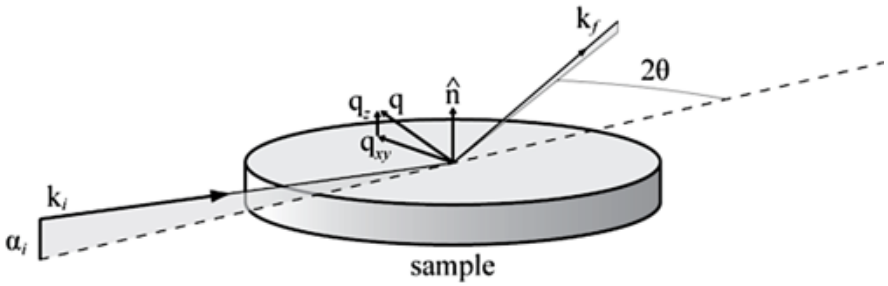

Figure 6.1: *Schematic representation of the GIXRD layout.*

GIXRD measurements were performed at the X-ray Diffraction beamline 5.2 at the Synchrotron Radiation Facility Elettra in Trieste (Italy). The X-ray beam emitted by the wiggler source on the Elettra 2 GeV electron storage ring was monochromatized by a Si(111) double crystal monochromator, focused on the sample and collimated by a double set of slits giving a spot size of 200 $\times$ 200 μm^2. The beam wavelength was monochromatized at 1 Å. The samples were oriented by means of a four-circle diffractometer with a motorized goniometric head. The X-ray beam direction was fixed, while the sample holder could be rotated about the different diffractometer axes, in order to reach the sample surface alignment in the horizontal plane containing the X-ray beam by means

of laser light reflection. Subsequently it was possible to rotate it around an axis perpendicular to this plane or, alternatively, vary the angle between beam and surface (angle of incidence).

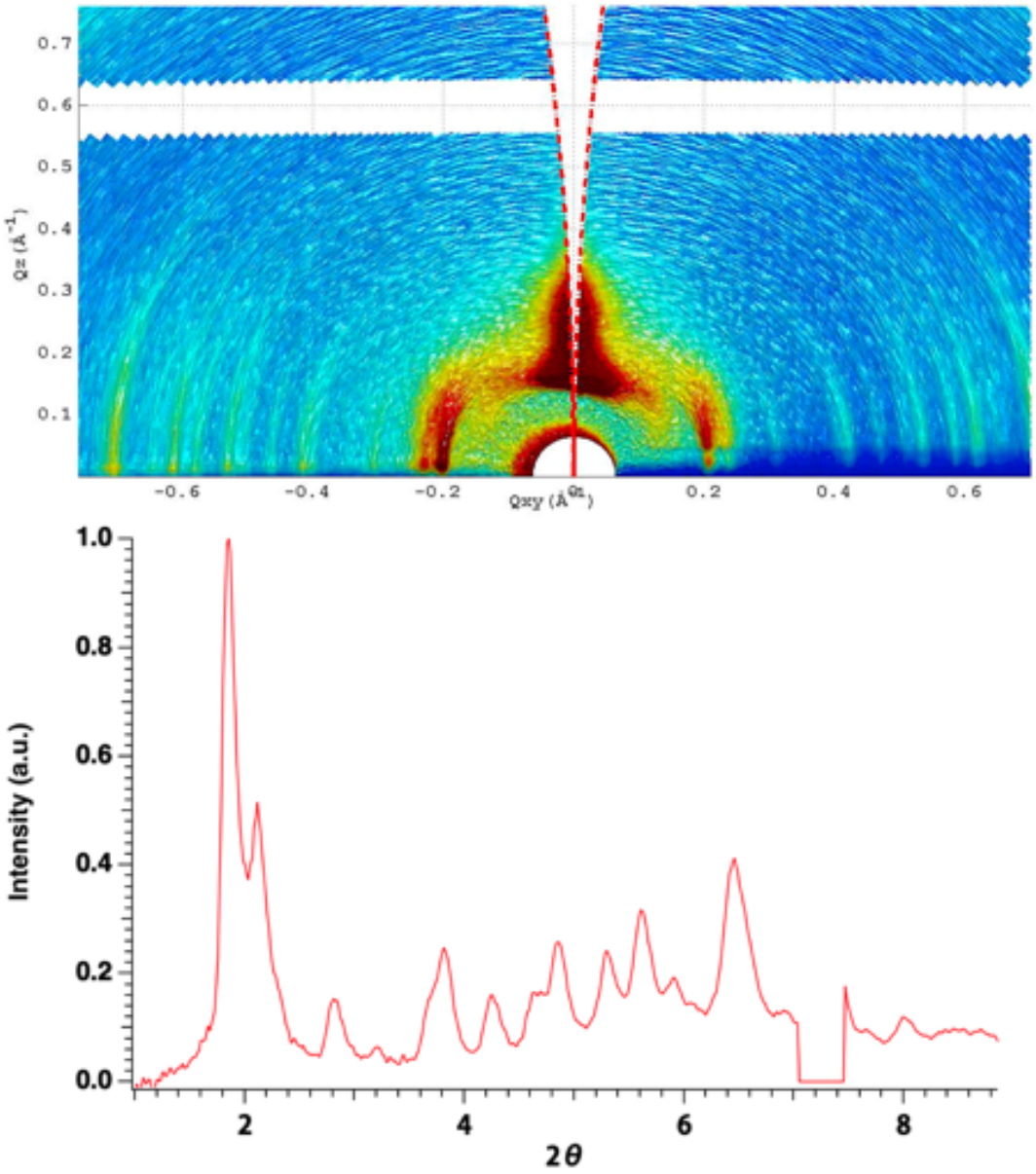

Figure 6.2: *Top - GIXRD from a powder-like disposition of bR single crystals. Bottom - the integrated trace over a circle. The trace presents a peak to a resolution equal to 7.00* Å.

Bidimensional diffraction patterns were recorded with a 2M Pilatus silicon pixel X-ray detector (DECTRIS Ltd., Baden, Switzerland) positioned perpendicular to the incident beam, at a distance of 350 mm from the sample. The sample inclination to the beam was kept as close as possible to the zero, in order to avoid interference of diffracted beams with the signal given by sample reflectivity. A scan of the whole sample width in the transversal direction was performed, at steps equal to beam dimension (200 μm), with an exposition time of 2 seconds per step. The long exposition time was required to obtain a significant signal, thus leading the sample (and conseguently part of the signal)

to be radiation damaged. Patterns were calibrated by means of a LaB_6 standard and integrated using the software fit2d [24] obtaining several series of powder-like patterns, corrected for geometry, Lorentz and beam polarization effects. The 2ϑ range spanned from 0.1 Å to 8.27 Å, with resolution reaching 7.14 Å. Peaks positions and FWHM were extracted by means of the program Winplotr [25]. Cell parameters and space group were already known from literature, and allowed to employ both representation (Mercury, CheckCell [26]) and X-ray diffraction pattern simulation (simDiffraction) [27] programs. It was then possible to find that the arrangement of the molecules on the surface corresponded to (a,b) plane (*i.e.*, $c = 0$ for every peak, see figure 6.4), coherently with literature findings. In the best case, enough peaks were detected to allow the employ of WAXX software [28] of peak profile analysis for the characterization of sample crystallinity.

Results & Conclusions

Initially, the diffraction patterns were overlaid with expected lattice positions calculated from assumed unit-cell parameters of $a = b = 62.45$ Å, $c = 100.9$ Å, and $\alpha = \beta = 90°$, $\gamma = 120°$ with $P3$ symmetry for bacteriorhodopsin. These unit-cell parameters were derived from both transmission electron microscope data of similarly prepared samples and from previous publications [2, 29, 30]. The expected lattice unit-cell parameters for an untilted crystal closely matched the observed reflections and were used as a local marker for subsequent peak searches [31, 32]. X-ray diffraction patterns from two-dimensional (2D) protein crystals obtained using synchrotron X-ray are presented. Bragg diffraction was acquired to better than 7.14 Å resolution for Bacteriorhodopsin protein crystal samples maintained at room temperature. Given the size of the focused beam, thousands of times bigger than the typical size of a bR crystal ($0.5 - 1.0$ μm [33]), we concluded that, given the random orientation of the bR crystals in an area equal to the beam size, we can only expect a powder-like ring patter. This makes, as attended, the GIXRD technique not sensitive enough to probe a single crystal structure. This results remarks the limitation of synchrotron based GIXRD on room temperature biological sample in a natural-like environment. This potential barrier, as we are seeing in the following, can be overcame exploiting the potential of Free Electron Lasers.

6.3 TXRD at PETRA III

Given the previous results, we focused our attention on the state of art of biological sample XRD facility, by submitting a proposal at the P11 endstation at PETRA III in Hamburg (Germany). The Bio-imaging and diffraction beamline P11 at PETRA III is dedicated to imaging and diffraction experiments of biological samples. The basic idea for the beamline design is to provide an extremely stable and flexible setup ideally suited for micro- and nano-beam applications. Here we designed the experiment to be a Transmission XRD, instead of being a Grazing Incidence one.

Wafers

The sample holder had been modified consequentely. A silicon chip with an area of 25×25 mm and 200 μm thickness, produced by Silson Inc., was used as a carrier. The chip had a 44×44 array of 100×100 μm windows made of a 20 μm thick Si_3N_4 membrane (see figs. 6.3 top)). A total of about 30 μl of two-dimensional bR crystal suspen-

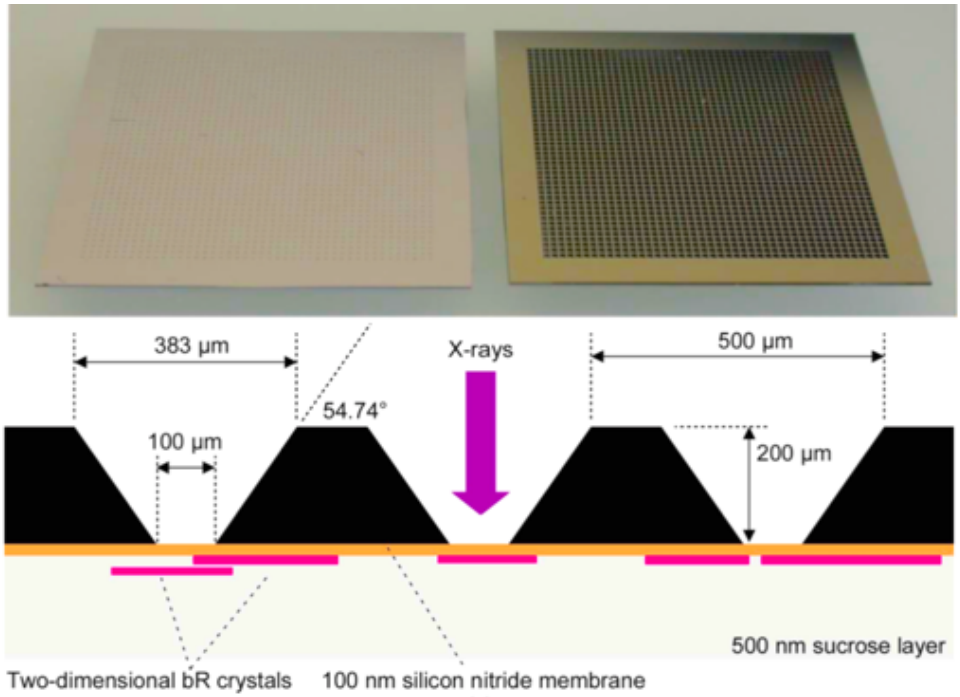

Figure 6.3: *Sample support. (a) Sketch of the chip carrying the two-dimensional bR crystals (the membrane thickness is not to scale). (b) Picture showing the two faces of the chip, with the face encountered by the incoming X-ray beam on the right.*

sion was deposited onto the silicon chip and allowed to dry in air. The resulting glucose layer served to protect the protein sample from dehydration.

Bacteriorhodopsin

Purple membranes (PM) were purchased from Sigma Aldrich. The two-dimensional crystals were washed with water and suspended in 0.5% (w/v) glucose to a final protein concentration of 0.5 mg/ml just before application onto the sample carrier for X-ray diffraction data collection and let them dry in a visible light-deprived environment. A schematic layout of the bR protein onto the Silicon chip is shown in figure 6.3.

Methods

TXRD measurements were performed at the Bio-Imaging and Diffraction beamline (P11) at PETRA III facility in Hamburg (Germany). The P11 X-ray optics consist of a LN_2 cooled double crystal monochromator and two horizontal deflecting and one vertical deflecting X-ray mirror. All three mirrors are dynamically bendable and were used to generate an intermediate focus at 65 m from the source with a size of 4×9 μm^2 rms ($v \times h$). The beam wavelength was monochromatized at 1 Å. The samples were positioned vertically with respect to the ground, and perpendicular to the incoming X-ray beam. The X-ray beam direction was fixed, while the sample holder could be rotated around the orizonthal axes, in order to reach the sample surface alignment in the horizontal plane containing the X-ray beam by means of laser light reflection. Bidimensional diffraction patterns were recorded with a 6M Pilatus Silicon pixel X-ray detector (DECTRIS Ltd., Baden, Switzerland) positioned perpendicular to the incident

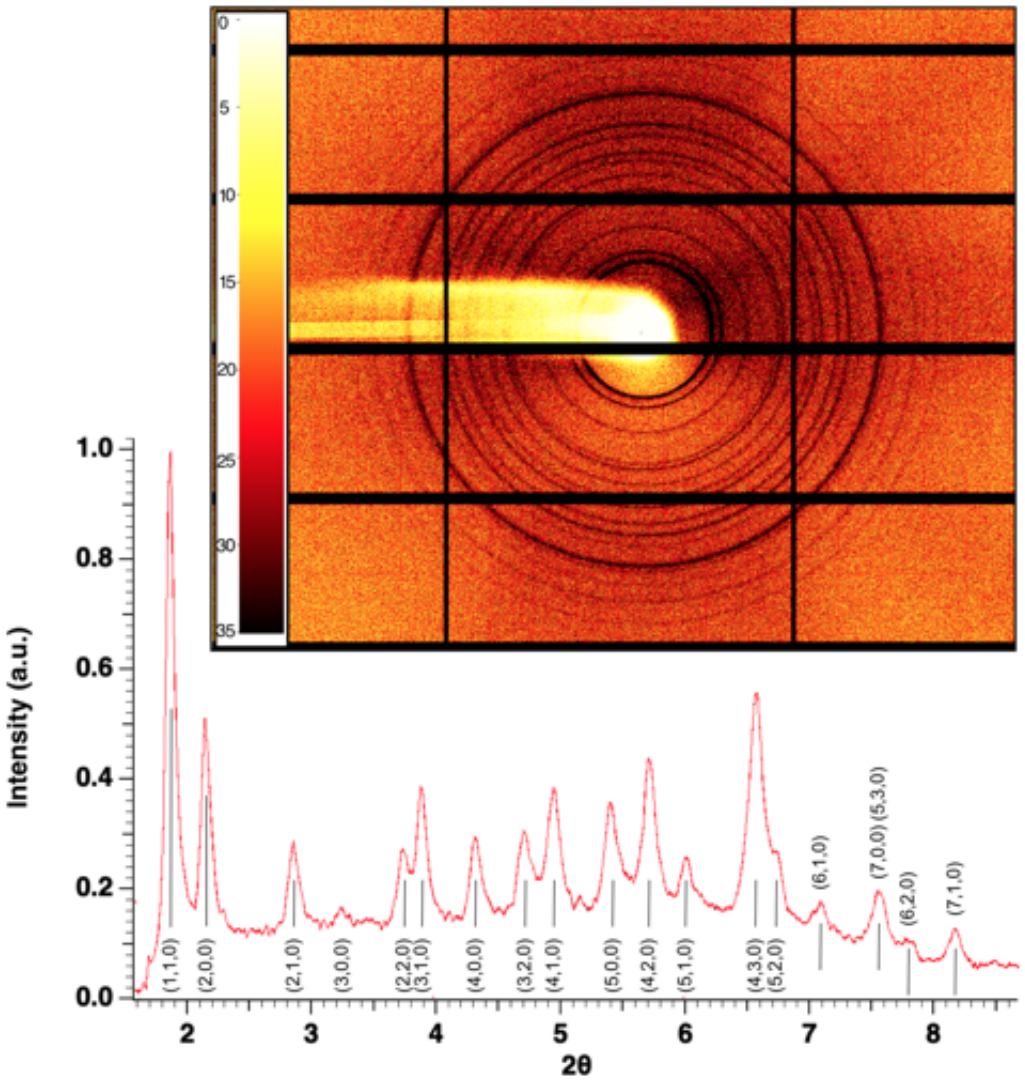

Figure 6.4: *Top - Transmission XRD from a powder-like disposition of bR single crystals. Bottom - the integrated trace over a circle. Miller index notation suggest the different diffraction planes. The trace presents a peak to a resolution equal to 7.00* Å.

beam, at a distance giving a 2.59 Å resolution at the edge of the detector. A scan of each windows width in both the transversal and longitudinal directions was performed, at steps equal to double the beam dimension (20 μm), with an exposition time of 0.1 seconds per step. This value seemed to be the best compromise for this measurement, considering the need of an exposition time long enough to produce a significant signal, together with the requirement of having the shorter possible exposition time due to radiation damage. Patterns were calibrated by means of a LaB_6 standard and integrated using the software fit2d [24] obtaining several series of powderlike patterns, corrected for geometry, Lorentz and beam polarization effects.

Results & Conclusions

X-ray diffraction patterns from the 2D bR protein crystals, obtained using synchrotron X-ray are presented. Bragg diffraction was acquired to better than 7.00 Å resolution for

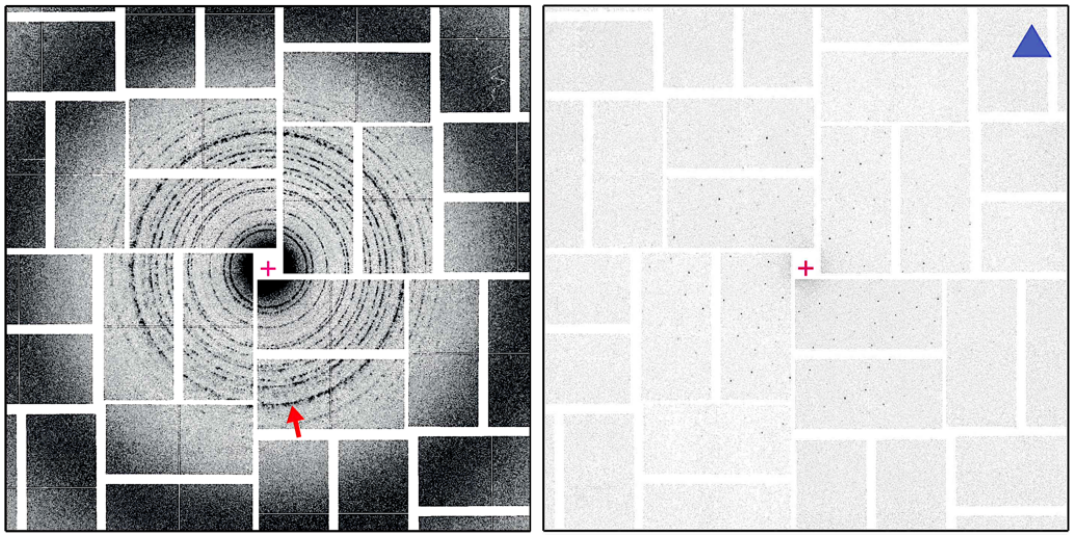

Figure 6.5: *Coherent XRD from a multi-layer of single crystal of Rhodopsin (on the left) and from a single crystal (on the right). The achieved resolution,* 7.00 Å *equals the resolution obtained in the TXRD experiment performed at PETRA III. Image adapted from [22]*

Bacteriorhodopsin protein crystal samples maintained at room temperature. The size of the focused beam, being $4 \times 9\ \mu m^2$ (rms), is $\sim 30 - 40$ times bigger than the typical protein crystal size ($\sim 1.0\ \mu m^2$ [33]), we concluded that, given the random orientation of the bR crystals in an area equal to the beam size, it was very likely to expect a powder-like ring patter. Nevertheless, following the work of C. M. Casadei et. al. [22], we also expected regions of the sample presenting a single crystals of the bR protein on areas larger than $\sim 1\ \mu m^2$ (see figure 6.5), condition that, given the high number of acquisitions, should have been present during our collection of spectra at least for low protein concentration. Our lack of data from single bR crystal suggests that the technique is not sensitive enough to such a single crystal structure. This results shows the limitation of even the state of art of synchrotron based XRD on room temperature biological sample in a natural-like environment. This result underlines the same conclusions as before, with the high resolution structural analysis of proteins arranged as 2D crystals, based on synchrotron facilities, requiring cryogenic conditions [34] or the formation of three-dimensional crystals. But again, this barrier, as we are seeing in the following, can be overcame exploiting the potential of Free Electron Lasers.

Coherent and Incoherent X-ray Diffraction Imaging

In this section we are going to highlight the techniques leading the state of art of protein structure research using FELs. Following a brief introduction on the subject, we present a new approach based on self-assembled monolayer of proteins probed through X-ray Diffraction Imaging. With the advent of FELs, it has been possible to produce the very short, ultra bright and coherent pulses in a range of wavelengths compatible with the intra-atomic bonds. The combination of these factors opened new possibilities in the molecule and protein structure fields *i.e.,* the development of promising techniques such as Coherent X-ray Diffraction Imaging (CXDI) and, lately, Incoherent X-ray Diffraction Imaging.

6.4 Coherent X-ray Diffraction Imaging

Since Miao experimentally demonstrated Coherent X-ray Diffraction Imaging (CXDI) with synchrotron radiation light source in 1999 [35], the structure determination using X-rays has been extended from crystalline to non-crystalline samples, thus ideally overcoming the crystallization problem [36–39]. CXDI is a relatively novel imaging method that can produce an image of a sample without using optics in between the sample and detector (for a clear visualization of the CDI technique, see fig. 6.6). This differs from conventional microscopy schemes which, instead, use objective lenses to produce an image of a given object. Taking into account the difficulties of producing highly resolving and efficient lenses in the hard X-ray regime, we clearly see the advantages of so-called lensless microscopy techniques. Many demonstrations of CXDI at synchrotron sources on non-biological samples have been made [35, 39, 40]. Due to the lack of resolution limiting optics and the penetrative ability of X-rays, this imaging technique ultimately offers new insights into the structure of intact, three-dimensional (3D) biological specimens.

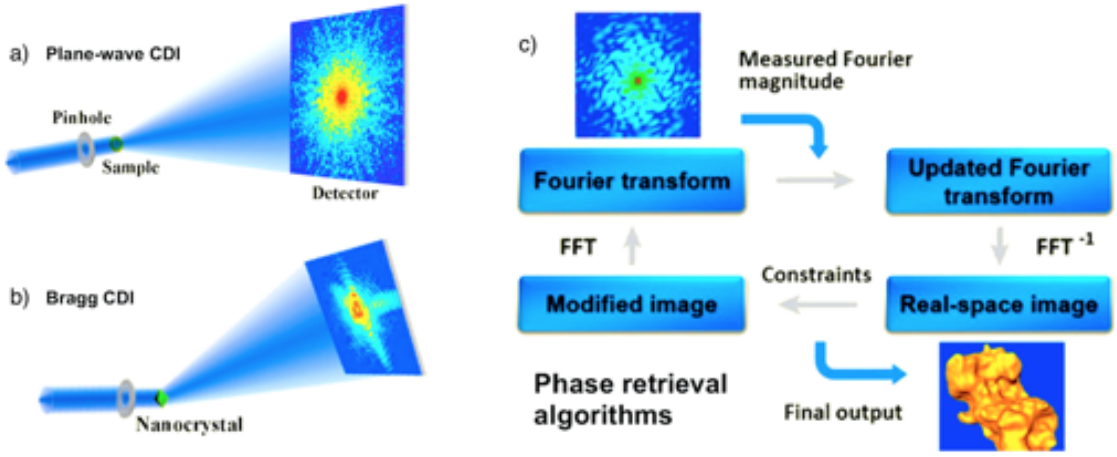

Figure 6.6: *Schematic layout of two CDI methods, and of the iterative phase retrieval algorithm. (a) Plane-wave CDI: This is the classic approach where a plane wave illuminates a sample, and an oversampled diffraction pattern is measured by a detector. (b) Bragg CDI: The diffraction pattern surrounding a Bragg peak is acquired from a nanocrystal, this is the variation required for our 2D crystals. Many other approaches to this technique such as Ptychography. Fresnel CDI, and Reflection CDI can be explored at [41]. (c) Phase retrieval algorithms iterate back and forth between real and reciprocal space. In each iteration, various constraints* (e.g., *the sample support, positivity* (i.e., *electron density cannot be negative), or partially overlapping regions) are enforced in real space, while the measured Fourier magnitude is updated in reciprocal space. Usually, after thousands iterations, the correct phase information can be recovered. Image adapted from [41]*

While conventional X-ray imaging of biological specimens at synchrotron sources [42] suffers from radiation damage [43], which limits the resolution of the resultant images, breaking this resolution limit may be possible by the use of ultrabright, ultrashort pulses from FELs. Indeed, one of the key goals of CXDI is to image beyond the conventional damage limit using these pulses of X-ray FEL radiation. If these pulses are short enough they may scatter from the specimen before it is destroyed by this pulse [8]. Structural information of the undamaged sample will be measured and reconstructed to produce an image of the object at a resolution higher than that typically obtained from conventional X-ray sources. To date, many facilities (*e.g.*, LCLS [44], SwissFEL

[45], and European XFEL [46]) demonstrated the feasibility of the production of reproducible sub-fs pulses in the X-ray regime with an intensity ranging between $10 - 30\ \mu J$.

The conventional CXDI experiment is performed with an isolated sample illuminated by a coherent, plane wave (see figure 6.6). The incident wave may be described by a complex valued field of uniform magnitude and phase. The radiation interacts with the sample, which affects both the amplitude and phase of this field. This scattered radiation, or exit-surface wave (ESW), from the sample propagates to a two-dimensional detector in the far-field from the sample and the diffracted intensities are measured. These diffracted intensities alone are insufficient to determine the exit-surface wave, since the phase information is lost during the measurement process (the measured quantity is intensity and not the complex amplitude). However, with some additional knowledge of constraints to be applied on the sample in the real space, the ESW from the sample can be reconstructed using phase retrieval algorithms based on an iterative approach [47–49]. More formally, during a diffraction experiment, we measure the scattered intensity $I_{sc}(\vec{q})$ which is directly proportional to the modulus squared of the single molecular form factor $F(\vec{q})$,

$$I_{sc}(\vec{q}) \propto |F(\vec{q})|^2. \tag{6.3}$$

The single molecular form factor can be represented as the summation of the scattering from all the atoms (index as j) of the molecule [50]:

$$F(\vec{q}) = \sum_j f_j(q) e^{-i\vec{q}\cdot\vec{r}_j} \tag{6.4}$$

where $f_j(q)$ is the atomic form factor of j^{th} atom, $\vec{q}$ is the scattering vector, $\vec{r}_j$ is the position vector. The molecular composition (f_j) and structure ($\vec{r}$) of molecule from single crystal diffraction can be found in Protein Data Bank (PDB). Then, the electron density map $\rho(\vec{r})$ of the model can be retrieved by the inversed Fourier transfer, that is:

$$\rho(\vec{r}) = \int_{-\infty}^{\infty} F(\vec{q}) e^{i\vec{q}\cdot\vec{r}} d\vec{q}. \tag{6.5}$$

It must be noted that the amplitude $F(\vec{q})$ is fully complex, while we can only measure its modulus squared, which is a real number. Here, of course, lies the phase retrieval problem. In general the inverse Fourier transform of $F(\vec{q})$ is not the electron density, but rather the ESW of the sample, however in the weak scattering case this reduces to the projection of electron density. The image reconstruction process begins with assigning random phases $\phi(\vec{q})$ to the known magnitudes in reciprocal space. This far-field wave-field, $A'(\vec{q}) = |F(\vec{q})|e^{i\phi(\vec{q})}$, is then inverse Fourier transformed to real space giving the first guess of the ESW, $s'(\vec{r})$. This first guess will look wholly unlike the correct ESW and constraints in the object space, most importantly the finite extent of the object, are applied to this guess. This typically involves setting the values of $s'(\vec{r})$ to zero outside some boundaries, known as the Error Reduction (ER) method, or forcing them towards zero, most commonly known as the Hybrid Input-Output (HIO) method [48]. After the constraints have been applied, the function, $s(\vec{r})$, is then Fourier transformed to the far-field. This new far-field guess then has its magnitude, $|A(\vec{q})|$, replaced by the measured amplitudes $|F(\vec{q})|$ while now the phases, $\phi(\vec{q})$, are kept. This process is then iterated over for typically thousands of iterations until it converges. The resulting function $s(\vec{r})$ is the exit-surface wave of the sample, and may be interpreted in terms of the physical properties of the sample. A necessary condition for the successful reconstruction of the ESW from a diffraction pattern is the appropriate sampling of that pattern

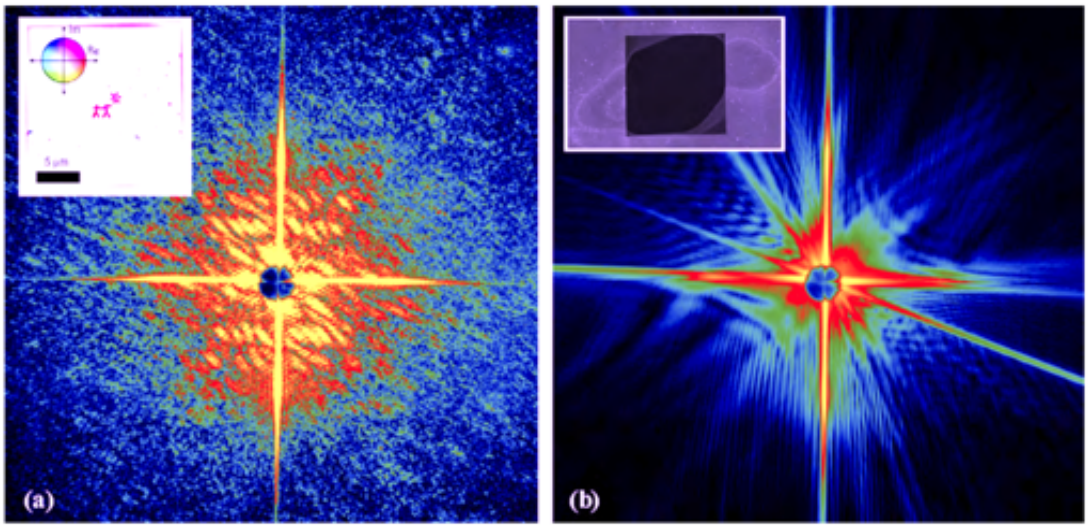

Figure 6.7: *a) Diffraction pattern produced from a single pulse of FEL radiation at FLASH. (Inset) A reconstruction of the complex image from this single pulse data. b) A subsequent diffraction pattern taken 20 seconds after (a). (Inset) an SEM image of the sample after exposure, showing its destruction due to the FEL beam. Image adapted from [54].*

[51]. A useful experimental rule is that at least two measurement points per fringe in the diffraction pattern are required for adequate sampling. This means that the auto-correlation function of the data is correctly sampled according to Shannon' sampling theorem [52]. This essential sampling consideration leads this method to be sometimes referred to as the oversampling method. The oversampling ratio should be taken care according to the size of the sample for the reconstruction. If we define the size of the object as W, the oversampling ratio σ can be calculated as [53];

$$\sigma = \frac{\lambda L}{\Delta x W} \tag{6.6}$$

where λ is the wavelength of X-ray beam, L is the distance between sample and detector, and Δx is the pixel size. Given the Shannon' sampling theorem, when σ is larger than 2, the phase problem can be solved. A larger value of oversampling can help to reach a converged solution.

The first experimental demonstration of a single pulse CXDI experiment at an FEL was shown in 2006 [54] (see figure 6.7). The experiment was performed with a 32 nm wavelength and a 25 fs pulse duration. Subsequent investigation demonstrated that the first pulse that hit the sample destroyed it. However, we clearly see in fig 6.7 that the information regarding this sample, up to a resolution of 62 nm, was recorded before the destruction of the sample. This proof-of-principle experiment, on a test sample, alludes towards the possibility of the single bio-molecule experiment being possible. Despite the initial sparkles of joy, a single molecule will produce only a very weak signal from even the brightest of FEL pulses. Simulations [53] showed that an increase of, at least, three order of magnitude of flux in the XFEL beam is necessary in order to achieve a nm resolution for biological particles. To partially overcome the flux limitation, a number of reports have addressed the enhancement of CXDI image using some forms of heavy X-ray scatters for weak objects [55]. Heavy elements, however, can possibly change the structure of a molecule. One way to overcome this difficulty is to use 2D or 3D peri-

odic samples to increase the signal diffracted from each unit for a given single pulse photon flux. Many proteins, including the purple membrane, form two-dimensional crystals rather than three-dimensional crystals [56]. The diffraction pattern produced from a two-dimensional crystal is amenable to a CXDI analysis as it has been demonstrated recently for non-biological specimen [57], while it as been demonstrated non yet feasible for a 2D bR crystal [22], given the very low photon counts in between Bragg spots.

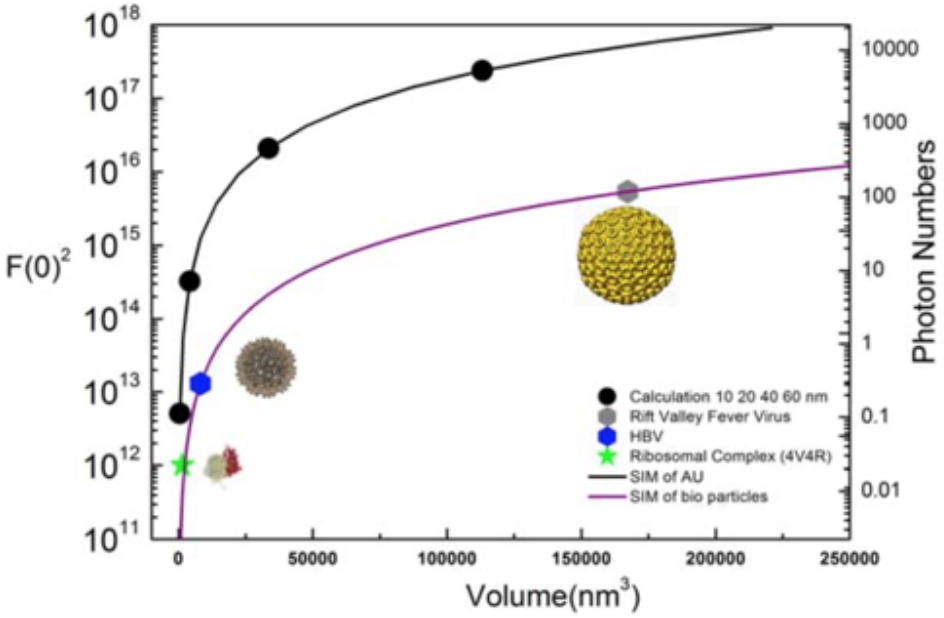

Figure 6.8: *The master curve of volume (in term of nm^3) vs. scattering intensity $F(0)^2$,* i.e., *the particle form factor at $q = 0$, and the equivalent number of scattered photons. Image adapted from [53].*

However, the resolution limitation is mainly resulted from insufficient photon flux at current XFEL facilities. As can be seen from figure 6.9, a photon-flux master curve of particle detection is generated from single shot computer simulation of different biological particles in Protein Data Bank and EMDataBank. The master curve can be applied to estimate scatted X-ray intensity and guide the design of CXDI experiments [53]. To conclude, even if promising for the near future, this technique applied to small biological samples such as proteins in natural environment, requires a photon flux on the sample several orders of magnitude higher than the most powerful one produced by current XFELs.

6.5 Incoherent X-ray Diffraction Imaging

As the reader saw in section 6.4, in CXDI it is assumed that a fixed phase relation between the incoming and scattered photons exists and this coherence of the radiation field is maintained throughout the imaging procedure. This produces a stationary interference pattern upon measurement of large numbers of photons. Incoherence induced by, *e.g.*, time dependent distortions of the wavefront or incoherent scattering processes such as fluorescence emission and Compton scattering, is generally viewed as obstacles in this approach, since these scattered photons, averaged on a large number of spectra, generate a constant intensity distribution producing a background that reduces the fi-

delity of CXDI measurements [58–60]. The situation changes fundamentally if the photons are recorded within their coherence time τ_c, *i.e.*, a time interval short with respect to the temporal phase fluctuations of the radiation field. Over such short times, the relative phases of the scattered photons can be considered stable, allowing the observation of a stationary fringe pattern. Of course, the pattern will spatially fluctuate over times longer than τ_c, however the autocorrelation of the intensity distribution calculated shot-by-shot is insensitive to the spatial pattern variations and will continuously build up when averaging over many short measurements. In 2017, A. Classen *et. al.* [23] proposed a new approach, which they called Incoherent Diffraction Imaging (IDI), exploiting that intensity correlations of incoherently scattered photons can be used to determine the 3D arrangement of atoms in crystals and molecules. For example, in the case of K-shell fluorescence photons from transition metal atoms, the coherence time is given by their radiative lifetime (for Fe atoms $\tau_c = h/\Gamma = 2.6\ fs$ for a linewidth of $\Gamma = 1.6\ eV$ [61]). Excitation of the atoms with femtosecond pulses from current X-ray FELs and measurement of the scattered radiation shot-by-shot fulfill the condition of a fixed phase relation for each exposure and can be applied to derive the 3D structure of the fluorescing atoms with atomic resolution. This approach, opens fundamentally new strategies for X-ray structure determination based on the measurement of incoherent radiation. It must be noted that transitions stimulated by X-rays for light elements such C, N, being the vast majority of the atoms present in biological sample, possess a line shape (and consequently a lifetime) of core-excitation spectra which is the result of a number of distinct processes, reflecting properties of both the atom and its environment. Generally speaking, the natural lifetime width Γ increase for larger molecules [62]. For the IDI approach, they considered incoherently scattered photons originating from the sample. For the mathematical derivation of the intensity correlations, they used a quantum mechanical treatment defining the far field, the positive frequency part of the operator of the outgoing electric field propagating in the direction $\vec{k}$ reads

$$\hat{E}^{(+)}(\vec{k}) = \left[\hat{E}^{(-)}(\vec{k})\right]^{\dagger} = \sum_i e^{i\vec{k}\vec{r}_i} e^{i\phi_i} \hat{a}_i \tag{6.7}$$

where the incoherence of the emission process is incorporated by the randomly and independently varying phases $\phi_i \in [0, 2\pi]$, while $\hat{a}_i$ denotes the annihilation operator for a photon coming from the emitter i. Measuring the first order correlation function $g^{(1)}(\vec{k}_1, \vec{k}_2) \propto G^{(2)} = \langle \hat{E}^{(-)}(\vec{k}_1)\hat{E}^{(+)}(\vec{k}_2)\rangle$ result to be hard even for macroscopic objects in the visible and entirely impractical in the X-ray regime. Considering the spatial (equal-time) second-order intensity correlation function $g^{(2)}(\vec{k}_1, \vec{k}_2)$, that is

$$g^{(2)}(\vec{k}_1, \vec{k}_2) = \frac{G^{(2)}(\vec{k}_1, \vec{k}_2)}{I(\vec{k}_1) I(\vec{k}_2)} \tag{6.8}$$

where $I(\vec{k}_i)$ is the intensity measured on the detector in the direction $\vec{k}_i$, and $G^{(2)}(\vec{k}_1, \vec{k}_2) = \langle \hat{E}^{(-)}(\vec{k}_1)\hat{E}^{(-)}(\vec{k}_2)\hat{E}^{(+)}(\vec{k}_2)\hat{E}^{(+)}(\vec{k}_1)\rangle$, it is possible to demonstrate that

$$g^{(2)}(\vec{k}_1, \vec{k}_2) \propto \left| \frac{F(\vec{q})}{F(0)} \right|^2, \tag{6.9}$$

where $\vec{q} = \vec{k}_2 - \vec{k}_1$ now refers to the difference between the two outgoing wave vectors $\vec{k}_2$ and $\vec{k}_1$. This shows that the measurement of the second-order intensity correlation function gives indeed access to the 3D Fourier magnitudes $|F(\vec{q})|^2$ .The 3D structure of

the arrangement of the emitting species in real space can then be reconstructed by using again well-known phase retrieval algorithms from CDI or crystallography. IDI based on second-order intensity correlation measurements bears several advantages with respect to CDI. The atomic cross section of incoherent fluorescence emission is generally significantly larger than the coherent one, producing higher signals compared to CDI. Furthermore, incoherent fluorescence emission displays a uniform angular distribution. This is unlike conventional crystallography or single-particle CDI where the coherently scattered intensities generally follow a $q^{-\beta}$, with $\beta \in [3,4]$ [63], dependence for small $|\vec{q}|$ values, *i.e.*, at low resolutions. In addition, considering crystals, the coherently scattered signal is concentrated into Bragg peaks. Both of these features require a high dynamic range of the detectors, which can limit the achievable resolution. By contrast, IDI does not require high dynamic range measurements, and it is as easy to measure $q = 0$ (auto correlation of each pixel) as it is to measure any other value up to the largest difference of wavevectors captured by the detector. Aside from providing simple access to larger

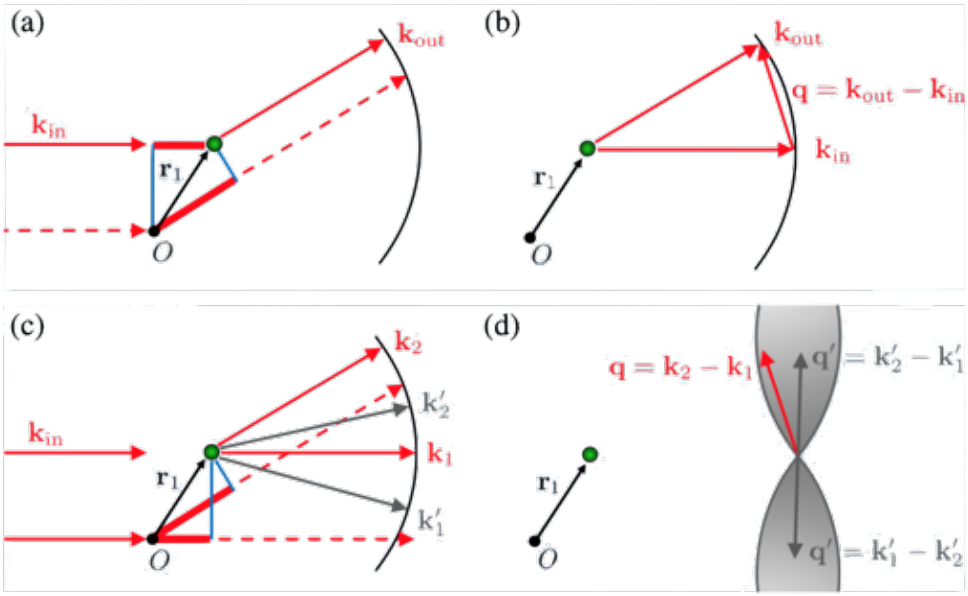

Figure 6.9: *(a) Phase acquired by a photon with wave vector $\vec{k}_{in}$ upon coherent scattering by an atom at $\vec{r}_i$ into direction $\vec{k}_{out}$, relative to scattering by an atom at the origin. (b) Corresponding Ewald sphere construction using the photon momentum transfer $\vec{q} = \vec{k}_{out} - \vec{k}_{in}$. The black arcs in (a) and (b) represent the angular extent of a detector in the far field and the 2D Ewald sphere coverage in 3D Fourier space, respectively. (c),(d) Phase difference between two photons incoherently scattered by an atom at $\vec{r}_i$, one into direction $\vec{k}_2$ and the other one into direction $\vec{k}_1$, relative to an atom at the origin. The incoming wave does not transfer any photon momentum on the outgoing wave. However, intensity correlations between outgoing wave vectors pairs,* i.e., *$(\vec{k}_i, \vec{k}_j)$, induce momentum transfers equal to $\vec{q} = \vec{k}_j - \vec{k}_i$, which contain information about the object. The consequence is that the coverage of $\vec{q}$ values in the Fourier space reaches out twice as far with respect to common detector geometries. Image adapted from [23].*

$\vec{q}$, IDI also doubles the accessible range in Fourier space compared to CDI for the same experimental geometry. This can be easily seen since all combinations $\vec{q} = \vec{k}_2 - \vec{k}_1$ accessible by the pixels of the detector build up the observable region in Fourier space, and the largest $\vec{q}$ vector reaches out twice as far as in CDI for common detector geometries as shown in figure 6.9. Furthermore, IDI leads to volumetric 3D information in Fourier space for a single sample (or detector) orientation, which means that only

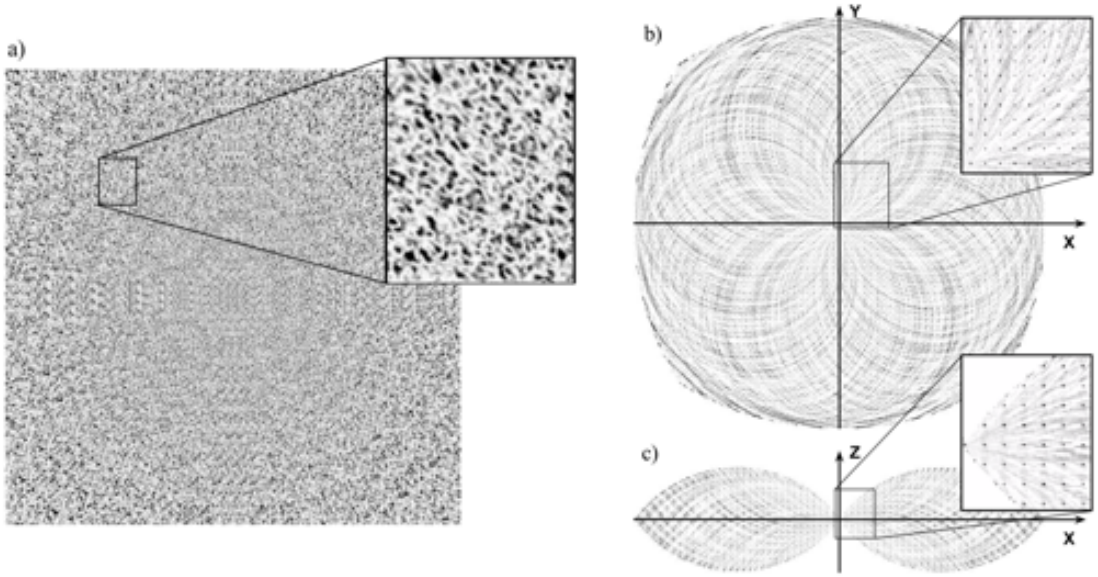

Figure 6.10: *Simulation of a mono-atomic cubic crystal with* $10 \times 10 \times 10$ *unit cells and a single fluorescing atom per cell showing Bragg peaks in the IDI signal. a) Intensity distribution on the detector resulting from a single* $\leq 2.6\ fs$ *XFEL excitation pulse. The inset shows random speckles with no indication that the object is periodic. b) and c) Orthogonal slices through the* $\vec{q}$*-space intensity autocorrelation. The insets show Bragg peaks corresponding to the lattice constant of the crystal. Image adapted from [23].*

a few orientations need to be measured to fill the full 3D Fourier space. In contrast, CDI requires fine angular sampling of the probe to build up sufficient completeness. Therefore, amazingly, atomic resolution can be achieved in IDI already with moderate X-ray photon energies and for very few orientations. In addition, since the number of $\vec{q}$ vectors obtained from a single frame scales as the square of the number of pixels, binning the resulting $\vec{q}$ vectors into a 3D grid results in a large amount of statistics from only a few images, as is well-known from 2D speckle pattern recognition [64]. In order to obtain $g^{(2)}$ signals with high visibility, the detection time should be on the order of (or below) the coherence time τ_c of the photons emanating from the sample. It is the virtue of IDI based on fluorescence emission that the detection time can be intrinsically replaced by the natural time-gating capability of ultrashort X-ray FEL pulses, where the detector needs merely to discriminate between individual pulses, and data acquisition needs to keep up with the pulse repetition rate. Typical pulse durations at current X-ray FEL facilities are on the order of 50 fs in the high bunch-charge mode, whereas low bunch-charge modes already enable pulse sub-fs durations [44–46]; this is already shorter than, *e.g.*, the radiative lifetime $\tau_c = 2.6\ fs$ of the K_α fluorescence in Fe atoms. Note that good statistics can be achieved rapidly due to the extreme brilliance and high pulse repetition rates of current X-ray FEL facilities. For example, the European XFEL is expected to produce 27000 pulses per second, where for IDI, a few hundred images may already suffice to obtain high-quality 3D diffraction data, corresponding to sub-second data acquisition times. We point out that the method also works with pulse durations $> \tau_c$, leading, however, to a reduced contrast of the $g^{(2)}$ signal [65]. The latter scales with the ratio of coherence time to time resolution resulting from the integration over independent temporal modes, where correlations of photons of the same mode lead to interferences, whereas correlations of photons of different modes add to the offset.

However, the reduced visibility can be overcome by averaging over more exposures in order to obtain a sufficient signal-to-noise ratio (SNR) in the underlying diffraction pattern.

This technique build up impressive expectations which are matched by simulations. A small crystal with $10 \times 10 \times 10$ unit cells and a single fluorescing atom per cell in a micro-focused X-ray beam has been simulateded (see fig. 6.10). A 1745×1745 pixel detector with 0.11 mm pixel size was placed 70 mm from the interaction point. Figure 6.10 a) displays the single shot intensity distribution from a short $\leq 2.6\ fs$ pulse on the detector, and figs. 6.10 b) and c) show orthogonal slices through the reciprocal-space intensity autocorrelation evaluated from this single image. In the simulation, the interference from spherical waves with random initial phases from each atom was calculated on each pixel and the intensities were Poisson sampled, where the mean number of photons on the entire detector was $1.7 \cdot 10^7$ (which corresponds to a 0.15 mJ, 7.2 keV XFEL pulse focused to $1 \times 1\ \mu m^2$ incident on a $1\ \mu m^3$ ferredoxin protein crystal [66]). Even though the intensity distribution on the detector does not seem to contain any information, the intensity autocorrelation depicted in figs. 6.10 b) and c) shows significant Bragg peaks related to the crystalline order of the sample just from the single exposure. For lower intensities, Bragg peaks may not rise above noise from the evaluation of a single shot, but averaging over many exposures will rapidly increase the SNR. For the reconstruction of the object, the Bragg peaks in figs. 6.10 b) and c) clearly provide sufficient SNR for peak finding and then indexing, which is facilitated by the volumetric 3D patterns as compared to 2D Ewald sphere patterns. Full 3D coverage in reciprocal space can be obtained by merging intensity correlation diffraction patterns from a few different orientations. Note that, as in CDI, the effect of the finite pixel size is to reduce contrast due to convolution of the reciprocal-space patterns by the (autocorrelation of the) pixel response function. Thus, to achieve maximum contrast, the condition $4\vartheta W \leq \lambda$ should be fulfilled, where ϑ is the angular extent of a detector pixel seen from the sample, and W is the size of the illuminated region. Finally, we note that fluorescence-based IDI enables element-specific imaging where, by use of appropriate energy filters, different species in the same or different molecules can be selectively resolved. As such, IDI can be combined with CDI, where IDI is recorded at a scattering angle of 90° (where stray light and coherently scattered radiation is highly suppressed), and CDI is recorded simultaneously with a second detector in the forward direction. For the reconstruction of the sample, the IDI signal can provide particular atom positions with very high resolution, which then can be used to phase the CDI Fourier amplitudes of large macromolecular proteins. In conclusion, IDI exploit the usage of noisy incoherent scattering as a perk to enhance the resolution of the measurement even for small samples and low scattered intensity, enabling a new path towards protein structure retrieval at high resolution, overcoming the intensity problem affecting CXDI.

6.6 Conclusions

In conclusion, we presented the Coherent Diffraction Imaging (CDI) technique which take advantage of the coherence of the FEL radiation to solve the phase problem affecting diffraction measurement and limiting the achievable resolution. Unfortunately, even with the state-of-art FELs, due to insufficient photon flux, this technique alone

does not allows the accomplishment of the atomic resolution needed to fully reveal the molecular structure of nanometer-sized objects such as proteins. To solve this problem, we presented a novel diffractive imaging technique, Incoherent Diffraction Imaging (IDI), which, based on the measurement of intensity correlations in the far-field, allows to extract 3D structural information from incoherently emitting objects with atomic resolution. Like CDI, IDI gives access to the modulus of the 3D scattering amplitudes, yet with twice the resolution compared to CDI for common detector geometries and additional volumetric information in Fourier space for a single sample orientation. The requirements for the implementation *i.e.,* high brilliance, ultra-short excitations and high repetition rates, are ideally met by current FEL facilities, making IDI a timely and cutting-edge technique with the potential to substantially improve X-ray structure determination. The method may also provide a new route to achieve 2D self-assembled monolayer and single-molecule diffractive imaging [8], which currently suffers from insufficient signal, excessive background, and difficulty in delivering container free molecules to the X-ray beam [67]. Resonant IDI targeted towards sulphur or phosphorous atoms, on the other hand, provides significantly more signal for a given incident intensity, and zero background even when delivering samples in a water micro-jet [68] aimed at the focused X-ray beam.

References

[1] Matteo Altissimo, Maya Kiskinova, Riccardo Mincigrucci, Lisa Vaccari, Corrado Guarnaccia, and Claudio Masciovecchio. A new route for the determination of protein structure in physiological environment. *arXiv preprint arXiv:1702.05998*, 2017.

[2] Stephan AW Verclas, Paul B Howes, Kristian Kjaer, Angelika Wurlitzer, Markus Weygand, Georg Büldt, Norbert A Dencher, and Mathias Lösche. X-ray diffraction from a single layer of purple membrane at the air/water interface. *Journal of molecular biology*, 287(5):837–843, 1999.

[3] https://photon-science.desy.de/e58/e176720/e177229/e179139/index_eng.html?preview=preview.

[4] Eva Nogales, Sharon G Wolf, and Kenneth H Downing. Erratum: Structure of the $\alpha\beta$ tubulin dimer by electron crystallography. *Nature*, 393(6681):191–191, 1998.

[5] Tamir Gonen, Yifan Cheng, Piotr Sliz, Yoko Hiroaki, Yoshinori Fujiyoshi, Stephen C Harrison, and Thomas Walz. Lipid-protein interactions in double-layered two-dimensional aqp0 crystals. *Nature*, 438(7068):633–638, 2005.

[6] https://www.ebi.ac.uk/pdbe/emdb/statistics_num_res.html/.

[7] Cameron M Kewish, Pierre Thibault, Oliver Bunk, and Franz Pfeiffer. The potential for two-dimensional crystallography of membrane proteins at future x-ray free-electron laser sources. *New Journal of Physics*, 12(3):035005, 2010.

[8] Richard Neutze, Remco Wouts, David Van der Spoel, Edgar Weckert, and Janos Hajdu. Potential for biomolecular imaging with femtosecond x-ray pulses. *Nature*, 406(6797):752–757, 2000.

[9] Erik Steen Redeker, Duy Tien Ta, David Cortens, Brecht Billen, Wanda Guedens, and Peter Adriaensens. Protein engineering for directed immobilization. *Bioconjugate chemistry*, 24(11):1761–1777, 2013.

[10] Richard Neutze, Gisela Brändén, and Gebhard FX Schertler. Membrane protein structural biology using x-ray free electron lasers. *Current Opinion in Structural Biology*, 33:115–125, 2015.

[11] Jan Kern, Vittal K Yachandra, and Junko Yano. Metalloprotein structures at ambient conditions and in real-time: biological crystallography and spectroscopy using x-ray free electron lasers. *Current opinion in structural biology*, 34:87–98, 2015.

[12] Henry N Chapman, Petra Fromme, Anton Barty, Thomas A White, Richard A Kirian, Andrew Aquila, Mark S Hunter, Joachim Schulz, Daniel P DePonte, Uwe Weierstall, et al. Femtosecond x-ray protein nanocrystallography. *Nature*, 470(7332):73–77, 2011.

[13] François-Xavier Gallat, Naohiro Matsugaki, Nathan P Coussens, Koichiro J Yagi, Marion Boudes, Tetsuya Higashi, Daisuke Tsuji, Yutaka Tatano, Mamoru Suzuki, Eiichi Mizohata, et al. In vivo crystallography at x-ray free-electron lasers: the next generation of structural biology? *Philosophical Transactions of the Royal Society B: Biological Sciences*, 369(1647):20130497, 2014.

[14] Ilme Schlichting. Serial femtosecond crystallography: the first five years. *IUCrJ*, 2(2):246–255, 2015.

[15] Jan Kern, Roberto Alonso-Mori, Rosalie Tran, Johan Hattne, Richard J Gildea, Nathaniel Echols, Carina Glöckner, Julia Hellmich, Hartawan Laksmono, Raymond G Sierra, et al. Simultaneous femtosecond x-ray spectroscopy and diffraction of photosystem ii at room temperature. *Science*, 340(6131):491–495, 2013.

[16] Christopher Kupitz, Shibom Basu, Ingo Grotjohann, Raimund Fromme, Nadia A Zatsepin, Kimberly N Rendek, Mark S Hunter, Robert L Shoeman, Thomas A White, Dingjie Wang, et al. Serial time-resolved crystallography of photosystem ii using a femtosecond x-ray laser. *Nature*, 513(7517):261–265, 2014.

[17] Cornelius Gati, Gleb Bourenkov, Marco Klinge, Dirk Rehders, Francesco Stellato, Dominik Oberthür, Oleksandr Yefanov, Benjamin P Sommer, Stefan Mogk, Michael Duszenko, et al. Serial crystallography on in vivo grown microcrystals using synchrotron radiation. *IUCrJ*, 1(2):87–94, 2014.

[18] Michael Heymann, Achini Opthalage, Jennifer L Wierman, Sathish Akella, Doletha ME Szebenyi, Sol M Gruner, and Seth Fraden. Room-temperature serial crystallography using a kinetically optimized microfluidic device for protein crystallization and on-chip x-ray diffraction. *IUCrJ*, 1(5):349–360, 2014.

[19] Kartik Ayyer, Oleksandr M Yefanov, Dominik Oberthür, Shatabdi Roy-Chowdhury, Lorenzo Galli, Valerio Mariani, Shibom Basu, Jesse Coe, Chelsie E Conrad, Raimund Fromme, et al. Macromolecular diffractive imaging using imperfect crystals. *Nature*, 530(7589):202–206, 2016.

[20] Richard K Hite, Stefan Raunser, and Thomas Walz. Revival of electron crystallography. *Current opinion in structural biology*, 17(4):389–395, 2007.

[21] Bryant R Gipson, Daniel J Masiel, Nigel D Browning, John Spence, Kaoru Mitsuoka, and Henning Stahlberg. Automatic recovery of missing amplitudes and phases in tilt-limited electron crystallography of two-dimensional crystals. *Physical Review E*, 84(1):011916, 2011.

[22] Cecilia M Casadei, C-J Tsai, Anton Barty, Mark S Hunter, Nadia A Zatsepin, Celestino Padeste, Guido Capitani, W Henry Benner, Sébastien Boutet, Stefan P Hau-Riege, et al. Resolution extension by image summing in serial femtosecond crystallography of two-dimensional membrane-protein crystals. *IUCrJ*, 5(1):103–117, 2018.

[23] Anton Classen, Kartik Ayyer, Henry N Chapman, Ralf Röhlsberger, and Joachim von Zanthier. Incoherent diffractive imaging via intensity correlations of hard x rays. *Physical review letters*, 119(5):053401, 2017.

[24] AP Hammersley. Fit2d: a multi-purpose data reduction, analysis and visualization program. *Journal of Applied Crystallography*, 49(2):646–652, 2016.

[25] Th Roisnel and Juan Rodríquez-Carvajal. Winplotr: a windows tool for powder diffraction pattern analysis. In *Materials Science Forum*, volume 378, pages 118–123. Transtec Publications; 1999, 2001.

[26] J Laugier and B Bochu. Chekcell: Graphical powder indexing cell and space group assignment software, 2004.

[27] Dag W Breiby, Oliver Bunk, Jens W Andreasen, Henrik T Lemke, and Martin M Nielsen. Simulating x-ray diffraction of textured films. *Journal of Applied Crystallography*, 41(2):262–271, 2008.

[28] S Enzo, G Fagherazzi, A Benedetti, and S Polizzi. A profile-fitting procedure for analysis of broadened x-ray diffraction peaks. i. methodology. *Journal of Applied Crystallography*, 21(5):536–542, 1988.

[29] Richard Henderson, Joyce M Baldwin, Thomas A Ceska, Friedrich Zemlin, Erich Beckmann, and Kenneth H Downing. Model for the structure of bacteriorhodopsin based on high-resolution electron cryo-microscopy. *Journal of molecular biology*, 213(4):899–929, 1990.

[30] Pierre-François Lenne, Bruno Berge, Anne Renault, Cécile Zakri, Catherine Vénien-Bryan, Sébastien Courty, Fabrice Balavoine, W Bergsma-Schutter, Alain Brisson, Gerhard Grübel, et al. Synchrotron radiation diffraction from two-dimensional protein crystals at the air/water interface. *Biophysical journal*, 79(1):496–500, 2000.

[31] Toshihiko Oka, Keiko Miura, Katsuaki Inoue, Tatzuo Ueki, and Naoto Yagi. High-resolution powder diffraction study of purple membrane with a large guinier-type camera. *Journal of synchrotron radiation*, 13(3):281–284, 2006.

[32] Richard Henderson. The structure of the purple membrane from halobacterium halobium: analysis of the x-ray diffraction pattern. *Journal of molecular biology*, 93(2):123–138, 1975.

[33] Bill Pedrini, Ching-Ju Tsai, Guido Capitani, Celestino Padeste, Mark S Hunter,

Nadia A Zatsepin, Anton Barty, W Henry Benner, Sébastien Boutet, Geoffrey K Feld, et al. 7 å resolution in protein two-dimensional-crystal x-ray diffraction at linac coherent light source. *Philosophical Transactions of the Royal Society B: Biological Sciences*, 369(1647):20130500, 2014.

[34] Nagayuki Hasegawa, Hideyuki Jonotsuka, Kunio Miki, and Kazuki Takeda. X-ray structure analysis of bacteriorhodopsin at 1.3 å resolution. *Scientific reports*, 8(1):1–8, 2018.

[35] Jianwei Miao, Pambos Charalambous, Janos Kirz, and David Sayre. Extending the methodology of x-ray crystallography to allow imaging of micrometre-sized non-crystalline specimens. *Nature*, 400(6742):342–344, 1999.

[36] Jianwei Miao, Tetsu Ohsuna, Osamu Terasaki, Keith O Hodgson, and Michael A O Keefe. Atomic resolution three-dimensional electron diffraction microscopy. *Physical review letters*, 89(15):155502, 2002.

[37] Jianwei Miao, James E Amonette, Yoshinori Nishino, Tetsuya Ishikawa, and Keith O Hodgson. Direct determination of the absolute electron density of nanostructured and disordered materials at sub-10-nm resolution. *Physical Review B*, 68(1):012201, 2003.

[38] Pierre Thibault, Martin Dierolf, Andreas Menzel, Oliver Bunk, Christian David, and Franz Pfeiffer. High-resolution scanning x-ray diffraction microscopy. *Science*, 321(5887):379–382, 2008.

[39] GJ Williams, MA Pfeifer, IA Vartanyants, and IK Robinson. Three-dimensional imaging of microstructure in au nanocrystals. *Physical review letters*, 90(17):175501, 2003.

[40] Mark A Pfeifer, Garth J Williams, Ivan A Vartanyants, Ross Harder, and Ian K Robinson. Three-dimensional mapping of a deformation field inside a nanocrystal. *Nature*, 442(7098):63–66, 2006.

[41] http://www.physics.ucla.edu/research/imaging/index.html.

[42] Dilworth Y Parkinson, Gerry McDermott, Laurence D Etkin, Mark A Le Gros, and Carolyn A Larabell. Quantitative 3-d imaging of eukaryotic cells using soft x-ray tomography. *Journal of structural biology*, 162(3):380–386, 2008.

[43] Malcolm R Howells, Tobias Beetz, Henry N Chapman, C Cui, JM Holton, CJ Jacobsen, J Kirz, Enju Lima, Stefano Marchesini, Huijie Miao, et al. An assessment of the resolution limitation due to radiation-damage in x-ray diffraction microscopy. *Journal of electron spectroscopy and related phenomena*, 170(1-3):4–12, 2009.

[44] S Huang, Y Ding, Y Feng, E Hemsing, Z Huang, J Krzywinski, AA Lutman, A Marinelli, TJ Maxwell, and D Zhu. Generating single-spike hard x-ray pulses with nonlinear bunch compression in free-electron lasers. *Physical review letters*, 119(15):154801, 2017.

[45] https://www.psi.ch/en/gfa/scientific-highlights/measured-spectrum-for-five-consecutive-fel-pulses.

[46] Praveen Kumar Maroju, Cesare Grazioli, Michele Di Fraia, Matteo Moioli, Dominik Ertel, Hamed Ahmadi, Oksana Plekan, Paola Finetti, Enrico Allaria, Luca Giannessi, et al. Attosecond pulse shaping using a seeded free-electron laser. *Nature*, 578(7795):386–391, 2020.

[47] Ralph W Gerchberg. A practical algorithm for the determination of phase from image and diffraction plane pictures. *Optik*, 35:237–246, 1972.

[48] James R Fienup. Phase retrieval algorithms: a comparison. *Applied optics*, 21(15):2758–2769, 1982.

[49] Veit Elser. Phase retrieval by iterated projections. *JOSA A*, 20(1):40–55, 2003.

[50] Jens Als-Nielsen and Des McMorrow. *Elements of modern X-ray physics*. John Wiley & Sons, 2011.

[51] David Sayre. Some implications of a theorem due to shannon. *Acta Crystallographica*, 5(6):843–843, 1952.

[52] Claude Elwood Shannon. Communication in the presence of noise. *Proceedings of the IRE*, 37(1):10–21, 1949.

[53] Chi-Feng Huang, Keng S Liang, Yeukuang Hwu, Ting-Kuo Lee, Yasumasa Joti, Yoshinori Nishino, and Tetsuya Ishikawa. Simulation of single bio particles in xfel coherent diffraction–master curve for photon counts estimation. In *AIP Conference Proceedings*, volume 2054, page 050006. AIP Publishing LLC, 2019.

[54] Henry N Chapman, Anton Barty, Michael J Bogan, Sébastien Boutet, Matthias Frank, Stefan P Hau-Riege, Stefano Marchesini, Bruce W Woods, Saša Bajt, W Henry Benner, et al. Femtosecond diffractive imaging with a soft-x-ray free-electron laser. *Nature Physics*, 2(12):839–843, 2006.

[55] AP Mancuso, OM Yefanov, and IA Vartanyants. Coherent diffractive imaging of biological samples at synchrotron and free electron laser facilities. *Journal of biotechnology*, 149(4):229–237, 2010.

[56] Egidijus E Uzgiris and Roger D Kornberg. Two-dimensional crystallization technique for imaging macromolecules, with application to antigen–antibody–complement complexes. *Nature*, 301(5896):125–129, 1983.

[57] AP Mancuso, A Schropp, B Reime, L-M Stadler, A Singer, J Gulden, S Streit-Nierobisch, C Gutt, G Grübel, J Feldhaus, et al. Coherent-pulse 2d crystallography using a free-electron laser x-ray source. *Physical review letters*, 102(3):035502, 2009.

[58] Jan Malte Slowik, Sang-Kil Son, Gopal Dixit, Zoltan Jurek, and Robin Santra. Incoherent x-ray scattering in single molecule imaging. *New Journal of Physics*, 16(7):073042, 2014.

[59] Henry N Chapman and Keith A Nugent. Coherent lensless x-ray imaging. *Nature photonics*, 4(12):833–839, 2010.

[60] O Yu Gorobtsov, Ulf Lorenz, Nicolai M Kabachnik, and Ivan A Vartanyants. Theoretical study of electronic damage in single-particle imaging experiments at x-ray free-electron lasers for pulse durations from 0.1 to 10 fs. *Physical Review E*, 91(6):062712, 2015.

[61] Manfred Otto Krause and JH Oliver. Natural widths of atomic k and l levels, k α x-ray lines and several kll auger lines. *Journal of Physical and Chemical Reference Data*, 8(2):329–338, 1979.

[62] F Sette, GK Wertheim, Y Ma, G Meigs, Silvio Modesti, and CT Chen. Lifetime and screening of the c 1s photoemission in graphite. *Physical review B*, 41(14):9766, 1990.

[63] PJ Brown, AG Fox, EN Maslen, MA O?keefe, and BTM Willis. Intensity of diffracted intensities. *International tables for crystallography*, 2006.

[64] Ori Katz, Pierre Heidmann, Mathias Fink, and Sylvain Gigan. Non-invasive single-shot imaging through scattering layers and around corners via speckle correlations. *Nature photonics*, 8(10):784–790, 2014.

[65] M Yabashi, K Tamasaku, and T Ishikawa. Measurement of x-ray pulse widths by intensity interferometry. *Physical review letters*, 88(24):244801, 2002.

[66] Emile D Duée, Eric Fanchon, Jean Vicat, Larry C Sieker, Jacques Meyer, and Jean-Marc Moulis. Refined crystal structure of the 2 [4fe-4s] ferredoxin from clostridium acidurici at 1.84 å resolution. *Journal of molecular biology*, 243(4):683–695, 1994.

[67] A Aquila, A Barty, C Bostedt, S Boutet, G Carini, D DePonte, P Drell, S Doniach, KH Downing, T Earnest, et al. The linac coherent light source single particle imaging road map. *Structural Dynamics*, 2(4):041701, 2015.

[68] Wenguo Zhu, Niko Eckerskorn, Avinash Upadhya, Li Li, Andrei V Rode, and Woei Ming Lee. Dynamic axial control over optically levitating particles in air with an electrically-tunable variable-focus lens. *Biomedical optics express*, 7(7):2902–2911, 2016.

Chapter 7

TRUECARS

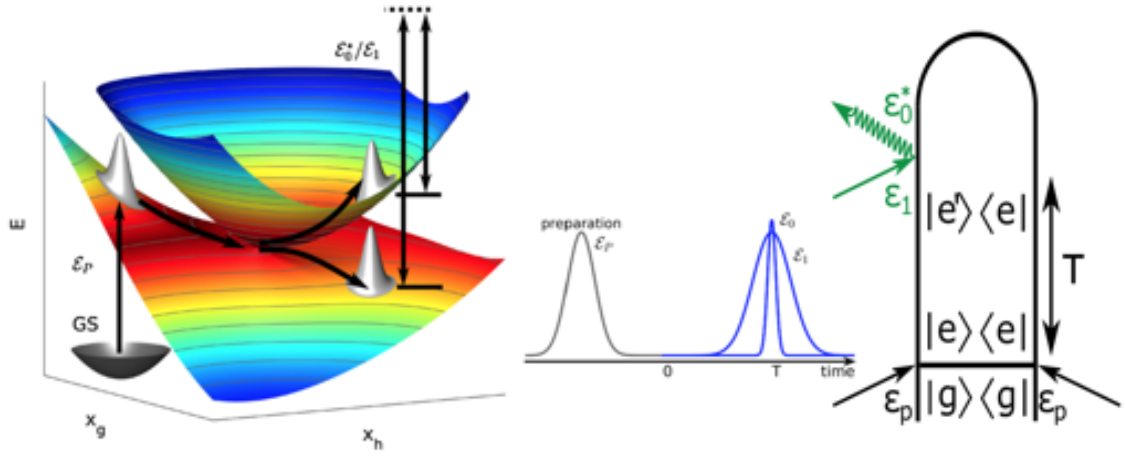

Figure 7.1: *Schematic representation of the TRUECARS detection scheme. (a) A nuclear WP is promoted from the ground state (GS) to an excited electronic state by a pump-pulse EP. As it passes the coupling region around the CI, a coherence is created between the two electronic states. The broadband ϵ_0/narrowband ϵ_1 hybrid pulse probes the electronic coherence between the nuclear WPs on different surfaces. (b) Schematics of the pump and hybrid-probe pulse sequence. Image adapted from [1].*

In the following Chapter, we are going to present a new technique named TRUECARS. Its development was make possible by the group of S. Mukamel, while its pratical realization have lately put together multiple groups from various facilities. This includes the group of S. Mukamel himself (UCI University in Irvine, CA), the group of M. Chergui (EPFL in Lausanne, Switzerland), and our group at FERMI. I personally put a lot of effort into its development towards a feasible experiment. For its presentation we are focusing our attention on the main work from M. Kowalewski *et al.* [1] (UCI University) where the technique have been presented fro the first time, and on the work of D. Keefer *et al.* [2] that demonstrate the potential of this technique on a realistic reaction. The TRUECARS technique was developed with the scope to directly observe the evolution of a Conical Intersection (CI). This is of extreme interest since the rates and outcomes of virtually all photophysical and photochemical processes are determined by CIs. These are regions of degeneracy between electronic states on the nuclear landscape of molecules where electrons and nuclei evolve on comparable timescales and thus become strongly coupled, enabling radiationless relaxation channels upon optical excitation. Due to their ultrafast nature and vast complexity, monitoring conical inter-

sections experimentally is, up to date, an open challenge. It follows that the existence of CIs is widely accepted based on simulations, yet has so far eluded direct experimental observation. However, indirect experimental evidence for CIs exists, and are usually based on the observation of ultrafast internal conversion rates via electronic-state population dynamics [3, 4]. Different approaches for visualizing CIs recently introduced include the Coulomb explosion imaging [5], multidimensional approaches such as [6, 7], and ultrafast electron diffraction [8]. The decisive impact of CIs on textbook examples of ultrafast dynamics, like the ring opening of $1,3-$ *cyclohexadiene* [9], has been revealed with unprecedented precision. An access to CI detection has been enabled recently by the emergence of coherent XUV and X-ray FEL sources since, as the reader should know very well by now, their unique temporal and spectral profiles can access faster timescales and wider energy windows for spectroscopic measurements.

7.1 The TRUECARS approach

In the TRUECARS (Transient Redistribution of Ultrafast Electronic Coherences in Attosecond Raman Signals) technique, as presented by M. Kowalevsky, a pump pulse (actinic pump) brings the molecule of interest from the ground state into an excited state, inducing a non-stationary nuclear wave packet (WP), which subsequently propagates towards the CI. The electronic coherence is automatically generated when the WP approaches the CI, where the nonadiabatic intersurface coupling arises. After a delay-time T, an hybrid X-ray pulse (*i.e.*, a spatial superposition of a broad-band pulse and a narrow-band pulse) probes this electronic coherence through the time-resolved positive (gain) and negative (loss) components of a stimulated Raman pocess (shown in fig. 7.1). In this approach, photon pulses having a few eV bandwidth and few femtosecond time duration are required. Up to date, only FEL's X-ray pulses provide the necessary temporal and spectral profiles to detect electronic coherences. Furthermore, the signal is more likely to be observed when the X-ray pulses are phase stable, even if suggestion from D. Keefer (unpublished results) suggest that the phase stability is not strictly necessary, enabling the usage of FELs based on SASE.

The WP simulations are carried out on the diabatic surfaces through the numerical evaluation of the time dependent Schrödinger equation on a position space grid by the Fourier method. The corresponding Hamiltonian in the diabatic representation reads:

$$\mathcal{H} = \frac{1}{2m}\mathbb{1} + \sum_{i\in h,g} \frac{d^2}{dx_i^2} + \begin{pmatrix} H_1(\boldsymbol{x}) & H_{12}(\boldsymbol{x}) \\ H_{21}(\boldsymbol{x}) & H_2(\boldsymbol{x}) \end{pmatrix}, \tag{7.1}$$

where $\boldsymbol{x} = (x_h, x_g)$, namely two nuclear coordinates of the system. The evolution of the wave-function follows the relation

$$\psi(\boldsymbol{x}, t+\Delta t) = e^{-i\mathcal{H}\Delta t}\psi(\boldsymbol{x}, t) \tag{7.2}$$

which is calculated with the Short Iterative Lanczos (SIL) method [3] of time steps equal to Δt. The corresponding diabatic wave-function is expressed in terms of the electronic states:

$$\psi(\boldsymbol{x}, t) = \begin{pmatrix} \phi_1(\boldsymbol{x}, t) \\ \phi_2(\boldsymbol{x}, t) \end{pmatrix} \quad \text{with} \quad \langle\psi|\psi\rangle = 1. \tag{7.3}$$

The resulting time series $\psi(\boldsymbol{x},t)$ is subsequently used for the calculation of the TRUECARS signal $S(\omega)$, which is defined as the time-integrated rate of change of the photon number, in the attosecond (broadband) electric field ε_0, that is:

$$S(\omega) = \int \frac{d}{dt} \langle \psi(\boldsymbol{x},t) | \hat{N}_\omega^0 | \psi(\boldsymbol{x},t) \rangle \, dt \tag{7.4}$$

where the $\hat{N}_\omega^0$ is the number operator for the photon mode with frequency ω and the superscript ^{0} indicates restriction to modes occupied by the ε_0 pulse. The Hamiltonian the overall photon-matter interaction, providing to be in an off-resonance condition with respect to any excitation of the system, can be written as:

$$\hat{\mathcal{H}}_{int} = \hat{\alpha}|\varepsilon_0 + \varepsilon_1|^2 = \hat{\alpha}(|\varepsilon_0|^2 + |\varepsilon_1|^2) + \underbrace{\hat{\alpha}(\hat{\varepsilon}_0\hat{\varepsilon}_1^\dagger + \hat{\varepsilon}_1\hat{\varepsilon}_0^\dagger)}_{\mathcal{H}_{int}^T} \tag{7.5}$$

where $\mathcal{H}_{int}^T$ is the true TRUECARS Hamiltonian, with $\hat{\alpha}$ being the electronic polarizability operator, and $\hat{\varepsilon}_j$ being the electric field operators. The latter is defined as:

$$\hat{\varepsilon}_j = i \sum_{\omega \in \varepsilon_j} \left(\frac{2\pi\omega}{\Omega} \right)^{\frac{1}{2}} e^{(\boldsymbol{k}\cdot\boldsymbol{r} - \omega t)} \hat{\alpha}_\omega \tag{7.6}$$

with Ω being the quantization volume. By applying the Ehrenfest theorem on the operator $\hat{N}_\omega^0$, using the TRUECARS interaction Hamiltonian $\mathcal{H}_{int}^T$, we get

$$\begin{aligned} \frac{d}{dt}\langle \hat{N}_\omega^0 \rangle &= \frac{1}{i\hbar} \langle [\hat{N}_\omega^0, \mathcal{H}_{int}^T] \rangle \\ &= \frac{1}{i\hbar} \langle \hat{\alpha} \sum_{\omega \in \varepsilon_0} \Big([a_\omega^\dagger \hat{a}_\omega, \hat{\varepsilon}_0]\hat{\varepsilon}_1^\dagger + \hat{\varepsilon}_1 [a_\omega^\dagger \hat{a}_\omega, \hat{\varepsilon}_0^\dagger] \Big) \rangle \\ &= \frac{1}{i\hbar} \langle \hat{\alpha}(\hat{\varepsilon}_1\hat{\varepsilon}_0^\dagger - \hat{\varepsilon}_0\hat{\varepsilon}_1^\dagger) \rangle = \frac{2}{i\hbar} \Im m \langle \hat{\alpha}\hat{\varepsilon}_1\hat{\varepsilon}_0^\dagger \rangle \end{aligned} \tag{7.7}$$

where we considered only the commutator with the field of interest $\hat{\varepsilon}_0$. We can now first Fourier transform $\hat{\varepsilon}_1$ and add a frequency gating $\delta(\omega - \bar{\omega})$. At this point we substitute $\bar{\omega} \to \omega$, We take the expectation values of the filed on the assumption of coherent states, and finally wereplace the field operators with field envelopes. Following the procedure, we get

$$\begin{aligned} S(\omega, T) = \frac{2}{\hbar} \Im m \int_{-\infty}^{+\infty} & \varepsilon_0^*(\omega)\varepsilon_1(t-T) e^{i\omega(t-T)} e^{i(\phi_1 - \phi_0)} \\ & \times \langle \psi(x,t) | \hat{\alpha}(t) | \psi(x,t) \rangle \, dt \end{aligned} \tag{7.8}$$

where both components have been assumed to have the same carrier frequency ω for simplicity. In equation 7.8, the signal carries the difference over phase factors $e^{i(\phi_0 - \phi_1)}$, where ϕ_j is the phase of the field ε_i. Here we can see that the phase factor causes the signal to vanish when averaged over an high number of random phases. Therefore, the state of art of the observation of the TRUECARS signal would requires control of the relative phases of the two pulses. However, provided that only few phases are involved, this should not be an only if condition on the experiment. The temporal and spectral resolutions of the technique are not independent, but rather they are *Fourier-conjugate* pairs, determined by the corresponding temporal and spectral profiles of the femtosecond pulse ε_1. In order to resolve the changing in the energy gap along the CI, ε_1 must

be shorter than the dynamics while spectrally narrower than any relevant energy splitting. For example, resolving a 0.1 eV energy difference implies at least a 6.5 fs pulse duration, so that, dynamics faster than this would, in principle, not be resolved. The reduced electronic density matrix is obtained by integrating over the nuclear degrees of freedom. Using the bra-ket notation, this is equal to:

$$\rho_{el} = \begin{pmatrix} \langle \phi_1 | \phi_1 \rangle & \langle \phi_1 | \phi_2 \rangle \\ \langle \phi_2 | \phi_1 \rangle & \langle \phi_2 | \phi_2 \rangle . \end{pmatrix} \tag{7.9}$$

At this point, it becomes clear that the coherence of the electronic subsystem, $\rho_{12} = \langle \phi_1 | \phi_2 \rangle$, is given by the overlap integral of the nuclear wave-functions on the two surfaces, and thus it arises only when the WP approaches the CI where the two surfaces are close to each other. The time-dependent polarizability $\hat{\alpha}(t)$ in eq. 7.8 is the relevant quantity of the sample that results from the wavepacket dynamics. Each element of $\hat{\alpha}$ is defined as a second-rank tensor with x, y, and z Cartesian components in the molecular frame, *i.e.*,

$$\hat{\alpha} = \begin{pmatrix} \alpha_{xx} & \alpha_{xy} & \alpha_{xz} \\ \alpha_{yx} & \alpha_{yy} & \alpha_{yz} \\ \alpha_{zx} & \alpha_{zy} & \alpha_{zz} \end{pmatrix} \tag{7.10}$$

Depending on the orientation of the molecule and on the pulse configuration (*i.e.*, polarization), a certain component of eq. 7.10 is selected. In general, each component of $\hat{\alpha}$ can be calculated [10] as

$$\alpha_{xy}^{fi} = \sum_{|n\rangle} \left[\frac{\langle f | \hat{\mu}_y | n \rangle \langle n | \hat{\mu}_x | i \rangle}{\omega_{nf} + \omega_0} + \frac{\langle f | \hat{\mu}_x | n \rangle \langle n | \hat{\mu}_y | i \rangle}{\omega_{ni} + \omega_0} \right] \tag{7.11}$$

where, with obvious notation, $\hat{\mu}_x$ and $\hat{\mu}_y$ are the Cartesian x and y components of the dipole operator in the molecular frame. Considering an off-resonant X-ray core process between valences states i and f, the summation is performed over all core-hole states $|n\rangle$, ω_{ni} is the energy difference between valence-state i and the core-state $|n\rangle$, and ω_0 is the carrier frequency of the probe field. The key quantities in this equation are the transition dipole moments $\langle f | \hat{\mu}_y | r \rangle$ between the valence and the core states, where $\hat{\mu}_y$ is the y component of the dipole operator. Finally, we can now write the polarizability part of eq. 7.8 in matrix form as

$$\hat{\alpha} = \begin{pmatrix} \alpha_{22} & \alpha_{21} \\ \alpha_{12} & \alpha_{11} \end{pmatrix} \tag{7.12}$$

where the diagonal elements α_{22} and α_{11} are the S_2 and S_1 electronic state polarizabilities, and the off-diagonal elements are the transition polarizabilities between them. Let's remind that all the elements are operators in the nuclear space. It is important to note that when taking the imaginary part in eq. 7.8, population terms do not contribute to the signal [1], thus α_{22} and α_{11} can be set to zero. This is an important feature of the TRUECARS technique that makes it a background-free probe of vibronic coherences that, in our model, exist only in the CI proximity. Since the electronic-state populations are larger than the coherence by $\sim$ three orders of magnitude, the latter would be

[1] note that we look at the change rate in the photon count for a give frequency: if the stimulated Raman process produces a final outcome $\Delta\omega = 0$, corresponding to $S_i \rightarrow S_i$, the TRUECARS signal is unchanged.

masked in more conventional transient Raman probing schemes. The hybrid narrowband/broadband X-ray pulse configuration used in TRUECARS provides the necessary temporal and spectral profiles to capture the energy splitting of the S_1/S_2 superposition, as well as the time resolution to resolve the ultrafast coherences, which is not accessible with visible pulses. The TRUECARS signal, in figure 7.2, is calculated in the Kowalevsky work by assuming the X-ray transition polarizability $\hat{\alpha}$ to be constant in the nuclear coordinate space:

$$\hat{\alpha} = \begin{pmatrix} 0 & 1 \\ 1 & 0 \end{pmatrix} \tag{7.13}$$

The time depended property of the material $\alpha(t)$ is then calculated sandwiching it between the wave-function, that is:

$$\alpha(t) = \langle \psi_1(\boldsymbol{x},t)|\hat{\alpha}(t)|\psi_2(\boldsymbol{x},t)\rangle = 2\Re e\,\langle \phi_1(\boldsymbol{x},t)|\phi_2(\boldsymbol{x},t)\rangle \tag{7.14}$$

The WP potential energy splitting $\Delta V(t)$, the black line in fig. 7.2 a), is obtained by a weighted energy difference between the adiabatic PESs S_1 and S_2:

$$\Delta V(t) = \frac{\int_{-\infty}^{+\infty} |\bar{\phi}_1(\boldsymbol{x},t)\bar{\phi}_2(\boldsymbol{x},t)|(V_2(\boldsymbol{x}) - V_1(\boldsymbol{x}))}{|\langle \bar{\phi}_1(\boldsymbol{x},t)|\bar{\phi}_2(\boldsymbol{x},t)\rangle|} \tag{7.15}$$

The adiabatic wave functions $\bar{\phi}_j(\boldsymbol{x},t)$ are obtained by the unitary transformation $\mathcal{U}(\boldsymbol{x})$ that diagonalizes the diabatic PESs:

$$\begin{pmatrix} \bar{\phi}_1(\boldsymbol{x},t) \\ \bar{\phi}_2(\boldsymbol{x},t) \end{pmatrix} = \begin{pmatrix} cos(\vartheta(\boldsymbol{x})) & sin(\vartheta(\boldsymbol{x})) \\ -sin(\vartheta(\boldsymbol{x})) & cos(\vartheta(\boldsymbol{x})) \end{pmatrix} \begin{pmatrix} \phi_1(\boldsymbol{x},t) \\ \phi_2(\boldsymbol{x},t) \end{pmatrix} \tag{7.16}$$

with the mixing angle ϑ following the relation

$$tan(2\vartheta(\boldsymbol{x})) = \frac{1}{2}\frac{H_{12}(\boldsymbol{x})}{H_2(\boldsymbol{x}) - H_1(\boldsymbol{x})}. \tag{7.17}$$

As stated before, in the TRUECARS measure, terms corresponding to electronic populations do not contribute since they carry no dynamical phase and vanish when taking the imaginary part in eq. 7.8. TRUECARS therefore, in contrast with Stimulated Raman Spectroscopy (SRS), provides a background-free measurement of electronic coherence. The signal is linear in the probe intensity $\varepsilon_1\varepsilon_2$, while on contrast SRS [11] uses the same pulse sequence but detects the quadratic signal $\varepsilon_1^2\varepsilon_2^2$. TRUECARS is therefore phase dependent whereas SRS is phase independent. The quadratic signal would allow a greater resolution, since temporal and spectral resolution could then be set by the broadband and narrowband pulses respectively and would not be Fourier limited [11]. However, the quadratic signal is typically dominated by contributions stemming from electronic populations [12], thus, it does not represent a background-free measurement of the electronic coherence. The linear TRUECARS signal is therefore a much cleaner way to measure the passage through a conical intersection. In the TRUECARS paper [1], it was assumed that the dominant (and only) transition dipole moments contributing to $\hat{\alpha}$ to be the core-to-valence transitions. Photo-ionization processes were not include, since it has been experimentally shown [13] that X-ray Raman signals can successfully compete with the ionization background.

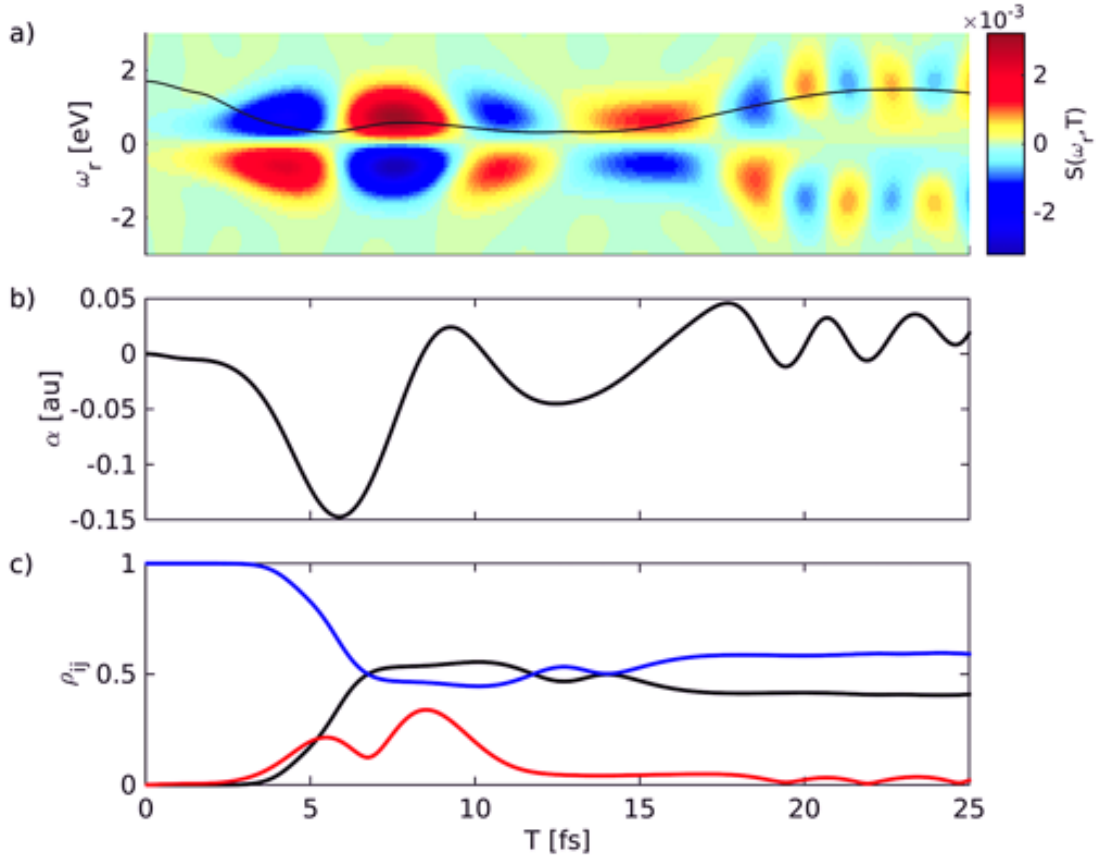

Figure 7.2: *(a) Simulated TRUECARS Signal as in eq. 7.8 for the a two-dimensional nuclear model with a pulse length of 1.2 fs (ε_1) . The solid line indicating the average splitting of the potential energy surfaces can be read from the Raman shift. (b) The time dependent expectation value of the polarizability. (c) Elements of the reduced density matrix of the electronic subsystem. Blue and black: populations of the adiabatic S_2 and S_1 state respectively. Red line: the magnitude of the electronic coherence. Image adapted from [1].*

In figure 7.2 is presented a WP simulation on a model system with two vibrational modes and two excited electronic states S_1 and S_2 and typical molecular parameters. This is, in fact, the minimal model required to describe a CI [14]. The two coordinates $\vec{x}_h$ and $\vec{x}_g$ (see fugure 7.1) resemble the branching space of a CI and rispectively represent the displacements along the derivative of the coupling vector, and the gradient difference vector. The initial condition is at the Franck-Condon point, chosen to be in the vicinity of the CI to allow the WP to reach the CI in a short period of time. Examples of molecules with ultrafast non-adiabatic dynamics include cyclohexadiene [15], ethylene [16], pyrazine [17], and Uracil [2]. The latter will be reviewed later on. The WP simulations are carried out numerically on a grid in the electronic and nuclear space using the diabatic basis, transformed into the adiabatic basis as needed, following eq. 7.16. The model used for this simulation was inspired by the $S_2 - S_1$ CI in Acrolein [18]. The molecule is assumed to be initially in its electronic ground state S_0. An actintic pump-pulse creates an excitation in the S_2 state, thus launching the dynamics. The diabatic coupling vanishes (just like my dreams, hopes and sleep) in the Franck-Condon region (here an electronic transition is most likely to occur without changes in the positions of the nuclei) to allow for an initial condition for which the Born-Oppenheimer approximation still holds. The initial S_1/S_2 splitting at the Franck-Condon point is around 2

eV. The WP propagates freely on the S_2 surface in the branching space and approaches the CI. The resulting TRUECARS signal (eq. 7.8) and the averaged time-dependent energy splitting is shown in fig. 7.2 a) (black solid line). The initial state created by the actinic pump contains no electronic coherence, whihc is indicated by the TRUECARS signal turning on at $\sim 2\ fs$, when the system approaches the non-adiabatic coupling region. The corresponding molecular property governing the signal, the off-resonant transition polarizability $\alpha(t)$, is shown in fig. 7.2 b). If the $\hat{\alpha}$ is assumed to be independent of the nuclear coordinates, $\alpha(t)$ is directly proportional to the real part of the electronic coherence. In fig. 7.2 c), the adiabatic populations are shown along with the magnitude of the electronic coherence. After the WP has passed the CI at $\sim 6\ fs$, it travels through a coordinate region where there is a small, but finite, splitting between adiabatic potential energy surfaces. Finally, when the splitting increases, the diabatic coupling vanishes and the TRUECARS signal with it. The signal broadening stems from two main contributions: the width of the nuclear WP, covering a certain range of potential energy differences, and the spectral width of the probe pulse. The peak maxima are slightly shifted to larger Raman shifts due to the fact the signal vanishes at $\omega_r = 0$. Additionally the information about the energy splitting is also contained in the oscillations in T, indicating that the system is in close vicinity of the CI, as the oscillation frequency is lowered . At around 15 fs, the energy splitting increases again as can be seen from ω_r. Since the S_1 and S_2 states have different gradients, the overlap between the nuclear WPs $\langle\phi_1|\phi_2\rangle$ decays and the signal fades out. As showed in fig. 7.2, the passage through the CI happens in less than 12 fs. Using a 1.2 fs pulses, the arrival of the WP at the CI can be timed within 10 fs. Note that, since the probe pulses are Fourier paired, an even shorter coherence lifetime would not allow for a clear determination of the energy splitting, nonetheless it would increase the time resolution. As is clear from the overlay of the energy splitting on the TRUECARS spectra, the technique is capable of mapping out the potential energy surfaces of the reaction coordinate near the CI. It thus gives both dynamical information on the temporal and spectral profile of the the CI by providing information about period of oscillations as well as the phase of the electronic coherences near the CI.

Lately, D. Keefer *et al.* [2] demonstrate the potential of this technique on a more realistic reaction, *i.e.,* the photorelaxation of the RNA-nucleobase Uracil after UV excitation. Of course the results of this work lie completely in the theoretical framework, nonetheless they shine more light on the feasibility of the experimental counterpart. With this in mind, we briefly review their main accomplishments and explore the suggestions for the practical realization of the technique. In this work, the two nuclear degrees of freedom q_1 and q_2 spanning the relevant coordinate space (fig. 7.3 A)) have been constructed from structures that were found to be important in the photorelaxation of the S_2 PES of Uracil [19, 20], and have originally been described in ref. [19]. The first coordinate q_1 describes the motion from the Franck-Condon (FC) to the CI and can be described as an out-of-plain motion of the planar ring structure. The second coordinate q_2 represents the motion from the FC to a local energy minimum in the S_2 state and is associated to the bending of one hydrogen atom out of the plane defined by the ring. The PES excited-state in this two-dimensional nuclear space are displayed in fig. 7.3 D) and have been shown to reproduce experimental kinetic rates in optical excitation regime [19, 20]. This 2D nuclear space has also been tested and verified by higher-dimensional treatments [19]. The nonadiabatic couplings (NACs) that are necessary to simulate the passage of the nuclear WP through the CI are displayed in fig. 7.3 B).

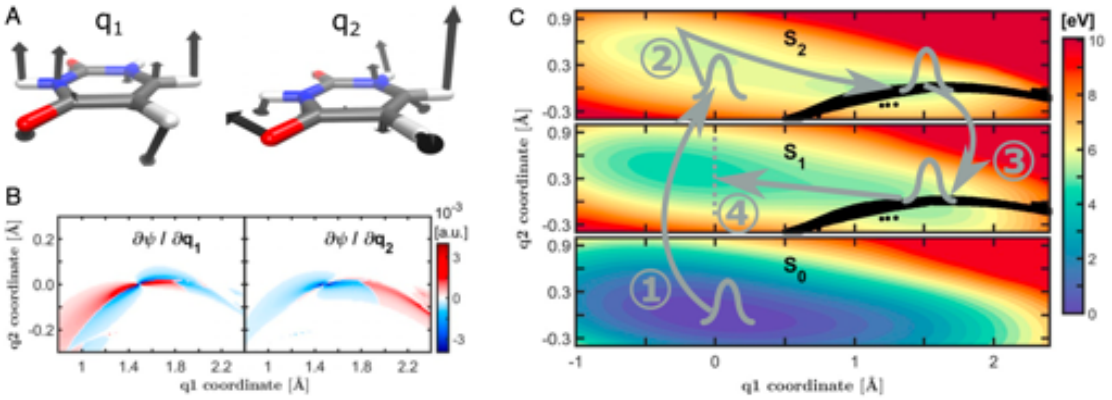

Figure 7.3: *WP dynamics of Uracil and key molecular quantities for the signal calculation. A) Uracil geometry structure at the ground state minimum, with the vectors indicating the molecular displacement according to the two nuclear degrees of freedom q_1 and q_2. B) Nonadiabatic couplings between S_2 and S_1 at the CI versus the two nuclear coordinates of the molecules. The characteristic peaked switch of the sign is clearly visible. C) Potential energy surfaces of the three electronic states: the ground-state S_0, the dark $n\pi*$ state S_1, and the bright $\pi\pi*$ state. The seam of the CI is marked in black, and the path followed by the WP is sketched in gray. 1) Optical excitation from S_0 to S_2 using a 34 fs UV pump. 2) Free evolution in the S_2 state through the local minimum, with subsequent barrier crossing toward the CI. 3) Nonadiabatic passage through the CI, creating the vibronic coherence. 4) Final relaxation in the S_1 state toward the energetic minimum, where the WP is absorbed. Image adapted from [2].*

Here we can see that they show a smooth variation, with the characteristic sign switch due to the changing of the electronic character of the adiabatic states. The nuclear dynamics are launched using a 34 fs (FWHM) Gaussian laser pump in resonance with the $S_0 \rightarrow S_2$ transition, following the experimental value exposed in [20]. The path of the WP is drawn in fig. 7.3 D). After excitation to the S_2 state, and following a free S_2 evolution period, the WP reaches the CI at ~ 100 fs. Here, a vibronic coherence between the S_2 and the S_1 electronic state arises due to the nuclear WP relaxing through the CI. Both electronic states are now populated, and the overlap integral of the S_2 and the S_1 nuclear WP becomes finite. This coherence is probed by the TRUECARS signal. The WP parts that reach the S_1 state evolve away from the CI toward the energy minimum. It must be noted that, in this work, after the passage through the S_1 region, the WP is absorbed through a Butter-worth filter [21], preventing the WP from oscillating through the S_1 minimum and evolving back to the CI region. This is due to the fact that the coordinate space defined by q_1 and q_2 is tailored to describe the S_2 evolution and does not accurately capture WP evolution in the S_1 PES far from the CI, since other nuclear degrees of freedom start to become important. For example, the exit channel for the WP to further CIs with the S_0 state is not included. Back evolution of the WP to the CI region should therefore lead to artifacts in the coherence, thus absorbing the WP in the S_1 minimum should lead to a more accurate description of the real process.
The TRUECARS signal of the $S_2 \rightarrow S_1$ transition displayed in fig. 7.4 exhibits some striking features. At the CI, a vibronic coherence is created and α, *i.e.*, the polarizability expectation value according to eq. 7.14, becomes finite as well. Given the presence of the vibronic coherence, a signal shows up and remains visible for several hundred femtoseconds, until the vibronic coherence decays. This long-lived coherence is due to the delocalized nature of the quantum nuclear WP on the S_2 surface. The delocalization implies that tails of the WP continue to reach the CI, and even with an instant

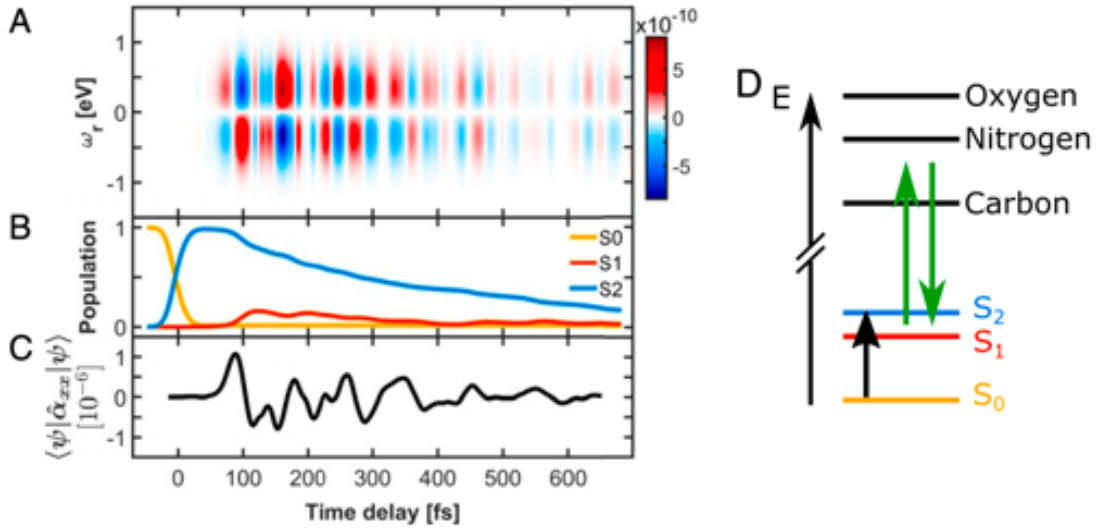

Figure 7.4: *TRUECARS signal of Uracil. (A) The frequency-dispersed signal $S(\omega_r, T)$, using $\hat{\alpha}_{xx}$ at 354 eV. (B) Valence-state population dynamics after an optical pump and the dynamics sketched in fig. 7.3 d). The Gaussian pump ϵ_p creates an electronic and nuclear population in the excited state. A coherence between e (S_2) and e′ (S_1) is probed by the hybrid field ϵ_0 (500 as) and ϵ_1 (2 fs) (see the loop diagram in 7.1, while for diagram rules see [22]). (E) Energy-level scheme of the measurement. Electronic-state color code is according to B, where blue and red correspond to the states i and f in eq. 7.11. The C, N, and O core edges at 291, 405, and 536 eV correspond to the states $|n\rangle$ in eq. 7.11. The green arrows represent the off-resonant Raman process. Image adapted from [2].*

exit channel for the WP in the S_1 state, the coherence survives for several hundred femtoseconds. This has profound implications for the observation and control of quantum events at CIs. Furthermore, since the vibronic coherence that determines the outcome of the photophysical process is long-lasting, its monitoring would require longer temporal windows rather than precise timings for molecules like Uracil. The signal depicted in fig. 7.4 A) exhibits temporal Stokes and anti-Stokes oscillations, both oscillating between positive (red) and negative (blue) values. This is due to the contributing vibronic states having different frequencies, whilst the dynamical phase evolution is contained in the signal. An interesting introduction was implemented in this work: in order to display the time-dependent frequency map, they introduced the Wigner spectrogram (fig. 7.5 E)) of a temporal trace $S(T)$ of the TRUECARS signal, taken at a fixed Raman shift ω_r (black line in fig. 7.5 A)), defined as:

$$W(T,\omega_{coh}) = \int_{-\infty}^{\infty} S(T+\tau)S(T-\tau)e^{i\omega_{coh}\tau}d\tau. \tag{7.18}$$

The frequency window spanned by $W(T,\omega_{coh})$, in this case $0-0.2\ eV$, represents the potential energy splitting of the CI where the vibronic coherence ω_r is located. The main feature at 0.1 eV (marked with the white arrow in fig. 7.5 E)) exhibits no temporal variation of ω_{coh}. The contributions visible in the Wigner spectrogram, map the vibronic frequencies that contribute to the coherence. This can be understood comparing the classical approach to the quantum treatment, *i.e.*, when the nuclei are treated as classical, the system has a well-defined, time-dependent energy splitting which vanishes at the CI. In the quantum treatment, this is replaced by a distribution of energy splittings given by the WP frequencies. The average of that distribution serves as the effective splitting. To extend this analysis even further, they reduced the 34 fs FWHM

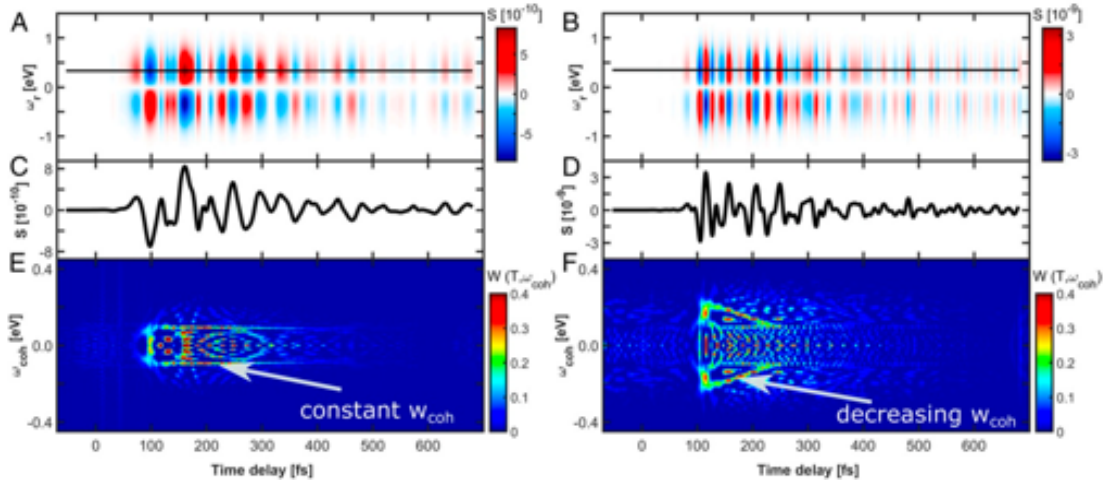

Figure 7.5: *Wigner spectrogram of the TRUECARS signal. A, C, and E use a 34 fs Gaussian pump (delocalized WP). (A) The signal $S(\omega_r, T)$. (C) Signal trace $S(T)$ at $\omega_r = 0.33$ eV (maximum signal intensity). (E) Wigner spectrogram $W(T, \omega_{coh})$ of the signal trace $S(T)$. B, D, and F use a 20 fs Gaussian pump which produces a more localized WP. Image adapted from [2].*

optical Gaussian pump to 20 fs, as shown in fig.7.5 B), D), and F). The WP, now more localized in the S_2 PES, shows no change in the Raman shift ω_r of the signal. However, the temporal oscillations are much faster, so that the frequency regime covered by the vibronic coherence is broader as showed in fig. 7.5 F). More importantly, the energy position of the main feature (marked with the white arrow) does vary with time. Starting at ~ 0.2 eV at 100 fs, the coherence evolves to lower frequencies until ~ 250 fs, where it eventually decays. Due to the quantum treatment of the nuclei, the time-resolved frequency map in the Wigner spectrogram is an experimental observable, independent of the basis set used, and reveals the exact vibronic-state landscape across the CI path.

7.2 SASE and Seeded FELs approaches

In this section we present two different approaches to the CI measurement which differ on the pulse configuration and, thus, on the subsequent data analysis procedure associated. The first one can be achieved using a seeded X-ray FEL. In this case a single-colour or a two-colour hybrid pulse [2], as shown in fig. 7.1, is focused on the sample at a delay-time T after the actinic pump. This configuration allows for a full control on the phase stablity during the measurement, however it requires a seeded or a self-seeded FEL. The second approach is based on the SASE configuration. In this case, the broadband-like feature is carried by the overall or partial envelope of the pulse. Each spike can be seen as an independent field carrying a random phase ϕ_j. Thus, using a few femtoseconds X-ray SASE pulse to hits the sample, the train of spikes would generate a noisy signal. Clearly, averaging over a great number of spectra, as the classic data analysis approach suggests, would cause the signal to vanish. Hence, a new data analysis mechanism, similar to the one implemented in the IDI techniques, from the recent work of

[2] the two colour exotic configuration can be achieved using a double seeded FEL [23]. It can even be achieved for the SASE configuration using a sextupole magnet in combination with a standard orbit control tool *i.e.*, the radiation from the bunch core is suppressed while the head and the tail of the beam keep lasing, each at a different photon energy [24].

[25] is presented.

7.2.1 Femtosecond Covariance Spectroscopy

Even if TRUECARS promises to provide a background-free measurement of electronic coherence, we still must take care of many undesired side effects such as the intrinsic beam and detectors noise and competing signals arising from different processes. In the following, we will focus our attention on the stochastic, noisy part of the unwanted signal. Noise is normally seen as a limitation in measurements and thus a quantity to eliminate. The desired signal-to-noise ratio is often reached by mitigating as much as possible the amount of experimental noise and taking the mean of a large number of repeated *identical* measurements. From an alternative perspective, where every repetition is considered to be a measurement under different conditions, noise can become an asset and be exploited as a source of additional information [26, 27]. In our case, since every single FEL pulse is to be considered providing a different conditions, the mean value loses significance and other statistical tools, such as higher-order moments, are required. If treated properly, noise can help clarify the interpretation of experiments and even amplify signals as, for instance, in stochastic resonance schemes [28]. In their work, Tolleroud *et al.* studied vibrational modes in a crystalline quartz sample via SRS. Ultrafast pulses from a regenerative amplifier ($\sim 40\ fs$) were transmitted through the sample and the spectrum of each transmitted pulse was detected using a spectrometer. An element generating stocastic noise (a programmable pulse shaper liquid crystal [29]), was placed between the laser and the sample as sketched in fig. 7.6 B). The pulse shaper changes the spectral phase with a defined modulation amplitude and correlation length. A reference beam was routed around the sample and directed to a second identical spectrometer, so that they could compare the spectral covariance with and without interacting with the sample. The time profiles resulting from the application of a spectral phase to initially transform limited pulses can be divided into a short coherent component (blue spike in fig. 7.6 A) which provides the impulsive excitation of the Raman modes, and noisy incoherent tails which probe the mode. Over the course of many measurements, the average of the noisy tails became a $\sim 1\ ps$ Gaussian pulse, shown in green in fig. 7.6 A). Finally, a covariance-based analysis to extract information about the sample through correlations induced by SRS was implemented in the form of the Pearson coefficient, which quantifies the degree of linear correlation between two random variables, *i.e.*, the measured intensity I at the frequencies ω_i and ω_j within the pulse bandwidth, that is:

$$P(\omega_i,\omega_j) = \frac{\langle I(\omega_i)I(\omega_j)\rangle - \langle I(\omega_i)\rangle\langle I(\omega_j)\rangle}{\sigma_i\sigma_j}. \tag{7.19}$$

The angular bracket indicates a mean across all measurements, and $\sigma_{i/j}$ is the standard deviation across all measurements of the intensity at frequency $\omega_{i/j}$. $P = 1$(-1) indicates perfect correlation (anti- correlation), while $P = 0$ indicates no correlation. The result of this data processing performed across all of the possible frequency combinations forms a 2D Pearson coefficient map, such as those shown in fig. 7.6 C) and D). The P map calculated using the reference pulses, shown in fig. 7.6 C), exhibits no features apart from an area of positive correlation at $\omega_i = \omega_j$ (the diagonal of the map). In contrast, when the pulse interacted with the sample (fig. 7.6 D)), the map is evidently structured. Most importantly, we observe signatures of correlation induced through SRS in the form of features offset of a quantity $\Delta\omega$ from the diagonal, with a finite width, which depends

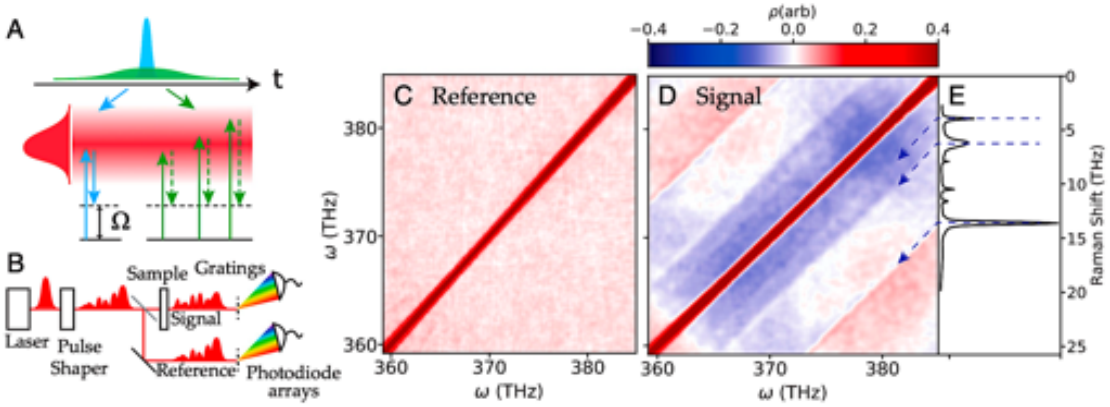

Figure 7.6: *(A) Simplified diagram of the SRS process, which induces correlations of spectral components at frequencies ω and $\omega \pm \Omega$. The shaped pulses can be divided into a coherent component (blue) and a noisy tail (green). (B) The experimental apparatus. C) and D) Pearson correlation plots for all pairs of frequencies within the excitation spectrum (C) after the pulse shaper, and (D) after the quartz sample. (E) Spontaneous Raman spectrum of quartz [30], matching the positions of the features in the covariance map in D. Images reproduced from [25].*

on the linewidth of the resonance and the correlation length. By comparing the correlation map to the spontaneous Raman spectrum [30] (fig. 7.6 E)), it is clear that $\Delta\omega$ matches the Raman shift given by phonon features. The signal presence is substantiated by the fact that frequency components separated by Ω must have the same phase for interference between the paths leading to the population of that vibrational level to occur [31]. In their work, thus, they showed that covariance-based detection can be combined with noisy input pulses to resolve the SRS spectrum, and more incisive analytical tools than the average value can access a great depth of information that is missed by standard experiments. The transmitted pulses averaged over many noise realizations do not show the Raman resonances, however, the resonances are recovered in the covariance spectrum that reveals correlations between two spectral components separated by the phonon frequencies. A high-resolution Raman spectrum is thus generated by exploiting the noise fluctuations, without the need for stable light sources, which is exactly the case of FELs based on SASE mode, where amplitude and phase noise are unavoidable.

7.3 Conclusions

In summary, we presented a new spectroscopic technique, named TRUECARS, that can directly monitor passage through Conical Intersections (CIs). The technique measures the frequency-resolved stimulated Raman scattering of a probe pulse as a function of the time delay with respect to the pump pulse. In contrast to existing methods, TRUECARS is only sensitive to electronic coherences and populations do not contribute, making it uniquely suited to probing passage through CIs by capturing the electronic coherences generated by non-adiabatic couplings in the CI vicinity. This study offers a novel window into ultrafast non-adiabatic transitions at CIs. The frequency, phase and duration of the vibronic coherence, created by the quantum nuclear wave packet (WP) evolution, is monitored in real time. Contrary to the common picture of precisely timed CI events, the coherence remains away from the CI toward the minimum, and it is con-

stantly rebuilt by other parts of the WP arriving at the CI in the S_2 state. Localized nuclear WPs provide a sensitive scan of the frequency landscape surrounding the CI. The magnitude and range of the energy splitting of the participating adiabatic vibronic states can be read directly from the signal. No further theoretical input is necessary to access this information from the signal. Uracil photorelaxation is experimentally accessible, and all quantities are produced at the fully *ab-initio* level. The presented Wigner spectrograms offer a novel physical picture of CI processes by picturing them through the complex coherence distributions rather than a change in absorption lines or a single vanishing energetic gap. The off-resonant probing scheme employed here with respect to core excitations renders the signal ubiquitous and translatable to other molecules with a non-vanishing dipole transition between a CI valence state and other core-hole states. An important step towards phase-controlled XUV/X-ray pulses, that are necessary to record the stimulated Raman signal, was recently made [32], and the proposed experiment (requiring broadband sub-femtosecond pulses of $\sim$ 100 eV or more and spectral widths of several eV) lies within the capabilities of state of the art X-ray sources [23, 24]. Altogether, the reported novel spectroscopic maps of CI passages provide direct access to the quantum WP pathways in CI passages, which opens the door for a deeper understanding of these ubiquitous processes. This insight is also beneficial for developing approaches for controlling photochemical reactions by modulating this coherence [33]. This makes TRUECARS an ideal tool to investigate ultra-fast, photophysical system dynamics.

A group of people (the undersigned among them) from FERMI, PSI, SLAC and the UCI are collaborating in order to generate and submit proposals to experimentally visualize CIs using the TRUECARS technique.

References

[1] Markus Kowalewski, Kochise Bennett, Konstantin E Dorfman, and Shaul Mukamel. Catching conical intersections in the act: Monitoring transient electronic coherences by attosecond stimulated x-ray raman signals. *Physical review letters*, 115(19):193003, 2015.

[2] Daniel Keefer, Thomas Schnappinger, Regina de Vivie-Riedle, and Shaul Mukamel. Visualizing conical intersection passages via vibronic coherence maps generated by stimulated ultrafast x-ray raman signals. *Proceedings of the National Academy of Sciences*, 117(39):24069–24075, 2020.

[3] Dario Polli, Piero Altoè, Oliver Weingart, Katelyn M Spillane, Cristian Manzoni, Daniele Brida, Gaia Tomasello, Giorgio Orlandi, Philipp Kukura, Richard A Mathies, et al. Conical intersection dynamics of the primary photoisomerization event in vision. *Nature*, 467(7314):440–443, 2010.

[4] MCE Galbraith, S Scheit, NV Golubev, G Reitsma, N Zhavoronkov, V Despré, Franck Lepine, AI Kuleff, MJJ Vrakking, O Kornilov, et al. Few-femtosecond passage of conical intersections in the benzene cation. *Nature communications*, 8(1):1–7, 2017.

[5] ME Corrales, J González-Vázquez, R de Nalda, and L Bañares. Coulomb explo-

sion imaging for the visualization of a conical intersection. *The journal of physical chemistry letters*, 10(2):138–143, 2018.

[6] Thomas AA Oliver and Graham R Fleming. Following coupled electronic-nuclear motion through conical intersections in the ultrafast relaxation of β-apo-8?-carotenal. *The Journal of Physical Chemistry B*, 119(34):11428–11441, 2015.

[7] Eric C Wu, Qinghui Ge, Eric A Arsenault, Nicholas HC Lewis, Natalie L Gruenke, Martin J Head-Gordon, and Graham R Fleming. Two-dimensional electronic-vibrational spectroscopic study of conical intersection dynamics: an experimental and electronic structure study. *Physical Chemistry Chemical Physics*, 21(26):14153–14163, 2019.

[8] Jie Yang, Xiaolei Zhu, Thomas JA Wolf, Zheng Li, J Pedro F Nunes, Ryan Coffee, James P Cryan, Markus Gühr, Kareem Hegazy, Tony F Heinz, et al. Imaging cf3i conical intersection and photodissociation dynamics with ultrafast electron diffraction. *Science*, 361(6397):64–67, 2018.

[9] Thomas JA Wolf, DM Sanchez, J Yang, RM Parrish, JPF Nunes, M Centurion, R Coffee, JP Cryan, M Gühr, K Hegazy, et al. The photochemical ring-opening of 1, 3-cyclohexadiene imaged by ultrafast electron diffraction. *Nature chemistry*, 11(6):504–509, 2019.

[10] Cristian Manzoni, Oliver D Mücke, Giovanni Cirmi, Shaobo Fang, Jeffrey Moses, Shu-Wei Huang, Kyung-Han Hong, Giulio Cerullo, and Franz X Kärtner. Coherent pulse synthesis: towards sub-cycle optical waveforms. *Laser & Photonics Reviews*, 9(2):129–171, 2015.

[11] Philipp Kukura, David W McCamant, and Richard A Mathies. Femtosecond stimulated raman spectroscopy. *Annu. Rev. Phys. Chem.*, 58:461–488, 2007.

[12] Weijie Hua, Sven Oesterling, Jason D Biggs, Yu Zhang, Hideo Ando, Regina de Vivie-Riedle, Benjamin P Fingerhut, and Shaul Mukamel. Monitoring conical intersections in the ring opening of furan by attosecond stimulated x-ray raman spectroscopy. *Structural Dynamics*, 3(2):023601, 2016.

[13] S Miyabe and P Bucksbaum. Transient impulsive electronic raman redistribution. *Physical review letters*, 114(14):143005, 2015.

[14] Wolfgang Domcke, David Yarkony, and Horst Köppel. *Conical intersections: electronic structure, dynamics & spectroscopy*, volume 15. World Scientific, 2004.

[15] Hiroyuki Tamura, Shinkoh Nanbu, Toshimasa Ishida, and Hiroki Nakamura. Ab initio nonadiabatic quantum dynamics of cyclohexadiene/hexatriene ultrafast photoisomerization. *The Journal of chemical physics*, 124(8):084313, 2006.

[16] H Tao, TK Allison, TW Wright, AM Stooke, C Khurmi, J Van Tilborg, Y Liu, RW Falcone, A Belkacem, and TJ Martinez. Ultrafast internal conversion in ethylene. i. the excited state lifetime. *The Journal of chemical physics*, 134(24):244306, 2011.

[17] Takuya Horio, Takao Fuji, Yoshi-Ichi Suzuki, and Toshinori Suzuki. Probing ultrafast internal conversion through conical intersection via time-energy map

of photoelectron angular anisotropy. *Journal of the American Chemical Society*, 131(30):10392–10393, 2009.

[18] AMD Lee, JD Coe, S Ullrich, M-L Ho, S-J Lee, B-M Cheng, MZ Zgierski, IC Chen, TJ Martinez, and Albert Stolow. Substituent effects on dynamics at conical intersections: α, β-enones. *The Journal of Physical Chemistry A*, 111(47):11948–11960, 2007.

[19] Daniel Keefer, Sebastian Thallmair, Spiridoula Matsika, and Regina de Vivie-Riedle. Controlling photorelaxation in uracil with shaped laser pulses: A theoretical assessment. *Journal of the American Chemical Society*, 139(14):5061–5066, 2017.

[20] Spiridoula Matsika, Michael Spanner, Marija Kotur, and Thomas C Weinacht. Ultrafast relaxation dynamics of uracil probed via strong field dissociative ionization. *The Journal of Physical Chemistry A*, 117(48):12796–12801, 2013.

[21] Stephen Butterworth et al. On the theory of filter amplifiers. *Wireless Engineer*, 7(6):536–541, 1930.

[22] Shaul Mukamel and Saar Rahav. Ultrafast nonlinear optical signals viewed from the molecule?s perspective: Kramers–heisenberg transition-amplitudes versus susceptibilities. In *Advances in atomic, molecular, and optical physics*, volume 59, pages 223–263. Elsevier, 2010.

[23] E Allaria, D Castronovo, P Cinquegrana, P Craievich, Massimo Dal Forno, MB Danailov, G D'Auria, A Demidovich, G De Ninno, S Di Mitri, et al. Two-stage seeded soft-x-ray free-electron laser. *Nature Photonics*, 7(11):913–918, 2013.

[24] Philipp Dijkstal, Alexander Malyzhenkov, Sven Reiche, and Eduard Prat. Demonstration of two-color x-ray free-electron laser pulses with a sextupole magnet. *Physical Review Accelerators and Beams*, 23(3):030703, 2020.

[25] Jonathan Owen Tollerud, Giorgia Sparapassi, Angela Montanaro, Shahaf Asban, Filippo Glerean, Francesca Giusti, Alexandre Marciniak, George Kourousias, Fulvio Billè, Federico Cilento, et al. Femtosecond covariance spectroscopy. *Proceedings of the National Academy of Sciences*, 116(12):5383–5386, 2019.

[26] Jochen Mikosch and Serguei Patchkovskii. Coincidence and covariance data acquisition in photoelectron and-ion spectroscopy. i. formal theory. *Journal of Modern Optics*, 60(17):1426–1438, 2013.

[27] Xiaoji G Xu, Stanislav O Konorov, John W Hepburn, and Valery Milner. Noise autocorrelation spectroscopy with coherent raman scattering. *Nature Physics*, 4(2):125–129, 2008.

[28] Luca Gammaitoni, Peter Hänggi, Peter Jung, and Fabio Marchesoni. Stochastic resonance: a remarkable idea that changed our perception of noise. *The European Physical Journal B*, 69(1):1–3, 2009.

[29] Andrew M Weiner. Femtosecond pulse shaping using spatial light modulators. *Review of scientific instruments*, 71(5):1929–1960, 2000.

[30] Andy Rundquist*, Jon Broman, David Underwood, and David Blank. Polarization-dependent detection of impulsive stimulated raman scattering in α-quartz. *Journal of Modern Optics*, 52(17):2501–2510, 2005.

[31] Nirit Dudovich, Dan Oron, and Yaron Silberberg. Single-pulse coherently controlled nonlinear raman spectroscopy and microscopy. *Nature*, 418(6897):512–514, 2002.

[32] Andreas Wituschek, Lukas Bruder, Enrico Allaria, Ulrich Bangert, Marcel Binz, Roberto Borghes, Carlo Callegari, Giulio Cerullo, Paolo Cinquegrana, Luca Giannessi, et al. Tracking attosecond electronic coherences using phase-manipulated extreme ultraviolet pulses. *Nature communications*, 11(1):1–7, 2020.

[33] Caroline Arnold, Oriol Vendrell, Ralph Welsch, and Robin Santra. Control of nuclear dynamics through conical intersections and electronic coherences. *Physical review letters*, 120(12):123001, 2018.

Chapter 8

Resonant Inelastic X-ray Spectroscopy

In the following Chapter, we present a simple overview of the Resonant Inelastic X-ray Scattering (RIXS) technique. We subsequently exploit its potential through an experiment held at the MagneDyn beamline of the FERMI FEL. Finally, we perform a simulation aimed at the obtaining the final design of the new spectrometer which will be used at the new RIXS beamline FURKA at SwissFEL.

8.1 Introduction to RIXS

Resonant Inelastic X-ray Scattering is a photon-in-photon-out spectroscopy for which one can, in principle, measure the energy, momentum, and polarization change of the scattered photons. The change in energy, momentum, and polarization of the photon are transferred to intrinsic excitations of the material under investigation, thus providing information about those excitations. RIXS is a resonant technique in which the energy of the incident photon is chosen to coincides (resonates with) one of the atomic X-ray transitions of the system. The resonance can enhance the inelastic scattering cross-section by many orders of magnitude, offering a unique way to probe charge, magnetic, and orbital degrees of freedom on selective atomic sites in a crystal [1–3]. Compared to other scattering techniques, RIXS has a number of unique features: *i.e.*, it covers a larger scattering phase-space, it is polarization dependent, it is element and orbital specific, bulk sensitive, and requires only small volumes of the sample. In fact, compared to other scatterers such as neutrons and electrons, an X-ray photon has much more energy, and the scattering phase space available to X-rays is therefore correspondingly larger. Hence, RIXS can probe the full dispersion of low energy excitations in solids (see figure 8.1) which is not possible with photon scattering experiments in the visible or infrared range. RIXS is also element and orbital specific: chemical sensitivity arises by tuning the incident photon energy to specific atomic transitions (absorption edges) of the different types of atoms in the studied material. RIXS can even differentiate between the same chemical element at sites with inequivalent chemical bondings, different valencies or at inequivalent crystallographic positions, when the absorption edges in these cases are distinguishable (this is the atomic shift we used for select a single Carbon atom in Chapter 6). In addition, the type of information that may be gleaned about the electronic excitations can be varied by tuning to different X-ray edges of the same chemical element since the photon excites different core-electrons into different

valence orbitals for each edge. In principle RIXS can probe a very broad class of intrinsic excitations of a system, and shows a finite cross-section for probing the energy, momentum and polarization dependence of many interactions such as the electron-hole continuum and excitons in band metals and semiconductors, charge transfer and *dd*-excitations in strongly correlated materials, and lattice excitations to name a few. Furthermore, magnetic excitations are also symmetry-allowed in RIXS, since the orbital angular momentum of incident photons can be transferred to the spin angular momentum of electrons. This versatility of RIXS is at the same time an advantage and a complicating factor, since different types of excitations are generally present in a single RIXS spectrum. The generic advantages of the RIXS technique listed above may raise the question on the reasons behind this spectroscopic technique not be as widely used as angle-resolved photoemission (ARPES) or neutron scattering. The main limitation is that the RIXS process is very photon-hungry, *i.e.,* it requires an extreme high incident photon flux to obtain enough scattered photons to collect spectra with a high enough resolution in energy and momentum in a reasonable time. With a required resolving power $\frac{E}{\Delta E} \sim 10^{-4}$, RIXS has been a real challenging technique to use. Up until a few years ago this has limited RIXS experiments to measuring energy losses on the order of half an eV or greater. Thus neutron scattering and ARPES offered a more direct examination of the low energy excitations near the Fermi level. However, recent progress in RIXS instrumentation combined with the advent of FELs have recently elevate RIXS into an important condensed matter physics tool for probing elementary excitations in solids. The elementary excitations of a material determine many of its important physical properties, including transport properties and its response to external perturbations. Understanding the excitation spectrum of a system is fundamental in order to to understand the system itself. In this respect, strongly correlated electron materials, *e.g.,* transition-metal oxides, are of special interest because the low-energy electronic properties are determined by high-energy electron-electron interactions (energies on the order of eVs). A set of quantum many-body problems emerge from these strong interactions and correlations, the understanding of which lies at the heart of present day condensed matter physics. This many-body physics is often explained through model Hamiltonians requiring a set of parameters to be determined experimentally. RIXS, along with other spectroscopic techniques, can play an important role there, though we note that this technique is applicable to many other materials and is, of course, not limited to correlated systems. In the following, we discuss the relevant excitation energy and momentum scales for which RIXS can probe the excitation spectrum of a solid. We then briefly introduce the kinds of elementary excitations that are accessible to RIXS.

8.2 Elementary excitations

Plasmons

Plasmon are described as sollective density oscillations of an electron gas. They can be observed by inelastic X-ray scattering (IXS) or by optical probes since they occur at finite energy for transferred momentum $|\vec{q}| = 0$. Plasmon-like excitations were also observed early on in RIXS [5], but their resonant enhancement with respect to IXS is weak, and little work has been done since.

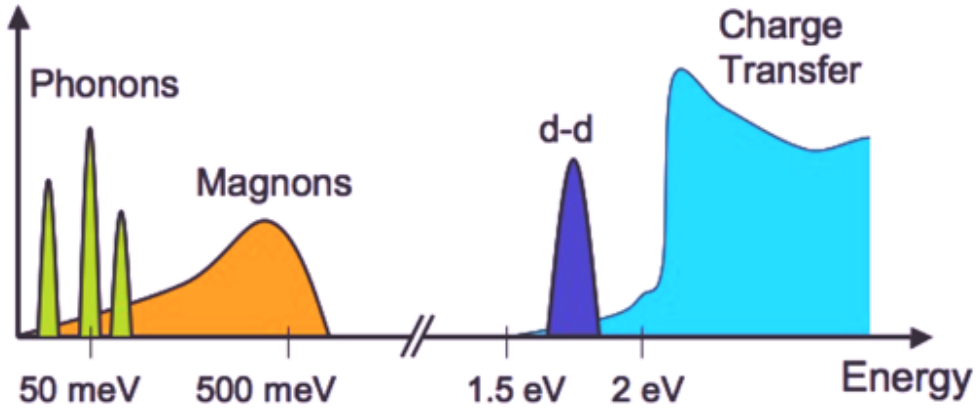

Figure 8.1: *Different elementary excitations in condensed matter systems and their approximate energy scales in strongly correlated electron materials such as transition-metal oxides. Image adapted from [4].*

Charge-transfer excitations

Charge transport in a condensed matter system is determined by the energetics of moving electrons from one site to another. In a transition-metal oxide, there are two relevant energy scales for this process. The first is the energy associated with an electron hopping from a ligand site to a metal site. This is known as the charge transfer energy, Δ, where $\Delta = E(d_{n+1}L) - E(d_n)$, and L represents a hole on the ligand site. The second energy scale is the energy U, associated with moving a d-electron from one metal site to another where $U = E(d_{n+1}) + E(d_{n-1}) - 2E(d_n)$. Strongly correlated insulators may be classified according to which of these two energies is the larger [6]. If $U > \Delta$, then the gap is a the charge transfer type and the system is said to be a charge-transfer insulator. On the contrary, if $U < \Delta$, then the gap is controlled by the $d - d$ Coulomb energy and the system is said to be a Mott-Hubbard insulator [7]. The bulk of interesting transition metal oxide compounds such as cuprates, nickelates and manganites lie in the charge transfer limit. This means that the lowest lying excitations across the optical gap are charge transfer excitations which, therefore, are of central importance in these materials. Key questions include the size of the gap (typically on the order of a few eV) and the nature of the excitations can thus be answered using RIXS.

Crystal-field and orbital excitations

Many strongly correlated systems exhibit an orbital degree of freedom, *i.e.*, the valence electrons can occupy different sets of orbitals. Orbitally active ions are also magnetic since they possess a partially filled outer shell. This orbital degree of freedom determines many physical properties of solids, and are an important aspect of strongly correlated systems. In many Mott insulators this orbital physics is governed by the crystal field: the levels of the orbitally active ion are split and the orbital ground state is uniquely determined by local, single-ion considerations. The orbital excitations from this ground state are transitions between crystal field levels. Crystal field transitions between different d-orbitals are called $d - d$ excitations. Such excitations are currently routinely seen by RIXS and are now well understood.

Magnetic excitations

Magnetism and long-range magnetic ordering are arguably the best known and most studied consequences of the electron-electron interactions in solids. When usual magnetic order sets in, be it either a ferromagnetic, ferrimagnetic, or antiferromagnetic type, the global spin rotation symmetry in the material is broken. As a result characteristic collective magnetic excitations emerge. The resulting low-energy quasiparticles, the magnons, and the interactions between them determine all low temperature magnetic properties. Magnon energies can extend up to $\sim 0.3\ eV$ (*e.g.*, in cuprates) and their momenta up to ~ 1 Å [8]. In K-edge RIXS bi-magnon excitations and their dispersions have also been observed [9]. A melting of the long-range ordering, can result in the formation of spin-liquid ground states. Spin liquids potentially have elusive properties such as high-temperature superconductivity or topological order, which one is only beginning to explore and understand. Some of the more exotic magnetic excitations that emerge from these ground states, such as spinons and triplons can also be observed by RIXS [10].

Phonons

Phonons are the quantized lattice vibration modes of a solid possessing a periodic structure. These are bosonic modes with energies typically below 0.1 eV, so that the detection of single phonon excitations has been possible within the last decade, *e.g.*, loss features were resolved for the first time with RIXS only in 2010, at the Cu L- [8] and K-edge [11, 12]. The study of phonons in RIXS promises quantitative investigations of the electron-phonon coupling [13] opening new insight on Cooper pairs formation mediate by lattice dynamics.

8.3 The RIXS process

The picture of the Resonant Inelastic X-ray Scattering process is easily explained in terms of an example. Since the experiment we are later going to present is based on Cu_2O, we choose a copper-oxide material as a typical sample, but it should be stressed once more that the focus of RIXS on transition-metal oxides is something of an accident of history and is not a fundamental limitation of the technique. In a copper-oxide material, one can tune the incoming photon energy to resonate with the copper K,L, or M absorption edges, where in each case the incident photon promotes a different type of core electron into an empty valence shell, see figs. 8.2 a) e b). The electronic configuration of Cu^{2+} is $1s^2 2s^2 2p^6 3s^2 3p^6 3d^9$, with the partially filled $3d$ valence shell characteristic of transition metal ions. The copper K-edge transition $1s \rightarrow 4p$, is around 9000 eV, thus in the hard X-ray regime. The $L_{2,3}$ edge $2p \rightarrow 3d$ ($\sim 900\ eV$) and $M_{2,3}$ edge $3p \rightarrow 3d$ ($\sim 80\ eV$) are soft X-ray transitions. Alternatively, by tuning to the O K-edge, one can choose to promote an O $1s$ to an empty $2p$ valence state, which takes ~ 500 eV. After absorbing a soft or hard X-ray photon, the system is in a highly energetic, unstable state: a hole deep in the electronic core is present. The system quickly decays from this intermediate state, typically within $1 - 2$ femtoseconds. Decay is possible through different processes, such as via an Auger decay, where an electron fills the core hole while simultaneously ejecting another electron from the atom. This non-radiative decay channel is not relevant for RIXS, which instead is governed by fluorescent decay, in which the empty core-state is filled by an electron and at the same time a photon is

emitted. There are two different scattering mechanisms by which the energy and momentum of the emitted photon can change from the incident one. These are known as direct and indirect RIXS. The distinction between these two is discussed below.

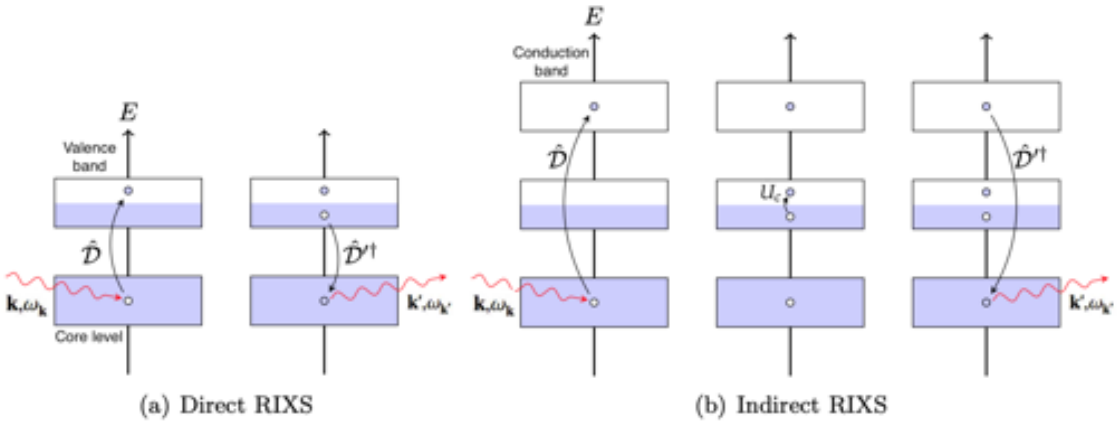

Figure 8.2: *a) In a direct scattering, the incident photon excites a core electron into an unoccupied state of a partially filled valence band slightly above the Fermi level. Afterwards, an electron from an occupied valence state slightly below the Fermi level decays and annihilates the core hole, and a photon is emitted. In this case, the scattering is inelastic and the system is left into an excited state, directly induced by the electron-photon interaction. This RIXS process creates a valence excitation with momentum $\vec{q} = \vec{k}' - \vec{k}$ and energy $\omega = \omega_k - \omega_{k'}$. b) In an indirect RIXS process, an electron is excited from a deep-lying core level into the valence shell. Excitations are created through the Coulomb interaction U_c between the core hole (and in some cases the excited electron) and the valence electrons. Image adapted from [14].*

Resonant inelastic X-ray scattering processes are classified as either direct or indirect [15, 16]. This distinction is useful because the cross-sections for each phenomena is quite different. When direct scattering is allowed, it is the dominant inelastic scattering channel, with indirect processes contributing only in higher orders. In contrast, for the large class of experiments for which direct scattering is forbidden, RIXS relies exclusively on indirect scattering channels. In direct RIXS, the incoming photon promotes a core-electron to an empty valence band state, see fig. 8.2 a). Subsequently an electron from a different state in the valence band decays and annihilates the core hole. The net result is a final state with an electron-hole excitation, since an electron was created in an empty valence band state and a hole in the filled valence band. The electron-hole excitation can propagate through the material, carrying momentum $\vec{q}$ and energy ω. Momentum and energy conservation require that $\vec{q} = \vec{k}' - \vec{k}$ and $\omega = \omega_k - \omega_{k'}$, where $\vec{k}$ ($\vec{k}'$) and ω_k (ω'_k) are the momentum and energy of the incoming (outgoing) photon, respectively.

8.3.1 Direct RIXS

For direct RIXS to occur, both the initial transition between the initial core state and the valence states, and the final transition from a different valence state to fill the core hole, must be allowed. As an example, the nitial dipolar transition can be a $1s \rightarrow 2p$ followed by the decay of a different electron in the $2p$ band from $2p \rightarrow 1s$, in wide-band gap insulators. This is the case at the K-edge of O, C, and Si. At L-edges of transition-metal, dipole transitions give rise to direct RIXS via $2p \rightarrow 3d$ absorption and subsequent

$3d \rightarrow 2p$ decay. In all these cases, RIXS probes the valence and conduction states directly. Although the direct transitions into the valence shell dominate the spectral line shape, the spectral weight can be affected by interactions in the intermediate-state driven by, for example, the strong core-hole potential.

8.3.2 Indirect RIXS

The indirect RIXS process is slightly more complicated. For pure indirect RIXS to occur, photoelectric transitions from the core-state to conduction-band states must be weak. Instead, the incoming photon promotes a core-electron into an empty state several eVs above the Fermi level. Subsequently the electron from the same state decays to fill the core hole, as can be seen in fig. 8.2 b). The most studied example is RIXS at the transition-metal K-edges ($1s \rightarrow 4p$). If no other interactions are present, the final state of the process coincide with the initial state of the system, and therefore inelastic scattering precesses cannot occur. However, in the highly excited and unstable intermediate state, the core hole and the excited electron are strongly interacting with each other and with the valence electron of the system. In particular, the core hole Coulomb interaction is usually the strongest and dominates the intermediate state dynamics. This strong interaction, usually described as a core hole potential U_c, can produce an excitation in the valence band of the system. In this way, after the $4p \rightarrow 1s$ decay, the system is left into an excited state, which is not induced by the mere electron-photon interaction, but it is indirectly produced by the core hole potential. Indirect RIXS is thus due to shakeup excitations created by the intermediate core hole state.

8.3.3 The Kramer-Hisenberg dispersion

In RIXS, the electron is taken from a ground state with energy E_i, to a final-state with excitations and an energy E_f. The energy and momentum of the excitation is determined by the difference in photon energy $\omega_k - \omega_{k'}$ and momentum $\vec{k}' - \vec{k}$, respectively. The RIXS intensity can in general be written in terms of a scattering amplitude, that is the Kramer-Hisenberg dispersion relation [17]

$$I_{RIXS} \propto \frac{d^2\sigma}{d\Omega_{k'} d(\hbar\omega_{k'})} = \frac{\omega_{k'}}{\omega_k} \sum_{|f\rangle} \left| \sum_{|n\rangle} \frac{\langle f|\hat{\mathcal{D}}'^{\dagger}|n\rangle\langle n|\hat{\mathcal{D}}|i\rangle}{E_i - E_n + \hbar\omega_k + i\frac{\Gamma_n}{2}} \right|^2 \delta(E_i - E_f + \hbar\omega_k - \hbar\omega_{k'}) \quad (8.1)$$

which represents the probability of the emission of photons of energy $\hbar\omega_{k'}$ in the solid angle $d\Omega_{k'}$ (centered in the $\vec{k}'$ direction), after the excitation of the system with photons of energy $\hbar\omega_k$. $|i\rangle$,$|n\rangle$,and $|f\rangle$ are the initial, intermediate and final states of the system with energy E_i ,E_n, and E_f respectively, while the delta function ensures the energy conservation during the whole process. The core hole intrinsic linewidth of the intermediate state Γ_n is assumed to be independent of the intermediate state energy, and ranges from 1 eV of transition metal edges to 8 eV of actinides L edges, which correspond to a core hole lifetime $\Delta t = \frac{\hbar}{\Gamma_n}$ from $\sim 2\ fs$ down to $\sim 0.2\ fs$. The optical transition operator $\hat{\mathcal{D}} = \hat{\vec{p}} \cdot \hat{\vec{A}}$ describes the dominant term of the electron-photon interaction in the low energy perturbative expansion of quantum electrodynamics. Expanding the vector potential $\hat{A}$ in terms of plane waves around any lattice site i, the optical transition operator $\hat{\mathcal{D}}$ ($\hat{\mathcal{D}}'^{\dagger}$) can be written as a function of the momentum $\vec{k}$ ($\vec{k}'$), and polarization

$\vec{\epsilon}$ ($\vec{\epsilon}'^{\dagger}$) of the incident (scattered) photon, as [4]

$$\mathcal{D} = \frac{1}{\sqrt{N}} \sum_{i}^{N} e^{i\vec{k}\cdot(\hat{r}_i + \vec{R}_i)} \vec{\epsilon} \cdot \hat{p}_i \tag{8.2}$$

where $\hat{r}_i$ and $\hat{p}_i$ are the position and momentum operators of the electron respect to the lattice site $\vec{R}_i$. In the intermediate state, virtual transitions have a finite probability in an energy range comparable with the core hole broadening Γ_n. The final state may or may not coincide with the initial state of the system.

8.4 RIXS experiment at FERMI

In this section we present an overview of the Time Resolved RIXS experiment performed on June 2020 at the MagneDyn beamline at the FERMI FEL. Given the well know $M_{2,3}$ transition of Cu ($\sim 76\ eV$), many RIXS experiments have focused their attention on the study of Cuprates [8, 11, 12, 18] which offers an extremely interesting pathway towards high temperature superconductors. In this experiments, we focalized out attention on cuprous oxide Cu_2O for a different reason. So far, many photocatalysts have been reported to decompose water into H_2 and O_2 under UV light irradiation [19–21]. From the view point of solar energy conversion, however, a photocatalyst which works under visible light irradiation ($> 400\ nm$) is indispensable. Such a photocatalyst has been found in Cu_2O [22], a well-known p-type semiconductor, that offers a narrow direct band gap [23] (2.0-2.2 eV) that is coupled with the appropriate positioning of its conduction band just above the reduction potential of water, thus acting as a photocatalyst for overall water splitting under visible light irradiation ($\leq$600 nm). Even if its photocatalyst property has been demonstrated, the reaction mechanism on Cu_2O is still under investigation. In this work we focused our attention in the elastic peak intensity change against the time delay between a 400 nm pump (second harmonic of a Ti:Sa laser) and a FEL probe (on the $M_{2,3}$ edge) in order to understand how the Cu^{1+} sites participate to the charge transfer and electron trapping. If the time occurring for the charge transfer process is longer than the the electron trapping process, we expect a change in the absorption at the $M_{2,3}$ edge of Cu and a subsequent change in the diffuse scattering.

Thus we aimed at measuring the charge trapping dynamics by taking advantage of (tr-RIXS). We propose to measure the tr-RIXS spectra resonant to the core transitions $M_{2,3}$ of Cu, after photoexcitation across the bandgap of the semiconductor and thereby investigate the charge and energy transfer dynamics. Here the femtosecond optical excitation pump is used to trigger the non-equilibrium dynamics. The X-ray probe, tuned to the resonant energy of Cu, monitors these transient dynamics as a function of time elapsed from the photoexcitation. In a direct resonant inelastic scattering process the hole is filled by a valence band electron upon emission of an X-ray photon of frequency $\omega_{k'}$ and momentum $\vec{k}'$, while the indirect process involves intermediate excitations in the core shell which are reflected in the energy and momentum of the scattered photon, as schematized in fig 8.3 a) for Cu^{1+}. Thus, since resonant X-ray absorption is element and orbital specific, the RIXS probe records snapshots of the occupied and unoccupied transient states in the electronic structure of the dopant atom and can directly monitor charge trapping and exciton localization processes [4]. These excitations will differ in nature depending on the position of the Fermi level within the semiconductor

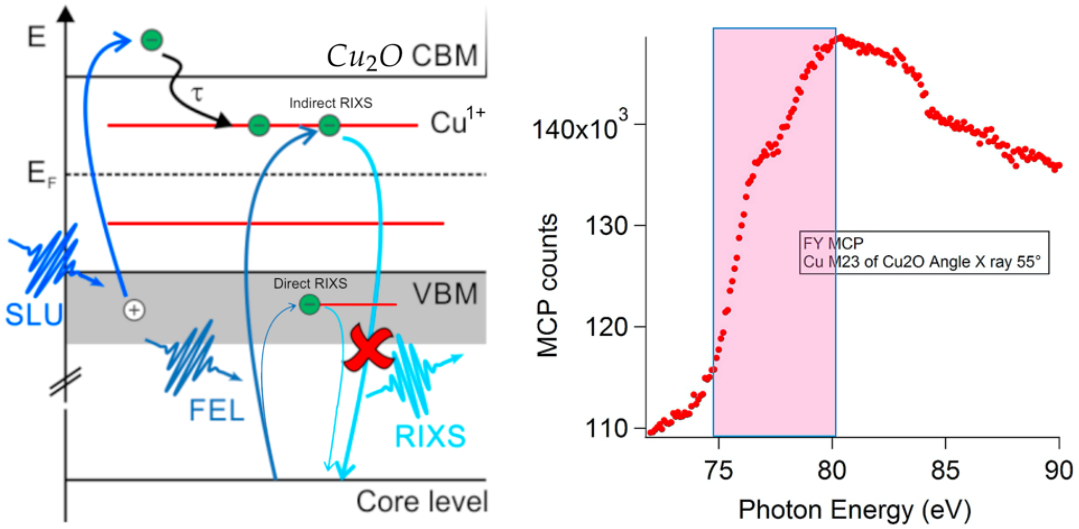

Figure 8.3: *Schematic of the expected RIXS process for the case of Cu^{1+}. Here the $M_{2,3}$ transition falls in the indirect RIXS regime. The trapping of electrons is expected to quench the scattering channel. b) Reference $M_{2,3}$ edge XAS taken at the BACH beamline.*

bandgap. Thanks to the FEL time resolved RIXS, our expected results are twofold: (i) Since transient exciton localization may affect the unoccupied density of states, we expect to observe spectral changes of the elastic component of the RIXS spectrum, which is inherent to the unoccupied density of states through the absorption process. (ii) On the other hand, charge trapping formation and dynamics will affect the inelastic component of the RIXS spectra. Given the very low intensity on the inelastic band peak, in this experiment we focused our attention only on the elastic peak which nonetheless gave us precious information on the Cu^{1+} dynamic upon excitation.

The Spectrometer

The Scienta XES 355 [24] is equipped with three reflecting gratings mounted at different fixed angles on a Rowland circle geometry: the entrance slits, the grating surfaces and the plane of the detector lie on the same circle for each grating.

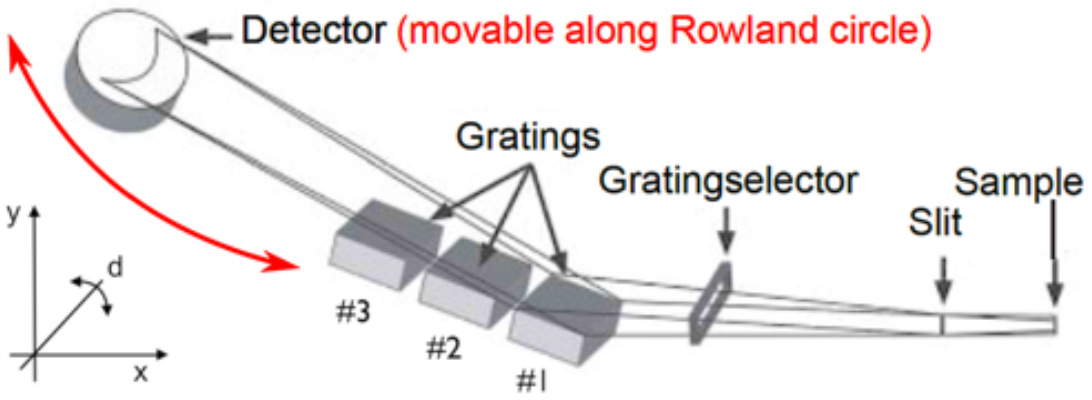

Figure 8.4: *Optical arrangement of Scienta XES 355. Image adapted from [25].*

The spectrometer is designed so that the detector images the entrance slits (see figure **??**): the luminosity and the resolution reach the maximum when the source is placed at the entrance slits. In this condition the maximum acceptance angle ($0 - 5°$ parallel to the slit, $0 - 0.5°$ perpendicular to the slit) is achieved. The entrance width can be adjusted in the range $0 - 100\ \mu m$; the two blades can rotate around an axis parallel to the slit. As the slits close, the spectrometer resolution can be improved. Selection of grating in use is carried out by means of two shutters (the grating selector), which define the illumination of the grating selected. When high resolution is required, a recommended (calculated) optimum part of the grating should be illuminated. The optical axis of the spectrometer can be adjusted by rotating the whole spectrometer flange by $\pm 2°$, which corresponds to an up-down movement of the entrance slit by $\pm 10\ mm$. When the gratings are changed, the light path to the gratings has to be adjusted.

The Gratings

The three spherical gratings are fixed-mounted on a precision slab together with an entrance slit. The gratings are made of quartz glass and are coated, each one with a dimension of $45 \times 25 \times 15\ mm^3$. The Rowland circles defined by the gratings intersect at the entrance slit. The three gratings cover an energy range of $50 - 1500\ eV$ in first order; the choice of the incidence grating angle is governed by the reflectivity in the X-ray range. The specification data of the three gratings are summarised below:

Grating	Radius	Groove density	Grazing angle	Operating range	Blaze energy
#1	$5\ m$	$1200\ l/mm$	$1.9\ °$	300 - 1500 eV	$\sim 400\ eV$
#2	$5\ m$	$400\ l/mm$	$2.6\ °$	100 - 450 eV	$\sim 275\ eV$
#3	$3\ m$	$300\ l/mm$	$5.4\ °$	20 - 200 eV	$\sim 100\ eV$

Table 8.1: *The specification data of the three gratings. Table adapted from [25].*

The Detector

The diffracted photons are collected on a two-dimensional $40\ mm$ diameter circle detector based on three micro-channel plates (MCPs). The incoming photons are converted in a cloud of electrons by a photon- multiplier stage through a strong electric field. Then, a phosphor screen intercepts the outgoing electrons emitting visible sparks, the complessive detection efficiency is of the order of 30%. The detector is free to move on the Rowland circle in a three-axis coordinate system using a X/Y-table translator and a detector angle rotator, in order to intercept the focus position at the various energies tangential to the Rowland circle. Finally, a CCD Basler camera with a resolution of roughly $550 \times 550\ px$ images the phosphor screen through a viewport flange, tracing the detected photons.

8.4.1 Methods

The experiment had been performed at the Magnedyn beamline on a Cu_2O sample. The RIXS photons were measured using the spectrometer Scienta XES355 previously presented [24], which hosts a movable sample stage to vary the X-Ray incidence angle on the sample in the range from 20 to 50 degrees with respect to the surface and an X-Ray emission spectrometer with a 87 degrees fixed angle to the incoming X-Rays. The

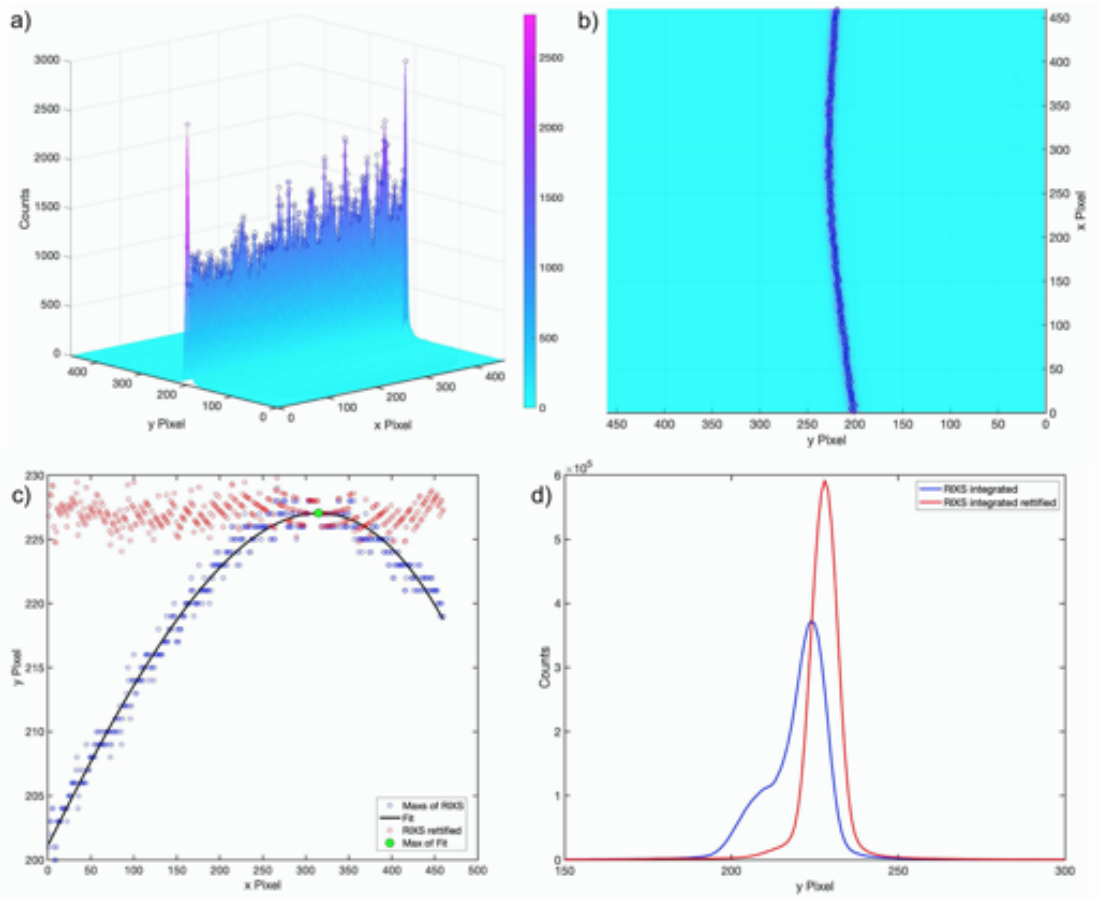

Figure 8.5: *a) and b) show the detector photon counts for each pixel from two different perspectives. The blue dot on top represent the maximum position for each pixel row in the y direction. In c) we show the set of blue dots, and the fit used to straighten up the data. The unbent data are shown as red dots. In d) it is presented the integral of the bent (in blue) and unbent (red) RIXS traces. The quasi-elastic scattering from the charge order appears symmetric and is the only spectral feature influenced by the pump. The shoulder feature on the left is a combination of dd excitations and Cu^{1+} emission, and charge transfer excitations.*

incoming beam is focused on the sample by the Magnedyn KB system. The spectrometer geometry required linear vertical polarization of the FEL pulses. The Cu_2O sample was excited at 400 nm using the second harmonic of a Ti:Sa femtosecond laser, and the RIXS spectra were acquired at the at the Cu $M_{2,3}$ edge (see figure 8.3 b)) using the FERMI FEL-2 at 50 Hz. Measurements were performed in a pump-unpumped configuration for four delays $\Delta t = [0.2, 0.5, 1.0, 2, 0]$ ps and two energies $\lambda_{FEL} = [76.48, 78.49]$ eV for a total of 25 scans for each possible $[\Delta t, \lambda_{FEL}]$ pair. After acquisition, files for each $[\Delta t, \lambda_{FEL}]$ pair were put together, pump and unpumped data were separated and 3D maps were generated by counting the photons seen for each pixel (see figure 8.5 a) and b)). Per each pixel column in the x direction we found the maximum (blue dots in fig. 8.5 a), b) and c)), and using the best fit (black curve) we rettified the trace (red dots) around the max of the fit itself (green dot in 8.5 c)). The gaussian-like traces (fig. 8.5 d)) were subsequently obtained by performing an integral in the x direction. Finally, the "intensity" values for the pumped and unpumped traces (I_p and I_u, respectively) used subsequently were obtained by integrating the trace in the y direction. The error of each trace were obtained taking the square root of the counts. In the following we

present the results through the normalized difference, defined as:

$$\text{pump/unpumped difference (\%)} = \frac{I_p - I_u}{max[I_p, I_u]}. \tag{8.3}$$

The associated error is the error propagation.

8.4.2 Results

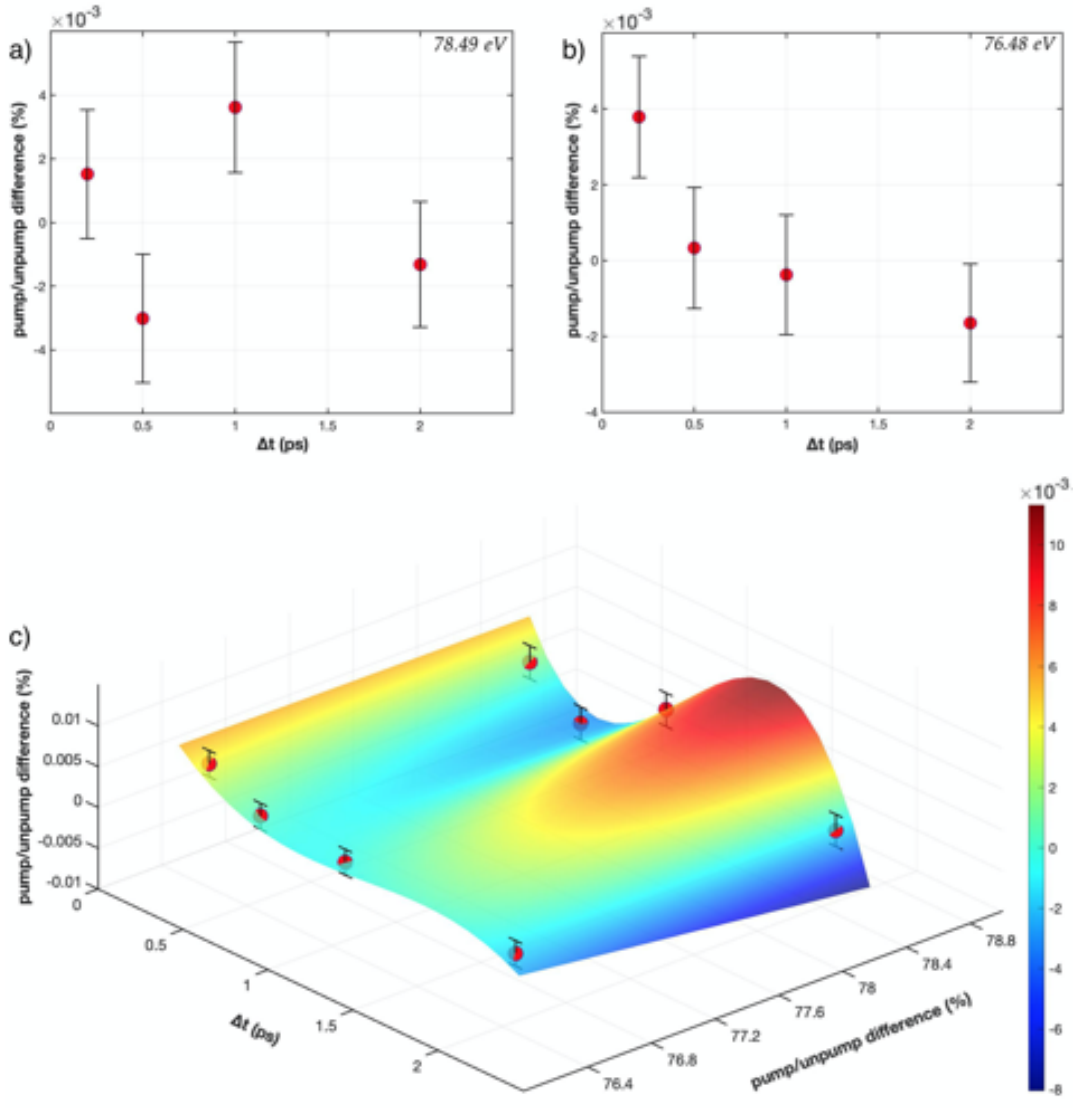

Figure 8.6: *The dynamic of the pump/unpumped difference (%) (see eq. 8.3) for an incoming beam energy of 78.49 eV a), and 76.48 eV b). In c) we show an interpolation between the points at the two different incident energies.*

In figure 8.6 we show the tr-RIXS pump/unpumped difference (%) on the elastic peak for 76.48 eV (b), and 78.49 eV (a) probe energies. Being at the top of the $M_{2,3}$ edge, the trace at 78.49 eV showed a slightly higher number of counts with respect to the other energy, which influence the error associated to the measure. Nevertheless, both

traces show a similar behaviour on the elastic peak. The other RIXS features, including the $d-d$ and charge transfer excitations and Cu^{1+} fluorescence emission, even if very low, seem to be unaffected by the pump. Furthermore we did not see any appreciable shift in the position of the elastic peak. We thus conclude that the effects observed are properties of the valence band and that the time response can directly reveal the charge dynamics of the system. Shortly after the pump, for delay time $\Delta t \leq 0.2\ ps$, we observe an increasing of the pumped peak intensity with respect to the unpumped case. The difference rapidly decrease until reaching 0 for delay time $\Delta t \leq 0.5\ ps$. Here we find the main difference: at $\Delta t \leq 1.0\ ps$ while for the lower energy, the difference between pump and unpumped traces barely moves from its previous value around 0, the difference at higher energy remarkably increased. Subsequently, at $\Delta t \leq 2.0\ ps$, both traces follows the same behaviour and the difference became more and more negative going towards higher delay times.

8.4.3 Conclusions

We reported a tr-RIXS experiment performed at the $M_{2,3}$ edge of the p-type semiconductor Cu_2O. Cu_2O has been found to be a photocatalysts in the decomposition of water into H_2 and O_2 under visible light radiation. With this in mind we explored the possibility which sees the Cu^{1+} partecipating in this reaction. Upon visible light excitation at 400 nm, an electron in the valence band in excited into the conductive band, where we expect it to be trapped in charge trapping states after few fs. This charge trapping process lasts for a time equal to its lifetime τ before undergo disexcitement. So that, we performed the tr-RIXS measurement to probe the trapping dynamics, which we should be able to see in the spectral variation of the RIXS signal. We focused our attention on the elastic peak, on which we saw an appreciable variation (within the errorbar) in its intensity for the excited (pumped) system with respect the not excited system. This measurement thus highlights the active participation of the Cu^{1+} in the charge trapping process. This is of extreme interest since, contrary to more surface-like technique, RIXS has the ability to probe the bulk to the material under investigation. We can finally conclude that the charge trapping process of Cu_2O does not merely depend on features given by the surface (in fact, since the surface is a breaking symmetry point, it easily shows defect points of the crystal which create new states for charge trapping), but rather it is a property of the material.

8.5 RIXS spectrometer for the FURKA beamline[1]

In the following section, we present the optical design of the Furka soft X-ray RIXS spectrometer to be located on the Furka beamline at SwissFEL. The spectrometer is designed to reach a resolving power above 11600 at 930 eV (Cu L-edge important, for example, for the physics of correlated cuprates) at its best resolution. With this energy taken as reference, the VLS coefficients are optimized to cancel the lineshape asymmetry (mostly from the coma aberrations) as well as minimize the symmetric aberration broadening at large grating illuminations, dramatically increasing the aberration-limited vertical acceptance of the spectrometer.

[1] Cristian Svetina, Danny Fainozzi, *et al*. Design of a soft X-Rays RIXS sprectrometer for SwissFEL. *To be submitted*, 2021.

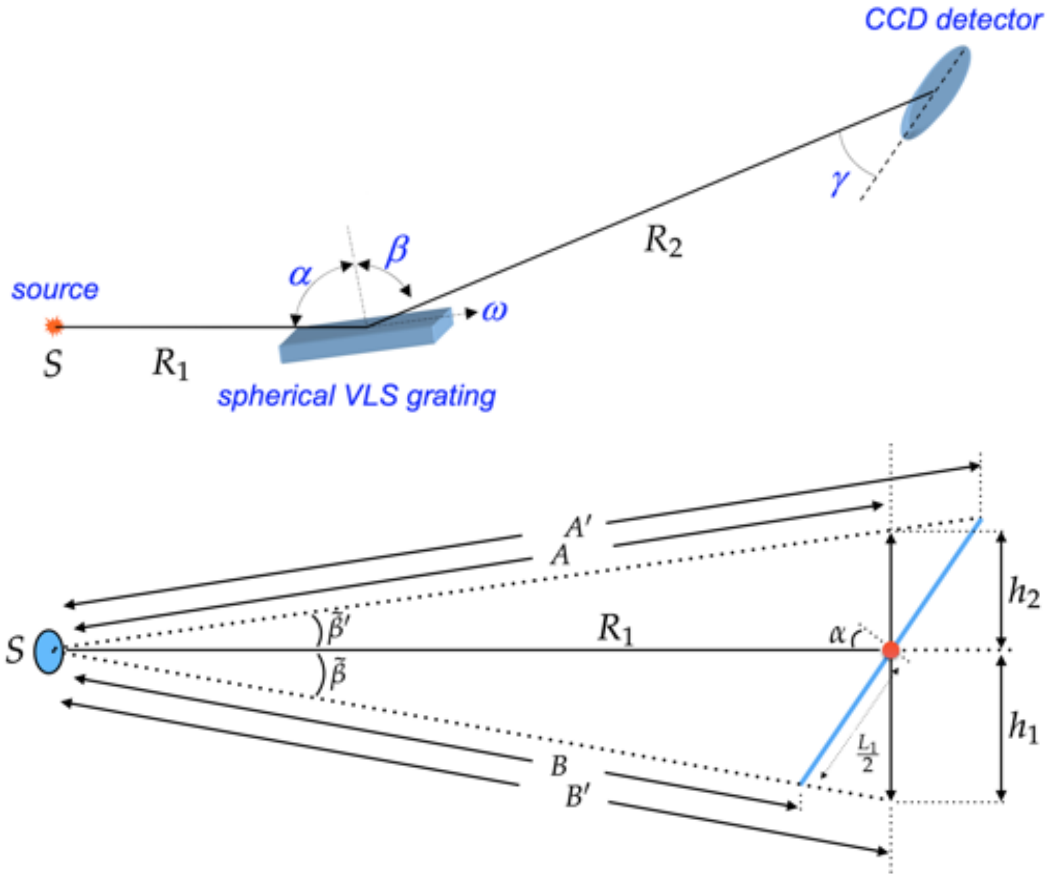

Figure 8.7: *Top - the layout configuration of the Furka grating spectrometer. Bottom - a zoom on the tilted grating which explain the need to find the value $h = h_1 + h_2$ used in the solid angle calculation.*

In order to process the spectrometer design we need three main quantities: the grating spectrometer efficiency, the grating spectrometer energy resolution ΔE, and the solid angle subtended by the grating $\Omega(\alpha, R_1)$. It is very important to note that the complete transmission T of the grating is proportional to $\Delta E \cdot \Omega(\alpha, R_1)$. The grating efficiency decreases with increasing incidence angles (α) while, on the contrary, the solid angle increases with increasing incident angles but decreases with increasing distance from the source R_1. The efficiency of the grating spectrometer was simulated with the REFLEC software [26] for a reflecting grating made of pure Si with a 30 nm Pt coating. The simulation was carried out for a density line range in between 300-3600 mm^{-1}, an incident angle range between 86-89.5 °, a grating height ranging 3-11 nm, and an incident beam energies in between 250-2000 eV. The 4D matrix generated was subsequently refined through a custom MATLAB code also used to generate the resolution and the solid angle of the grating.
The equations required to determine the resolution of a grating spectrometer are presented in the following. The grating equation states the diffraction condition (where η is the grating line density, α is the incident angle, β is the diffracted angle, m is the diffraction order, λ the wavelength, and E is the energy)

$$\sin\alpha + \sin\beta = m\eta\lambda \xrightarrow{E=\frac{hc}{\lambda}} E = \frac{hcm\eta}{\sin\alpha + \sin\beta}. \tag{8.4}$$

Here, we use the convention that the angles are measured relative to the surface normal; α and β have opposite signs if they are on opposite sides of the normal; it follows that positive orders are the inside orders. In the following we are going to consider only the first diffraction order, thus setting $m = 1$. From the perspective of the grating, a finite source size results in a finite spread ($d\alpha = \frac{\sigma_S}{R_1}$) of incident angles at a given point on the grating, where σ_S is the source size and R_1 is the distance from the source to the grating. Differentiating equation 8.4 with respect to α yields the source term. The source size Δ_S is taken as the FWHM of the source distribution, which corresponds to 2.355 times the standard deviation if the distribution is Gaussian. We define the resolution as [27, 28]

$$|dE|_S = \frac{E^2}{hc\eta}\cos\alpha d\alpha = \frac{E^2}{hc\eta}\cos\alpha\frac{\Delta_S}{R_1} \tag{8.5}$$

From the point of view of the grating, in a monochromator, the exit slit allows a finite range of diffracted angles ($d\beta = \frac{\sigma_{Ex}}{R_1}$) and hence energies to leave from the instrument, where σ_{Ex} is the exit slit size and R_2 is the distance from the grating to the exit slit. In a spectrometer, the exit slit is typically replaced by a position sensitive detector, and the resolution is determined by a Gaussian like spatial resolution rather than the hard cutoff of an exit slit. If Δ_D is the FWHM of the detector spatial resolution, then Differentiating equation 8.4 with respect to β yields the exit term3,4 spatial resolution of the detector Δ_D

$$|dE|_D = \frac{E^2}{hc\eta}\cos\beta d\beta = \frac{E^2}{hc\eta}\cos\beta\Big(\frac{\Delta_D\sin\gamma}{R_2}\Big) \tag{8.6}$$

In a high resolution grating instrument, the surface quality of the optics is a significant factor limiting the resolution, and cannot be ignored. For a grating, the slope error can be viewed as locally changing both α and β, and the contribution to the resolution can be expressed as [28, 29]

$$|dE|_{gr} = 2.355\cdot\Delta_{gr}\frac{E^2}{hc\eta}(\cos\alpha + \cos\beta) \tag{8.7}$$

where Δ_{gr} is the rms slope error (FWHM $\sim rms\cdot 2.355$, see appendix for more info) on the grating. If the optical design has additional optics, the slope error on these must also be considered. If there are mirrors upstream and downstream of the grating, then slope errors act to broaden the range of incident angles on the grating, and the effects can be found from eq. 8.4 considering the effect on α and β

$$|dE|_{opt} = 2\cdot 2.355\cdot\frac{E^2}{hc\eta}(\Delta_{pre}\cos\alpha + \Delta_{post}\cos\beta) \tag{8.8}$$

where Δ_{pre} and Δ_{post} are the *rms* slope error on the mirror pre-granting and post-grating, respectively. In our case, we chose to neglect these last terms since Δ_{pre} and Δ_{post} will be much smaller than the other parameters. The total energy resolution ΔE is found by adding the various components in quadrature, that is:

$$\Delta E(\alpha,\beta,\eta,E) = \sqrt{|dE|_S^2 + |dE|_D^2 + |dE|_{gr}^2}. \tag{8.9}$$

For our model spectrometer, we have used realistic parameters $\Delta_S = 5\ \mu m$ [30], $\Delta_D = 5\ \mu m$ [27], $\Delta_{gr} = 0.2\ \mu rad\ rms$ (which is the present technological limit for spherical optics), and $\gamma = 20^\circ$ (which grant a flat curve in its neighbourhood). In the discussion here,

for the sake of clarity, we only consider the optics needed for the vertical dispersion direction. A horizontal deflection parabolic collection mirror can be added to any of the designs and in principle does not affect the energy resolution. The maximum overall length L is given by the experimental hutch and is taken equal to $L = R_1 + R_2 = 6.4\ m$ while the minimum distance from the source was set to 1 m. The grating line density η_0, the incidence angle α_0, and the grating height h_0 are chosen such that the spectrometer resolution is equal to 80 meV at 930 eV, and the grating efficiency ΔE times the solid angle subtended by the grating $\Omega(\alpha, R_1)$ is maximized at 930 eV. This last term, grating efficiency times the grating solid angle, is of fundamental importance for the beamline: we expect to have an extremely low RIXS scattered photons per each FEL pulse, thus it is crucial that we can achieve the greatest possible outcome for the transmission. The soldi angle Ω was calculated for a square grating with dimensions $L_1 = L_2 = 28\ mm$ tilted with respect to the incidence beam (see figure 8.7). Being L_1 the tilted side we had to take into account its projection h on the parallel plane to the incoming beam. Thus, we had:

$$\Omega(\alpha, R_1) = 4 \arccos\left(\sqrt{\frac{1 + x^2 + y^2)}{(1 + x^2)(1 + y^2)}}\right) \tag{8.10}$$

where we defined

$$x = \frac{h}{2R_1} \quad \text{and} \quad y = \frac{L_2}{2R_1} \tag{8.11}$$

with the value of h given by

$$h = h_1 + h_2 = R_1(\tan\tilde{\beta} + \tan\tilde{\beta}'). \tag{8.12}$$

In figure 8.8 we show the result of the simulation. In fig 8.8 a) the simulation of $\Delta E(\alpha, \beta, \eta, E)$ against the incidence angle α and the beam energy E is presented. Here a filter is applied: the only parameter allowed after the filter application are the ones that satisfy the requirement $\Delta E(\alpha, \beta, \eta, E_0) \leq 80\ meV$, with $E_0 = 930\ eV$. The parameter allowed are shown as white dots. It is useful to notice that the energy resolution does not depend on the height of the grating, thus the filter does not impose any restrictions on the parameter h. In fig 8.8 b), c) and d) are shown the simulation of the grating efficiency $\times\Omega(\alpha, R_1)$ against the incidence α, the height of the grating h, and the lines density of the grating η respectively. The maximum of the surface is shown as a blue dot while the maximum of the filtered surface is shown as a green dot. In fig 8.8 d), the reader can see a whited wide spot on the surface: this is due to the surface being unstable for high values of η and beam energy E. A filter on the derivative has been applied to exclude such region of the surface. The outcome of the simulation gave the best parameters shown in table 8.2. There has been a significant amount of work in

$R_1\ [mm]$	$\alpha_0\ [^\circ]$	$h_0\ [nm]$	$\eta_0\ [mm^{-1}]$	$\Delta E(\alpha_0, \beta_0, \eta_0, E_0)\ [meV]$	Eff$\times\Omega(\alpha_0, R_1)$
1000	88.4	6.6	1290	79.7	2.8×10^{-6}

Table 8.2: *Parameters that maximize the quantity Efficiency $\times\Omega$ at $E = 930\ eV$ with the requirement $DeltaE(\alpha, \beta, \eta, E_0) \leq 80\ meV$.*

the development of soft X-ray RIXS spectrometers, which leaves a variety of choices for the designer, and as always, the correct choice depends to a large extent on what goal

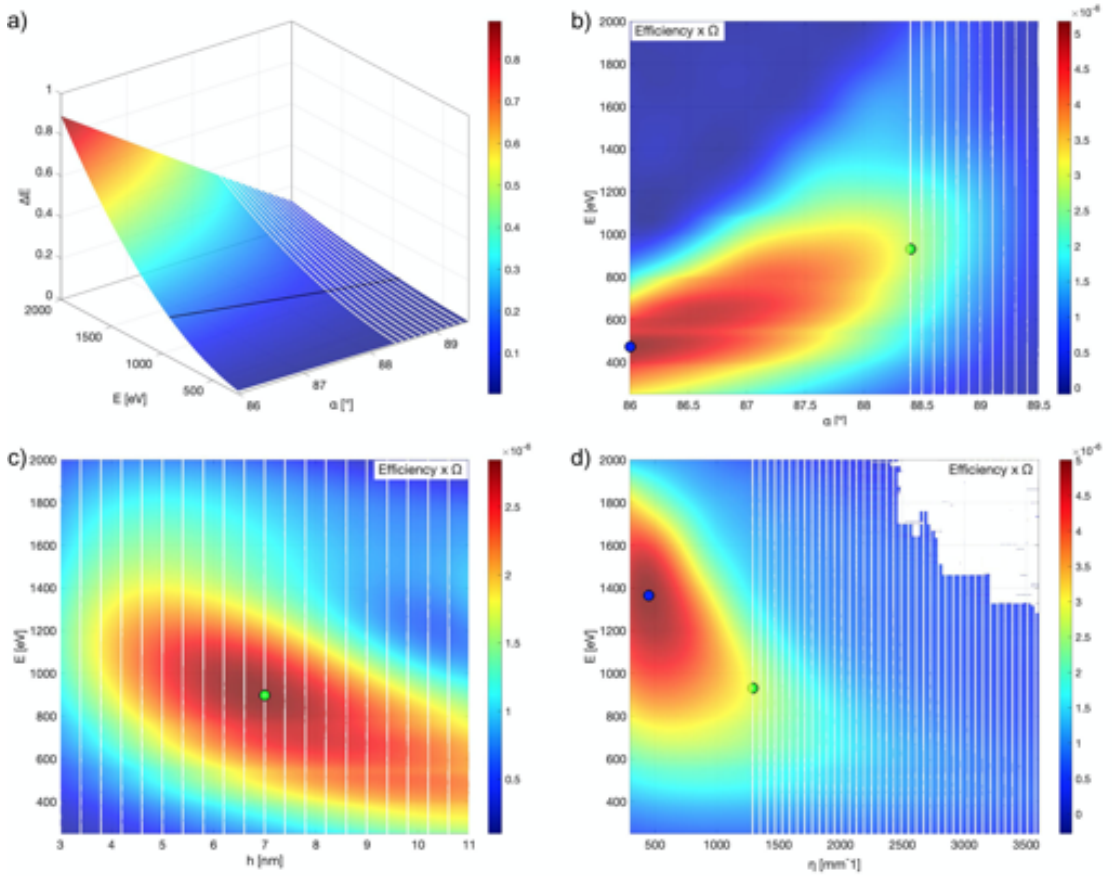

Figure 8.8: *a) the simulation of $\Delta E(\alpha, \beta, \eta, E)$ against the incidence angle α, the values of this surface is subsequently used to apply a filter on the Efficiency $\cdot\Omega(\alpha, R_1)$ surface in b). In c) and d) the simulation of $\Delta E(\alpha, \beta, \eta, E)$ against the height of the grating h and the grating line density η, respectively. For b), c) and d) the maximum of the surface is shown as a blue dot while the maximum of the filtered surface is shown as a green dot.*

is to be achieved. The RC spectrometer uses a spherical constant line density grating. The source, the grating pole, and the focus of the dispersed beam are constrained to lie on the Rowland circle. The design features several nice optical properties, in that the defocus and coma aberration terms are zero. However, this comes at a price: the focal plane is tangent to the Rowland circle and hence is near grazing. Furthermore, focusing at the grazing incidences required for soft X-rays requires a large Rowland circle (~ 100 m for energies and resolution similar to ours), and hence a very large translation of the detector to stay on the Rowland circle *i.e.,* single grating requires an unreasonable large translation of the detector to cover a wide energy range. To go from 180 to 2300 eV requires a horizontal translation of over 16 m and a vertical translation to almost 6 m above beam height. This is clearly unworkable [27]. The first step in the right direction is to consider a Variable Line Spacing (VLS) design. Using a plane figure for the grating allows one to achieve figure errors of ~ 50 $nrad$, and thus to reach the highest resolution for a given line density. The focusing property and aberration correction afforded by the VLS grating allows one to work off of the Rowland circle and tune the spectrometer magnification to suit the detector, and at the same time achieve excellent resolution over a very wide energy range.
For designs involving a VLS grating, the line density η is varied as a function of the

longitudinal position along the grating ω as

$$\eta(\omega) = \eta_0 + \eta_1\omega + \eta_2\omega^2 + \eta_3\omega^3 + ... \tag{8.13}$$

where the positive ω direction is taken as away from the source as seen in figure 8.7 top. The VLS parameters are chosen to zero all aberration terms up to η_3 at 930 eV (*i.e.*, Cu L edge). We make use of some analytic expressions to obtain the VLS coefficients, which will be subsequently used in the paper to evaluate the effect of aberrations by raytracing. Spectrometers are typically designed to have an angular acceptance as large as possible, thus their aberrations at large acceptance cannot be ignored. Another contribution to the resolution is optical aberrations, which are specific to a given optical design and must be analyzed on a case by case basis.
The grating radius R and the linear VLS term η_1 are then calculated as the analytical solutions of a system of two equations in 8.14, which are the condition on the focus to be at R_2 (bottom) plus the condition imposed on the focal curve inclination angle γ (top) to match the optimal detector inclination angle [27, 28]

$$\begin{cases} \eta_1 = \dfrac{E_0}{hc}\left(\dfrac{\cos^2\alpha_0}{R_1} + \dfrac{\cos^2\beta_0}{R_2} - \dfrac{\cos\alpha_0 + \cos\beta_0}{R}\right) \\ \tan\gamma = \dfrac{\cos\beta_0}{2\sin\beta_0 - R_2\left(\frac{\tan\beta_0}{R} + \frac{\eta_1}{\eta_0}\right)} \end{cases} \tag{8.14}$$

Given the parameter in table 8.2 and $R_1 = 1000\ mm$ and $R_2 = 5400\ mm$, eq 8.14 gave use a grating radius $R = 52949\ mm$ and the first correcting term $\eta_1 = -0.1449\ mm^{-2}$. The profile generated by the expansion until the second term should produce a profile highly asymmetric due to aberrations dominated by the (primary) coma (*i.e.*, the aberration inherent to certain optical designs or due to imperfection in the lens or other components that results in off-axis point sources such as stars appearing distorted, appearing to have a tail (coma)). With the Gaussian linewidth broadening, the aberrations deteriorate the spectrometer resolution higher than 80 meV [29]. The line asymmetry can be corrected by the η_2 coefficient of the VLS expansion. The first step is to try to cancel the coma aberration predominantly contributing to the asymmetry. Evaluationg of the optical path function [28, 31] and setting the F_{30} (primary coma) term of its Maclaurin expansion to zero yields the condition:

$$\eta_2 = \frac{3E}{2hc}\left[-\frac{\sin\alpha}{R_1}\left(\frac{\cos^2\alpha}{R_1} - \frac{\cos\alpha}{R}\right) + \frac{\sin\beta}{R_2}\left(\frac{\cos^2\beta}{R_2} - \frac{\cos\beta}{R}\right)\right] \tag{8.15}$$

which allows analytical calculation of η_2 to cancel the coma. In our case it yields $\eta_2 = -1.910 \cdot 10^{-4}\ mm^{-3}$. Applying this correction, the line asymmetry should be greatly reduced, remaining only in some asymmetry of its foot. The remaining symmetric broadening can be reduced by the optimization of the η_3 coefficient defined as [28]

$$\begin{aligned} \eta_3 = \frac{E}{2hc}\Bigg[&\frac{4\sin^2\alpha}{R_1^2}\left(\frac{\cos^2\alpha}{R_1} - \frac{\cos\alpha}{R}\right) - \frac{1}{R_1}\left(\frac{\cos^2\alpha}{R_1} - \frac{\cos\alpha}{R}\right)^2 + \frac{1}{R^2}\left(\frac{1}{R_1} - \frac{\cos\alpha}{R}\right) \\ &+ \frac{4\sin^2\beta}{R_2^2}\left(\frac{\cos^2\beta}{R_2} - \frac{\cos\beta}{R}\right) - \frac{1}{R_2}\left(\frac{\cos^2\beta}{R_2} - \frac{\cos\beta}{R}\right)^2 + \frac{1}{R^2}\left(\frac{1}{R_2} - \frac{\cos\beta}{R}\right)\Bigg] \end{aligned} \tag{8.16}$$

It is useful to note that the refinement of η should imply a crosstalk between η_3 and η_2 *i.e.,* the optimization of η_3 with the highest accuracy should be performed under re-optimization of η_2 at each iteration step to keep the profile symmetric. For our model case (for which the iteration has not been applied) returned $\eta_3 = -5.369 \cdot 10^{-5}\ mm^{-4}$. The iteration process is supposed to apply a correction on η_2 of the order $\sim 10^{-5}$ at convergence [29]. At this point, the spectrometer resolution should have reached the Gaussian linewidth limit, delivering a resolving power higher than 11600. No attempt has been made to optimize VLS expansion coefficients higher than η_3 because they can hardly be realized with sufficient accuracy in a realistic manufacturing process. The overall parameters of the VLS grating are summarized in table 8.3.

$R\ [mm]$	$\eta_0\ [mm^{-1}]$	$\eta_1\ [mm^{-2}]$	$\eta_2\ [mm^{-3}]$	$\eta_3\ [mm^{-4}]$
52949	1290	-0.1449	$-1.910 \cdot 10^{-4}$	$-5.369 \cdot 10^{-5}$

Table 8.3: *Parameters of the grazing spectrometer that maximize the quantity Efficiency* $\times\Omega$ *at* $E = 930$ *eV with the requirement* $DeltaE(\alpha, \beta, \eta, E_0) \leq 80\ meV$.

8.5.1 Conclusions

In summary, we simulated the VLS-grating based soft X-ray RIXS spectrometer to be located on the new Furka beamline at SwissFEL optimizing the grating parameters and spectrometer geometry. The spectrometer was designed using the Lagrangian multiplier approach *i.e.,* the energy resolution ΔE was set to be $< 80\ meV$ at 930 eV, whilst maximizing the solid angle Ω subtended by the grating. These measures allowed to maximize the transmission T of the grating while keeping the energy resolution lower than 80 meV. The lineshape asymmetry, due to the coma aberrations, was minimized by the optimization of the η_2 coefficient of the VLS power expansion. Furthermore, the remaining symmetric line broadening at large illuminations (due to higher-order aberrations) is reduced by optimization of η_3 which in turn allows an increase of the aberration-limited acceptance of the spectrometer. In routine experimental work, the optimal experimental parameters and spectrometer settings can be easily calculated using our code. Our analysis will also be implemented with a ray-tracing tool and will give a recipe to design and operate VLS spectrometers at large angular acceptance and in extended energy range without any major degradation of resolution beyond the Gaussian broadening factors.

References

[1] Winfried Schülke. *Electron dynamics by inelastic X-ray scattering*. Number 7. Oxford University Press, 2007.

[2] Akio Kotani and Shik Shin. Resonant inelastic x-ray scattering spectra for electrons in solids. *Reviews of Modern Physics*, 73(1):203, 2001.

[3] M Blume. Magnetic scattering of x rays. *Journal of Applied Physics*, 57(8):3615–3618, 1985.

[4] Luuk JP Ament, Michel Van Veenendaal, Thomas P Devereaux, John P Hill, and Jeroen Van Den Brink. Resonant inelastic x-ray scattering studies of elementary excitations. *Reviews of Modern Physics*, 83(2):705, 2011.

[5] ED Isaacs, PM Platzman, P Metcalf, and JM Honig. Inelastic x-ray scattering study of the metal-antiferromagnetic insulator transition in v 2 o 3. *Physical review letters*, 76(22):4211, 1996.

[6] J Zaanen, GA Sawatzky, and JW Allen. Band gaps and electronic structure of transition-metal compounds. *Physical review letters*, 55(4):418, 1985.

[7] Yao Wang, Yuan Chen, Chunjing Jia, Brian Moritz, and Thomas P Devereaux. Time-resolved resonant inelastic x-ray scattering in a pumped mott insulator. *Physical Review B*, 101(16):165126, 2020.

[8] Lucio Braicovich, J Van den Brink, Valentina Bisogni, M Moretti Sala, LJP Ament, NB Brookes, GM De Luca, M Salluzzo, T Schmitt, VN Strocov, et al. Magnetic excitations and phase separation in the underdoped la 2- x sr x cuo 4 superconductor measured by resonant inelastic x-ray scattering. *Physical review letters*, 104(7):077002, 2010.

[9] JP Hill, Girsh Blumberg, Young-June Kim, DS Ellis, S Wakimoto, RJ Birgeneau, Seiki Komiya, Yoichi Ando, B Liang, RL Greene, et al. Observation of a 500 mev collective mode in la 2- x sr x cuo 4 and nd 2 cuo 4 using resonant inelastic x-ray scattering. *Physical review letters*, 100(9):097001, 2008.

[10] J Schlappa, T Schmitt, F Vernay, VN Strocov, V Ilakovac, B Thielemann, HM Rønnow, S Vanishri, ANDREA Piazzalunga, X Wang, et al. Collective magnetic excitations in the spin ladder sr 14 cu 24 o 41 measured using high-resolution resonant inelastic x-ray scattering. *Physical review letters*, 103(4):047401, 2009.

[11] H Yavaş, M Van Veenendaal, J van den Brink, LJP Ament, A Alatas, BM Leu, MO Apostu, N Wizent, G Behr, W Sturhahn, et al. Observation of phonons with resonant inelastic x-ray scattering. *Journal of Physics: Condensed Matter*, 22(48):485601, 2010.

[12] Young-June Kim, JP Hill, H Yamaguchi, T Gog, and D Casa. Resonant inelastic x-ray scattering study of the electronic structure of cu 2 o. *Physical Review B*, 81(19):195202, 2010.

[13] LJP Ament, M Van Veenendaal, and J Van Den Brink. Determining the electron-phonon coupling strength from resonant inelastic x-ray scattering at transition metal l-edges. *EPL (Europhysics Letters)*, 95(2):27008, 2011.

[14] Pasquale Marra. Theoretical approach to direct resonant inelastic x-ray scattering on magnets and superconductors. *arXiv preprint arXiv:1605.03189*, 2016.

[15] Jeroen van den Brink and Michel van Veenendaal. Theory of indirect resonant inelastic x-ray scattering. *Journal of Physics and Chemistry of Solids*, 66(12):2145–2149, 2005.

[16] J Van den Brink and M Van Veenendaal. Correlation functions measured by indirect resonant inelastic x-ray scattering. *EPL (Europhysics Letters)*, 73(1):121, 2005.

[17] Jun John Sakurai. *Advanced quantum mechanics*. Pearson Education India, 1967.

[18] Leah Y Isseroff and Emily A Carter. Electronic structure of pure and doped cuprous oxide with copper vacancies: suppression of trap states. *Chemistry of Materials*, 25(3):253–265, 2013.

[19] Dung Duonghong, Enrico Borgarello, and Michael Graetzel. Dynamics of light-induced water cleavage in colloidal systems. *Journal of the American Chemical Society*, 103(16):4685–4690, 1981.

[20] K Domen, S Naito, T Onishi, and K Tamaru. Photocatalytic decomposition of liquid water on a nio? srtio3 catalyst. *Chemical Physics Letters*, 92(4):433–434, 1982.

[21] K Sayama and H Arakawa. Photocatalytic decomposition of water and photocatalytic reduction of carbon dioxide over zirconia catalyst. *The Journal of Physical Chemistry*, 97(3):531–533, 1993.

[22] JunkoáN Kondo et al. Cu 2 o as a photocatalyst for overall water splitting under visible light irradiation. *Chemical Communications*, (3):357–358, 1998.

[23] G Nagasubramanian, Alberto S Gioda, and Allen J Bard. Semiconductor electrodes: Xxxvii. photoelectrochemical behavior of p-type in acetonitrile solutions. *Journal of the Electrochemical Society*, 128(10):2158, 1981.

[24] Martina Dell'Angela, F Hieke, Marco Malvestuto, L Sturari, S Bajt, IV Kozhevnikov, J Ratanapreechachai, Antonio Caretta, Barbara Casarin, Filippo Glerean, et al. Extreme ultraviolet resonant inelastic x-ray scattering (rixs) at a seeded free-electron laser. *Scientific reports*, 6:38796, 2016.

[25] Jonathan Owen Tollerud, Giorgia Sparapassi, Angela Montanaro, Shahaf Asban, Filippo Glerean, Francesca Giusti, Alexandre Marciniak, George Kourousias, Fulvio Billè, Federico Cilento, et al. Femtosecond covariance spectroscopy. *Proceedings of the National Academy of Sciences*, 116(12):5383–5386, 2019.

[26] F Schaefers and M Krumrey. *REFLEC: A Program to Calculate VUV/X-ray Optical Elements and Synchrotron Radiation Beamlines*. BESSY, 1996.

[27] Joseph Dvorak, Ignace Jarrige, Valentina Bisogni, Scott Coburn, and William Leonhardt. Towards 10 mev resolution: The design of an ultrahigh resolution soft x-ray rixs spectrometer. *Review of Scientific Instruments*, 87(11):115109, 2016.

[28] G Ghiringhelli, ANDREA Piazzalunga, CLAUDIA Dallera, GABRIELE Trezzi, LUCIO Braicovich, T Schmitt, VN Strocov, R Betemps, L Patthey, X Wang, et al. Saxes, a high resolution spectrometer for resonant x-ray emission in the 400–1600 ev energy range. *Review of Scientific Instruments*, 77(11):113108, 2006.

[29] VN Strocov, T Schmitt, U Flechsig, L Patthey, and GS Chiuzbăian. Numerical optimization of spherical vls grating x-ray spectrometers. *arXiv preprint arXiv:1011.6310*, 2010.

[30] Gerhard Ingold, Rafael Abela, Christopher Arrell, Paul Beaud, Pirmin Böhler, Marco Cammarata, Yunpei Deng, Christian Erny, Vincent Esposito, Uwe Flechsig, et al. Experimental station bernina at swissfel: condensed matter physics on femtosecond time scales investigated by x-ray diffraction and spectroscopic methods. *Journal of synchrotron radiation*, 26(3):874–886, 2019.

[31] William Burling Peatman. *Gratings, mirrors and slits: beamline design for soft X-ray synchrotron radiation sources*. CRC Press, 1997.

Chapter 9

Conclusions

This thesis is focused on the innovative aspects related to the use of Free Electron Laser (FEL) radiation, consequently there is not a single scientific objective that is deeply discussed, but rather a constellation of different topics are outlined (*e.g.,* transport phenomena, molecular dynamics, chemical reactions, and biological structures) each one discussed with little details. To summarize this work in a few words, here i) we demonstrated the feasibility of X-ray Transient Grating (XTG) using a novel setup, which, together with its extent to Full XTG, allows to access regimes of transport so far inaccessible, thus opening a new field in nonlinear optics. ii) we showed the first vibrational dynamics with enantiomeric selectivity via time-resolved soft X-ray absorption unlocking the ability to access the dynamics of a selected atom in molecules, and iii) we reported a time resolved RIXS in the extreme ultraviolet where we explored the possibility which sees the Cu^{1+} participating in the decomposition of water into H_2 and O_2 under visible light radiation through photocatalysis mediated by the p-type semiconductor Cu_2O. In regards of the RIXS technique, we also presented the simulation on the design of the Furka soft X-ray RIXS spectrometer to be located on the Furka beamline at SwissFEL. We also elaborated on two additional experiments: macromolecular crystallography (synchrotron-based X-ray diffraction experiments have been also carried out and presented) through the novel Incoherent Diffraction Imaging technique which promises to overcome the nowadays limitation on biological samples resolution, and a multi-pulse approach, termed TRUECARS, that combines broadband and narrowband X-ray hybrid pulses with the scope to directly observe the evolution of a Conical Intersection with both high time and spectral resolution.

Each of these experiments shows pioneering aspects and may have a wide relevance in the near/mid future; the first two experiments are already in an advanced stage of development and interpretation, and will likely result in high-profile publications. The two latter experiments, here introduced only in the theoretical frame, are being constantly developed by multi-groups collaborations and will be soon converge in state-of-art experiments.

Finally, without the slightest doubt, the future of FELs is bright. The challenges will be many, but with more and most important scientific discoveries to come.

Stay curious.

Appendix

Fresnel propagation for the Talbot Effect

The following calculation seems to be nowhere to be found in literature. Thus, I thought that it might be useful to solve it here for the unfortunate student who will look for its solution in literature, not find it, and surrender because too lazy to perform him/herself. Since I often find myself to be that student, I would like to thank my friend Marco Pasini, belonging to the dark side of theoretical physics (University of Trieste), for the result.

We start from equation 4.10 which is reported for simplicity

$$E(x,y,z) = \frac{ik}{2\pi z} e^{-ikz} \int\int_{-\infty}^{+\infty} E_0(x',y',z_G) T(x') e^{-\frac{ik(x'-x)^2}{2z}} e^{-\frac{ik(y'-y)^2}{2z}} dx'dy' \tag{9.1}$$

where we set the incoming electric field as an incident plane wave $E_0(x',y',z_G) = E_0 e^{-ikz_G}$ and we remind the expression for $T(x)$ from eq. 4.5

$$T(x) = \sum_n c_n e^{-ink_G x}. \tag{9.2}$$

The full expression now reads:

$$E(x,y,z) = E_0 \frac{ik}{2\pi z} e^{-ik(z+z_G)} \sum_n c_n \int\int_{-\infty}^{+\infty} e^{-ink_G x'} e^{-\frac{ik(x'-x)^2}{2z}} e^{-\frac{ik(y'-y)^2}{2z}} dx'dy' \tag{9.3}$$

which can be cleverly subdivided as follows:

$$E(x,y,z) = E_0 \frac{ik}{2\pi z} e^{-ik(z+z_G)} \sum_n c_n \underbrace{\left(\int_{-\infty}^{+\infty} e^{-ink_G x'} e^{-\frac{ik(x'-x)^2}{2z}} dx' \right)}_{A} \underbrace{\left(\int_{-\infty}^{+\infty} e^{-\frac{ik(y'-y)^2}{2z}} dy' \right)}_{B}. \tag{9.4}$$

We start with B being the simplest of the two:

$$B \equiv \int_{-\infty}^{+\infty} e^{-\frac{ik(y'-y)^2}{2z}} dy' \tag{9.5}$$

Here we simply change the variable $\frac{k}{2z}(y'-y)^2 \to u^2$ which leads to the differential $dy' \to du\sqrt{\frac{2z}{k}}$, thus we get:

$$B = \sqrt{\frac{2z}{k}} \underbrace{\int_{-\infty}^{+\infty} e^{-iu^2} du}_{\sqrt{\frac{\pi}{2}}(1-i)} = \sqrt{\frac{\pi z}{k}}(1-i) = \sqrt{\frac{\pi z}{k}} e^{-i\frac{\pi}{4}} \tag{9.6}$$

We now focus on A:

$$A \equiv \int_{-\infty}^{+\infty} e^{-ink_G x'} e^{-\frac{ik(x'-x)^2}{2z}} dx' = \int_{-\infty}^{+\infty} e^{-\frac{ik}{2z}\left(x'^2 - 2x'\left(\frac{nk_G z}{k} - x\right) + x^2\right)} dx'. \tag{9.7}$$

We complete the square by adding and subtracting the quantity $\frac{2nk_G z}{k}x - \frac{n^2 k_G^2 z^2}{k^2}$ inside the exponential term. By doing so, we obtain:

$$A \equiv e^{-ink_G x} e^{\frac{in^2 k_G^2}{2k} z} \int_{-\infty}^{+\infty} e^{-\frac{ik}{2z}\left(x' - \left(\frac{nk_G z}{k} - x\right)\right)^2} dx'. \tag{9.8}$$

We recognize the same integral form as B which gives a now known result equal to $\sqrt{\frac{\pi z}{k}} e^{-i\frac{\pi}{4}}$. Combining the results for A and B, we finally have:

$$A \cdot B = \frac{\pi z}{k} e^{-i\frac{\pi}{2}} e^{-ink_G x} e^{\frac{in^2 k_G^2}{2k} z} = -i\frac{\pi z}{k} e^{-ink_G x} e^{\frac{in^2 k_G^2}{2k} z}. \tag{9.9}$$

Combining the result, we obtain the final result

$$E(x,y,z) = \frac{E_0}{2} e^{-ik(z+z_G)} \sum_n c_n e^{-ink_G x} e^{\frac{in^2 k_G^2}{2k} z}. \tag{9.10}$$

We can finally consider $z_G = 0$ and rescale the electric field amplitude $\frac{E_0}{2} \to E_0$. Thus, we obtain:

$$E(x,y,z) = E_0 e^{-ikz} \sum_n c_n e^{-ink_G x} e^{\frac{in^2 k_G^2}{2k} z}. \tag{9.11}$$

which is the desired result.

Slope Error of a VLS grating

The slope errors could be thought as imperfections that locally change the direction of the normal to the optical surface and therefore change the direction of the reflected radiation. In the figure 9.1 $\delta\vartheta$ is the change in the normal direction and $2\delta\vartheta$ (since the angle is doubled by the reflection) is the change in the reflected beam.

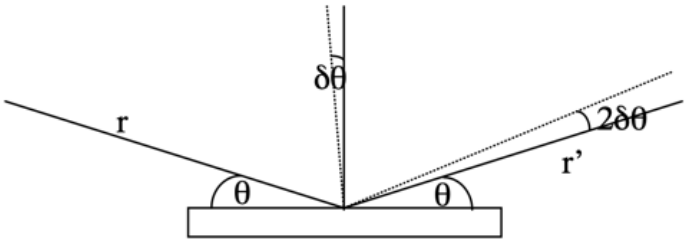

Figure 9.1: *The angular change in the normal direction and in the reflected beam direction due to local imperfections of the grating.*

Given a set of measurement of this angle $y_1, ..., y_n$ with an overall mean $\bar{y}$, we define the sample variance σ and the rms as:

$$\sigma = \sqrt{\frac{\sum_i (y_i - \bar{y})^2}{n-1}}; \quad rms = \sqrt{\frac{\sum_i y_i^2}{n}}. \tag{9.12}$$

For a spherical VLS grating, the set of measured $y_i = \delta\vartheta_i$ (for a large number of samples *i.e.*, $n \gg 1$) is attended to have a Gaussian distribution around a mean value $\bar{y} = \bar{\delta\vartheta} = 0$. Thus, we can see that $\sigma \sim rms$. It follows that the FWHM of the distribution is $FWHM = 2.355 \cdot \sigma \sim 2.355 \cdot rms$, which is the formula we used.

Acknowledgements

A special gratitude goes to my supervisor Dr. Claudio Masciovecchio. You encouraged me, helped me, and above all beard with me throughout my PhD. Your non-restrincting method allowed me to grow both from a personal and working perspective.

A mention goes to Prof. Dr. Loredana Casalis and Dr. Pietro Parisse. You let me join the NanoInnovation Lab and helped me understand the bio-world and experience the FAM. A mention goes to the NanoInnovation Lab members and collaborators throughout the years. We shared and enjoyed a lot of moments inside and outside the working time.

A mention goes to the IUVS beamline memebers: Dr. Francesco D'amico, Dr. Barbara Rossi, and Dr. Maria Pachetti: you introduced me to the fascinating world of Synchrotron Raman spectroscopy.

A mention goes to the BioLab coordinator Dr. Paola Storici and to Dr. Barbara Giabbai who let me join them and introduced me to the magical world of protein synthesis, purification and crystallization. A mention goes to the ICEGB members Dr. Corrado Guarnaccia and Dr. Sotir Zahariev who supported me in my 2D protein crystallization research.

A mention goes to Dr. Luisa Barba and Dr. Alberto Cassetta who helped me in the sample preparation and XRD experiments.

A mention goes to Dr. Sara Catalini and Prof. Dr. Renato Torre who let me, and helped me perform measurements at LENS.

A mention goes to the FERMI members Dr. Riccardo Mincigrucci, Dr. Alessandro Gessini, Dr. Filippo Bencivenga , Dr. Emiliano Principi, Dr. Laura Foglia, Dr. Marco Malvestuto, Dr. Antonio Carretta and Simone Laterza. We shared a lot of interesting experimental time together.

A mention goes to Prof. Dr. Majed Chergui. You introduced to your team at the EPFL and you have always been ready to share your never-banal opinion on different subjects.

A mention goes to Prof. Dr. Christoph Bostedt, who let me join the Alvra group at PSI. A mention goes to my co-supervisor in Switzerland, Dr. Chris Milne, who took several interesting science and non-science related talks with me and let me complete my year abroad. A mention also goes to the Alvra group. Among them, I'd like to thank Dr.

Claudio Cirelli for explaining to me all the mechanism behind the endstation. A mention goes to Dr. Benedikt Rosner and Dr. Gregor Knopp. We shared a lot of discussions on possible experiment pathways. A special mention goes to Dr. Eugenio Ferrari: you introduced me to the wonderful world of programming and data analysis. I'll never ~~forgive~~ forget you for this.

A special mention goes to my fake, but more than real, co-supervisor in Switzerland, Dr. Cristian Svetina. You helped me feeling warm in a cold place. I sense a bright future together.

A mention goes to Dr. Elia Razzoli, his wife and daughter. We shared a lot of happy work- and non work-related experiencies. A mention goes to Dr. Eugenio Paris which granted the opportunity to perform Laue measurement. A mention goes Prof. Dr. Luc Patthey who let me join the Furka group.

To my life-coaches, my mother Elena and my father Sandro: I owe it all to you.
To Emanuele: you are always there for me and mom.
To Wilma: we share small amounts of time together, but it is the proof that quality overcome quantity.
To my grandparents, Fiorina and Sergio who raised me. Each of you is part of what I am now.
To Elisabetta, who keeps on choosing and supporting me.
To DAM+G, Paso and Michele who somehow like share things with a weirdo.
To Luigi, my flatmate. We joined unforgettable battlefields together.
To Rocket, Tekcor, Volpe, Ninja, SypherPK, Tfue and Fresh.

To all the other people who have been there when I needed, you made me strong.
To all the people who broke promises and left without a trace, you made me even stronger.

To you all,

Thank you.

The End.